DOCTORAL THESIS

Particle-fluid interactions under heterogeneous reactions

Thamali Rajika Jayawickrama

Thermochemical conversion

LULEÅ UNIVERSITY OF TECHNOLOGY

In memory of Chinedu and all mothers who sacrificed their lives and lost their dreams for the sake of their children...

Abstract

Particle-fluid flows are involved in many natural processes and industrial applications; some examples are drying, solid fuel combustion, gasification, and catalytic cracking. It is vital to understand the phenomena involved in particle-fluid flows in depth for design, predictions and process improvements. Computational fluid dynamics (CFD) can be a robust tool for these studies that complements costly experimental trials. Current computational power and resources do not allow numerical simulations to resolve all physical and chemical scales in a single simulation. State-of-the-art in large-scale numerical simulations is to carry out simulations at larger scales with sub-grid models for small-scale phenomena. Therefore, the accuracy of the models is key to better predictions in large-scale simulations.

Particle-fluid flows have complexities due to many reasons. One of the main challenges is to describe how the particle-fluid interactions vary when the particles are reacting. Particles and the fluid interact through momentum, heat, and mass exchange. Momentum, heat, and mass exchange are presented by the drag coefficient (C_d), Nusselt number (Nu), and Sherwood number (Sh) in fluid dynamics. Conventional models neglect the effects of net fluid flow generated by heterogeneous chemical reactions called *Stefan flow*.

This work aims to study how Stefan flow affects the momentum, heat, and mass transfer between particles and fluid in a particle-fluid flow. A series of numerical simulations were performed by increasing complexity step by step. Particle boundary layers were resolved in all the simulations, and the particle interior was also resolved in the last stage. With a special interest in entrained flow biomass gasification (EFBG), this work has chosen parameters relevant to EFBG.

In the first step, particle-resolved numerical simulations were carried out for an isolated particle immersed in a uniform, isothermal (and non-isothermal) bulk fluid with a uniform Stefan flow. Both isothermal and non-isothermal simulations have shown that the Stefan flow has significant effects on drag coefficient (C_d) and Nusselt number (Nu). We have observed from isothermal results that the decrease/increase of the drag coefficient (C_d) is due to expansion/shrinkage of the boundary layer thickness, which leads to a change in the viscous force. Based on that, a physics-based drag coefficient (C_d) model was developed. For the next step, the drag coefficient (C_d) model was extended and modified for a uniform non-isothermal bulk fluid flow. Furthermore, a new Nusselt number (Nu) model was developed using volume-averaged temperature, which captures the variation of thermo-physical parameters due to the temperature gradient between particle and bulk fluid. The model agrees well with the simulation data with a single fitting parameter.

The second step was to explore the effects of neighboring particles on the drag coefficient (C_d) with a uniform Stefan flow under isothermal conditions. Stefan flow and neighbor particle effects act on the particle independently when particle distance is greater than 2.5 diameters ($L/D > 2.5$). However, at $L/D \leq 2.5$, Stefan flow effects dominate, and a strong force that expels particles from each other was observed.

The models previously developed under ideal conditions (uniform Stefan flow, atmospheric pressure) might not represent realistic conditions at reacting flows. Therefore, the last step of this thesis was particle interior resolved numerical simulations for an isolated char particle under gasifying conditions. The drag coefficient (C_d), Nusselt number (Nu) and Sherwood number (Sh)

from the simulations have been compared with conventional models without Stefan flow. We have observed that conventional drag coefficient (C_d) and Nusselt number (Nu) models do not accurately predict the force acting on a particle and heat transfer between the particle and bulk fluid.

The performance of the point-particle approach for reacting particle-fluid flows, commonly used in large-scale simulation, was also investigated by comparing it with particle interior resolved simulations for a gasifying particle. The results showed a significant deviation between the results of the point particle model and resolved particle simulations. Several key uncertainties in the models, such as the effectiveness factor and external heat and mass transfer, were identified.

This work has shown that the effects of Stefan flow are not negligible in reacting particle-fluid flows. Developed drag coefficient (C_d) and Nusselt number (Nu) models can be used to improve large-scale simulations' predictions. The study also contributes to widening the understanding physics of particle-fluid interactions in reacting particle-fluid flows. Conventional models for drag coefficient (C_d) and Nusselt number (Nu) (and Sherwood number (Sh)) do not represent the momentum and heat transfer (and mass transfer) between a particle and the bulk fluid accurately when there is a Stefan flow due to heterogeneous reactions during char gasification. Therefore, the models should be further improved considering the effects of Stefan flow.

The models developed in this work are idealized for a uniform Stefan flow, atmospheric pressure, and spherical particle. It could be further improved for non-uniform Stefan flow, high pressure, and different geometries. This study mainly focused on the parameter range of gasification for model development. Therefore, it is important to test the effects of Stefan flow for a wider range applicable to other applications, such as combustion, and test whether the phenomena are the same as observed in this work. We focused on char gasification to study the effects of Stefan flow in more realistic conditions and to compare it with the point-particle method. That also could be studied for a wider range of applications and find at what conditions one has to consider the effects of Stefan flow on drag coefficient (C_d), Nusselt number (Nu), and Sherwood number (Sh). Furthermore, it would be important to find the models predicting closer to the resolved-particle simulations for a particle with Stefan flow to be used in the point-particle approach. Improving effectiveness factor models, including non-uniform temperature inside the particle, is also vital.

Acknowledgment

First and foremost, I would like to express gratitude to my principal supervisor: Kentaro Umeki (professor at the Luleå University of Technology), for his utmost patience in working with me, continuous guidance throughout this period, and input for the research. Thanks again for creating a stress-free environment for the PhD students.

I want to thank Nils E. L. Haugen (Senior Research Scientist at SINTEF and Adjunct professor at the Luleå University of Technology) for allowing me to work under his supervision at the Norwegian University of Science and Technology. I feel lucky to work with him; he was always an inspiration. Thank you very much for your support and contribution to the research.

Matthaus Babler (associate professor at KTH Royal Institute of Technology) was always ready to help by providing his opinion whenever necessary. Thank you very much for all the suggestions and corrections.

Thanks to Muhammad Aqib Chishty (post-doctoral researcher at Luleå Unversity of Technology) for the assistance during difficult times of research and for being available for help.

The research work presented here has been carried out with financial support from Swedish Research Council (Vetenskapsrådet) under the grant: 2015-05588. The simulations of this work were performed on resources, *Kebnekaise*, provided by the Swedish National Infrastructure for Computing (SNIC) at High-Performance Computing Center North (HPC2N) and *Fram*, provided by the Norwegian Research Infrastructure Services (NRIS). I want to thank all the staff of HPC2N and NRIS for their support.

I want to thank unknown people who shared their code snippets for free on many internet platforms, which made the work easier.

I also want to thank all the group members of the 'Thermochemical conversion' group and colleagues of the energy science division for our *fika* discussions and for making a friendly environment in the division. Further, I want to thank all the administrative staff of the university.

Special thank goes to my closest friends at Luleå: Shikha, although she is no longer with us; Chinedu, Rosa, Zahra-Mehradad, David, Angel, Tayebeh, Akila, Prasanna, Thilini-Harindu, and Sri Lankan friends, for being with me during ups and downs of my life here in Luleå. All the other friends back in Sri Lanka and around the world are not forgotten, especially: Asanthi and Nishanthi.

Most importantly, I want to thank my mother for going through all the hardships of her life because of us. Last but not least, I want to thank my sisters Hiranthi, Madhuri, Chandima, and Madumali, my all brothers-in-law, and my lovely nephews for being with me through thick and thin and for the unconditional love given to me.

List of appended papers

This thesis is based on work presented in the following papers. The contribution from the author to each paper is followed by its reference (also summarized in Table 1).

1. Paper I
   Thamali R. Jayawickrama; Nils Erland L. Haugen; Matthaus U. Babler; M.A. Chishty; Kentaro Umeki. (2019). The effect of Stefan flow on the drag coefficient of spherical particles in a gas flow. International Journal of Multiphase Flow, 117, 130–137.

   The author made necessary changes to the simulation codes, conducted the simulations, and developed the model with the co-authors' support. The author drafted the manuscript, and revisions were made together with the co-authors.

2. Paper II
   Thamali R. Jayawickrama; Nils Erland L. Haugen; Matthaus U. Babler; M.A. Chishty; Kentaro Umeki. (2021). The effect of Stefan flow on Nusselt number and drag coefficient of spherical particles in non-isothermal gas flow. International Journal of Multiphase Flow, 140, 103650.

   The author developed the necessary codes and carried out the simulations. The author developed the models with the support of co-authors. The author drafted the manuscript, and revisions were made together with the co-authors.

3. Paper III
   Thamali R. Jayawickrama; M.A. Chishty; Nils Erland L. Haugen; Matthaus U. Babler; Kentaro Umeki. (2022). The effect of Stefan flow on flow surrounding two closely located particles. Submitted.

   The author carried out the simulations. The author drafted the manuscript, and revisions were made together with the co-authors.

4. Paper IV
   Thamali R. Jayawickrama; Nils Erland L. Haugen; Matthaus U. Babler; M.A. Chishty; Kentaro Umeki. (2022). Drag during heterogeneous char reactions: particle-resolved approach. Unpublished manuscript.

   The author developed a code for the numerical simulation of char gasification and carried out the simulations. Post-processed and analyzed the simulation data with the support of

co-authors. The author drafted the manuscript, and revisions were made together with the co-authors.

5. Paper V
Thamali R. Jayawickrama; Nils Erland L. Haugen; Kentaro Umeki. (2022). On the inaccuracies of point-particle approach for char conversion modeling. Unpublished manuscript.

The author developed a code for the numerical simulation of char gasification and carried out the simulations. The author developed a point-particle simulation code and improved it with co-authors' support. Post-processed and analyzed the simulation data with the support of co-authors. The author drafted the manuscript, and revisions were made together with the co-authors.

Table 1: Contribution of author for all the publications in the thesis.

Contribution	Paper I	Paper II	Paper III	Paper IV	Paper V
Conceptualization	-	-	-	-	-
Methodology	TRJ	TRJ	TRJ	TRJ	TRJ
Software	TRJ	TRJ	TRJ	TRJ	TRJ
Validation	TRJ	TRJ	TRJ	TRJ	TRJ
Formal analysis	TRJ	TRJ	TRJ	TRJ	TRJ
Investigation	TRJ	TRJ	TRJ	TRJ	TRJ
Resources	-	-	-	-	-
Data curation	TRJ	TRJ	TRJ	TRJ	TRJ
Writing original draft	TRJ	TRJ	TRJ	TRJ	TRJ
Visualization	TRJ	TRJ	TRJ	TRJ	TRJ

Contents

Chapter 1

Introduction

"Some people say, How can you live without knowing? I do not know what they mean. I always live without knowing. That is easy. How you gect to know is what I want to know."

—Richard Feynman

This thesis attempts to answer some fundamental and specific questions related to the thermochemical conversion of biomass. The fundamental work carried out for this thesis deals with the effects of reactions on particle-fluid interactions in particle-fluid flows. Results can be applied not only to thermochemical conversion of biomass but to any particle-fluid flow with reacting particles. Specific questions address char gasification during entrained flow biomass gasification (EFBG) out of thermochemical processes.

This chapter discusses the importance of biomass as a source of energy and the challenges in using biomass for thermochemical conversion due to the complex nature. Then, research questions are introduced with special emphasis on EFBG. At the end of this chapter, the aim of the thesis and its research procedure is summarized.

1.1 The role of biomass as an energy source

Our ancestors have utilized biomass for producing energy since the day, one of them struck two wood pieces together and produced fire. Even before the Industrial Revolution, wood made about 40% of the world's energy usage [1]. After petroleum fuels came into play, wood became less noticed in developed countries while developing countries continued to use wood. However, during the last decades, climate change has brought back the interest in biomass as a clean energy source.

The major culprit of climate change is carbon dioxide (CO_2) among other Green House gases (GHGs), and high concentration of CO_2 in the atmosphere is due to anthropogenic emissions. There are two main approaches to mitigating the effects of GHGs. One way is to remove the CO_2 from the atmosphere, and the other is to stop further emissions. CO_2 already in the atmosphere can be sequestered by capturing and storing. Future emissions can be reduced using renewable sources of energy, sustainable ways of living, using efficient methods and machinery in the industry, Etc.

Having the largest forest area in European Union, which is continuing to increase annually, biomass is one of the best renewable sources for Sweden. Biomass has its advantages and disad-

vantages compared to other renewable energy sources. Biomass may not be as environmentally friendly as wind and hydro-power due to processing activities, but the certainty of availability is higher. Non-engineered biomass may be cumbersome to use too.

The next section will discuss the complexities of biomass as a source for energy generation purposes.

1.1.1 Biomass and its complexities

Biomass can be very complicated due to the heterogeneity inherited from the source such as different parts of a tree and the huge number of sources where it can come from such as many varieties of trees and different sources. Heterogeneity can make differences in density, chemical compounds, and physical structure, including porosity. Then, the pre-processing such as milling can also vary the size and shape.

Further, biomass conversion is a multi-phase process involving fluid and solid (a.k.a, particle-fluid flow). Particle and fluid flow dynamics vary significantly with particle concentration, size, fluid parameters, Etc. As an example, the behavior of an isolated particle in a fluid will not be the same as a particle in a fluid with high particle concentrations (fluidized bed or moving-bed processes). Reactions of the particles with fluid (heterogeneous reactions) and fluid phase reactions (homogeneous reactions) make the variations of thermo-physical properties of all phases and interactions between particles and fluid. This complicated nature of biomass itself, phenomenon due to reactions, and multi-particle effects make it harder to understand and predict in particle-fluid flows.

A huge variation in parameters such as size, shape, and many more makes it hard to design experiments related to biomass conversion due to the requirement of many experiments to be conducted. Therefore, theoretical and numerical methods backed up by experimental data would be the more practical way of studying biomass conversion as the variation of parameters can be easily fed into a code or a model than conducting an experiment in many ways (space, money, time, Etc.). This thesis focuses only on the thermochemical conversion methods of biomass. The next section will discuss the thermochemical conversion methods available for biomass and their advantages/disadvantages.

1.2 Thermochemical conversion of biomass

Thermochemical conversion of biomass can be categorized into pyrolysis, combustion and gasification. This thesis will mainly focus on the gasification. *Gasification* is the conversion of any carbonaceous fuel to a gaseous product with usable heating value [2]. Gasification produces syngas (synthesis gas) which consists of different concentrations of carbon monoxide (CO) and hydrogen (H_2) with other gases.

The reactors used for gasification can be classified as; packed-bed, fluidized-bed or entrained-flow reactors based on how fuel interacts with the gasifying agent. Each reactor type has common features, while there are differences based on the manufacturer. Table 1.1 shows the advantages and disadvantages of each reactor type. Among three types of processes, entrained flow gasification (EFG) has the highest share of syngas production in coal gasifiers due to its advantages over other technologies [3] such as high carbon conversion, high syngas yield, high single unit capacities, Etc. Although the EFG is at the commercial level with large-size plants utilizing coal, EFG utilizing biomass is not at the commercial level yet due to some barriers [4, 5]. Further, there are certain challenges in EFG process itself. The major is modeling char gasification [6, 7].

First, let us look at specific issues in biomass that hinder the industrialization of EFBG and then discuss the challenges in modeling the char gasification process.

Table 1.1: Advantages and disadvantages of different gasification reactors [2, 3].

Reactor	Advantages	Disadvantages
Fixed-bed	less fuel preparation simple feeding system less process control less oxygen demand low capitol and operational expenditure	low exit gas temperature (tar in gas) low carbon conversion low heat recovery from the exit gas more gas cleaning required
Fluidized-bed	better gas quality moderate oxygen and steam consumption potential for large capacities littel fuel preparation high fuel flexibility	complex process control less carbon conversion tar in the product gas
Entrained-flow	high carbon conversion high syngas yield high single unit capacities clean syngas	lot of fuel preparation high oxygen demand soot formation

1.2.1 Entrained flow biomass gasification (EFBG) and challenges

Coal gasification technologies are not suitable for biomass gasification due to the differences in properties: different reactivity, particle size, feeding issues related to biomass, Etc. Therefore, it is harder to use coal gasification technology for biomass without tailoring. There are very few studies on the fluid dynamics of particle-fluid flows of an entrained flow biomass gasifier. To fill the gap of knowledge, it is vital to know the following:

- what are the differences between biomass and coal, and where it affects the gasification process as opposed to the industrialization of EFBG
- studying particle-fluid interactions under EFBG reactor conditions in detail

Biomass and coal vary physically (size, shape, particle density, bulk density, moisture content, morphology, Etc) and chemically (C, H, O, N, S, Etc.). Biomass particles have a more elongated shape due to their fibrous nature while coal particle are more spherical. The moisture content of biomass is generally higher in contrast to coal, and biomass is also hygroscopic. That makes biomass cohesive and less flowable, negatively affecting the feeding system and mixing with the gasifying agent (CO_2, steam) [5].

High soot concentration of syngas in entrained-flow biomass gasifiers is another main issue that needs to be addressed [8, 9, 4]. Soot formation reduces gasification efficiency and causes fouling and clogging of systems. Göktope et al. [10] showed that the primary soot formation can be reduced by varying inter-particle distance in a high-temperature entrained-flow biomass gasification process. They observed an interaction between fuel particles due to the overlap of the wake behind the particles. Overlap occurs in high particle concentrations leading to high soot volume fractions.

The observations suggest that the particle-fluid interactions are affecting the soot formation. This also can be related to the hygroscopic nature of biomass, making particles sticky, and hindering the proper mixing of particles in the bulk fluid. Therefore, **we can hypothesize particle-fluid interactions play a major role in soot formation**.

EFBG can be categorized into particle-laden flows according to fluid dynamics. Particle-laden flows are multi-phase flows with one or more dispersed phases and a continuous bulk phase.

Particles may be solid particles, liquid droplets, or gas bubbles. In gasification, the suspended phase is solid biomass particles. More specifically EFBG process is a particle-laden flow with heterogeneous and homogeneous reactions. Further, above observations suggest that the particle interactions via the fluid (indirect particle-particle interactions) play an important role (Soot formation reaction phenomena will not be discussed here). Let us try to understand particle-fluid interactions of reacting particles with closely spaced particles in particle-laden flows.

1.3 Particle-fluid interactions

Particle-fluid interactions in particle-laden flow occurs through momentum, heat and mass exchange between particle and fluid. In fluid dynamics momentum, heat and mass exchange is represented by drag coefficient (C_d), Nusselt number (Nu) and Sherwood number (Sh). Particle-fluid interaction posibilities in a particle-laden flow can be listed as follows according to classical fluid mechanics (see Fig.1.1):

1. One way coupling
   The particle is affected by the fluid, but the feedback from the particles to the fluid is not considered or negligible (classical C_d, Nu and Sh models can be used),

2. Two way coupling
   The particle immersed in the fluid is affected by the fluid and the fluid is also affected by the particle (classical C_d, Nu and Sh models can be used),

3. Three way coupling
   Apart from two way coupling, indirect interactions between the particles exist via the fluid and not negligible (classical C_d, Nu and Sh do not consider the effect),

4. Four way coupling
   Direct interaction between particles, i.e. particle-particle collisions.

There are two important factors in classical particle-fluid interactions. One is; classical models (C_d, Nu and Sh) neglect the indirect particle interactions via the fluid (Three-way coupling). The other is; the effect of reactions on particle-fluid interactions is neglected in classical particle-fluid interactions (see Fig. 1.1) . Since the particle volume fraction in EFBG is less than 0.001, we can neglect direct particle-particle interactions (four-way coupling).

Interaction between neighboring particle effects via the fluid in a particle-laden flow can also affect the exchange of momentum, mass, and heat between particle and fluid. These are also further discussed in section 2.1 and 2.2.

When a non-equimolar reaction occurs during a heterogeneous reaction, the reaction generates an inward/outward flow to/from the solid phase. This flow is usually called *Stefan flow*. Non-equimolar heterogeneous reactions occur during gasification, such as the Buoduard reaction:

$$\mathrm{C}_s + \mathrm{CO}_{2g} \rightarrow 2\,\mathrm{CO}_g, \tag{1.1}$$

Water-gas reaction:

$$\mathrm{C}_s + \mathrm{H_2O}_g \ \rightarrow \mathrm{CO}_g + \mathrm{H}_{2g}. \tag{1.2}$$

Apart from changes in thermophysical properties of the gas occurring around the vicinity of a reaction, when there is a Stefan flow, a no-slip boundary will not be applicable, and it can vary the momentum, heat, and mass exchange between the particle and fluid. There is some research work on the effect of Stefan flow on the force acting on a particle, and very few work on the mass and heat transfer. More details can be found in section 2.2.

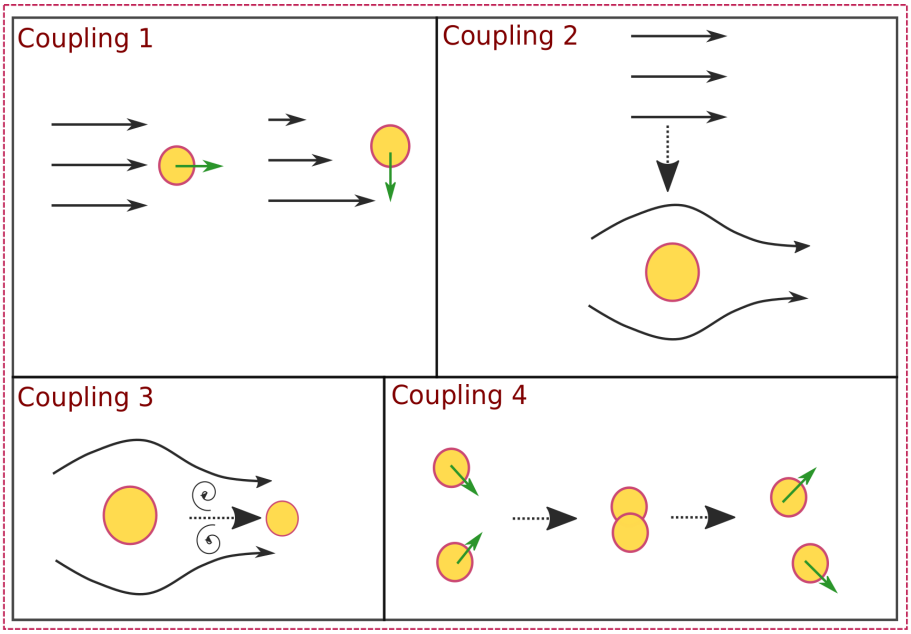

Figure 1.1: Interactions occurring in particle-laden flow between particles and the bulk fluid. Coupling 1 alone is called one-way coupling, 1 and 2 together is called two-way coupling, 1, 2 and 3 together is called 3-way coupling and 1, 2, 3 and 4 together is called 4-way coupling. Dark arrows represent the particle velocity and dashed arrows represent transition in stages. Particles are schematically represented with yellow circles.

There are no models for C_d, Nu and Sh, or studies found in literature considering both effects of Stefan flow and neighboring particle. Considering the lack of knowledge on the effects of Stefan flow alone and the effects of closely located particles with Stefan flow on momentum, heat, and mass exchange between particle and fluid in particle-laden flow; the research gaps can be addressed by the following research questions.

- **RQ1-What are the effects of Stefan flow on the interaction between particles and the bulk fluid?**
- **RQ2-How do reacting neighboring particles interact through the change in fluid flow?**

The next section discusses about the challenges in modeling char gasification, which is a major challenge in overall EFG process.

1.3.1 Char gasification

Char gasification is the slowest process during char conversion [11, 6, 7]. Therefore, it controls the whole fuel conversion process.

Char gasification can lie in 3 regimes based on reactive time scales (τ_r) and diffusive time scales (τ_D). When $\tau_r >> \tau_D$, diffusion is fast, and char conversion is controlled by the chemical reaction rates. This region is called 'Zone I' where particle reacts uniformly, varying the density of the particle and diameter is constant [12, 11, 13]. When $\tau_r << \tau_D$, diffusion time scales are high, and the diffusion of species controls the reaction to the particle. As the τ_r is lower, and

reaction rates are high, species do not reach inside the particle, and the reaction happens at the particle's periphery, varying the particle's diameter and density constant. This region is called 'zone III'. When the $\tau_r \approx \tau_D$, both diffusive and reactive time scales are important, and both particle density and diameter vary. This is non-trivial to the model since both intrinsic chemical reaction rates and pore-diffusion affect the overall reaction rate. One can resolve the whole particle instead of using models in a Computational Fluid Dynamics (CFD) simulation. However, this is expensive in terms of computational power and time specially when there are many particles in a flow. Then, the point-particle method can be used where a particle is considered a point in space that does not occupy any volume. The effectiveness factor (η) is used to predict internal properties using surface properties of a char particle in CFD simulations based on Thiele modulus (Th) [13]. The momentum, heat, and mass exchange between particle and fluid are modeled respectively through C_d, Nu and Sh. Therefore, it is critical to use accurate models in this approach for C_d, Nu and Sh. In general, the models used for the approaches are classical models, which do not consider either the effect of Stefan flow or the effect of neighboring particles.

No previous studies are refining a gasifying particle's exterior and interior. Therefore, it is important to study the variation of C_d, Nu and Sh during char gasification and see the effects of Stefan flow. Furthermore, to compare refined simulation results with point-particle methods to study the accuracy of the point-particle approach in char gasification and other particle-laden flows with Stefan flow. This can identify current point particle approaches' drawbacks and ways to improve predictions.

Previous research questions will address the effects of Stefan flow in particle-fluid flows in general. However, one of our purposes is to enhance the knowledge of particle-fluid interactions in EFBG. Therefore, we will focus on the more specific case of char gasification in EFBG where research questions can be formulated as follows:

- **RQ3-What are the effects of Stefan flow on the interaction between particles and the bulk fluid during char gasification?**
- **RQ4-How does the point-particle methods perform in char gasification compared to particle-resolved simulations?**

So far we have discussed the importance of modeling momentum (C_d), heat (Nu) and mass transfer (Sh) for particle-laden flows with reacting particles. Let's have a general look why development of models is important and status of model development for thermochemical conversion of biomass.

1.4 Why models?

The effects of reactions in particle-laden flow can be studied using experimental methods, theoretical methods or numerical simulations. The main focus of this work is numerical and theoretical (model development). In numerical simulations, computational power is used to solve the governing equations of the fluid flow (Navier-Stokes equations and other) using numerical methods.

Particle-laden reactive flows tend to be very complex due to multi-phase interactions, turbulence, reactions and many other phenomena. These phenomena are occurring at different length and time scales. The wide variation of length scales in particle-laden flow are shown in Fig. 1.2.

The reactor scales can be in the order of meters ($\mathcal{O}(10^1 - 10^0)$ m), multi-particle effects in order of millimeters ($\mathcal{O}(10^{-2} - 10^{-3})$ m), single particle effects in order of millimeters to micrometers ($\mathcal{O}(10^{-3} - 10^{-6})$ m), particle pore scales in micrometers to nanometers ($\mathcal{O}(10^{-6} - 10^{-9})$ m) and reaction scales in the order of nanometers ($\mathcal{O}(10^{-9})$ m). Time scales also have a wide variation. It is not possible to do simulations that refine all the scales of a reactor with current state in computational resources. Therefore, models are used to bridge the gap between small

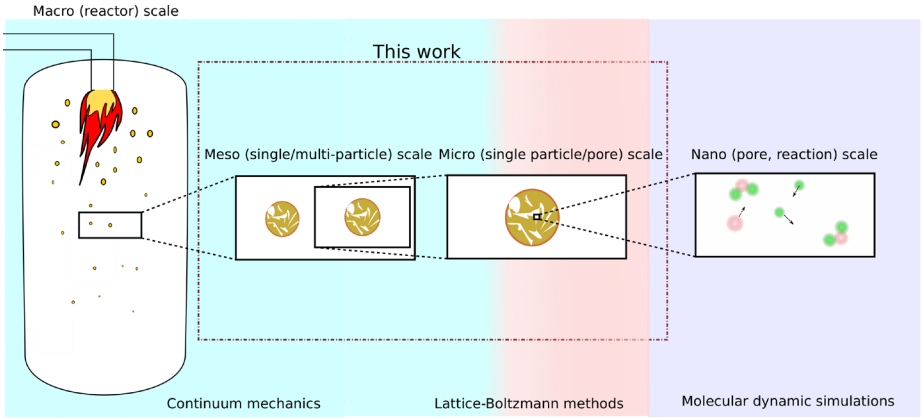

Figure 1.2: The wide variation of length scales in a large scale reactor. Macro scales are in the magnitude of meter (m), mesoscale is in the magnitude of milimeter (mm), microscale is in the magnitude of micometer (μ m) and nanometer is in the magnitude of nanometer (nm).

and large scales. For example, reaction models are used for the simulation of reactions inside the particles. Detailed reaction models are developed using molecular dynamic simulations (MDS). These reaction models can be used in single or multiple refined, reacting particle simulations using Lattice-Boltzmann methods or contimuum methods to develop C_d models for a reacting particle. The C_d models developed for a single particle can be used in reactor scale simulations using point-partcle simulations.

Single particle scale in EFBG lies in the $\mathcal{O}(10^{-3} - 10^{-6})$ m and multi-particle scales can vary in the $\mathcal{O}(10^{-4} - 10^{-2})$ m. According to RQ1, RQ2 and RQ3 this study is focused on coupling 2 and 3 of particle-fluid interactions when the particles are reacting. In all cases the interactions occur though momentum, heat and mass exchange between particle and fluid. Therefore it is important to study drag coefficient (C_d), Nusselt number (Nu) and Sherwood number (Sh) with Stefan flow and neighboring particle effects. Let's have a look at what is to be considered in overall model development for thermochemical conversion of biomass.

1.4.1 Modeling thermochemical conversion of biomass

According to the author's knowledge, there is no perfect model so far in any field of science. A perfect model is the ultimate goal of natural sciences. Thermochemical conversion of biomass requires a model that can consider all the initial and time-varying parameters. However, a model should be as simple as possible to be used. Among many parameters important in the thermochemical conversion of biomass, some are particle size, shape, porosity, material density, pore distribution, neighbor particle effects, and effect of reactions.

As we have discussed previously, it is important to know the overall exchange of momentum, heat, and mass between a particle and the bulk fluid in particle-laden flows such as pulverized fuel gasification/combustion. Momentum, heat, and mass exchange are presented as dimensionless numbers in transport phenomena; drag coefficient (C_d), Nusselt number (Nu), and Sherwood number (Sh) respectively. A perfect model for C_d, Nu and Sh would consider the effects of; bulk fluid properties, inherent particle properties, transient particle properties, neighbor particle interactions, the effect of heterogeneous and homogeneous reactions.

One can depict the development of models for C_d and Nu differently (based on literature). Figure 1.3 has summarized based on current development and forecast for the remaining developments for momentum and heat transfer models relevant for reacting particles in particle-laden

flows. Further, Fig. 1.3 shows the contributions of this thesis to the development and improvement of models via research questions (RQs). This thesis covers part of Levels 2 and 3, which will be discussed more in the next section under the aim of the thesis.

Knowing the RQs and what parameters need to be studied to answer the questions, the aim and scope of the thesis can be discussed.

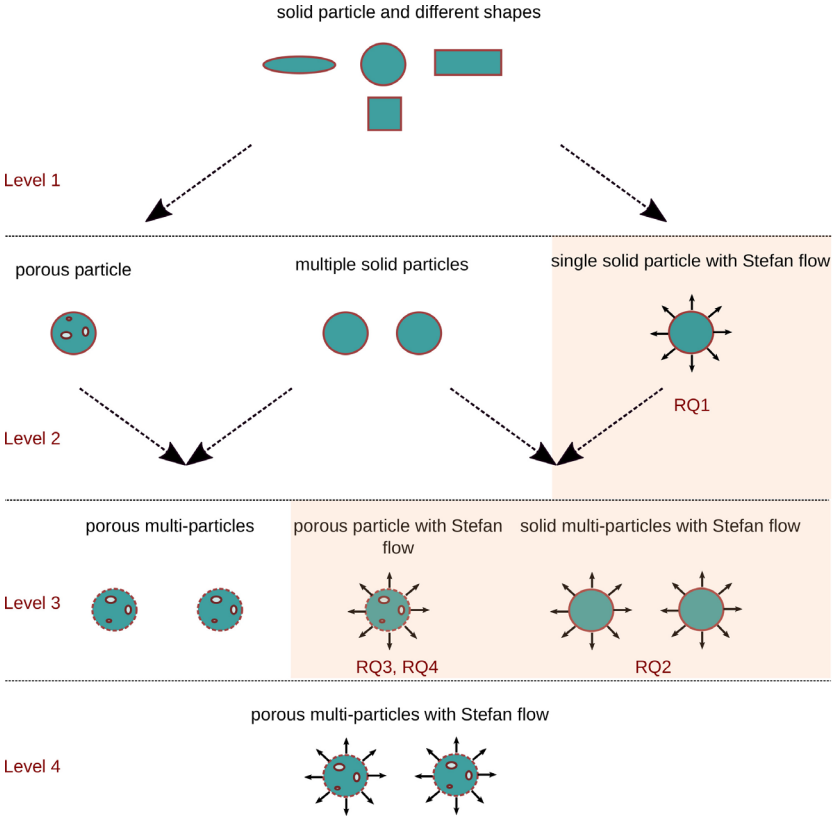

Figure 1.3: Development of momentum exchange (C_d), heat exchange (Nu) and mass exchange (Sh) models between a particle and fluid in a particle-laden flow. Here neighbor particles have represented by two particles which can be more than two. Particle shape, porosity, Stefan flow and neighbor particle effects have used to categorize the levels here. The effect of thermophyscial property changes are not shown here.

1.5 Aim and scope of the thesis

This study aims to develop and improve models for the exchange of momentum and heat transfer between particles and the bulk fluid in reacting particle-laden flow. More specifically, the thesis has the following seven goals:

- To develop a model for the drag coefficient (C_d) for flow around a spherical particle with uniform Stefan flow around the particle-**RQ1**.
- To develop a Nusselt number (Nu) model for flow around a particle with uniform Stefan flow around the particle-**RQ1**.

- Detailed analysis of the effect of reacting neighbor particles on the flow around the particles and effect on the drag coefficient (C_d) of each particle-**RQ2**.
- To develop a numerical platform for the char gasification that resolves both interior and exterior of the particle-**RQ3** and **RQ4**.
- To evaluate the drag coefficient (C_d), Nusselt number (Nu) and Sherwood number (Sh) in a more realistic case of char gasification with non-uniform Stefan flow from the particle-**RQ3**.
- Detailed analysis of parameters and flow field variations during char gasification of biomass in EFBG-**RQ3** and **RQ4**.
- To find the suitability of using point particle simulation methods for biomass char gasification at EFBG conditions-**RQ4**.

1.6 Methods of research

The overview of the research work is summarized in Fig. 1.4. According to the figure, there are four major steps in the work. The first and second steps are isothermal and non-isothermal simulations of gas flow surrounding an isolated particle with uniform Stefan flow around the particle. This covers **RQ1**, and more details can be found in the paper I and II. The third step is studying the effect of neighboring particles with uniform Stefan flow around the particles in an isothermal bulk fluid flow. This work studied **RQ2**, and details can be found in paper III. The fourth work is reacting particle simulations, where an isolated particle reacts under gasification. This work studied **RQ3** and **4**. Further details are available in papers IV and V.

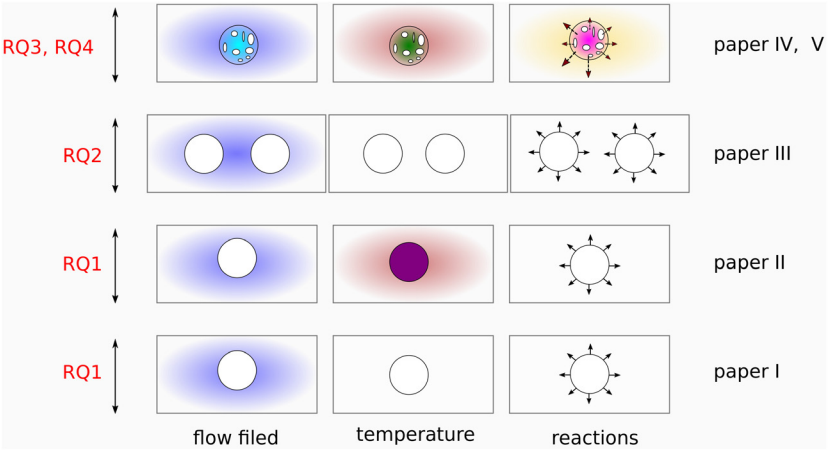

Figure 1.4: Step-wise simulations carrying out during this work. The plain color indicates the assumption of uniform fields (e.g.: isothermal)

RQ1 is the interactions between an isolated reacting particle and the bulk fluid in a particle-laden flow. Therefore, the length scales are in the range of particle diameters to the boundary layer size. Single particle simulations need to resolve the particle and the boundary layer to capture the effects of reactions. This simulation category is often called particle-resolved direct numerical simulations (PR-DNS).

RQ2 is the interaction of reacting particles with the neighbor particles via the bulk fluid. The study is limited to two particles in line with each other; therefore, length scales are in the range

of two particles and boundary layer thickness. PR-DNS simulations are carried out for this work too.

Both RQ1 and RQ2 are theoretical studies where the effect of the reaction is considered as a uniform Stefan flow around the particle/particles. Therefore, the particle interior is not resolved. However, to study the effects of reactions during char gasification (RQ3 and RQ4), one reaction is considered inside the particle, creating a Stefan flow. Therefore, both the interior and exterior are resolved in these simulations.

The step-wise procedure followed to answer all research questions is explained in detail below (see Fig.1.4 also for the summary).

- Step 1: isothermal flow around an isolated particle with uniform Stefan flow from/to the particle.
  The particle is considered a boundary immersed in the bulk fluid. There is a uniform Stefan flow from the surface of the particle. This work aims to study the effect of Stefan flow on momentum exchange (C_d) between the particle and the fluid in the absence of temperature and concentration gradients.

- Step 2: non-isothermal flow around an isolated particle with uniform Stefan flow from/to the particle.
  A temperature difference is also applied between the particle and the bulk fluid in addition to the Step 1 conditions. The exchange of momentum (C_d) and heat (Nu) between the particle and bulk fluid due to Stefan flow is studied under non-isothermal conditions.

- Step 3: isothermal flow around two particles in tandem (in-line) arrangement with uniform Stefan flow from the particles.
  One more particle is added behind the particle in Step 1, in the bulk fluid flow direction. This work aims to study the effect of Stefan flow with the effect of neighbor particles via the fluid on momentum exchange (C_d) between the particle and the fluid in the absence of temperature and concentration gradients.

- Step 4: flow around a particle under char gasification with non-uniform Stefan flow.
  The particle interior and exterior are both resolved and solved for governing equations. Only one heterogeneous and no homogeneous reactions are considered for simplicity and to create a Stefan flow. The Stefan flow created might be a uniform/non-uniform one. The effect of Stefan flow on C_d, Nu, Sh, and many other parameters will be studied. Point particle calculations will be performed analytically and compared with resolved particle simulations.

Considering the small length and time scales of a particle compared to reactor scales, quasi-steady-state can be assumed in uniform Stefan flow conditions (steps 1-3). Therefore, steady-state simulations were carried out to study the effects. When the particle is also reacting and creating a non-uniform Stefan flow, and to study the effect of the progress of reactions on the particle, transient simulations must be carried out (step 4).

Chapter 2

Literature review

"Essentially, all models are wrong, but some are useful. However, the approximate nature of the model must always be borne in mind.."

—George Box

This chapter discusses previous studies on interactions between particles and fluid in particle-fluid flows. A special attention has given on models on momentum exchange (drag coefficient), heat exchange (Nusselt number) and their development to more complex conditions associated with reacting particles. Modeling and simulation practices for char gasification is also discussed. Particle Reynolds numbers considered here are always in the laminar range.

We have already discussed the importance of model development for particle-fluid flows and necessity of improved models in particle-fluid flows with reacting particles compared to classical models. Figure 1.3 also shows the model development for drag coefficient and Nusselt number in terms of complexity. Starting from classical models, drag coefficient (C_d) for spherical and cylindrical particles will be discussed. Then, improvements to the classical models; effect of porosity, effect of neighboring particles and effects of Stefan flow will be discussed for each shape. After the C_d, classical models for the heat exchange (Nu) between a particle and fluid in particle-fluid flows will be discussed. Details of classical models will be followed by the improvements including the effects of porosity, neighboring particles and Stefan flow.

This thesis mainly focuses on effects of Stefan flow on drag coefficient (C_d) and Nusselt number (Nu). Therefore, a separate section is added on the models with effects of Stefan flow for each shape.

2.1 Drag coefficient

Drag coefficient (C_d) is used to calculate the total force acting around a body due to pressure and viscosity in fluid dynamics:

$$C_d = \frac{\overrightarrow{F}_{\mathrm{p}} + \overrightarrow{F}_{\mathrm{visc}}}{\frac{1}{2}\rho U_\infty^2 A}, \tag{2.1}$$

where $\overrightarrow{F}_{\mathrm{p}}$ is pressure force, $\overrightarrow{F}_{\mathrm{visc}}$ is viscous force, ρ is bulk fluid density, U_∞ is slip velocity of the body and A is the reference area of the body. Drag coefficient presents as average over the whole body or point-wise.

It is important to know the drag acting on a body for many engineering calculations. Apart from that as mentioned in the section 1.4, models for drag coefficient are essential in modeling interaction between particle and bulk fluid in particle-laden flow simulations when the particle is not resolved. Drag depends on the shape, orientation of the body and Reynolds number (Re) for a solid particle immersed in an isothermal, non-reacting flow [14, 15]. The drag may vary on many other parameters depending on the complexity of the flow and the body. It is hard to find a universal drag model which is applicable for all shapes and all Reynolds numbers in classical drag models.

2.1.1 Spherical particles

Classical models

There are many models based on experiments, theory and numerical methods applicable for different regions of Re and different shapes.

Classical drag models for spherical particles are applicable for isothermal conditions and few of them are depicted in Table 2.1. Reynolds number:

$$\mathrm{Re} = \frac{\rho \mathrm{U}_\infty \mathrm{D}}{\mu}, \tag{2.2}$$

where ρ is fluid density, U_∞ is particle slip velocity, D is particle diameter and μ is fluid viscosity.

Table 2.1: Classical drag models for flow around a sphere.

Model	Range	Reference
$C_d = \frac{24}{\mathrm{Re}}$	$\mathrm{Re} < 1$	Stokes law
$C_d = \frac{24}{\mathrm{Re}}(1 + 0.1806\mathrm{Re}^{0.6459}) + 0.4251\left(1 + \frac{6880.95}{\mathrm{Re}}\right)^{-1}$	$Re < 2.6 \times 10^5$	[16]
$C_d = \frac{24}{\mathrm{Re}}(1 + 0.15\mathrm{Re}^{0.687})$	$1 < \mathrm{Re} < 800$	[17]

Improvements for the classical models

Recently, Ellendt et al. [18] have suggested a correction factor to the Schiller-Naumann model [17] when variation of thermophysical properties in the boundary layer are not negligible:

$$C_d = \frac{24}{\mathrm{Re}}(1 + 0.15Re^{0.687})\phi; \quad \phi = 0.273(1 - 0.883^{\mathrm{Re}})(\frac{\rho_\infty}{\rho_p} - 1) + 1, \tag{2.3}$$

where ρ_∞ is fluid density calculated at far-field conditions, ρ_p is fluid density calculated at particle surface temperature and Re is when the density and viscosity is calculated at the particle surface temperature (T_p) for Eq. 2.2. The model is valid for the range of $1 < \mathrm{Re} < 130$ for Helium and Nitrogen.

When comparing with Fig. 1.3, the classical drag coefficient models of a spherical particle can be further improved considering; porosity, effect of Stefan flow, effect of neighboring particles, etc. Effect of different shapes will not discuss here. A summary of previous studies on drag coefficient and heat transfer of porous particles can be found in recent work by [19]. Wittig et al. [20] have developed 2 models for the drag coefficient (C_d) for a porous spherical particle:

$$C_{d,I} = 0.375\epsilon + 0.325S''^{-0.5}\frac{38.9 + 7.33\epsilon - 8.39S''^{-0.5}}{\mathrm{Re}} + \frac{4.37 - 3.22S''^{-0.5}}{\sqrt{\mathrm{Re}}}, \tag{2.4}$$

$$C_{d,II} = 0.686\epsilon + \frac{(51.3 - 18.4\epsilon)}{\mathrm{Re}} + \frac{2.35}{\sqrt{\mathrm{Re}}}, \tag{2.5}$$

where ϵ is porosity of the particle and S'' is the ratio of porous particle surface area to solid particle surface area. The model is applicable for the range of $10 < \mathrm{Re} < 250$. Wittig et al. have observed that at low porosity ($\epsilon \leq 0.7$) particle act as a solid particle and at high porosity ($\epsilon > 0.7$) fluid passes through the particle. At low Re, an increase of porosity leads to a decrease of C_d and Nu while at high Re, an increase of porosity leads to an increase of C_d and Nu. Figure 2.1 shows the difference between isothermal, non-isothermal solid particle drag coefficient models and porous particle models.

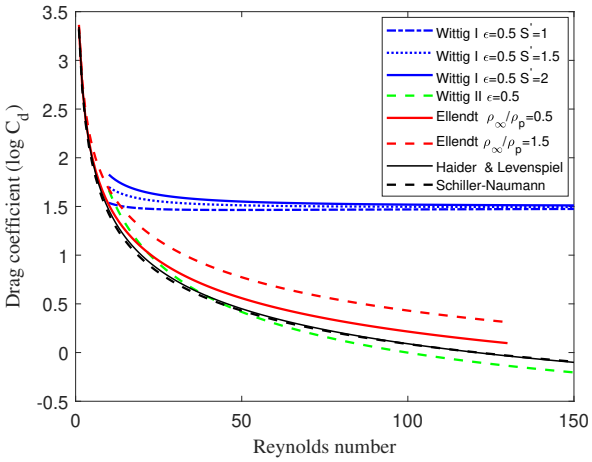

Figure 2.1: Models for the drag coefficient of a solid spherical particle at isothermal conditions (Haider & Levenspiel, Schiller-Naumann), non-isothermal conditions (Ellendt) and porous spherical particle at isothermal conditions (Wittig) (see Table 2.2).

Neighboring or closely located particle effects discuss below refer to 'Coupling 3' in Chapter 1, section 1.3. There are many studies on neighboring particle effects in packed-bed and fluidized-bed porosity limits where particle number density is high [21, 22, 23] and cannot be used for EFBG applications where particle concentrations are less than 0.001. There are studies on neighboring particle effects on momentum and heat transfer related to droplet evaporation. Those works also lie in the range of higher particle concentrations and also there are some thermo-physical and chemical differences in droplet evaporation in contrast to gasification or combustion [24, 25, 26]. There are not many works on closely located particles in particle-fluid flows in combustion or gasification. Sayadi et al. [27] have studied effects of particle distance and particle arrangement on coal combustion. More details can be found in paper III in this thesis.

Models with effects of Stefan flow

There are some models developed for the drag coefficient for a flow around an isolated sphere with Stefan flow. Most of the earliest models were for droplet evaporation and suction/blowing applications. Some recent models have developed for the generalized case based on numerical simulations. There are three drawbacks identified in those models:

- none of the models is applicable for non-isothermal flow,
- models are having more than one fitting parameter, and

- some models cannot consider the negative Stefan flow (Ex: condensation).

Dukowicz [28] has developed an analytical model for the drag of a solid sphere with blowing/suction. The model is applicable for creeping bulk flow ($\mathrm{Re} \to 0$). The models developed by experiments and numerical works are having more than one fitting parameter and they do not interpret the variation of physics due to the Stefan flow [29, 30]. In most practical situations, the flow is non-isothermal, specially in reacting environments like solid fuel combustion, gasification and so on (except phase change situations). Considering these drawbacks of the current models, it is important to develop drag models which are applicable for non-isothermal flow conditions based on physical interpretation for flow around a sphere with Stefan flow. One model is developed by Kestel et al. [30] which is applicable for a high Re and Re_{Sf} range ($\mathrm{Re} \leq 200$ and $\mathrm{Re}_{Sf} \leq 20$):

$$C_{d,Sf} = \frac{C_{d,0}}{(1 + 0.138\mathrm{Re}_{Sf}^{1.153})^{a}}, \tag{2.6}$$

where $a = (\frac{1.063}{1+0.223\mathrm{Re}})^{0.568}$, Re_{Sf} is Re calculated based on Stefan flow velocity and $C_{d,0}$ is calculated based on Clift model;

$$C_{d,0} = \frac{24}{\mathrm{Re}}(1 + 0.15\mathrm{Re}^{0.687}). \tag{2.7}$$

More information about drag coefficient models for an isolated spherical particle with Stefan flow can be found in paper I.

There are few studies on considering both effects of Stefan flow and neighboring particles [31, 32, 33]. This has discussed more detail in Paper III. Du et al. [32] have developed a drag force model for a particle with Stefan flow surrounded by sea of inert particles. What is missing from literature are fundamental studies on effects of neighboring particles on momentum and heat transfer in particle-fluid flows at low particle concentrations and low Res.

2.1.2 Cylindrical particles

Classical models

Cylinder is a simple geometry in contrast to a sphere. Still, drag models for a circular cylinder can vary a lot depending on the ratio of length to diameter (aspect ratio) and the range of Re of the bulk fluid. When the aspect ratio of a cylinder is high, the effect of bottom surface on the drag can be neglected. Flow can be considered as 2-dimensional at low $\mathrm{Re} < 150$ [34], and steady at $\mathrm{Re} < 47$. This is similar to considering an infinitely long cylinder. Earlier works by Tritton [35] has experimental data for drag coefficient of cylinders at low Reynolds numbers ($0.5 < \mathrm{Re} < 100$).

Khan et al. [36] have shown the none/less availability of models for C_d and Nu for fluid flow around an infinitely long cylinder for a wide range of Re and Pr. They have developed an analytical model for the drag coefficient:

$$C_d = \frac{5.786}{\sqrt{\mathrm{Re}}} + 1.152 + \frac{1.26}{\mathrm{Re}}, \tag{2.8}$$

which is applicable for a large range of Reynolds number. However, for the low Reynolds numbers ($\mathrm{Re} < 1$) the best way to calculate the drag around an infinite cylinder with a cross flow might be to use the C_d vs Re curve in [37]. There are various models available for cylinders of finite aspect ratios [16, 15].

Improvements to the classical models

Effect of porosity on the drag coefficient of a circular cylinder has studied by many researchers [38, 39] and recently a model was developed by Zhang et al. [40]:

$$C_d = 10.452 \times \mathrm{Re}^{-0.733}\mathrm{Da}^{-0.017} + 0.818, \tag{2.9}$$

for $10 \leq \mathrm{Re} \leq 40$ and Darcy number $10^{-6} \leq \mathrm{Da} \leq 10^{-2}$ when $\mathrm{Pr} = 0.71$.

$$\mathrm{Da} = \frac{K}{D^2}, \tag{2.10}$$

where K is permeability and

$$\mathrm{Pr} = \frac{c_p \mu}{\lambda}, \tag{2.11}$$

where c_p is specific heat capacity, μ is viscosity and λ is thermal conductivity of the fluid. All the classical models above consider the effect of bulk fluid on the particle alone (coupling 2) and coupling 3 is neglected. As mentioned under spherical particles, the works related to neighboring particles [21] are mainly for high particle concentrations which is not applicable for EFBG. Recently, Zhang et al. [41] have studied the effect of neighboring particles on C_d and Nu of porous particles. However, there are no models for C_d or Nu of a porous particle considering effect of neighboring particles as per author's knowledge.

Models with effects of Stefan flow

As discussed earlier, most of the works related to Stefan flow in the past was related to droplet evaporation. Later on there are some works related to Stefan flow due to coal combustion or gasification. The droplets and coal particles resemble more spherical shape. Therefore, most of the Stefan flow related research were on spherical particles. It is hard to find such work (effect of Stefan flow) related to cylindrical particles which is more suitable for biomass gasification and combustion.

2.2 Nusselt number

Average Nusselt number, Nu, is used to calculate overall heat transfer from an immersed body in a fluid. Heat transfer coefficient, h, is calculated by the Nu number as follows:

$$\mathrm{Nu} = \frac{\mathrm{hD}}{\lambda}, \tag{2.12}$$

where D is the characteristic length of the particle and λ is the thermal conductivity of the fluid. Available models for the Nusselt number are also specific to shape, Reynolds number range and Prandtl number range [14]. There can be more complicated models with additional parameters such as considering variation of thermo-physical properties due to non-isothermal conditions. The following section discusses Nu number models for flow around a sphere and a cylinder. For each shape, classical models and improvement to the classical models are discussed with a special emphasis on models with effects of Stefan flow.

2.2.1 Spherical particles

Classical models

Among many Nusselt number models for spherical particles, Ranz-Marshall [42] and Whitaker [43] models are widely used for convective flow around spherical bodies. The Ranz-Marshall model is:

$$\mathrm{Nu} = 2 + 0.6\mathrm{Re}^{\frac{1}{2}}\mathrm{Pr}^{\frac{1}{3}}, \tag{2.13}$$

Nu, Re and Pr are calculated based on the properties at film condition. Film condition is defined as the condition at the film temperature (T_f); $T_f = \frac{T_\infty + T_p}{2}$ where T_p is the particle surface temperature and T_∞ is the far-field temperature of the bulk fluid. The model is applicable when $\mathrm{Re} < 200$. The Whitaker model is:

$$\mathrm{Nu} = 2 + \left(0.4\mathrm{Re}^{\frac{1}{2}} + 0.06\mathrm{Re}^{\frac{2}{3}}\right)\mathrm{Pr}^{0.4}\left(\frac{\mu_\infty}{\mu_\mathrm{p}}^{\frac{1}{4}}\right), \tag{2.14}$$

where Nu, Re and Pr are calculated based on properties at far-field temperature. μ_∞ and μ_p are viscosity based on far-field and particle surface temperature respectively. The model is valid for $3.5 \leq \mathrm{Re} \leq 7.6 \times 10^4$, $0.71 \leq \mathrm{Pr} \leq 380$ and $1.0 < \mu_\infty/\mu_0 < 3.2$.

Improvements to the classical models

One of the main issues of these available Nu models is that they are not considering the variation of thermo-physical properties. The variation of thermo-physical properties are not negligible in high temperature gradient applications like combustion and gasification of solids. Recently, Ellendt et al. [18] has shown that the Ranz-Marshall model at film conditions is suitable for applications where the temperature difference between the particle and the bulk fluid is high ($1 < \mathrm{Re} < 130$). When models are not available for the required flow conditions, making own models by fitting simulation data to the particular range is also observed from literature [44].

Wittig et al. [20] has not only developed a drag model for a porous spherical particle but also a Nusselt number model:

$$\begin{aligned}\mathrm{Nu} =& 2.56 - 8.42\epsilon + 9.89\epsilon^2 \\ &+ 1.37S''^{-0.5} + (-1.63 + 12.8\epsilon - 12\epsilon^2 - 2.26S''^{-0.5})\mathrm{Re}^{\frac{1}{2}}Pr^{\frac{1}{3}} \\ &+ (1.42 - 6.88\epsilon + 6.06\epsilon^2 + 0.987S''^{-0.5})\mathrm{Re}^{\frac{2}{3}}\mathrm{Pr}^{\frac{1}{3}},\end{aligned} \tag{2.15}$$

where S'' is ratio of porous particle surface area to solid particle surface area. The model is valid for $10 < \mathrm{Re} < 250$ and $\mathrm{Pr} = 0.744$.

Models for effects of neighboring particles on the Nusselt number (Nu) of particles in particle-fluid flows have studied by Kravets et al. [21] recently. The study is applicable for high particle concentrations conditions such as packed-bed and fluidized-bed.

Models with effects of Stefan flow

The models developed at early stage are for the droplet evaporation applications which has summarized in Zhifu et al. [45]. More details are available in paper II. Murphy & Shaddix have developed a theoretical model for the Nusselt number with a Stefan flow in a quiescent environment. The model has developed assuming constant properties:

$$\mathrm{Nu} = \mathrm{Nu}_0 \frac{(\mathrm{PrRe}_{Sf})/\mathrm{Nu}_0}{e^{(\mathrm{PrRe}_{Sf})/\mathrm{Nu}_0} - 1}, \tag{2.16}$$

where Nu_0 is Nusselt number without Stefan flow which is equal to 2.

$$\mathrm{Re}_{Sf} = \frac{\rho U_{Sf} D}{\mu}, \tag{2.17}$$

where U_{Sf} is the Stefan flow velocity. Recently, Kestel [44] has developed a Nusselt number model with Stefan flow for a sphere immersed in a convective environment. The model is applicable for high temperature gradient conditions such as gasification and combustion (Please see paper II, section 2.2 for more details). However, the model has many fitting parameters.

2.2.2 Cylindrical particles

Classical models

Some of the models available for calculation of average Nusselt number for an infinitely long cylinder are listed in Table 2.2 and shown in Fig. 2.2. McAdam's model is more suitable for small Re and very high Pr. Khan et al. [36] have developed an analytical model recently, based on Von Karman–Pohlhausen method. Bharti et al. [46] have developed a model which is applicable for higher Pr range using numerical simulations. Most recent model is developed by Abdelhady et al. [47] using numerical simulations ($10 \leq \mathrm{Re} \leq 3000$).

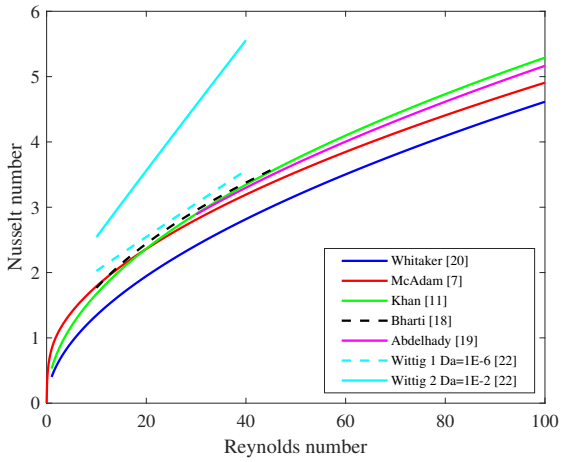

Figure 2.2: Different classical and improved models for the Nusselt number around an infinite cylinder (see Table 2.2).

Table 2.2: Classical Nusselt number models for a cross flow around an infinite cylinder.

Model	**Range**	**Reference**
$\mathrm{Nu}_\infty = (0.4\mathrm{Re}_\infty^{1/2} + 0.06\mathrm{Re}_\infty^{2/3})\mathrm{Pr}_\infty^{0.4}(\frac{\mu_\infty}{\mu_p})^{\frac{1}{4}}$	$1.0 < \mathrm{Re} < 1.0 \times 10^5$ $0.67 < \mathrm{Pr} < 300$ $0.25 < \mu_\infty/\mu_p < 5.2$	Whitaker [43]
$\mathrm{Nu} = (0.37\mathrm{Re}^{1/2} + 0.057\mathrm{Re}^{2/3})\mathrm{Pr}^{1/3} + 0.92[ln(\frac{7.4055}{\mathrm{Re}}) + 4.18\mathrm{Re}]^{-1/3}\mathrm{Re}^{1/3}\mathrm{Pr}^{1/3}$	Small Re and $\mathrm{Pr} \to \infty$	McAdam [14, 48]
$\mathrm{Nu} = 0.593\mathrm{Re}^{1/2}\mathrm{Pr}^{1/3}$	$1.0 < \mathrm{Re} < 2.0 \times 10^5$ $\mathrm{Pr} \geq 0.71$	Khan [36]
$\mathrm{Nu} = 0.6738\mathrm{Re}^{0.4679}\mathrm{Pr}^{1/3}$	$10 \leq \mathrm{Re} \leq 45$ $0.7 \leq \mathrm{Pr} \leq 400$	Bharti [46]
$\mathrm{Nu} = 0.633 + 0.315\mathrm{Re}^{0.579}$	$30 \leq \mathrm{Re} \leq 300$ $\mathrm{Pr} = 0.7$	Abdelhady [47]

Improvements to the classical models

Similar to the models for flow around sphere, Nu models for cylinders also have the drawback of neglecting the variation of thermal and physical properties. Those models might not be suitable when there is a significant variation of thermo-physical properties such as in reacting particle-laden flows. Only the Whitaker model accounts the variation of viscosity. There is a question whether accounting variation of viscosity alone is sufficient in high temperature gradient applications.

Zhang et al. [40] have recently developed a Nusselt number model for a porous cylindrical particle:

$$\mathrm{Nu} = 1.231 \times \mathrm{Re}^{0.971}(\mathrm{Da}^{0.673} + 0.047) + 1.483, \tag{2.18}$$

for $(10 \leq \mathrm{Re} \leq 40)$, $(10^{-6} \leq \mathrm{Da} \leq 10^{-2})$ and $\mathrm{Pr} = 0.71$.

As mentioned under the C_d of cylindrical particles as well, there are no models for Nu with

effects of Stefan flow for cylindrical particles.

So far, we have discussed the necessity of proper models for momentum, heat and mass transfer for reacting particles in particle-laden flows for large scale simulations when the particle interior and boundary layer around the particle is not resolved. We discussed available models from previous studies for the drag coefficient (C_d) and Nusselt number (Nu). Our specific interest is on solid fuel gasification using EFG (which is applicable to biomass/coal gasification and to solid fuel combustion to some extent). Therefore, in the next section we will discuss the numerical methods to model particles in particle-laden flows.

2.3 Numerical methods for char gasification in EFG

Carrying out numerical simulations without models (models only for the reactions) would be the best approach to know all the thermal and physical parameters of a gasyfying particle. This method is called particle-resolved direct numerical simulations (PR-DNS). This is practical for one or few particles when the bulk fluid flow is laminar. When there are many particles in the bulk fluid and also turbulence is involved, it is not practical to do PR-DNS simulations due to limitations of computational resources and numerical methods. Current state-of-the-art is to consider particle as a point in space and use different approaches to handle the turbulence. Point-particle method together with DNS (PP-DNS) can be used for small scale simulations such as laminar flow simulations, isotropic turbulence [13]. Point-particle methods together with large-eddy simulations (PP-LES) can be used for semi-industrial pulverized furnaces [49]. LES resolves only larger scale turbulence and small scale turbulence is modeled. Point-particle method with Reynolds-Averaged Navier-Stokes equations (PP-RANS) is used for reactor scale simulations where every phenomena is modeled [50].

2.4 Point-particle (PP) methods

Point-particle method is one numerical approach used to model particle phenomena in particle-fluid simulations, specially when the particle concentrations are low. Other methods used for simulation of particles in particle-fluid flows can be found in [51]. Particle is considered as a zero volume mass with no fluid displacement due to particle. This method can be applied when particle size is much smaller than the mesh used for simulations. PP method cannot be used when thermal Biot number (Bi_{th}) is greater than 0.1 ($Bi_{th} > 0.1$), which leads to non-uniform particle temperatures.The presence of a particle is represented by the momentum (C_d), heat (Nu), and mass transfer (Sh) between the particle and the fluid. The temperature, velocity, and gas species of a reacting particle can be calculated using its' overall conservation of momentum, mass, and heat transfer. Please refer paper V for the equations.

Most point-particle studies related to pulverized coal/biomass have used heat (h_{th}) and mass transfer coefficients (h_m) including Stefan flow effects as follows;

$$h = h_0 \theta_{Sf}, \tag{2.19}$$

where h_0 is the convective heat/mass transfer coefficient without Stefan flow which can be calculated using the models discussed in section 2.2. θ_{Sf} is the term due to effect of Stefan flow [52, 53, 54, 55, 56]. The term used for those studies only includes variation of thermo-physical parameters around a particle due to Stefan flow and effects of Stefan flow due to advection at the particle surface are neglected. This can create deviations in point-particle method results when the Stefan flow is important. Therefore, it would be helpful to compare the point-particle results with particle-resolved simulations and identifying the drawbacks of current methods, models and error if Stefan flow is neglected.

PP methods also require other models to predict variation of particle diameter, density, evolution of particle surface area, etc. Haugen et al. have developed models for the variation of

particle diameter and particle density instead of using power-law models [6]. The results are applicable for an spherical particle and developed based on Thiele modulus, effectiveness factor based approach which can be used for a reacting porous particle.

2.5 Char gasification modeling challenges

As mentioned in section 1.3.1 also, char gasification is the most challenging process in terms of modeling. It is necessary to develop better models to predict C_d, Nu, Sh, variation of particle diameter, particle density, evolution of internal surface area, etc. Most improved models [6] are developed for spherical particles. But, biomass particles resemble more of a cylindrical particle and it is important to develop models for the cylindrical shape. Further, it is important to identify problems associated with using models valid for coal based simulations to biomass based simulations. So far, there are no particle-resolved simulations carried out for a biomass particle gasification with both particle exterior and interior refined. Particle-interior resolved simulations would give more insights into what is happening in interior of a particle during gasification and results can be compared with PP simulations. Results would support identifying drawbacks of PP simulations and help identifying better models to be used to get better results.

Chapter 3

Particle-resolved numerical simulations

"Everything should be made as simple as possible, but not simpler."

—Albert Einstein

This chapter focuses on summarizing numerical simulation methodology and some post-processing calculations. Governing equations, boundary conditions, initial conditions, mesh refinement, domain independence, and solution procedure are discussed briefly for the numerical simulations. Then the calculation of C_d and Nu is discussed. Detailed information about each work can be found in the papers in the appendix.

This thesis aims to find the effects of Stefan flow; on the interaction between the particle and the bulk fluid (RQ1, RQ3, RQ4) and the interaction between neighboring particles via the bulk fluid (RQ2). RQ1, RQ3, and RQ4 focus on an isolated particle as mentioned in section 1.5 and 1.6. Three main studies were carried out for isolated particle simulations :

- **Isothermal**, uniform bulk fluid flow around a spherical particle with uniform Stefan flow at the particle interface,
- **Non-isothermal**, uniform bulk fluid flow around a spherical particle with uniform Stefan flow at the particle surface,
- **Non-isothermal** uniform bulk fluid flow around a **reacting**, **porous** particle (cylindrical). Stefan flow is created by the reactions.

The first two steps create reaction-generated flow as a boundary condition at the particle's external surface, called *Stefan flow*. This flow is considered either the inward or outward flow of the particle. Inward Stefan flow depicts situations similar to condensation and oxidation of metal particles (metal combustion, chemical looping combustion). Outward Stefan flow depicts situations similar to evaporation and gasification. The nature of the fluid flow and governing equations are summarized separately in Table 3.1 for all three studies.

RQ2 is about neighbor particle effects, so multi-particle effects must be considered in simulations. A study was carried out for an **isothermal**, uniform bulk fluid flow around two spherical particles in a tandem arrangement. Particles have a uniform Stefan flow at the surface. The methodology is the same for the multi-particle case and single particle, isothermal case (RQ1), except there are two particles in the simulation domain for the multi-particle study. Therefore, the same governing equations apply and will not discuss in detail in the thesis separately. Details about domain size and mesh refinement can be found in Paper III.

Table 3.1: Variation of parameters and flow conditions during isothermal, non-isothermal and reacting simulations.

Flow condition	Isothermal	Non-isothermal	Reacting
Governing equations: bulk gas flow	Navier-Stokes equations: -continuiy -momentum	Navier-Stokes equations: -continuiy -momentum -energy	Navier-Stokes equations: -continuiy -momentum -energy -species
Governing equations: particle interior	Not solved	Not solved	Porous media equations: -continuiy -energy -species
Mesh	3-D	3-D	2-D
Particle shape	Spherical	Spherical	Infinitely long cylinder
Simplifications of the flow	Axi-symmetric, steady, incompressible flow	Axi-symmetric, steady, incompressible flow	Axi-symmetric, incompressible flow
Thermophysical properties	Constant	Temperature dependent	Temperature-species dependent

3.1 Navier-Stokes equations for incompressible flow

For all the simulations, bulk gas flow surrounding the particle is assumed as incompressible (see Table 3.1). Therefore incompressible Navier-Stokes equations are shown below. The continuity equation is:

$$\frac{\partial(\rho_g)}{\partial t} + \nabla \cdot (\rho_g \overrightarrow{u}) = 0, \tag{3.1}$$

where ρ_g is fluid density, $\overrightarrow{u}$ is velocity vector of the fluid. Momentum conservation of the fluid gives:

$$\frac{\partial(\rho_g \overrightarrow{u})}{\partial t} + (\rho_g \overrightarrow{u} \cdot \nabla)\overrightarrow{u} = -\nabla p + \nabla \cdot \mu[\nabla \overrightarrow{u} + \nabla \overrightarrow{u}^T - \frac{2}{3}(\nabla \cdot \overrightarrow{u})\overrightarrow{I}], \tag{3.2}$$

where μ is dynamic viscosity of the fluid, $\overrightarrow{I}$ is identity matrix and p is pressure. Finally, from energy conservation, we get:

$$\frac{\partial(\rho_g c_{p,g} T)}{\partial t} + \nabla \cdot (\rho_g c_{p,g} \overrightarrow{u} T) = -\nabla \cdot \lambda_g \nabla T, \tag{3.3}$$

where $c_{p,g}$ is specific heat capacity of the fluid, T is temperature and λ_g is thermal conductivity of the fluid.

3.2 Reacting char particle simulations

One objective of the reacting char particle simulations is to study the effects of Stefan flow on the C_d, Nu and Sh during more realistic conditions of EFBG compared to uniform Stefan flow. Therefore, a single non-equimolar gasification reaction (Boudouard reaction) is considered to

observe Stefan flow's effects clearly. Homogeneous reactions are neglected. A char particle is considered an infinitely long porous cylinder. The shape was selected since biomass particle resembles more of a cylinder than a sphere. At low Re ($\mathrm{Re} < 3.2$), flow around a cylinder can be considered symmetric and steady, and there is no flow separation [35]. Therefore, half of the particle was simulated in 2D geometry. The particle is stationary and considered a porous media, and the local porosity increases with the reaction progress. Local shrinkage of the particle is neglected. Furthermore, the gas phase and solid phase inside the particle are assumed to be in local thermal equilibrium ($T_g = T_s$). Radiation absorption by the gas phase is neglected. Transient simulations have been carried out monitoring particle and bulk fluid conditions with the progress of the reaction, and high-pressure atmospheres have been considered as in EFGs.

Other objective is to compare the numerical simulation results with point-particle simulations and study the applicability of the point-particle approach for a reacting particle with Stefan flow. Detailed equations are available in paper V, and a summary is available in section 3.7.

3.2.1 Governing equations inside a char particle

Governing equations for the gas phase of porous media are presented below.
Continuity equation reads as:

$$\frac{\partial(\epsilon\rho_g)}{\partial t} + \nabla.(\rho_g \overrightarrow{u}) = R_C, \tag{3.4}$$

where ϵ is the local porosity and R_C is char reaction rate due to Boudouard reaction.
Momentum equation reads as:

$$\frac{\partial(\epsilon\rho_g \overrightarrow{u})}{\partial t} + (\rho_g \overrightarrow{u} \cdot \nabla)\overrightarrow{u} = -\nabla p + \nabla \cdot \mu[\nabla \overrightarrow{u} + \nabla \overrightarrow{u}^T - \frac{2}{3}(\nabla \cdot \overrightarrow{u})\overrightarrow{I}] - F_d, \tag{3.5}$$

where F_d is momentum source term calculated based on Darcy-Forchcheimer law (second term of the equation is neglected) [57].
Energy equation is:

$$\frac{\partial(\epsilon\rho_g c_{p,g} T + c_{p,s}\rho_s(1-\epsilon)T)}{\partial t} + \nabla.(\rho_g \epsilon c_{p,g} \overrightarrow{u} T) = \nabla(\nabla.\lambda_{\text{eff}} T) + \dot{Q}_{\text{rad},p} + \dot{Q}_s, \tag{3.6}$$

where $c_{p,s}$ is specific heat capacity of char, ρ_s is density of char, λ_{eff} is effective thermal conductivity, $\dot{Q}_{\text{rad,p}}$ is the radiation exchange between the reactor wall and the particle surface, $\dot{Q}_s$ is enthalpy change due to solid phase reaction. Gas species equation is:

$$\frac{\partial(\epsilon\rho_g Y_i)}{\partial t} + \nabla.(\rho_g \overrightarrow{u} Y_i) = -\nabla.(Y_i \rho_g \overrightarrow{v_i^c}) + \nu_i R_C, \tag{3.7}$$

where Y_i is mass fraction of gas specie i, ν_i is stoichiometric coefficient in the Boudouard reaction related to i and v_i^c is diffusion velocity of i gas specie.
Please refer paper IV for further details.

3.3 Solution of governing equations

The solution of governing equations involves many steps, such as setting up the domain with initial and boundary conditions, discretization and solving set of equations, domain size and mesh refinement tests, validation/verification and choice of CFD software. Some important information is summarized in sections below.

3.3.1 Boundary conditions and initial conditions

In all the simulations, the slip velocity (U_∞) between the particle and the gas is considered as the velocity at the *inlet* to the domain (left-hand side of the Fig. 3.1 and Fig. 3.3). The right-hand side of the domains (*outlet*) is considered as an 'outflow' boundary condition (zero gradients for all parameters except pressure). Boundaries along the symmetry plane are considered *symmetric* boundary condition (velocity normal to the boundary is zero, and gradient of all other properties is zero). Side walls are considered as *slip walls* (velocity normal to the boundary is zero).

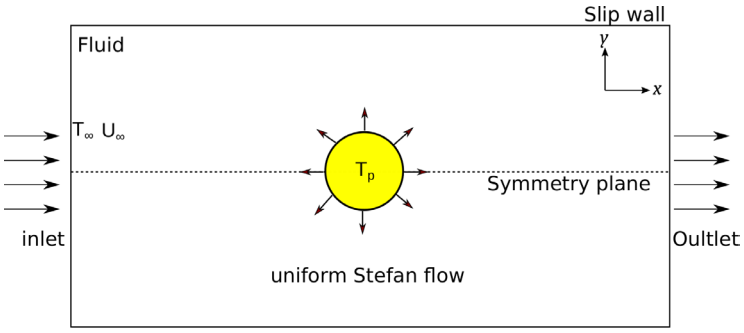

Figure 3.1: Arrangement of the simulation domain of isothermal and non-isothermal cases. $T_p = T_\infty$ in isothermal simulations. T_p is varied in non-isothermal simulations.

Only the Re and Stefan flow velocity (U_{Sf}) were changed in the isothermal simulations. The temperature at the particle surface (T_p) was also varied in non-isothermal simulations, keeping far-field temperature (T_∞) constant. For all the simulations, Particle slip velocity ($U_\infty \leq 3$ m/s), diameters ($D \leq 1$ mm), and all the temperature ranges were selected in the range of EFBG (400 K $\leq T \leq$ 2000 K). All the cases with uniform Stefan flow were simulated at atmospheric pressure. The distance between particles has varied from $1.1D - 10D$ for the work on neighboring particle effects.

Reacting particle simulations were carried out considering the particle is char with 100% carbon. Simulation cases have chosen to keep the estimated particle Reynolds number (Re) and effectiveness factor (η) in the ranges of 0.5-3.0 and 0.2-0.7, respectively. More details can be found in Paper IV and V. Particle interior and exterior resolved simulations have been carried out for 6 cases with 3 cases of high effectiveness factor and 3 cases with low effectiveness factor.

In reacting particle simulations, always the *inlet* gas temperature increased from room temperature to far-field temperature (T_∞) with a delay of 10 ms to mimic more realistic conditions of a reactor. Accordingly, gas density and wall temperature for radiation heat transfer calculations were also varied. The initial field was considered nitrogen (N_2), and the gas entering from the *inlet* is a mixture of nitrogen (N_2) and carbon dioxide (CO_2).

3.3.2 Calculation conditions and solution procedure

Isothermal and non-isothermal simulations with uniform Stefan flow were carried out in *OpenFOAM* environment called *foam-extend*. An incompressible, steady-state, immersed boundary, finite volume solver was used for the simulations. Reacting particle simulations were carried out on our solver made upon *OpenFOAM* 6. Variable-density based, transient set of governing equations (Eq. 3.1 - Eq. 3.7) were solved using PISO (Pressure Implicit with Split Operator) algorithm. The courant number was kept less than 0.5 during all the transient simulations.

Second-order finite volume schemes were used to discretize terms in the governing equations. Convergence criteria were kept less than 10^{-6} for all the parameters solved in steady-state simulations.

3.4 Domain independence and mesh refinement

The simulation arrangement of the isolated particle simulations with uniform Stefan flow is shown in Fig. 3.1, and the interior-resolved isolated particle simulation arrangement is shown in Fig. 3.3. Figure 3.2 shows the domain arrangement of the isothermal simulations with neighboring particles and uniform Stefan flow. The choice of domain size and mesh refinement is discussed separately in papers I, II, III and IV.

Isothermal and non-isothermal simulations used a domain of $64D \times 16D \times 16D$. The smallest mesh around the boundary layer of the particle was $0.01D$. For the reacting particle simulation, a domain of $57.6D \times 16D$ is used. The smallest mesh around the boundary layer is $0.02D$. Multi-particle simulations were carried out on a domain $(64D + L) \times 16D \times 16D$ with $0.02D$ mesh. L is the distance between 2 particle centers.

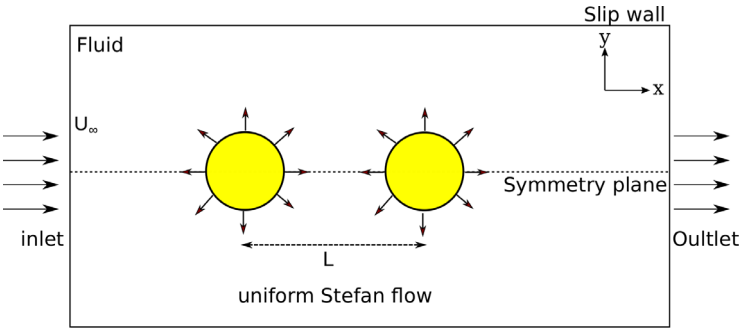

Figure 3.2: Arrangement of the domain of isothermal multi-particle simulations.

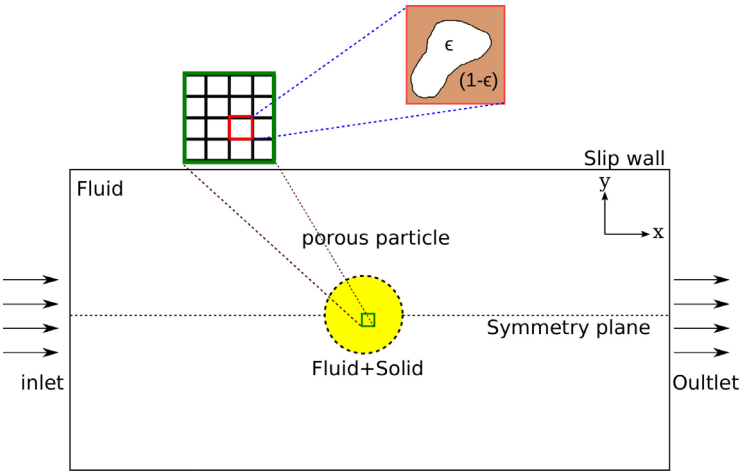

Figure 3.3: Arrangement of the simulation domain for reacting particle simulations.

3.5 Validation and verification

It is hard to find experimental data related to drag coefficient (C_d) and Nusselt number (Nu) for flow around a sphere with Stefan flow. Therefore, for the validation/verification of isothermal

and non-isothermal simulations: C_d and Nu without Stefan flow were compared against the available models in literature which are already validated with experimental data.

The isothermal drag coefficient without Stefan flow is compared with Haider & Levenspiel model [16] for flow around a sphere. Non-isothermal drag coefficient without Stefan flow is compared with the Schiller-Naumann drag model modified by Ellendt et al. [18] for non-isothermal conditions. Paper I and Paper II show the validation of isothermal and non-isothermal drag, respectively. Nusselt number without Stefan flow is compared with the Ranz-Marshall model for flow around a sphere which is shown in paper II.

The solver developed for reacting particle simulation in Step 4 (section 1.6) is validated in a step-wise procedure as follows:

1. compare the drag coefficient (C_d) of a cylinder from simulations with data from literature [36, 35],
2. compare the drag coefficient (C_d), and Nusselt number (Nu) of a cylinder from simulations with data from literature [36, 43, 46, 47],
3. compare conversion time of reacting particle with experimental data [58] on coal char gasification. We have chosen the coal type *coal char SM* from the publication for comparison with simulation data.

3.6 Evaluation of drag coefficient and Nusselt number

The drag coefficient can be calculated as Eq. 2.1 and local or point-wise pressure and viscous forces can be calculated as follows:

$$\overrightarrow{F}_P = \oint_S (P_{sur} - P_{ref})\overrightarrow{n}\, dS, \tag{3.8}$$

and

$$\overrightarrow{F}_{visc} = -\oint_S \mu(\nabla\overrightarrow{u} + \nabla\overrightarrow{u}^T)\overrightarrow{n}\, dS. \tag{3.9}$$

Here, the integration is over the external surface of the particle. In the above, P_{sur} and P_{ref} are the interpolated pressure at the particle surface and in the far-field, respectively, and $\overrightarrow{n}$ is the unit vector in the surface-normal direction.

In non-isothermal uniform Stefan flow simulation, Nusselt number was calculated based on the overall enthalpy difference in the solution domain as follows :

$$Nu_\infty = \frac{(\rho\overrightarrow{u}\, c_p T S)_{in} + \overrightarrow{u}_{Sf}(\rho c_p T S)_p - (\int(\rho\overrightarrow{u}\, c_p T)\overrightarrow{n}\, dS)_{out}}{S_{sph}(T_p - T_\infty)} \times \frac{D}{\lambda_\infty}, \tag{3.10}$$

where subscripts *in*, *out*, *p* and ∞, refer to the conditions at the *inlet* boundary, the *outlet* boundary, particle surface (see Fig. 3.1) and far-field, respectively, S is the surface area of the relevant boundary, λ is thermal conductivity, D is the particle diameter, and c_p is the specific heat capacity.

In particle-interior resolved simulations, Nusselt number (Nu) and Sherwood number (Sh) both calculated with and without Stefan flow. Nu/Sh without Stefan flow is calculated based on total diffusive heat/mass transfer over the discrete surfaces of the particle:

$$\mathrm{Nu}_\infty = \frac{\oint_S(-\lambda_g\nabla T_g)_p}{S_{particle}(T_p - T_\infty)} \times \frac{D}{\lambda_\infty}, \tag{3.11}$$

where S is the surface area of the cylinder. Nu/Sh with Stefan flow is calculated by including advective heat/mass transfer at the particle surface into Eq. 3.11.:

$$\mathrm{Nu}_{\infty,Sf} = \frac{\oint_S(-\lambda_g\nabla T_g)_p - \oint_S(\rho_g\overrightarrow{u}_r c_{p,g} dT_g dS)_p}{S_{particle}(T_p - T_\infty)} \times \frac{D}{\lambda_\infty}, \tag{3.12}$$

where $\overrightarrow{u_r}$ is velocity in the surface normal direction to the discrete surface of the particle.

3.7 Point-particle approach (PPA)

PPA is based on various models and assumptions, and it considers the particle as a point in space without occupying any volume. The existence of a particle is modeled through momentum, heat, and mass transfer between a particle and bulk fluid in particle-fluid flows. Detailed information on PPA can be found in paper V. Equations for calculating particle temperature and species mass fractions based on enthalpy and species mass conservation of the overall particle are shown below. Temperature equation is as follows:

$$[\epsilon\rho_g c_{p,g} + (1-\epsilon)\rho_c c_{p,s}]V_p\frac{dT_p}{dt} = hA_p(T_\infty - T_p) + \sigma\alpha A_p(T_w^4 - T_p^4) - R_C\Delta H - Q_{Sf} - Q_{Dufour}, \tag{3.13}$$

where $c_{p,i}$ are specific heat of gas ($i = g$) and char ($i = s$) inside the particle, V_p is the volume of the particle, h is heat transfer coefficient, A_p is the external surface area of the particle, T_∞ and T_w are far-field gas and wall temperature, σ is Stefan-Boltzman coefficient, α is the emissivity, ΔH is heat of reaction, Q_{Sf} is the advective transport of heat by the Stefan flow and Q_{Dufour} is the dofour term, enthalpy transfer due to gas species diffusion to/out of the particle. Species equation reads as follows:

$$\epsilon\rho_g V_p\frac{dY_{i,p}}{dt} = h_{m,i}W_i A_p(C_{i,\infty} - C_{i,p}) + \nu_i\frac{W_i}{W_C}R_C - M_{i,Sf}, \tag{3.14}$$

where $Y_{i,p}$ is the mass fraction of species i inside the particle, $h_{m,i}$ is the mass transfer coefficient of species i on a molar basis, C_i is the concentration of species i, W_i is molecular weight of gas ($i = g$) and char ($i = C$), and $M_{i,Sf}$ is the advective transport of species by the Stefan flow.

Chapter 4

Results and discussion

"The task is not to see what has never been seen before, but to think what has never been thought before about what you see everyday."

—Erwin Schrodinger

This chapter will summarize the results of numerical simulations discussed in chapter 3. First, the effects of a uniform Stefan flow around an isolated particle is discussed. Then, the effects of neighboring particles are discussed for particles with uniform Stefan flow. After that, the effects of Stefan flow on a reacting particle under more realistic conditions are discussed. Finally, the validity of using the point-particle approach in reacting particles with Stefan flow is discussed. All the discussions are carried through particle-resolved numerical simulation results, and for the last step, point-particle calculations were also performed.

4.1 Effect of Stefan flow on an isolated particle with uniform Stefan flow

The effect of Stefan flow on an isolated particle is first tested by immersing it in an isothermal bulk fluid flow at different Reynolds numbers (Re) and different Stefan Reynolds numbers (Re_{Sf}). The results will provide a simplified case without effects of temperature gradients, variation of thermophysical properties, and other conditions which could create further complications due to non-isothermal conditions. Isothermal simulations provide the effects of Stefan flow alone on pressure and viscous forces.

4.1.1 Drag coefficient

Figure 4.1a shows the variation of the normalized drag coefficient with the normalized Stefan flow velocity at different Reynolds numbers of the bulk fluid flow. Clearly, an outward Stefan flow (positive values) decreases the drag coefficient, while an inward Stefan flow (negative values) increases the drag coefficient. Velocity contours around the particle in Fig. 4.1b show an expansion of the velocity boundary layer with an outward Stefan flow. Inward Stefan flow has shown a shrinkage of the boundary layer. Figures 4.1c and 4.1d show how viscous stress and pressure vary around the particle for the case with a Reynolds number of 14. The pressure force is not affected by the Stefan flow, while the viscous force is reducing/increasing with an outward/inward Stefan flow. The change of viscous stress might be due to boundary layer expansion which causes less velocity gradient leading to a lower viscous force. A more detailed analysis can be found in paper I.

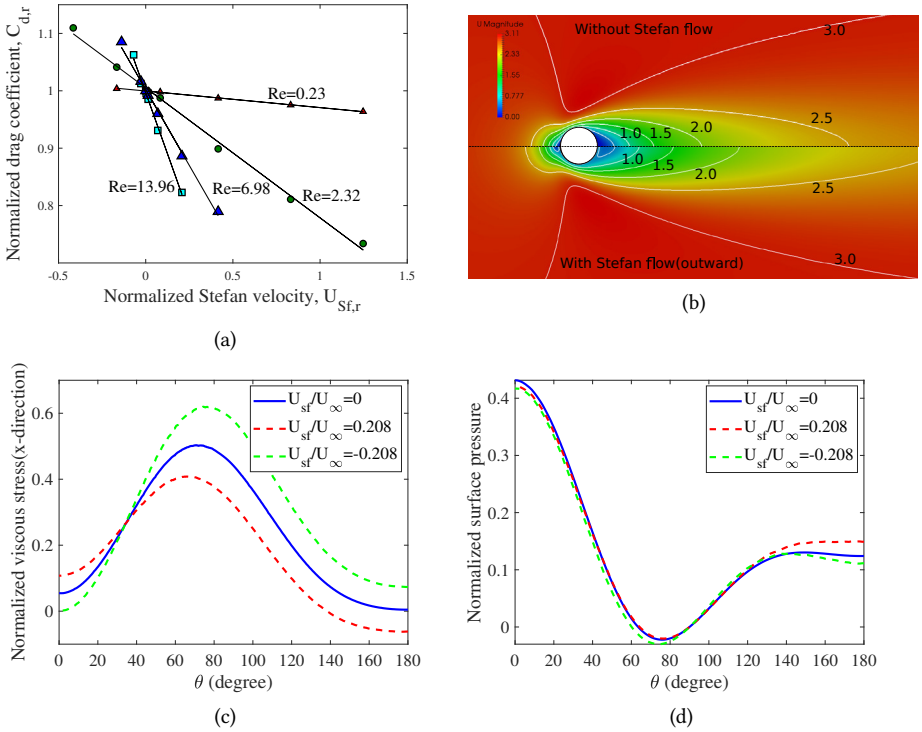

Figure 4.1: Isothermal simulation results with a uniform Stefan flow around the particle. (a) Normalized drag coefficient $C_{d,Sf}/C_d$ vs normalized Stefan flow velocity U_{Sf}/U_∞ at different Re. Symbols: simulations, lines: linear regression to the data. (b) Velocity boundary layer around the particle, with and without Stefan flow. (c) Normalized viscous stress and (d) Normalized surface pressure around the particle from upstream of the particle to the downstream [59].

The deviation of C_d with Stefan flow and without Stefan flow is not negligible in the range of Reynolds number and Stefan flow velocity.

Therefore, a model was developed based on the variation of boundary layer thickness due to Stefan flow in a time scale of bulk fluid passing the particle. Further details are available in paper I. According to the model, the ratio of drag with Stefan flow vs drag without Stefan flow is:

$$C_{d,r} = \frac{1}{1 + f(\mathrm{Re})\mathrm{Re}_{Sf}}, \tag{4.1}$$

with

$$f(\mathrm{Re}) = \frac{3}{\mathrm{Re}}\left(1 + \frac{2A}{\sqrt{\mathrm{Re}}}\right)\frac{1}{\left(\frac{3A}{\sqrt{\mathrm{Re}}} + 6\left(\frac{A}{\sqrt{\mathrm{Re}}}\right)^2 + 4\left(\frac{A}{\sqrt{\mathrm{Re}}}\right)^3\right)}, \tag{4.2}$$

where $A = 3.01 \pm 0.13$ and Re_{Sf} is Reynolds number based on Stefan flow velocity.

The effects observed in isothermal conditions can be aggravated or alleviated by the non-isothermal effects. Non-isothermal effects have been studied by applying a temperature difference between the particle and the bulk fluid. Particle temperature has been varied, keeping the far-field temperature constant at 1400 K. Isothermal simulations include the physical effects due to Stefan flow. Non-isothermal simulations have both physical and thermal effects. Figure 4.2a shows the isothermal case with $\mathrm{Re} = 13.96$ in non-isothermal conditions. There is a clear difference between the drag coefficients at isothermal and non-isothermal conditions, at least for cases

with high-temperature gradients between the particle and the far-field temperature. Although there are deviations between isothermal and non-isothermal results, the trends are similar for all cases. An outward Stefan flow reduces the drag coefficient, and an inward Stefan flow increases the drag coefficient, while an outward/inward Stefan flow expands/shrinks boundary layers for both isothermal and non-isothermal cases (see Fig. 4.2b). The thermal boundary layer also shows similar trends to the velocity boundary layer.

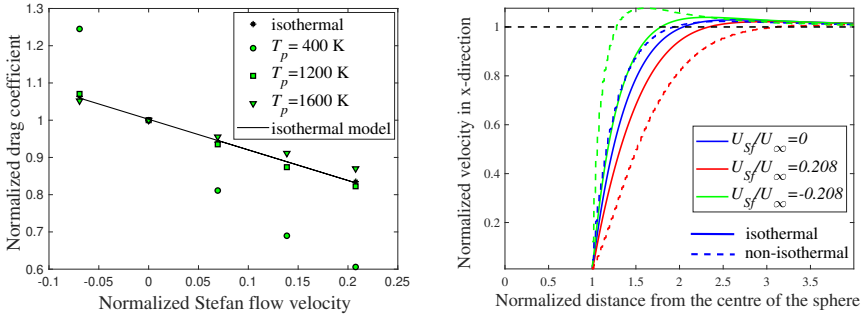

(a) (b)

Figure 4.2: Non-isothermal simulation results with a uniform Stefan flow around the particle. (a) Normalized drag $C_{d,Sf}/C_d$ at film condition and Normalized Stefan flow velocity U_{Sf}/U_∞. Far-field temperature ($T_\infty = 1400$ K) and different particle temperatures (T_p =400 K, 1200 K,1600 K) [60]. (b) Velocity boundary layer variation in isothermal and non-isothermal cases.

Deviation of the isothermal line from non-isothermal results (symbols) shows the importance of thermal effects. The importance of thermal effects increases when the temperature difference between the particle (T_p) and the bulk fluid (T_∞) increases. Therefore, the isothermal drag model has to be modified to consider the thermal effects. Thermal effects are twofold. One is due to variation of thermophysical properties due to the difference between particle temperature (T_p) and bulk fluid temperature (T_∞). The other one is the variation of thermophysical properties due to Stefan flow. A new characteristic temperature $\tilde{T}$, based on the volume of the boundary layer at film temperature, $T_f = \frac{T_p+T_\infty}{2}$, and volume of Stefan flow at the temperature of Stefan flow, $T_p = T_{Sf}$, is introduced. It eventually yields (see paper II for detailed derivation),

$$\tilde{T} = \frac{T_f + \frac{U_{Sf}}{U_\infty} f(\mathrm{Re}_f) T_{Sf}}{1 + \frac{U_{Sf}}{U_\infty} f(\mathrm{Re}_f)}, \tag{4.3}$$

where U_∞ is far-field velocity, Re_f is Reynolds number at film condition and U_{Sf} is Stefan flow velocity. The drag coefficient with Stefan flow at non-isothermal conditions will be calculated as follows:

$$C_{d,Sf} = \tilde{C}_d \times C_{d,r}, \tag{4.4}$$

where $\tilde{C}_d$ is calculated from Schiller-Naumann model in section 2.1 and

$$C_{d,r} = \frac{1}{1 + \frac{U_{Sf}}{U_\infty} f(\mathrm{Re}_f)}. \tag{4.5}$$

Comparison of model with the simulation data and further details available in paper II [60]. Model and simulation results agree for the range of considered parameters.

4.1.2 Nusselt number

There is a theoretical model developed for the effect of Stefan flow for the Nusselt number around a spherical particle in a quiescent flow [61]:

$$\mathrm{Nu}_{Sf,0} = \mathrm{Nu}_0 \frac{(\mathrm{PrRe}_{Sf})/\mathrm{Nu}_0}{e^{(\mathrm{PrRe}_{Sf})/\mathrm{Nu}_0} - 1}, \tag{4.6}$$

where Nu_0 is the Nusselt number in a quiescent environment for a sphere. Meanwhile, there are Nusselt number models developed, for a sphere immersed in a forced convective flow, such as Ranz-Marshall [42] and Whitaker [43] models. A Ranz-Marshall type model has been developed for the Nusselt number without Stefan flow which is applicable when there is a high-temperature difference between the particle and the bulk fluid. Using simulation data, we gained :

$$\mathrm{Nu}_f = 2 + 0.5703\mathrm{Re}_f^{0.5373}\mathrm{Pr}_f^{1/3}, \tag{4.7}$$

where Nu, Re, and Pr are calculated at the film condition. We developed a model for a sphere immersed in a convective fluid with a Stefan flow. The model combines the Nusselt number with Stefan flow in a quiescent environment (Eq. 4.6), and the model developed for the Nusselt number in a convective flow (Eq. 4.7) by replacing Nu_0 in Eq. 4.6 by Nu_f in Eq. 4.7. Variation of properties in the boundary layer is added by calculating $\mathrm{Nu}_{\tilde{T}}$ instead of Nu_f in the model Eq. 4.7. The model for the Nusselt number of a sphere in a convective flow with a uniform Stefan flow around it can be modeled as:

$$\mathrm{Nu}_{Sf} = \mathrm{Nu}_{\tilde{T}} \frac{q}{e^q - 1}, \tag{4.8}$$

where $q = \frac{(\mathrm{PrRe}_{Sf})}{\mathrm{Nu}_{\tilde{T}}}$.Here, the Nusselt number with Stefan flow (Nu) is calculated based on the film condition. The Stefan flow Reynolds number (Re_{Sf}) is calculated based on particle surface condition, and the Prandtl number (Pr) is calculated based on film condition. Further details on limits of calculating $\tilde{T}$, comparison of simulation results with model results, and further details can be found in paper II [60].

4.2 Effects of Stefan flow on closely spaced particle pair with uniform Stefan flow

Neighboring particle simulations were carried out for three Reynolds numbers and three Stefan Reynolds numbers. The following effects were observed:

- neighboring particle effects were non-negligible at all the distances considered in this work ($1.1 \leq L/D \leq 10$),
- outward Stefan flow reduces the drag coefficient with an expansion of the boundary layer (see Fig. 4.3a) and inward Stefan flow increases the drag coefficient of particles with a shrink in the boundary layer when particle distances (L/D) were greater than 2.5 (compare Fig. 4.3b b with a and c),
- the drag coefficient of both particles is less than that for an isolated particle with Stefan flow when particle distance is greater than 2.5 (compare dotted lines of each figure with solid and dashed lines in Fig. 4.3b). I.e., both neighboring particle effects, and Stefan flow effects are affecting on the particles,
- When particle distances (L/D) are less than 2.5, outward Stefan flow repels particles from each other, and inward Stefan flow attracts each other. Stefan flow effects dominate between the particles due to blockage of bulk flow when the particle distances are small.

The pressure and viscous force both increase, and pressure force has a large impact on the particles compared to viscous force leading to very high drag coefficients on downstream particles with outward Stefan flow and upstream particles with inward Stefan flow.

More details can be found in Paper III.

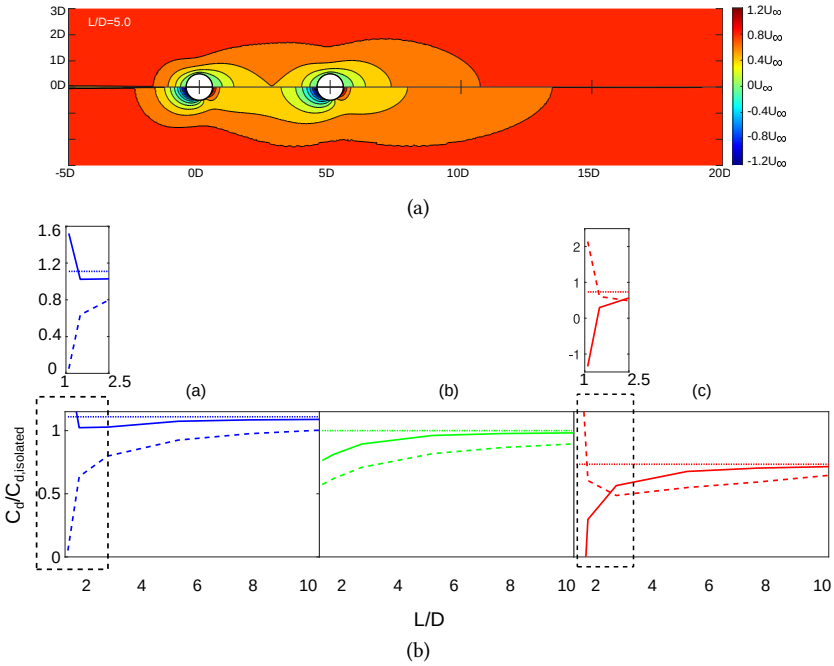

Figure 4.3: (a) Velocity contours in the mean flow direction around the particles with $\mathrm{Re} = 2.3$. The top half shows the case without Stefan flow while the bottom half is case with outward Stefan flow ($U_{Sf} = 0.62$ m/s corresponding to $\mathrm{Re}_{Sf} = 2.9$). (b) Relative drag coefficient, normalized with the value of an isolated particle without Stefan flow, as a function of the particle separation (L/D). (a) $U_{Sf} = -0.2$ m s^{-1}; (b) $U_{Sf} = 0$ m s^{-1}; (c) $U_{Sf} = 0.6$ m s^{-1}.

4.3 Effect of Stefan flow on a reacting particle

Table 4.1 shows particle-resolved simulation case details. Effects of Stefan flow on a gasifying particle under more realistic conditions have been tested and analyzed for the drag coefficient, Nusselt number, and Sherwood number.

4.3.1 Drag coefficient of a reacting particle

Figure 4.4 shows normalized C_d, pressure force, and viscous force of the six cases simulated in this work. Results have shown complex behavior in the variation of C_d, Nu and Sh compared to simplified cases studied before with a uniform Stefan flow and single component bulk fluid. There are similarities within low and high effectiveness factor (η) cases. Here, low η cases have a range of 0.21-0.44, and high η cases have a range of 0.58-0.74. Common features of cases with low η and high η have listed as follows.

Low η case C_d and the related parameter variations can be summarized as follows:

- normalized C_d is higher than or close to one ($C_{d,\mathrm{norm}} \geq 1$) at all conditions (see Fig. 4.4a),

Table 4.1: List of parameters that varied for different simulation cases. Effectiveness factor (η), particle Reynolds number (Re), and Stefan Reynolds number (Re_{Sf}) are the values estimated from the results of the resolved particle simulation.

Case	$\mathbf{T}_\infty$ (K)	$\mathbf{p}_\infty$ (atm)	$\mathbf{d_p}$ (μm)	$\mathbf{U}_\infty$ (m/s)	$\mathbf{Y}_{\mathbf{CO_2},\infty}$ (-)	$\boldsymbol{\eta}$	**Re**	$\mathbf{Re_{Sf}}$
1	1999	1.807	189.3	0.45	0.512	0.23	0.5	0.09
2	1999	1.807	189.3	2.70	0.512	0.44	3.0	0.03
3	1851	4.201	442.6	0.44	0.512	0.21	3.0	0.04
4	1891	4.506	97.21	0.32	0.512	0.74	0.5	0.08
5	1891	4.506	97.21	1.93	0.512	0.69	3.0	0.02
6	1735	7.672	228.1	0.32	0.99	0.58	3.0	0.03

- normalized viscous force is lower than or close to one ($F_{\mathrm{visc,norm}} \leq 1$) except at the very early stage of the particle conversion (see Fig. 4.4c),
- pressure component of the C_d (C_p) is higher than the viscous (C_{vis}) component during the conversion. I.e., the pressure force is higher than the viscous force (see paper IV for more details),
- there is a region of gradual increase and decrease (bump) in pressure force during particle conversion (see Fig. 4.4e). In the same region of the bump in pressure force, there is a gradual decrease and increase of viscous force (pothole) .

High η case C_d and the related parameter variations can be summarized as follows:

- normalized C_d is higher than one ($C_{d,\mathrm{norm}} > 1$) at an early stage of conversion for cases with a higher ratio of $\mathrm{Re}_{Sf}/\mathrm{Re}$. Normalized C_d is lower than one ($C_{d,\mathrm{norm}} < 1$) for cases with lower ratio of $\mathrm{Re}_{Sf}/\mathrm{Re}$ (see Fig. 4.4b),
- normalized viscous force is lower than one ($F_{\mathrm{visc,norm}} < 1$; see Fig. 4.4d),
- normalized pressure force is higher than one until particle shape starts to change or conversion is greater than 0.75 ($X_p > 0.75$; see Fig. 4.4f),
- pressure component of the C_d (C_p) dominates throughout the conversion. I.e., the pressure force is higher than the viscous force (see paper IV for more details).

The normalized drag coefficient greater than one ($C_{d,\mathrm{norm}} > 1$) is in contradiction with our previous findings on the effects of Stefan flow; a uniform outward Stefan flow around a particle has a lower C_d compared to a particle without Stefan flow. However, the viscous force is lower than one (in most of the particle conversions), corresponding with our findings on the effect of Stefan flow on the viscous force. The reason for $C_{d,\mathrm{norm}}$ greater than one ($C_{d,\mathrm{norm}} > 1$) was the pressure force which we did not observe under uniform Stefan flow conditions. Identified reasons for the high-pressure force were:

- localized reaction rates under regime II (low η) conditions create non-uniform Stefan flow around the particle. Non-uniform Stefan flow leads to high-pressure force during particle conversion for low-effectiveness factor cases,
- during the conversion, pressure increases inside the porous media because of the additional resistance due to Stefan flow. Its variation is much more significant than the gas phase leading to high pressure for high-effectiveness factor cases.

More details on explanation can be found in paper IV.

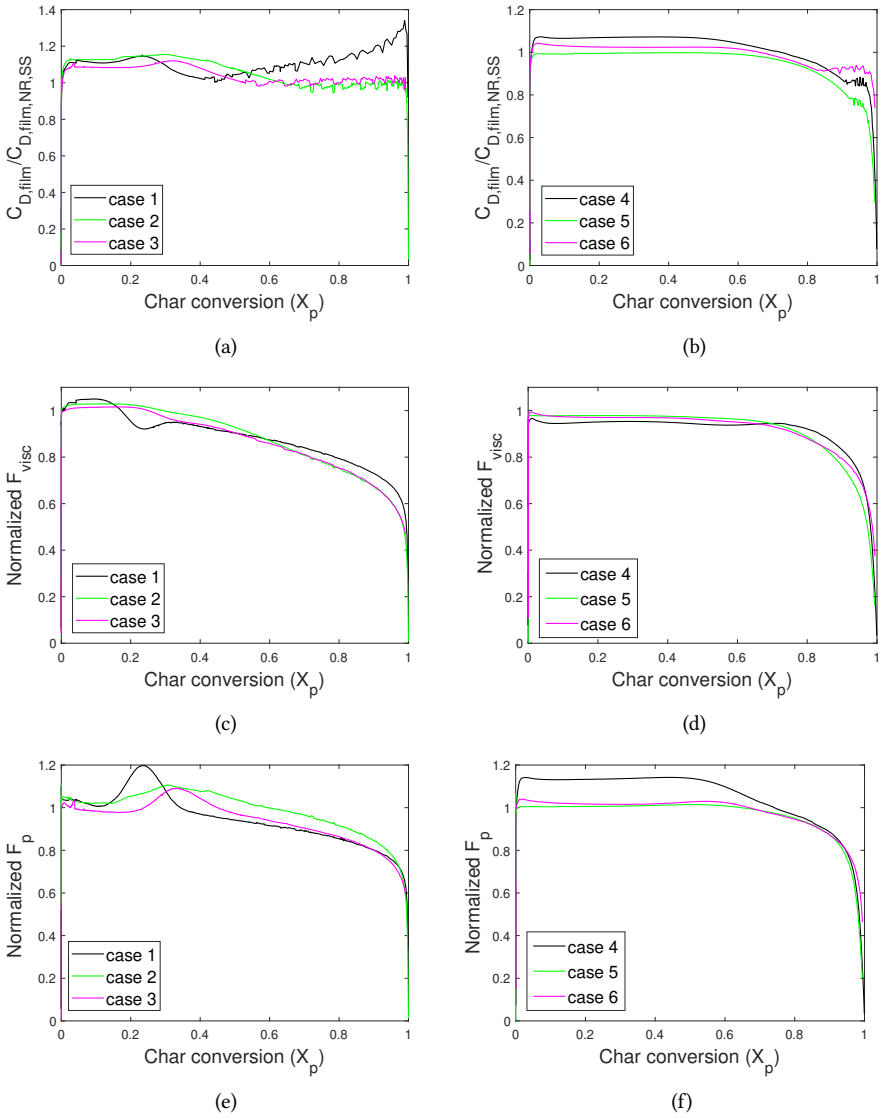

Figure 4.4: Variation of parameters with char conversion. (a) Comparison of normalized average drag coefficient ($C_{d,\mathrm{norm}}$) of the particles in low η and (b) high η cases in Table 4.1. (c) Normalized average viscous force for low η and (d) high η cases. (e) Normalized average pressure force for low η and (f) high η cases. Forces and C_d are normalized with the corresponding values of the same case without reaction at steady state.

4.3.2 Nusselt number

Figure 4.5 shows the variation of Nusselt number: considering advective effects due to Stefan flow ($\mathrm{Nu}_{\infty,Sf}$), neglecting Stefan flow (Nu_{∞}) and, for the same case without reactions after reaching steady-state ($\mathrm{Nu}_{\infty,NR,SS}$). Except for the case with low Re and high η, all the other cases have significantly lower Nusselt number ($\mathrm{Nu}_{\infty,Sf}$) compared to Nusselt number of a particle without

reactions at steady-state ($Nu_{\infty,NR,SS}$). These results correspond with the previous findings on effect of uniform Stefan flow on the average Nusselt number (Nu) of the particle where outward Stefan flow decreases the Nu. I.e., advective effects due to Stefan flow in a reacting particle is significant.

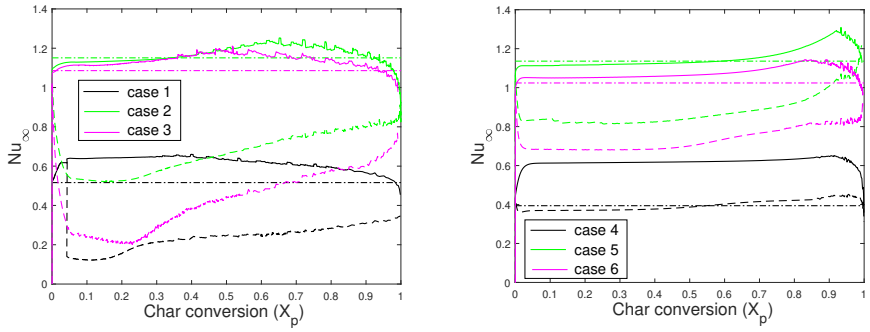

(a) (b)

Figure 4.5: Comparison of Nusselt number (Nu) of each case with char conversion. (a) low η and (b) high η cases. Solid line - Nu without considering advective heat transfer due to Stefan flow effects (Nu_{∞}). Dashed line - Nu considering advective heat transfer due to Stefan flow effects also ($Nu_{\infty,Sf}$). Dash-dot line - Nu at steady state in a non-reacting flow with same conditions ($Nu_{\infty,NR,SS}$).

4.3.3 Sherwood number

Figure 4.6 shows the effects of Sherwood number (Sh) for CO_2 and CO with and without Stefan flow (advective) during particle conversion. There is a negligible difference between Sh with and without Stefan flow. However, the Nusselt number (Nu) with and without Stefan flow significantly differs. In general, the Sh number is calculated based on Nu models considering the unity Lewis number (Le$=1$) in literature. This will not be valid for a reacting particle with a Stefan flow due to changes in the Nusselt number.

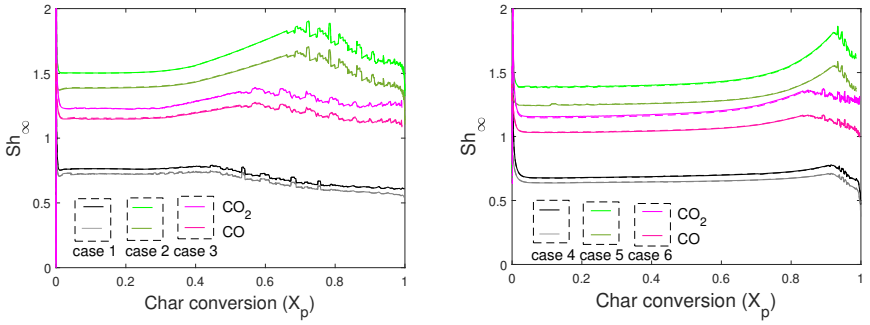

(a) (b)

Figure 4.6: Comparison of Sherwood number (Sh) of each case with char conversion. (a) low η (b) high η cases. solid line - Sh without considering advective mass transfer due to Stefan flow. Dashed line - Sh considering advective mass transfer due to Stefan flow.

4.4 Applicability of point-particle approach for a particle reacting with a Stefan flow

Resolved-particle simulation (RPS) results discussed in section 4.3 are used for comparison with point-particle simulation results (PPS) discussed in this section. Details of point-particle simulation equations can be found in paper V. First, the deviations between PPS and RPS are discussed. Then the reasons behind the deviations are discussed briefly.

Figure 4.7 shows the comparison of effectiveness factor and volume-averaged temperature from RPS and PPS for the six cases. Results have shown that there is a significant difference between RPS and PPS results, and major observations are summarized below:

- high η case PPS and RPS results are closer to each other compared to low η cases,
- PPS underestimates char conversion rates for high η cases while it overestimates char conversion for low η cases,
- deviation of PPS with RPS is highest for cases with a high ratio of Stefan Reynolds number to particle Reynolds number ($\mathrm{Re}_{Sf}/\mathrm{Re}$),
- effectiveness factor is always overestimated in PPS compared to RPS,
- variation of particle diameter always has delayed in PPS compared to RPS.

Some tests have been conducted to identify the source of inaccuracies between PPS and RPS. Tests were based on replacing PPS equations with RPS simulation values for particle surface temperature and particle surface gas concentrations and carrying out particle resolved simulations with very high thermal conductivity of the particle to create uniform temperature within the particle. The following has been identified as major sources for inaccuracies of PPS results compared to RPS:

- external heat transfer models underestimate the rates,
- external mass transfer overestimates the rates,
- effectiveness factors do not consider the effects of non-uniform temperature, leading to higher effectiveness factors,
- in high η cases, errors in external heat transfer dominate the overall conversion rates,
- for low η cases, the inaccuracy of using uniform particle temperature becomes more important, and the PPS tends to overestimate the conversion rates.

4.5 Summary of results

Table 4.2 shows a summary of research questions and the answers obtained through this study. Overall, the effects of Stefan flow on a reacting particle seem to affect during all the conditions we considered in this work, although a high Reynolds number shows steeper gradients for the decrease/increase of drag coefficient (see Fig. 4.1a). Nusselt number is also affected by the Stefan flow. Effects of Stefan flow on neighboring particles are also non-negligible, especially at low particle distances when Stefan flow effects dominate.

When comparing results from more realistic conditions (char gasification), Stefan flow effects deviate from uniform Stefan flow conditions results. The main reason was the increased pressure force due to non-uniform Stefan flow (low η cases) and the increase of pressure in the porous media due to Stefan flow. Point-particle approach results with resolved-particle simulations have shown large deviations due to the inability of the point-particle approach to predict external heat transfer, mass transfer, and effectiveness factor accurately.

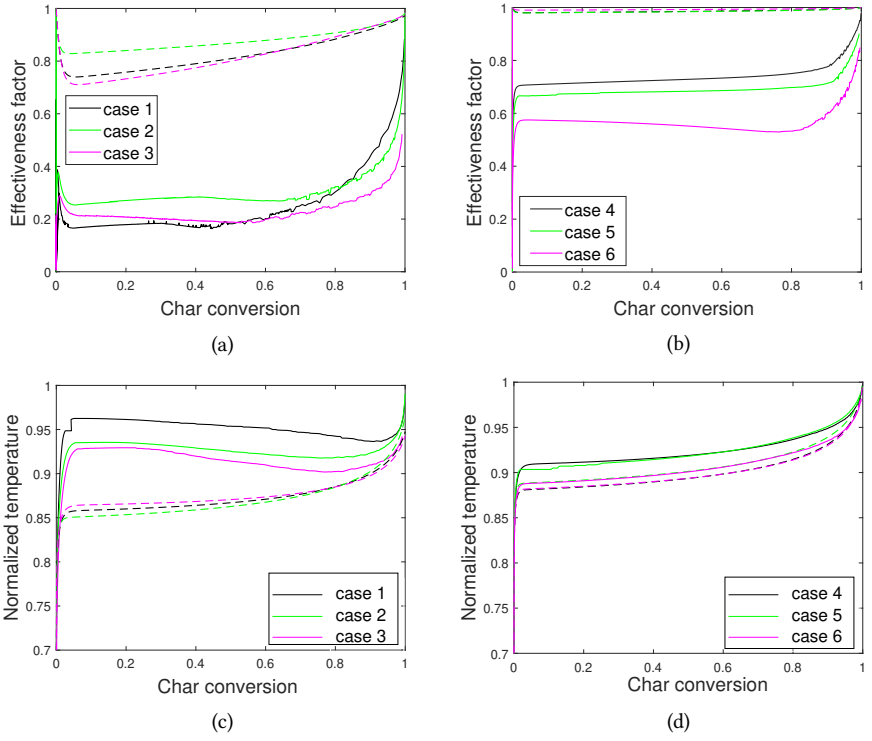

Figure 4.7: Comparison of RPS and PPS results. Effectiveness factor variation as a function of char conversion for (a) low η and (b) high η cases. Volume-averaged temperature variation with char conversion for (c) low η and (d) high η cases. Solid lines - RPS; Dashed lines - PPS. Temperature is normalized with a far-field temperature of each case.

Table 4.2: The summary of research questions and answers from this study. It should be noted that the results are valid for the range of parameters considered in this study which is not specifically mentioned in the table.

RQ	Question	Answer
1	What are the effects of Stefan flow on the interaction between particles and the bulk fluid?	-Stefan flow vary both physical and thermal properties around the particle in a non-isothermal flow -Stefan flow changes the velocity and thermal boundary layer -A uniform Stefan flow affects the viscous force of the particle, and pressure force is unaffected and therefore the C_d is affected -Uniform Stefan flow changes Nu between a particle and bulk fluid
2	How do reacting neighboring particles interact through the change in fluid flow?	-Neighbor particle and Stefan flow effects are independent on the particles for large particle distances ($L/D > 2.5$) -Stefan flow effects dominate, creating repulsive/attractive forces with outward/inward Stefan flow for small particle distances ($L/D \leq 2.5$)
3	What are the effects of Stefan flow on the interaction between particles and the bulk fluid during char gasification?	-Stefan flow affects momentum and heat transfer varying C_d and Nu compared to a non-reacting particle -Both pressure force and viscous force is varied due to gasification -In general, pressure force is higher, viscous force is lower and C_d is higher than a non-reacting particle -Nu is lower than a non-reacting particle -Sh is almost constant
4	How does the point-particle simulations (PPS) perform in char gasification compared to particle-resolved simulations (RPS)?	- There is a significant difference between PPS results and RPS results in all cases -Deviations were due to: - neglecting non-uniform temperature in the effectiveness factor - underestimation of heat transfer - overestimation of mass transfer

Chapter 5

Conclusions and future work

"Nothing in life is to be feared, it is only to be understood. Now is the time to understand more, so that we may fear less."

—Marie Curie

This chapter has two sections. The first part discusses the conclusions drawn from this work. The second part recognizes the necessary future studies for a better explanation of some results and suggestions to further improvements in model development for using in large-scale simulations.

5.1 Conclusions

This thesis investigated the effect of Stefan flow generated by chemical reactions in particle-laden fluid flows. Particle-resolved numerical simulations were carried out to elucidate its effects. The step-wise approach for increased complexity was adopted, starting from a simpler model to a realistic one. All the particle Reynolds numbers (Re) used in this work were less than 15. Simulation conditions were based on Entrained-flow biomass gasification even though the studies are general for the cases within the range of parameters studied in this work (Reynolds number, Stefan Reynolds number).

Initially, the effect of uniform Stefan flow on the drag coefficient (C_d) of a spherical particle is studied in a uniform bulk fluid flow at a constant temperature. This study aimed at studying the physical effects of uniform Stefan flow. Results showed that outward Stefan flow reduces the drag coefficient (C_d) and inward Stefan flow increases the drag coefficient (C_d). Stefan flow changes the average viscous force on a particle, although the average pressure force is not affected. A model was developed for the drag coefficient (C_d) with the effect of Stefan flow based on physical interpretation. The model was based on the variation of boundary layer thickness with only one fitting parameter. Non-isothermal effects were added to the simulations by creating a temperature difference between the particle and the bulk fluid. This study aimed to understand the physical and thermal effects of the uniform Stefan flow. The effect of Stefan flow on the drag coefficient (C_d) and the Nusselt number (Nu) were studied. The results show that the isothermal drag coefficient and the non-isothermal drag coefficient were different. Therefore, the model developed from isothermal simulations was modified based on thermal effects due to Stefan flow. A new model is developed for the effect of Stefan flow on the Nusselt number (Nu) for a spherical particle in a convective flow using non-isothermal simulation results. The model is developed by combining a model for the Nusselt number (Nu) of a spherical particle in a quiescent environment with Stefan flow and a model for the Nusselt number (Nu) of a spherical particle in a uniform convective flow.

Then, the effect of uniform Stefan flow on neighboring spherical particles was studied in a uniform bulk fluid flow under isothermal conditions. Particles were affected independently by both neighbor particle and Stefan flow effects when the distance between particles is greater than 2.5 ($L/D > 2.5$). Stefan flow effects dominate when the distance between particles is less than or equal to 2.5 ($L/D \leq 2.5$), and both pressure and viscous force show steep variations. An outward Stefan flow causes repulsion, and an inward Stefan flow causes attraction between neighboring particles.

Finally, a porous particle reacting under a heterogeneous reaction was considered by resolving the interior and exterior of the particle. Char gasification is considered as the heterogeneous reaction which creates a realistic Stefan flow rather than a uniform Stefan flow considered in previous works. A numerical code was developed to study particle-resolved simulations with heterogeneous reactions. Particle-resolved simulations (PRS) were carried out for different particle Reynolds numbers, effectiveness factors, and Stefan Reynolds numbers. Point-particle simulations (PPS) were also carried out to find the accuracy of PPS by comparing it with RPS results for reacting particles with a Stefan flow. Drag coefficient (C_d), Nusselt number (Nu), and Sherwood number (Sh) were analyzed for each case from PRS results, and an effort has been made to explain the variation of the drag coefficient during reactions. Results showed that the drag coefficient (C_d) is higher than a case without reactions under the same conditions, which contradicts our previous findings. However, viscous force is less than or close to a case without reactions under the same conditions for most of the conversion time. Therefore, the pressure force is responsible for increasing the drag coefficient during heterogeneous reactions with a Stefan flow. Decreasing in viscous force corresponds with uniform Stefan flow results. Two reasons have been identified for the increase of pressure force. One is the localized reaction of a particle under regime II conditions creating a non-uniform Stefan flow. The other is the increase of pressure inside the particle (porous media) due to high resistance created by the Stefan flow.

Comparison of Particle-resolved simulation (PRS) results with Point-particle simulation (PPS) results have shown variations for different parameters such as effectiveness factor, particle radius, and gas compositions. Gas compositions have shown significant variation between PRS and PPS results. Different tests have been carried out to identify the reason for deviations between the two approaches. Main reasons were negligence of non-uniform temperature within the particle in effectiveness factor and deviation of external heat and mass transfer models from the Nusselt number and the Sherwood number.

5.2 Future work

Stefan flow is available everywhere in the nature such as in evaporation. Our main interest on the effects of uniform Stefan flow was for the range in entrained-flow biomass gasification (EFBG). Therefore, it would be important to develop physics based models for a wider range of Reynolds number and Stefan Reynolds number. Same applies to rest of the work since it is important to gain insight of Stefan flow effects in a wider range to be used in different applications. One more important part of modeling would be to suggest at which conditions one can neglect the Stefan flow effects.

Effects of Stefan flow on neighboring particles were also studied only for particles in tandem arrangement. In reality, particles can be at any direction to one another in 3-D space. Therefore, it is important to study other arrangements of particle positioning and find common features of neighboring particles with a Stefan flow.

Particle interior and exterior resolved simulations (RPS) have shown that drag coefficient and Nusselt number vary for a particle with heterogeneous reactions producing a Stefan flow. Observations suggest that Stefan flow affects the variation of the C_d and Nu. It would have been easier to compare and draw conclusions about cases with Stefan flow, if RPS cases had results without Stefan flow. Therefore, it would be an important addition to this work to compare the

results of cases with Stefan flow with cases without it.

Comparisons of RPS results with PPS have shown significant deviations between the two, and this work has identified some of them. It is important to find the models for heat and mass transfer coefficients (Sh, Nu) that predict PPS results closer to RPS results for different applications. Further, improving the models we have developed for a uniform Stefan flow to be modified for cases with non-uniform Stefan flow and creating more advanced models is important. In addition, it is important to improve the effectiveness factor models currently used for char gasification to consider the non-uniform temperatures, the convective effects within a particle and to include the history of particle conversion.

Bibliography

[1] C. W. Lewis, Biomass through the ages, Biomass 1 (1) (1981) 5–15. doi:10.1016/0144-4565(81)90011-1.

[2] C. Higman, M. Burgt, Gasification, Gulf Professional Publishing, 2008.

[3] P. A. Nikrityuk, B. Meyer, Gasification Processes Modeling and Simulation, 1st Edition, Wiley-VCH, 2014.

[4] F. Weiland, Pressurized entrained flow gasification of pulverized biomass: Experimental characterization of process performance, Ph.D. thesis, Luleå University of Technology (2015).

[5] B. Goktope, Entrained flow gasification of biomass soot formation and flame stability, Ph.D. thesis, Luleå University of Technology (2015).

[6] N. E. L. Haugen, M. B. Tilghman, R. E. Mitchell, The conversion mode of a porous carbon particle during oxidation and gasification, Combustion and Flame 161 (2014) 612–619. doi:10.1016/j.combustflame.2013.09.012.

[7] T. Kreitzberg, A. Phounglamcheik, N. E. L. Haugen, R. Kneer, K. Umeki, A Shortcut Method to Predict Particle Size Changes during Char Combustion and Gasification under regime II Conditions, Combustion Science and Technologydoi:10.1080/00102202.2019.1678919.

[8] K. Qin, P. A. Jensen, W. Lin, A. D. Jensen, Biomass Gasification Behavior in an Entrained Flow Reactor: Gas Product Distribution and Soot Formationdoi:10.1021/ef300960x.

[9] B. Göktepe, A. H. Saber, R. Gebart, T. S. Lundström, Cold flow experiments in an entrained flow gasification reactor with a swirl-stabilized pulverized biofuel burner, International Journal of Multiphase Flow 85 (2016) 267–277. doi:10.1016/j.ijmultiphaseflow.2016.06.016.

[10] B. Göktepe, K. Umeki, R. Gebart, Does distance among biomass particles affect soot formation in an entrained flow gasification process?, Fuel Processing Technology 141 (2016) 99–105. doi:10.1016/j.fuproc.2015.06.038.

[11] T. Kreitzberg, S. Pielsticker, B. M. Gövert, R. Kneer, CO2 and H2O Gasification under Chemically and Diffusion Controlled Conditions (2016).

[12] N. E. L. Haugen, R. E. Mitchell, M. B. Tilghman, A comprehensive model for char particle conversion in environments containing O2 and CO2, Combustion and Flame 162 (4) (2015) 1455–1463. doi:10.1016/j.combustflame.2014.11.015.

[13] N. E. L. Haugen, B. K. Y. Loong, R. E. Mitchell, Numerical approaches for thermochemical conversion of char, Progress in Energy and Combustion Science 91. doi:10.1016/j.pecs.2022.100993.

[14] R. B. Bird, W. E. Stewart, E. N. Lightfoot (Eds.), Transport Phenomena, 2nd Edition, John Wiley & Sons Inc, 2006.

[15] A. Hölzer, M. Sommerfeld, New simple correlation formula for the drag coefficient of non-spherical particles, Powder Technology 184 (3) (2008) 361–365. doi:10.1016/j.powtec.2007.08.021.

[16] A. Haider, O. Levenspiel, Drag coefficient and terminal velocity of spherical and nonspherical particles, Powder technology 58 (1989) 63–70. doi:10.1016/0032-5910(89)80008-7.

[17] L. Schiller, A. Naumann, A drag coefficient correlation, Zeitschrift des Vereins Deutscher Ingenieure 77 (1935) 318–320.

[18] N. Ellendt, A. M. Lumanglas, S. I. Moqadam, L. Mädler, A model for the drag and heat transfer of spheres in the laminar regime at high temperature differences, International Journal of Thermal Sciences 133 (July) (2018) 98–105. doi:10.1016/j.ijthermalsci.2018.07.009.

[19] H. Miao, H. Zhang, X. An, C. Ke, A. Yu, Numerical study on the momentum and heat transfer of porous spheroids under laminar flow, Powder Technology 395 (2022) 14–25. doi:10.1016/j.powtec.2021.09.045.

[20] K. Wittig, P. Nikrityuk, A. Richter, Drag coefficient and Nusselt number for porous particles under laminar flow conditions, International Journal of Heat and Mass Transfer 112 (2017) 1005–1016. doi:10.1016/j.ijheatmasstransfer.2017.05.035.

[21] B. Kravets, D. Schulz, R. Jasevičius, S. R. Reinecke, T. Rosemann, H. Kruggel-Emden, Comparison of particle-resolved DNS (PR-DNS) and non-resolved DEM/CFD simulations of flow through homogenous ensembles of fixed spherical and non-spherical particles, Advanced Powder Technology 32 (4) (2021) 1170–1195. doi:10.1016/j.apt.2021.02.016.

[22] T. Yali, E. A. J. P. Frank, H. Kuipers, S. Kriebitzsch, M. Van Der Hoef, A New Drag Correlation from Fully Resolved Simulations of Flow Past Monodisperse Static Arrays of Spheres, American Institute of Chemical Engineers AIChE J 61 (2014) 688–698. doi:10.1002/aic.14645.

[23] L. W. Rong, K. J. Dong, A. B. Yu, Lattice-Boltzmann simulation of fluid flow through packed beds of spheres: Effect of particle size distribution, Chemical Engineering Science 116 (2014) 508–523. doi:10.1016/j.ces.2014.05.025.

[24] L. Prahl, A. Hölzer, D. Arlov, J. Revstedt, M. Sommerfeld, L. Fuchs, On the interaction between two fixed spherical particles, International Journal of Multiphase Flow 33 (7) (2007) 707–725. doi:10.1016/j.ijmultiphaseflow.2007.02.001.

[25] T. Kékesi, M. Altimira, G. Amberg, L. P. Wittberg, International Journal of Multiphase Flow Interaction between two deforming liquid drops in tandem and various off-axis arrangements subject to uniform flow, International Journal of Multiphase Flow 112 (2019) 193–218. doi:10.1016/j.ijmultiphaseflow.2018.11.009.

[26] N. Kishore, Numerical Investigation of Interaction between Spheroid Particles in Tandem Arrangement at Moderate Reynolds Numbersdoi:10.1021/ie3012424.

[27] T. Sayadi, S. Farazi, S. Kang, H. Pitsch, Transient multiple particle simulations of char particle combustion, Fuel 199 (2017) 289–298. doi:10.1016/j.fuel.2017.02.096.

[28] J. K. Dukowicz, An exact solution for the drag of a sphere in low Reynolds number flow with strong uniform suction or blowing, Physics of Fluids 25 (1982) 1117–1118. doi:10.1063/1.863875.

[29] R. Miller, J. Bellan, Direct numerical simulation of a confined three-dimensional gas mixing layer with one evaporating hydrocarbon-droplet-laden stream, J. Fluid Mech 384 (1999) 293–338. doi:10.1017/S0022112098004042.

[30] M. Kestel, Numerical Modeling of Moving Carbonaceous Particle Conversion in Hot Environments, Ph.D. thesis, TU Bergakademie (2016).

[31] X. Chen, S. Du, L. Zhao, B. Yang, Q. Zhou, Effect of Stefan flow on the drag force in flow past random arrays of spheres, Chemical Engineering Journal 412. doi:10.1016/j.cej.2021.128691.

[32] S. Du, L. Zhao, X. Chen, B. Yang, Q. Zhou, Effect of Stefan flow on the drag force of single reactive particle surrounded by a sea of inert particles, Chemical Engineering Science 253 (2022) 117546. doi:10.1016/j.ces.2022.117546.

[33] Y. Wang, M. Zhang, H. Wang, H. Jin, The influence of Stefan flow on the flow and heat-transfer characteristics of spherical-particle pair in supercritical water, International Journal of Multiphase Flow 151 (2022) 104045. doi:10.1016/Jj.imultiphaseflow.2022.104045.

[34] E. Constant, J. Favier, M. Meldi, P. Meliga, E. Serre, An immersed boundary method in OpenFOAM: Verification and validation, Computers and Fluidsdoi:10.1016/j.compfluid.2017.08.001.

[35] D. J. Tritton, Experiments on the flow past a circular cylinder at low reynolds numbers, Journal of Fluid Mechanics 6 (4) (1959) 547–567. doi:10.1017/S0022112059000829.

[36] W. A. Khan, J. R. Culham, M. M. Yovanovich, Fluid flow around and heat transfer from an infinite circular cylinder, Journal of Heat Transfer 127 (7) (2005) 785–790. doi:10.1115/1.1924629.

[37] H. Schlichting, K. Gersten, Boundary Layer Theory, Springer Berlin Heidelberg, 2017. doi:10.1007/978-3-662-52919-5.

[38] S. Bhattacharyya, S. Dhinakaran, A. Khalili, Fluid motion around and through a porous cylinder, Chemical Engineering Science 61 (13) (2006) 4451–4461. doi:10.1016/j.ces.2006.02.012.

[39] P. Yu, Y. Zeng, T. S. Lee, X. B. Chen, H. T. Low, Steady flow around and through a permeable circular cylinder, Computers and Fluids 42 (1) (2011) 1–12. doi:10.1016/j.compfluid.2010.09.040.

[40] M. Zhang, Q. Zhao, Z. Huang, L. Chen, H. Jin, Numerical simulation of the drag and heat-transfer characteristics around and through a porous particle based on the lattice Boltzmann method, Particuology 58 (2021) 99–107. doi:10.1016/J.PARTIC.2021.01.013.

[41] M. Zhang, H. Jin, Q. Zhao, S. Shen, Drag and heat transfer characteristics around and through two interactive porous particles, Powder Technology 390 (2021) 555–568. doi:10.1016/j.powtec.2021.05.097.

[42] W. Ranz, W. Marshall, Evaporation from drops, Chemical Engineering Progress 48 (3) (1952) 141–146.

[43] S. Whitaker, Forced Convection Heat Transfer Correlations for Flow In Pipes, Past Flat Plates, Single e Cylinders, Single Spheres, and for Flow In Packed Beds and Tube Bundles, AIChE Journal 18 (1972) 361–371.

[44] M. Kestel, Numerical Modeling of Moving Carbonaceous Particle Conversion in Hot Environments, Ph.D. thesis, TU Bergakademie (2016).

[45] Z. Zhifu, W. Guoxiang, C. Bin, W. Liejin, G.and Yueshe, Evaluation of Evaporation Models for Single Moving Droplet with a High Evaporation Rate, Powder Technology 240 (2013) 95–102. doi:10.1016/j.powtec.2012.07.002.

[46] R. P. Bharti, R. P. Chhabra, V. Eswaran, A numerical study of the steady forced convection heat transfer from an unconfined circular cylinder, Heat and Mass Transfer/Waerme- und Stoffuebertragung 43 (7) (2007) 639–648. doi:10.1007/s00231-006-0155-1.

[47] M. Abdelhady, D. Wood, Effect of thermal boundary condition on forced convection from circular cylinders, Numerical Heat Transfer; Part A: Applications 76 (6) (2019) 420–437. doi:10.1080/10407782.2019.1638169.

[48] A. P. Hatton, D. D. James, H. W. Swire, Combined forced and natural convection with low-speed air flow over horizontal cylinders, Journal of Fluid Mechanics 42 (1) (1970) 17–31. doi:10.1017/S0022112070001040.

[49] M. Rieth, F. Proch, M. Rabaçal, B. M. Franchetti, F. Cavallo Marincola, A. M. Kempf, Flamelet LES of a semi-industrial pulverized coal furnace, Combustion and Flame 173 (2016) 39–56. doi:10.1016/j.combustflame.2016.07.013.

[50] E. Karchniwy, N. E. L. Haugen, A. Klimanek, Ø. Langørgen, S. Sładek, The effect of turbulence on mass transfer in solid fuel combustion: RANS model, Combustion and Flame 227 (2021) 65–78. doi:https://doi.org/10.1016/j.combustflame.2020.12.040.

[51] S. Subramaniam, Lagrangian–Eulerian methods for multiphase flows, Progress in Energy and Combustion Science 39 (2-3) (2013) 215–245. doi:10.1016/j.pecs.2012.10.003.

[52] Y. Bai, K. Luo, K. Qiu, J. Fan, Numerical investigation of two-phase flame structures in a simplified coal jet flame, Fuel 182 (2016) 944–957. doi:10.1016/j.fuel.2016.05.086.

[53] S. Farazi, J. Hinrichs, M. Davidovic, T. Falkenstein, M. Bode, S. Kang, A. Attili, H. Pitsch, Numerical investigation of coal particle stream ignition in oxy-atmosphere, Fuel 241 (2019) 477–487. doi:10.1016/j.fuel.2018.11.108.

[54] K. Luo, H. Wang, J. Fan, F. Yi, Direct Numerical Simulation of Pulverized Coal Combustion in a Hot Vitiated Co-flowdoi:10.1021/ef301253y.

[55] M. Rieth, A. M. Kempf, A. Kronenburg, O. T. Stein, Carrier-phase DNS of pulverized coal particle ignition and volatile burning in a turbulent mixing layer, Fuel 212 (2018) 364–374. doi:https://doi.org/10.1016/j.fuel.2017.09.096.

[56] M. Muto, K. Yuasa, R. Kurose, Numerical simulation of ignition in pulverized coal combustion with detailed chemical reaction mechanism, Fuel 190 (2017) 136–144. doi:10.1016/j.fuel.2016.11.029.

[57] G. L. Tufano, O. T. Stein, A. Kronenburg, G. Gentile, A. Stagni, A. Frassoldati, T. Faravelli, A. M. Kempf, M. Vascellari, C. Hasse, Fully-resolved simulations of coal particle combustion using a detailed multi-step approach for heterogeneous kinetics, Fueldoi:10.1016/j.fuel.2018.11.139.

[58] S. Kajitani, N. Suzuki, M. Ashizawa, S. Hara, CO 2 gasification rate analysis of coal char in entrained flow coal gasifier, Fuel 85 (2005) 163–169. doi:10.1016/j.fuel.2005.07.024.

[59] T. R. Jayawickrama, N. E. L. Haugen, M. U. Babler, M. A. Chishty, K. Umeki, The effect of Stefan flow on the drag coefficient of spherical particles in a gas flow, InternationalJournalofMultiphaseFlow 117 (2019) 130–137. doi:10.1016/j.ijmultiphaseflow.2019.04.022.

[60] T. R. Jayawickrama, N. E. L. Haugen, M. U. Babler, M. A. Chishty, K. Umeki, The effect of Stefan flow on Nusselt number and drag coefficient of spherical particles in non-isothermal gas flow, International Journal of Multiphase Flow 140 (2021) 103650. doi:10.1016/j.ijmultiphaseflow.2021.103650.

[61] J. J. Murphy, C. R. Shaddix, Effects of Stefan Flow on Heat Transfer from reacting Carbon particles, Sandia-Report 2003-8720J (2003) 1–24.

Appendices

Appendix A

Paper I

International Journal of Multiphase Flow 117 (2019) 130–137

Contents lists available at ScienceDirect

International Journal of Multiphase Flow

journal homepage: www.elsevier.com/locate/ijmulflow

The effect of Stefan flow on the drag coefficient of spherical particles in a gas flow

Thamali R. Jayawickrama[a,*], Nils Erland L. Haugen[b,c], Matthaus U. Babler[d], M.A. Chishty[a], Kentaro Umeki[a]

[a] Energy Engineering, Div. Energy Science, Luleå University of Technology, Luleå 971 87, Sweden
[b] Department of Energy and Process Engineering, Norwegian University of Science and Technology, Kolbjørn Hejes vei 1 B, Trondheim 7491, Norway
[c] Department of Thermal Energy, SINTEF Energy Research, Kolbjørn Hejes vei 1 A, Trondheim 7491, Norway
[d] Department of Chemical Engineering, KTH Royal Institute of Technology, Stockholm SE-10044, Sweden

ARTICLE INFO

Article history:
Received 19 November 2018
Revised 8 March 2019
Accepted 23 April 2019
Available online 24 April 2019

Keywords:
Drag coefficient
Stefan flow
Boundary layer
Multiphase reactive flow

ABSTRACT

Particle laden flows with reactive particles are common in industrial applications. Chemical reactions inside the particle can generate a Stefan flow that affects heat, mass and momentum transfer between the particle and the bulk flow. This study aims at investigating the effect of Stefan flow on the drag coefficient of a spherical particle immersed in a uniform flow under isothermal conditions. Fully resolved simulations were carried out for particle Reynolds numbers ranging from 0.2 to 14 and Stefan flow Reynolds numbers from (−1) to 3, using the immersed boundary method for treating fluid-solid interactions. Results showed that the drag coefficient decreased with an increase of the outward Stefan flow. The main reason was the change in viscous force by the expansion of the boundary layer surrounding the particle. A simple model was developed based on this physical interpretation. With only one fitting parameter, the performance of the model to describe the simulation data were comparable to previous empirical models.

1. Introduction

Many industrial applications involve particle laden flows with reactive particles, such as combustion of solid fuels, catalytic cracking and drying applications. Unlike ordinary particle-laden flows, reacting particles exchange mass with the surrounding fluid. A Stefan flow, induced by chemical reactions inside or at the surface of the particle, has effects on the gas-solid interaction, i.e. momentum (C_D-drag coefficient), heat (*Nu*-Nusselt number) and mass transfer (*Sh*-Sherwood number) between the particle and the bulk flow (Hayhurst, 2000; Yu and Zhang, 2009; Yu et al., 2013; Kalinchak, 2001). This can be exemplified by gasification and combustion processes, where, upon being released into the hot environment, fuel particles undergo fast devolatilization that results in a pronounced gas stream leaving the particles. Although momentum, heat, and mass transfer could be affected by the Stefan flow, as a first step, we focus on the effect of Stefan flow on C_D in isolation from the effects of heat and mass transfer in this study.

Resolved simulations of multiphase reactive flows demand high computational resources due to its complexity and the multi-scale nature of the processes. The smallest scale in such systems typically corresponds to the scale of the particles and their boundary layers ($10^{-6} - 10^{-3}$ m), while the largest scales are set by the entire reactor, which typically contains millions of reactive particles and has a length scale ($10^{0} - 10^{2}$ m) that is several orders of magnitudes larger than the particle scale. Therefore, it is impractical to carry out particle resolved simulations for a large domain. Instead, it is useful to develop constitutive models based on the results from particle resolved simulations of single or multiple particles, which can then be implemented in large scale reactor simulations that do not resolve the individual particles. Compared with the many particle-resolved simulations in the literature, only a few studies have used their results to develop models suitable to use in large scale simulations (e.g. models for Stefan flow developed by Miller and Bellan (1999) and Kestel (2016), while models taking into account particle porosity and particle shape are presented in Wittig et al. (2017) and Richter and Nikrityuk (2012), respectively.)

Previous studies on Stefan flow effects mainly investigated droplet evaporation/condensation (Bagchi et al., 2001; Renksizbulut and Yuen, 1983; Dukowicz, 1984) and suction/blowing

* Corresponding author.
E-mail address: thamalirajika@gmail.com (T.R. Jayawickrama).

https://doi.org/10.1016/j.ijmultiphaseflow.2019.04.022

effects (Chuchottaworn et al., 1983; Dukowicz, 1982; Cliffe and Lever, 1985). Models developed for the drag coefficient of evaporating/condensing droplets are based on both experimental and simulation data. Recently, the performance of the model by Renksizbulut and Yuen (1983) was assessed for a char particle during oxy-fuel combustion (Farazi et al., 2016). The model contains a case-specific blowing number and had to be adjusted by introducing a new blowing number. However, some studies have proposed more general models for the drag coefficients of a reacting particle, based on the suction/blowing effect directly. In early models, the mass flux inward/outward (hereafter called Stefan flow) was represented by 'a non-dimensional blowing number (Λ)', which is the ratio of Stefan flow velocity and slip velocity ($=U_{sf}/U_{\infty}$) (Cliffe and Lever, 1985). More recently, the Stefan velocity has been non-dimensionalized by the Stefan Reynolds number, Re_{sf}, which is based on particle radius (R), Stefan velocity (U_{sf}) and fluid viscosity (ν) (Kestel, 2016):

$$Re_{sf} = \frac{2U_{sf}R}{\nu}. \tag{1}$$

Another relevant Reynolds number is the particle Reynolds number, Re, which is based on the particle slip velocity (U_{∞}),

$$Re = \frac{2U_{\infty}R}{\nu}, \tag{2}$$

such that $U_{sf,r} = Re_{sf}/Re$.

Dukowicz (1982) developed an analytical relation for the drag of a spherical solid particle with suction/blowing in creeping flows ($Re \to 0$). For higher Re, a number of works addressed the effects of Stefan flow on the drag coefficient (Cliffe and Lever, 1985; Miller and Bellan, 1999; Kestel, 2016; Nour et al., 2017). Miller and Bellan (1999) developed an empirical model based on the numerical simulation results of Cliffe and Lever (1985) for an isothermal flow around a sphere. Kurose et al. (2003) has modified the model coefficients of the same model to fit the data for an outflow in a linear shear flow around a solid sphere. Later, another empirical model was introduced by Kestel (2016), which is applicable for the wider range of mass fluxes that appeared in a 200 MW commercial gasifier data. It is apparent that the change of drag coefficient due to Stefan flow cannot be neglected. However, available models are not based on physical observations, and they rely on a number of fitting parameters. In addition, none of the models are suitable for negative Stefan flows (suction).

This study investigates the interaction between a gas flow and an embedded reacting particle that experience a Stefan flow. The main aim is to develop a physics-based simple model describing the change of the drag coefficient due to the Stefan flow for a particle in an isothermal flow. Direct numerical simulations that resolve the boundary layer at the particle surface were carried out for a laminar flow surrounding a stationary particle with either an outgoing or an incoming Stefan flow. Simulation results were analyzed and a model was developed with a physical interpretation from the simulations. The developed model and two previous models from the literature (Miller and Bellan, 1999; Kestel, 2016) were compared with the simulation results. The range of particle Reynolds numbers (Re) in this study is limited to the conditions relevant to entrained-flow gasification or pulverized combustion.

2. Methodology

The numerical simulations considered a static particle in a uniform isothermal flow. The generation and consumption of gas in the solid phase were considered as a uniform outgoing or incoming mass flux at the particle surface in the surface-normal direction. In all of the simulations performed here, the Reynolds number is smaller than the critical Reynolds number that yields von Karman oscillations. This means that there are no transients in the flow, and hence, a steady state solver can be used.

2.1. Governing equations

Steady state simulations were carried out under isothermal conditions, with the gas phase assumed to be incompressible. The discrete phase was described as a static spherical particle with constant size. The gas phase is governed by mass conservation,

$$\nabla \cdot \vec{u} = 0, \tag{3}$$

and momentum conservation,

$$(\rho \vec{u} \cdot \nabla)\vec{u} = -\nabla p + \mu \nabla^2 \vec{u}, \tag{4}$$

where ρ is the density of the fluid, $\vec{u}$ is velocity vector, p is pressure and μ is dynamic viscosity. Eqs. (3) and (4) were discretized with the finite volume method using second-order schemes.

2.2. Boundary conditions

The slip velocity between the particle and the bulk gas was set as the inlet velocity at the front boundary (left side of the calculation domain in Fig. 1). An 'outflow' boundary condition (i.e. zero velocity gradient) was applied at the back boundary (right side of the calculation domain in Fig. 1). The side boundaries of the domain were treated as 'slip walls'. A 'slip wall' boundary condition enforces both the velocity component normal to the wall and the gradients of the other velocity components in the normal direction to be zero. Boundaries along the symmetry axes were considered as 'symmetric' boundaries, which means that the component of velocity normal to the symmetry plane is zero and that the gradient of all the other properties normal to the plane is zero.

The immersed boundary method (IBM) was used at the surface of the particle. The current work used the discrete forcing approach (Mittal and Iaccarino, 2005), which uses the direct imposition of boundary conditions (Jasak et al., 2014), and the presence of the immersed surface/body is formulated through the boundary conditions. The value of any parameter inside the cells that contain the immersed boundary was calculated by interpolating values at the immersed boundary points and the neighbour cells (Fadlun et al., 2000). To implement Stefan flow, the velocity is fixed (Dirichlet boundary condition) at the immersed boundary normal to the particle surface as:

$$\dot{m} = \rho \oint_S (\vec{u}_{sf} \cdot \vec{n})\, dS, \tag{5}$$

where integration is over the surface S of the particle, $\vec{n}$ is unit vector in the direction normal to the surface element dS and $\dot{m}$ is mass flow rate due to the Stefan flow. Furthermore, for pressure the gradient is set to zero at the immersed boundary (Neumann boundary condition). The treatment of Dirichlet and Neumann boundary conditions for an immersed boundary method in *foam-extend* is shown in the Appendix A (Jasak et al., 2014).

2.3. Calculation conditions and procedure

In this work, we used the OpenFoam environment, called *foam-extend*-3.2 (Weller et al., 1998). The numerical simulations were carried out using the incompressible, steady-state, immersed boundary solver. The solver uses quadratic interpolation (Jasak et al., 2014) for the reconstruction of the solid phase boundary conditions into the closest fluid cells.

Flow conditions were selected based on practical applications of pulverized combustion and gasification at atmospheric pressure. Four different Re were selected by considering particle size (0.1–1.0 mm), slip velocity (0.5–3 m s^{-1}), and gas properties of N_2 at

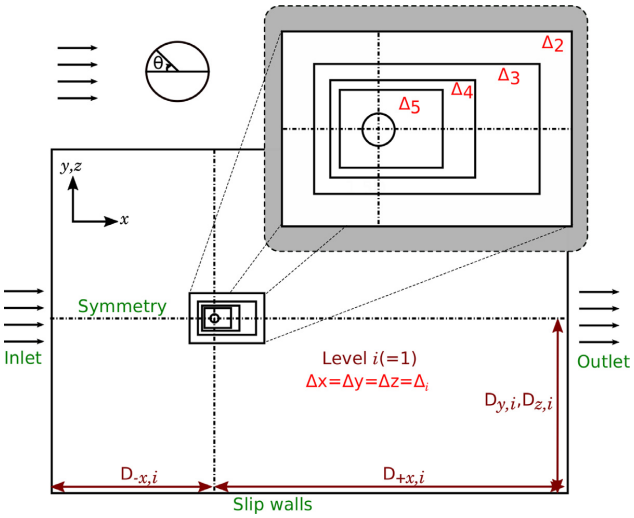

Fig. 1. Computational domain for the simulations, with D denoting the particle diameter, and Δ_i, $i = 1$ to 5 representing the coarsest mesh to finest mesh. $D_{-x,i}$ is the distance from the centre of the sphere to negative x-direction and $D_{+x,i}$ is the distance from the centre of the sphere to positive x-direction in level i (See the Table 1).

Table 1
Distance from the centre of the particle in diameters (D) in the computational domain (See Fig. 1).

i	$D_{-x,i}$	$D_{+x,i}$	$D_{y,i}$, $D_{z,i}$	Δ_i/D
1	16	48	16	0.16
2	3	6	3	0.08
3	2	5	2	0.04
4	1.5	3	1.5	0.02
5	1.2	2	1.2	0.01

1400 K. The considered *Re* are: 0.232, 2.32, 6.98, 13.96. The magnitude of the Stefan-flow mass flux was calculated from data relevant for devolatilization and char conversion of biomass (Kreitzberg et al., 2016; Umeki et al., 2012). Since the *Re* was always less than 20 in this study, the flow is steady, axisymmetric and topologically similar (Johnson and Patel, 1999). Therefore, only a quarter of the domain was simulated with symmetric boundaries.

Initially, the domain size and mesh resolution was selected based on previous studies (Constant et al., 2017; Richter and Nikrityuk, 2012) for flow around a sphere. Then, mesh refinement tests were carried out for the highest *Re*. Based on these tests, we arrived at five levels of refinement that were eventually used for the simulations, with the mesh size of the finest refinement being $0.01D$ (see the Fig. 1 and Tab. 1). After the mesh refinement test, domain size tests were carried out for the smallest *Re* and the highest Stefan flow velocity, i.e. because the boundary layer is expected to be the largest under such condition. Based on the results (see Table 2), mesh 2 was selected considering accuracy and economy of computational resources. The final mesh and domain are shown in Fig. 1, consisting of around 9.6 million cells in total.

Table 2
Domain size test for $Re = 0.23$ at $Re_{sf} = 2.90$ and 1.45 for different domain sizes.

Re_{sf}	Mesh	Domain size	Refinement levels	C_D	Error (% of mesh 3)
2.90	mesh 1	$32 \times 16 \times 16$	4	86.25	19.2
	mesh 2	$64 \times 32 \times 32$	4	75.45	4.2
	mesh 3	$128 \times 64 \times 64$	4	72.38	–
1.45	mesh 2	$64 \times 32 \times 32$	4	90.28	2.8
	mesh 3	$128 \times 64 \times 64$	4	87.85	–

For isothermal conditions, the drag coefficient of a particle with no Stefan flow should depend only on *Re*. As preliminary tests, we confirmed this with two different sets of particle diameters and slip velocities at the same *Re*.

2.4. Estimation of the drag coefficient

The drag coefficient can be calculated as

$$C_D = \frac{\vec{F}_{P,x} + \vec{F}_{visc,x}}{\frac{1}{2}\rho U_\infty^2 (\pi R^2)}, \tag{6}$$

when the pressure and viscous forces are given as

$$\vec{F}_P = \oint_S (P_{sur} - P_{ref})\,\vec{n}\,ds, \tag{7}$$

and

$$\vec{F}_{visc} = -\oint_S \mu(\nabla\vec{u} + \nabla\vec{u}^{\,t})\,\vec{n}\,ds, \tag{8}$$

respectively. Here, the integration is over the surface S of the particle. In the above, P_{sur} and P_{ref} are the interpolated pressure at the particle surface and in the far field, respectively, and $\vec{n}$ is the unit vector in the surface-normal direction. Only the components $\vec{F}_P$ and $\vec{F}_{visc}$ in the direction of the mean flow were accounted for when calculating the drag coefficient, since the other components are canceled out due to symmetry.

3. Results and discussion

3.1. Validation

The numerical implementation was validated for the estimated drag coefficient using four *Re* without Stefan flow. The obtained drag coefficient was compared to the empirical formula of Haider and Levenspiel (1989),

$$C_D = \frac{24}{Re}(1 + 0.1806Re^{0.6459}) + 0.4251\left(1 + \frac{6880.95}{Re}\right)^{-1}, \tag{9}$$

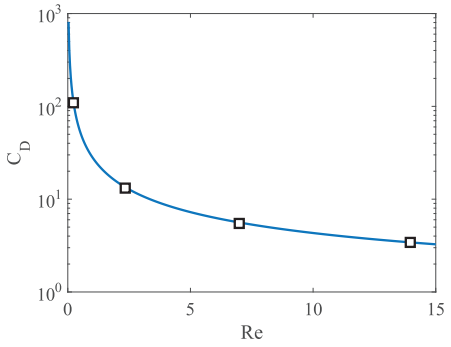

Fig. 2. Drag coefficient as a function of *Re* for the case where there is no Stefan flow. Line: Correlation of Haider and Levenspiel (1989), symbols: numerical simulations.

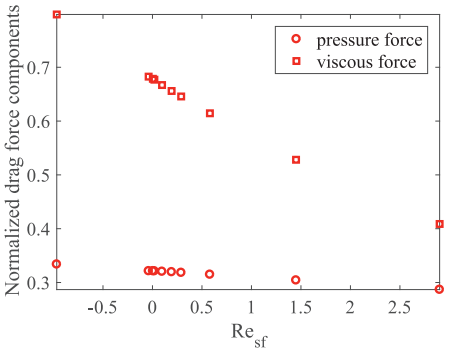

Fig. 4. Drag force due to pressure (F_p, circles) and viscous stress(F_{visc}, squares) on the sphere normalized by the total drag force ($F_p + F_{visc}$) for $Re_{sf} = 0$.

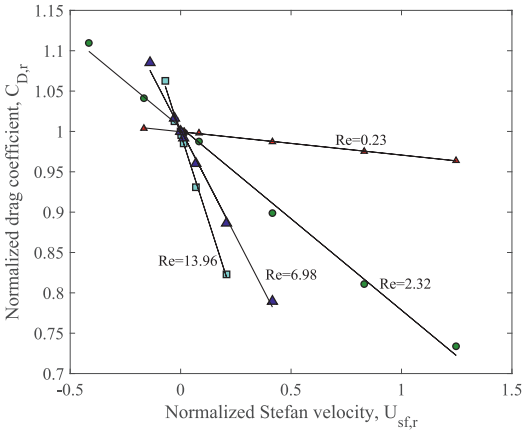

Fig. 3. Normalized drag coefficient $C_{D,sf}/C_{D,0}$ vs normalized Stefan flow velocity U_{sf}/U_∞ at different *Re*. Symbols: simulations, lines: linear regression to the data.

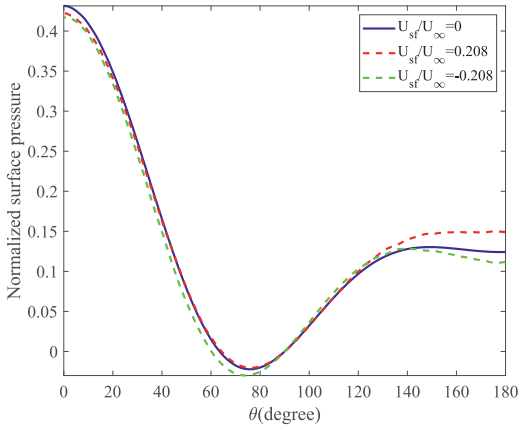

Fig. 5. Pressure component $(P_{surf} - P_{ref})\vec{n}_x$ in the flow direction at the surface of the sphere normalized by the characteristic pressure $\vec{F}_{tot,x}/\pi R^2$ for $Re = 13.96$ and different U_{sf}/U_∞.

which was derived from 408 experimental data points. Fig. 2 shows that the drag coefficients obtained from our simulations (symbols) are in agreement with this empirical formula (solid line). The data is also listed in Table B.1.

The velocity profile surrounding the particle generated by Stefan flow was validated in a quiescent fluid by comparing it to the analytical solution,

$$\vec{u_d} = \frac{\vec{u_{sf}} R^2}{d^2}, \tag{10}$$

where $\vec{u_d}$ is the velocity vector at a distance d from the centre of the sphere, and $\vec{u_{sf}}$ is the Stefan flow velocity vector at its surface.

3.2. Effects of Stefan flow on drag coefficient

Fig. 3 shows the normalized drag coefficient, $C_{D,r} = C_{D,sf}/C_{D,0}$, plotted against the normalized Stefan flow velocity, $U_{sf,r} = U_{sf}/U_\infty$, for different *Re*. Here, $C_{D,0}$ and $C_{D,sf}$ refer to the drag coefficients without and with Stefan flow, respectively, while U_∞ is the inlet velocity. The results show a nearly linear relationships between $C_{D,r}$ and $U_{sf,r}$ for every given *Re*, with the slope of the relationship getting steeper with increasing *Re*.

According to Fig. 3, the normalized drag coefficient was as low as 0.7 (for *Re*=2.32 and $U_{sf,r} = 1.3$), and is expected to decrease even further at higher Stefan velocity. This significant reduction in drag shows the relevance of the Stefan flow in entrained flow gasification and combustion applications.

Fig. 4 explores the effect of Stefan flow in more detail by showing the pressure and viscous forces separately. In all cases studied here, both with and without Stefan flow, we found that the viscous force was larger than the pressure force by a factor of roughly two, as is expected for low *Re*. We do see, however, that this factor is decreasing for increasing Re_{sf}, and for much larger values of Re_{sf} it can not be excluded that it may even be less than one. The bottom line is that a positive Stefan flow give a significant reduction of the viscous force while the pressure force remains almost constant.

To elucidate the observed effects, the pressure force component in the mean flow direction, $(P_{surf} - P_{ref})\vec{n}_x$ is shown in Fig. 5 as a function of surface angle from the front of the particle (See schematic in the inset of Fig. 1). The Stefan flow velocity at the surface is given as U_{sf}/U_∞, where the positive values indicate outgoing flows. The figure confirms the observation from Fig. 4, i.e.; the pressure force is hardly affected by the Stefan flow and it is almost constant for a given *Re*.

On the contrary, Fig. 4 showed that the viscous force decreased with an outgoing Stefan flow and increased with an incoming Stefan flow. To explore this effect, Fig. 6 shows the viscous stress com-

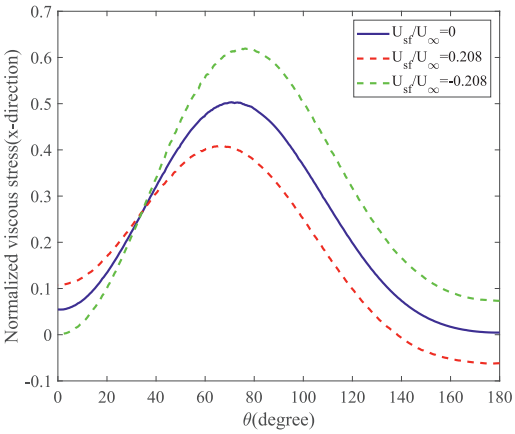

Fig. 6. Viscous stress component $[-\mu(\nabla\vec{U}+\nabla\vec{U}^t).\vec{n}\,]_x$ in the mean flow direction at the surface of the sphere, normalized by the characteristic pressure $\vec{F}_{tot,x}/\pi R^2$ for $Re = 13.96$ and different U_{sf}/U_∞.

ponent in flow direction as a function of the surface angle from the front of the particle. It shows that the viscous stress is actually higher at the front of the particle for the simulations with outgoing Stefan flow. On the other hand, the viscous stress behind the particle is smaller with outgoing Stefan flow. The changes in the viscous stress at the front and the back of the particle cancel each other and have no significant net effect. The shear stress at the side of the particle ($40 < \theta < 140$) is smaller with outgoing Stefan flow. As a result, the overall viscous stress for the particle decreased under the influence of outward Stefan flow. The main factor that affects the viscous force is the velocity gradient as shown in Eq. (8). The observation in Fig. 6 implies that the change in the boundary layer thickness is more significant than the change in velocity difference that appear at the front and back of the particle.

Fig. 7 shows the flow field (i.e. velocity magnitude) with (lower half panel) and without (upper half panel) outward Stefan flow. Comparison of the flow fields showed that the boundary layer thickness increased with outgoing Stefan flow. On the contrary, the boundary layer thickness decreased with incoming Stefan flow. This change in boundary layer thickness due to the Stefan flow is clearly seen by inspecting the velocity magnitude along the *y*-axis crossing the centre of the sphere, as shown in Fig. 8. For an outgoing Stefan flow (red dashed line in Fig. 8) we observed a slower relaxation of the velocity magnitude to the free stream velocity, while vice versa, a faster relaxation was observed for incoming Stefan flow (green dashed line). This effect can be understood as the boundary layer being pushed away from the particle surface in case of an outward Stefan flow, while it was pulled towards the surface for an inward Stefan flow. This change in boundary layer thickness with the Stefan flow affects the velocity gradient, and hence it explains the observed change in the viscous force and, consequently, also the drag.

3.3. A model for the drag coefficient with Stefan flow

In this section, a simple expression is suggested for the drag coefficient under the influence of Stefan flow for small *Re*. The net drag on a particle is entirely determined by the boundary layer around the particle. Any change to the boundary layer due to the presence of Stefan flow would therefore have an effect on the drag. Indeed, we observed in the previous section that Stefan flow reduced/enhanced the drag coefficient by modifying the viscous force through the expansion/contraction of the boundary layer. As a first approximation, we assume that the change in the normalized drag coefficient depends on the change in the volume of the boundary layer. By assuming that the volume of boundary layer with Stefan flow simply becomes the sum of its original volume (V_B) and the volume of Stefan flow (V_{sf}), the normalized drag coefficient can be expressed as

$$C_{D,r} = \frac{V_B}{V_B + V_{sf}}. \tag{11}$$

Here, the volume of the Stefan flow is defined as the volume of fluid emitted from the particle during a typical flow time-scale, τ_f, such that

$$V_{sf} = 4\pi R^2 U_{sf} \tau_f, \tag{12}$$

where the flow time-scale is given by

$$\tau_f = \frac{2(R+\delta)}{U_\infty}, \tag{13}$$

where δ is the boundary layer thickness. We can assume $\delta \gg R$ at small *Re*. Hence,

$$\tau_f \approx \frac{2\delta}{U_\infty}. \tag{14}$$

Based on the above, the volumes of the Stefan flow and its approximation at low *Re* are now given by

$$V_{sf} = 8\pi R^2 (R+\delta)\frac{U_{sf}}{U_\infty} \approx 8\pi R^2 \delta \frac{U_{sf}}{U_\infty}. \tag{15}$$

Furthermore, the volume of the boundary layer is given as

$$V_B = \frac{4}{3}\pi (R+\delta)^3 - \frac{4}{3}\pi R^3, \tag{16}$$

and when $\delta \gg R$,

$$V_B \approx \frac{4}{3}\pi \delta^3. \tag{17}$$

Adopting the result from classical boundary layer theory, the boundary layer thickness is given by

$$\delta = \frac{2AR}{\sqrt{Re}}, \tag{18}$$

where A is a constant with a value of the order of one. Combining Eqs. (15) and (17) with Eq. (11) yields

$$C_{D,r} = \frac{1}{1 + \frac{3Re_{sf}}{2A^2}}. \tag{19}$$

Fig. 9 shows the normalized drag coefficient $C_{D,r}$ for various *Re* obtained from the simulations as a function of Re_{sf}, together with the prediction given in Eq. (19) (solid line). The parameter A in Eq. (19) was calculated by fitting to the data for the smallest *Re* ($A = 3.25 \pm 0.25$ at $Re = 0.232$).

Eq. 19is based on the assumption that *Re* is small enough to satisfy $\delta \gg R$, and it is not applicable for higher *Re*.

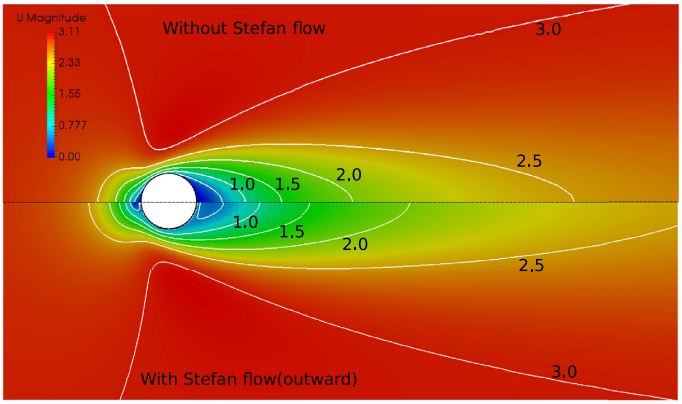

Fig. 7. Velocity magnitude map with contour lines (velocity magnitude step 0.5) surrounding the sphere at $Re = 13.96$. Upper half without Stefan flow ($U_{sf}/U_{\infty} = 0$) and lower half with Stefan flow ($U_{sf}/U_{\infty} = 0.208$).

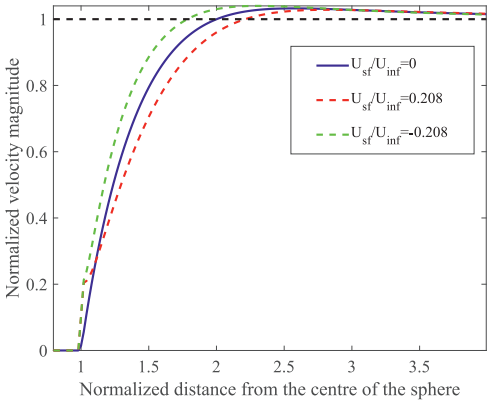

Fig. 8. Velocity magnitude normalized by U_{∞} along the y-axis crossing the sphere centre ($\theta = 90^{\circ}$; distance normalized with particle radius, R) for $Re = 13.96$ at different U_{sf}/U_{∞}.

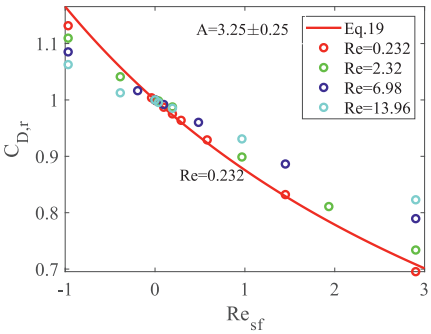

Fig. 9. The normalized drag coefficient as a function of the Stefan based Re.

Without the assumptions of $\delta \gg R$, i.e. keeping the particle radius when estimating the boundary layer volumes using Eqs. (15) and (16), the normalized drag coefficient based on Eq. (11) follows as :

$$C_{D,r} = \frac{1}{1 + f(Re)Re_{sf}}, \tag{20}$$

with

$$f(Re) = \frac{3}{Re}\left(1 + \frac{2A}{\sqrt{Re}}\right)\frac{1}{(\frac{3A}{\sqrt{Re}} + 6(\frac{A}{\sqrt{Re}})^2 + 4(\frac{A}{\sqrt{Re}})^3)}, \tag{21}$$

where $A = 3.01 \pm 0.13$ as obtained by fitting to the simulation data using the least squares methods. The performance of the model was compared against the previous models by Miller and Bellan (1999) (Eq. (22)) and Kestel (2016) (Eq. (23)); the former reads as:

$$C_D = \frac{24}{Re}\left[\frac{1 + 0.054Re + 0.1Re^{\frac{1}{2}}(1 - 0.03Re)}{1 + a|Re_{sf}|^b}\right], \tag{22}$$

where $a = 0.09 + 0.77\exp(0.4Re)$ and $b = 0.4 + 0.77\exp(-0.04Re)$ which is valid for $0 \le Re \le 100$ and $0 \le Re_{sf} \le 10$ (Miller and Bellan, 1999) and Kestel (2016) model reads as;

$$C_{D,r} = \frac{1}{(1 + 0.138{Re_{sf}}^{1.153})^a}, \tag{23}$$

where $a = (\frac{1.063}{1+0.223Re})^{0.568}$, which is valid for $0 \le Re \le 200$ and $0 \le Re_{sf} \le 20$.

Fig. 10 compares the performances of three models with the data from the simulations. All the models are in good agreement with the simulation results for positive Re. The maximum error of the current model was less than 6% in the simulated range that is $0 \le Re \le 14$ and $(-1) \leqslant Re_{sf} \leqslant 3$. However, there are two major differences between the current and previous models. First, the previous models contain several fitting parameters without clear physical background. The current model, however, contains only one fitting parameter, which is related to the relationship between Re and the boundary layer thickness (Eq. (18)). Moreover, the previous models by Miller and Bellan (1999) and Kestel (2016) are not applicable to negative Re_{sf} while the current model expands to negative Re_{sf} and is in good agreement with simulation data, at least down to $Re_{sf} = (-1)$. For strongly negative Re_{sf}, $C_{D,r}$ given by Eq. (20) di-

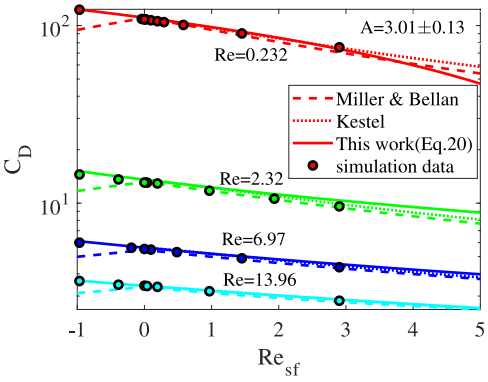

Fig. 10. Drag coefficient as a function of the Re_{sf}, for different Re.

verges. However for $Re = 0.232$, Re_{sf} has to become as small as (-7) before $C_{D,r}$ diverges.

4. Conclusions

Fully resolved numerical simulations of flow surrounding a gas-emitting particle were carried out to elucidate the effect of Stefan flow on the drag acting on a particle in a uniform flow. The application of this study is limited to steady, axisymmetric flow ($Re < 14$), and low Stefan flow velocity ($-1 \leqslant Re_{sf} \leqslant 3$).

Results showed that the drag coefficient has a nearly linear relationship with the Stefan flow velocity. An outward Stefan flow lead to a reduction of the drag coefficient, whereas the magnitude of the reduction increases with increasing Re. For the Reynolds numbers in this study, the main reason for the reduction/increase in the drag coefficient was the change in viscous force. This was caused by the expansion/contraction of the boundary layer surrounding the particle, rather than the change in relative velocity at the particle surface.

A simple model was developed based on the change in the volume of the boundary layer due to Stefan flow. Although the model contains only one fitting parameter, it showed as good agreement with the simulation data as previous models with several fitting parameters. The proposed model also showed good agreement with the simulation data for negative Re_{sf} while previous models could not be computed because of non-integer indexes for Re_{sf}. Similar studies for Nusselt number and Sherwood number would be important for future works.

Acknowledgements

The authors are grateful to the Swedish Research Council (Vetenskapsrådet) for financial support for the study (grant number: 2015-05588). The simulations were performed on resources, *Kebnekaise*, provided by the Swedish National Infrastructure for Computing (SNIC) at High Performance Computing Center North (HPC2N). The authors thank all the staff of HPC2N for the technical assistances. Furthermore, M.U.B. thanks the Swedish for Gasification Center and its industrial and academic partners for financial suppport. N.E.L.H. acknowledge the Research project Gaspro, financed by the research council of Norway (267916) the European Union's Horizon 2020 research and innovation programme (No 764697). This work also benefitted from computer resources made available through Norwegian NOTUR program, under award NN9405K.

Appendix A. Boundary treatment with immersed boundary (IB) method in *foam-extend* (Jasak et al., 2014)

In the IB method, the mesh is categorized into three types of cells called IB cells, Fluid cells or solid cells, which is shown in the Fig. A.1a.

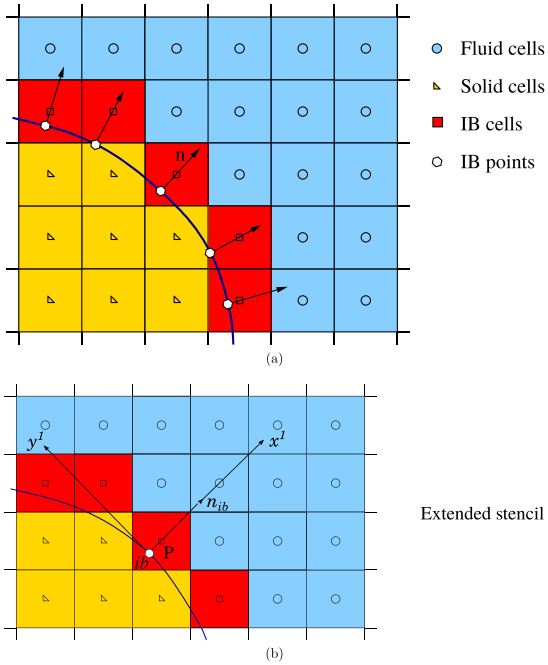

Fig. A1. (a) Different cells around an Immersed boundary(IB), IB cell normals, (b) Extended stencil around an IB and local co-ordinate system for Neumann boundary conditions. adopted from Jasak et al. (2014) with the permission from the authors.

Velocity (Dirichlet boundary condition) of an immersed boundary cell(ϕ_p) is calculated using quadratic interpolation as

$$\begin{aligned}\phi_p = \phi_{ib} &+ C_0(x_P - x_{ib}) + C_1(y_P - y_{ib}) \\ &+ C_2(x_P - x_{ib})(y_P - y_{ib}) \\ &+ C_3(x_P - x_{ib})^2 + C_4(y_P - y_{ib})^2,\end{aligned} \tag{A.1}$$

and pressure (Neumann boundary condition) of an immersed boundary cell is calculated as

$$\phi_p = C_0 + [n_{ib}.(\nabla\phi)_{ib}]x_P^1 + C_1 y_P^1 + C_2 x_P^1 y_P^1 + C_3(x_P^1)^2 + C_4(y_P^1)^2, \tag{A.2}$$

where the coefficients C_0, C_1, C_2, C_3 and C_4 are calculated using weighted least squares method in the extended stencil shown in Fig. A.1b and x^1 and y^1 are local co-ordinates where x^1 is normal to the point *ib*.

Appendix B. Data tables of Figure 2

Table B.1
Data tables of Fig. 2.

Re	Simulations	Model	Difference (% of model value)
13.96	3.431	3.424	0.20
6.98	5.521	5.617	1.71
2.32	13.074	13.562	3.60
0.232	108.490	110.720	2.01

Appendix C. Data tables of Figure 10

Table C.1
Data tables of Fig. 9.

Re	Re_{sf}	C_D -simulations	Current model	Kestel model	Error of current model (% of numerical results)
13.96	2.90	2.82	2.87	2.87	1.6
	0.97	3.19	3.22	3.232	0.7
	0.19	3.38	3.38	3.392	0.02
	0.04	3.42	3.42	3.42	0.01
	0	3.43	–	–	–
	−0.39	3.48	3.52	–	1.2
	−0.97	3.65	3.66	–	0.4
6.98	2.90	4.36	4.53	4.44	4.0
	1.45	4.89	5.02	5.00	2.5
	0.48	5.30	5.40	5.42	1.9
	0.10	5.48	5.58	5.59	1.8
	0	5.52	–	–	–
	−0.20	5.61	5.71	–	1.7
	−0.97	6.00	6.10	–	1.9
2.32	2.90	9.60	10.37	9.90	8.0
	1.93	10.60	11.25	10.98	6.1
	0.97	11.75	12.30	12.25	4.7
	0.20	12.91	13.29	13.34	2.9
	0	13.07	–	–	–
	−0.39	13.61	14.14	–	3.9
	−0.97	14.51	15.12	–	4.2
0.232	2.90	75.45	78.20	74.88	3.7
	1.45	90.28	91.56	91.00	1.4
	0.58	100.80	102.01	102.79	1.2
	0.29	104.57	106.05	106.85	1.4
	0.19	105.80	107.46	108.15	1.6
	0.10	107.09	108.92	109.39	1.7
	0.02	108.27	110.11	110.25	1.7
	0	108.49	–	–	–
	−0.04	108.90	111.02	–	2.0
	−0.97	122.78	127.99	–	4.2

References

Bagchi, P., Ha, M.Y., Balachandar, S., 2001. Direct numerical simulation of flow and heat transfer from a sphere in a uniform cross-Flow. J. Fluids Eng. 123, 347–358. doi:10.1115/1.1358844.

Chuchottaworn, P., Fujinami, A., Asano, K., 1983. Numerical analysis of the effect of mass injection or suction on drag coefficients of a sphere. J. Chem. Eng. Jpn. 16, 18–24. doi:10.1252/jcej.16.18.

Cliffe, A., Lever, D., 1985. Isothermal flow past a blowing sphere. Int. J. Numer. Methods Fluids 5, 709–725. doi:10.1002/fld.1650050804.

Constant, E., Favier, J., Meldi, M., Meliga, P., Serre, E., 2017. An immersed boundary method in OpenFOAM: verification and validation. Comput. Fluids doi:10.1016/j.compfluid.2017.08.001.

Dukowicz, J.K., 1982. An exact solution for the drag of a sphere in low Reynolds number flow with strong uniform suction or blowing. Phys. Fluids 25, 1117–1118. doi:10.1063/1.863875.

Dukowicz, J.K., 1984. Drag of evaporating or condensing droplets in low Reynolds number flow. Phys. Fluids 27, 1351–1358. doi:10.1063/1.864776.

Fadlun, E.A., Verzicco, R., Orlandi, P., Mohd-Yusof, J., 2000. Combined immersed-boundary finite-Difference methods for three-Dimensional complex flow simulations. J. Comput. Phys. 161, 35–60. doi:10.1006/jcph.2000.6484.

Farazi, S., Sayadi, T., Pitsch, H., 2016. Numerical analysis of the drag force acting on the reactive single char particle under oxy-fuel condition. In: Proc. of the China National Symposium on Combustion 2016. Ma'anshan

Haider, A., Levenspiel, O., 1989. Drag coefficient and terminal velocity of spherical and nonspherical particles. Powder Technol. 58, 63–70. doi:10.1016/0032-5910(89)80008-7.

Hayhurst, A.N., 2000. The mass transfer coefficient for oxygen reacting with a carbon particle in a fluidized or packed bed. Combust.Flame 121, 679–688. doi:10.1016/s0010-2180(99)00178-9.

Jasak, H., Rigler, D., Tukovic, Z., 2014. Design and implementation of Immersed Boundary method with discrete forcing approach for boundary conditions. In: In Proceedings of 6th European Congress on Computational Fluid Dynamics - ECFD VI, pp. 5319–5332. Barcelona, Spain

Johnson, T.A., Patel, V.C., 1999. Flow past a sphere up to a reynolds number of 300. J. Fluid Mech 378, 19–70. doi:10.1017/S0022112098003206.

Kalinchak, V., 2001. Influence of Stefan flow and convection on the kinetics of chemical reactions and heat and mass exchange of carbon particles with gases. J. Eng. Phys. Thermophys. 74, 323–330. doi:10.1023/A:1016696203987.

Kestel, M., 2016. Numerical Modeling of Moving Carbonaceous Particle Conversion in Hot Environments. TU Bergakademie Ph.D. thesis.

Kreitzberg, T., Pielsticker, S., Gvert, B.M., Kneer, R., 2016. CO2 and H2O Gasification under chemically and diffusion controlled conditions. In: 33rd Annual International Pittsburgh Coal Conference. Cape Town

Kurose, R., Makino, H., Komori, S., Nakamura, M., Akamatsu, F., Katsuki, M., 2003. Effects of outflow from the surface of a sphere on drag, shear lift, and scalar diffusion. Phys. Fluids 15, 2338–2351. doi:10.1063/1.1591770.

Miller, R., Bellan, J., 1999. Direct numerical simulation of a confined three-dimensional gas mixing layer with one evaporating hydrocarbon-droplet-laden stream. J. Fluid Mech. 384, 293–338. doi:10.1017/S0022112098004042.

Mittal, R., Iaccarino, G., 2005. Immersed boundary methods. Annu. Rev. Fluid Mech 37, 239–261. doi:10.1146/annurev.fluid.37.061903.175743.

Nour, Z., Amberg, G., Do-Quang, M., 2017. Kinematics and dynamics of suspended gasifying particle. Acta Mech. 228, 1135–1151. doi:10.1007/s00707-016-1748-5.

Renksizbulut, M., Yuen, M.C., 1983. Numerical study of droplet evaporation in a high-temperature stream. J. Heat Transf. 105, 389–397. doi:10.1115/1.3245591.

Richter, A., Nikrityuk, P.A., 2012. Drag forces and heat transfer coefficients for spherical, cuboidal and ellipsoidal particles in cross flow at sub-critical reynolds numbers. International Journal of Heat and Mass Transfer 55 (4), 1343–1354. doi:10.1016/j.ijheatmasstransfer.2011.09.005.

Umeki, K., Kirtania, K., Chen, L., Bhattacharya, S., 2012. Fuel particle conversion of pulverized biomass during pyrolysis in an entrained flow reactor. Ind. Eng. Chem. Res. 51, 13973–13979. doi:10.1021/ie301530j.

Weller, H.G., Tabor, G., Jasak, H., Fureby, C., 1998. A tensorial approach to computational continuum mechanics using object-oriented techniques. Comput. Phys. 12, 620–631. doi:10.1063/1.168744.

Wittig, K., Nikrityuk, P., Richter, A., 2017. Drag coefficient and Nusselt number for porous particles under laminar flow conditions. Int. J. Heat Mass Transf. 112, 1005–1016. doi:10.1016/j.ijheatmasstransfer.2017.05.035.

Yu, J., Zhang, M.C., 2009. Mass transfer coefficients for the combustion of a char particle in O_2/CO_2. Energy Fuels 23, 5717–5724. doi:10.1021/ef900481c.

Yu, J., Zhou, K., Ou, W., 2013. Effects of stefan flow and CO oxidation on char particle combustion in O2/CO2 atmosphere. Fuel 106, 576–585. doi:10.1016/j.fuel.2013.01.005.

Appendix B

Paper II

International Journal of Multiphase Flow 140 (2021) 103650

Contents lists available at ScienceDirect

International Journal of Multiphase Flow

journal homepage: www.elsevier.com/locate/ijmulflow

The effect of Stefan flow on Nusselt number and drag coefficient of spherical particles in non-isothermal gas flow

Thamali R. Jayawickrama[a,*], Nils Erland L. Haugen[b,c], Matthaus U. Babler[d], M.A. Chishty[a], Kentaro Umeki[a]

[a] Energy Engineering, Div. Energy Science, Luleå University of Technology, Luleå 971 87, Sweden
[b] Department of Energy and Process Engineering, Norwegian University of Science and Technology, Kolbjørn Hejes vei 1 B, 7491 Trondheim, Norway
[c] Department of Thermal Energy, SINTEF Energy Research, Kolbjørn Hejes vei 1 A, 7491 Trondheim, Norway
[d] Department of Chemical Engineering, KTH Royal Institute of Technology, SE-10044 Stockholm, Sweden

ARTICLE INFO

Article history:
Received 17 August 2020
Revised 21 December 2020
Accepted 25 March 2021
Available online 29 March 2021

Keywords:
Drag coefficient
Nusselt number
Stefan flow
Boundary layer
multiphase reactive flow

ABSTRACT

A Stefan flow can be generated during a phase change or reactions of a particle immersed in a fluid. This study investigates the effect of Stefan flow on the exchange of momentum (drag coefficient (C_D)) and heat transfer (Nusselt number (Nu)) between the particle and bulk-fluid. Fully resolved simulations were carried out for a flow near a spherical particle immersed in a uniform bulk flow. The immersed boundary method is used for implementing fluid-solid interactions and the particle is considered as a static boundary with fixed boundary conditions. In a non-isothermal flow, the changes in thermophysical properties at the boundary layer played a role in the variation of C_D and Nu by a Stefan flow further. The previously developed model for the drag coefficient of a spherical particle in a uniform isothermal flow was modified for a uniform non-isothermal flow. The model is developed based on physical interpretation. A new model is developed for the Nusselt number for a spherical particle with a uniform Stefan flow combining available models in literature. The models are validated for Stefan Reynolds number $-8 \leqslant \mathrm{Re}_{sf,p} \leqslant 25$ and particle Reynolds number of $2 \leqslant \mathrm{Re}_f \leqslant 30$ in gas flow (i.e. Pr$\approx$ 0.7).

1. Introduction

Particle-laden flows have many complexities due to *e.g.* flow separation, particle wakes, multi-particle effects, Stefan flow effects and reactions. Such flows are associated with physical effects that have a wide range of length and time scales. For example, the largest length scale in pulverized boilers (reactor) is $\mathcal{O}(10^1\mathrm{m})$ while the smallest physical scale (particle boundary layer) is $\mathcal{O}(10^{-5}\mathrm{m})$ and the smallest chemical scale is $\mathcal{O}(10^{-10}\mathrm{m})$. Therefore, it is currently impossible to resolve all scales in any numerical setup of practical relevance. This gap can be bridged by developing models describing the effects occurring at smaller scales (smallest physical/chemical scales). The smallest physical scales ($\mathcal{O}(10^{-5}\mathrm{m})$) can be studied through detailed numerical simulations. In contrast to experimental data, numerical simulations create a virtual environment that is much more versatile to elucidate the relevant transport phenomena and that can be used for developing models. In the current study, we investigate the Stefan flow effects in particle-laden flows using numerical simulations.

A Stefan flow is created when there is a net flow of gas/fluid towards or away from a solid surface that is reacting or undergoing a phase change (Murphy and Shaddix, 2003). Some examples are: evaporation, condensation and combustion of droplets as well as pulverized fuel combustion and gasification. The Stefan flow can affect the exchange of mass, momentum and heat between the surface and the bulk fluid in particle-laden flows. Models for Nusselt number (Nu), Sherwood number (Sh) and the drag coefficient (C_D) are used to calculate heat, mass and momentum transfer between the particle and the fluid, respectively. However, this study will only consider the Nusselt number and the drag coefficient.

In the past, the Stefan flow effect was considered for droplet evaporation and combustion (Renksizbulut and Yuen, 1983b; 1983a; Abramzon and Sirignano, 1989; Harpole, 1981). Lately, an interest for the effect of the Stefan flow has emerged for coal combustion applications due to high reactive gas concentration in Oxy-fuel combustion (O_2/CO_2) compared to air-fuel combustion (N_2/O_2). The importance of Stefan flow in Oxy-fuel combustion of coal is emphasized by Yu et al. (2013). According to them, a Ste-

* Corresponding author.
E-mail address: thamalirajika@gmail.com (T.R. Jayawickrama).

https://doi.org/10.1016/j.ijmultiphaseflow.2021.103650

Nomenclature

Roman Symbols

Symbol	Description (Units)
A	cross section area (m^2)
c_p	specific heat capacity (J kg^{-1} K^{-1})
D	diameter of the particle (m)
F	force (N)
h	heat transfer coefficient (W m^{-2} K^{-1})
$\overrightarrow{I}$	identity matrix (1)
L	latent heat of evaporation (J kg^{-1})
$\overrightarrow{n}$	unit normal vector (1)
p	pressure (Pa)
R	radius (m)
S	surface area (m^2)
T	temperature (K)
t	weighting factor (between 0 to 1) (-)
U	velocity (m s^{-1})
$\overrightarrow{u}$	velocity vector (m s^{-1})
V	volume (m^3)

Greek Symbols

δ	boundary layer thickness (m)
μ	viscosity (Pa s)
ρ	density (kg m^{-3})
τ	time scale (s)
λ	thermal conductivity (W m^{-1} K^{-1})

Subscripts

b	boiling point (-)
B	boundary layer (-)
∞	parameters calculated at the far-field condition (-)
f	parameters calculated at the film condition (when $t = 0.5$) (-)
l	liquid (-)
sf	with Stefan flow conditions (-)
p	parameters calculated at the particle surface (-)

Dimensionless numbers

B_T	Spalding heat transfer number ($B_T = \frac{c_p(T_b - T_\infty)}{L}$)
C_D	Drag coefficient ($C_D = \frac{F}{0.5\rho U^2 A}$)
Nu	Nusselt number ($\mathrm{Nu} = \frac{hd}{\lambda}$)
Pe	Peclet number ($\mathrm{Pe} = \mathrm{Re} \times \mathrm{Pr}$)
Pr	Prandtl number ($\mathrm{Pr} = \frac{c_p \mu}{\lambda}$)
Re	Reynolds number ($\mathrm{Re} = \frac{\rho U D}{\mu}$)

fan flow has a strong influence on the mass transfer rate in Zone II conversion (kinetically and diffusion controlled) while the effect is insignificant in Zone III (diffusion controlled) during burnout period. Still it is not clear from their results when Stefan flow can be neglected.

The main objective of the current paper is to study the effect of Stefan flow on Nusselt number and drag coefficient for non-isothermal conditions (*i.e.* when there is a temperature difference between particle and gas field). Even though the model is generic and meant to be applicable for a variety of conditions, it was developed and validated with a primary interest on entrained-flow biomass gasification. As summarized in the next section, we aim to fill a gap in knowledge and models, especially under the presence of large temperature differences (*i.e.* >100 K). Hereafter 'temperature difference (ΔT)' means the temperature difference between the solid particle (sphere) surface and the far-field of the fluid. Simulations resolving the boundary layer are carried out for a laminar flow surrounding a static spherical particle. Multi-component effects were avoided for the simplicity of work. The applicability of our model for the drag coefficient, developed in our previous work under isothermal conditions (Jayawickrama et al., 2019), is assessed and extended to non-isothermal conditions. In addition, a new model describing the effect of Stefan flow on the Nusselt number is developed.

2. Previous studies

2.1. Nusselt number at high temperature difference

The Nusselt number ($\mathrm{Nu}=hD/\lambda$) is usually expressed as a function of Reynolds number ($\mathrm{Re}=\rho UD/\mu$) and Prandtl number ($\mathrm{Pr}=c_p\mu/\lambda$). A Nusselt number formula that is applicable for both high and low temperature difference conditions is hard to find in the literature. Two popular models are the models of Whitaker (1972) and the model of Ranz-Marshall Ranz and Marshall (1952). The former reads as:

$$\mathrm{Nu} = 2 + (0.4\mathrm{Re}^{\frac{1}{2}} + 0.06\mathrm{Re}^{\frac{2}{3}})\mathrm{Pr}^{0.4}\left(\frac{\mu_\infty}{\mu_p}\right)^{\frac{1}{4}}, \quad (1)$$

where thermophysical properties (*i.e.* λ, ρ, μ, and c_p) for the calculation of Nusselt number, Reynolds number, and Prandtl number are based on far-field conditions, μ_∞ is the viscosity at far-field condition and μ_p is the viscosity at particle surface condition. The Ranz-Marshall model Ranz and Marshall (1952) is given as:

$$\mathrm{Nu} = 2 + 0.6\mathrm{Re}^{\frac{1}{2}}\mathrm{Pr}^{\frac{1}{3}}, \quad (2)$$

where thermophysical properties at film condition are used to calculate Nusselt number, Reynolds number and Prandtl numbers, instead of those at far-field conditions. Film condition is defined as the average between the far-field condition and the surface condition, i.e. $T_f = (T_\infty + T_p)/2$ where T_∞ and T_p are the far-field and surface temperatures, respectively. At low temperature differences and Reynolds numbers ($\approx 0 < \mathrm{Re} < 100$), the Whitaker model (Eq. 1) typically gives predictions that are closer to the actual values (Nikrityuk and Meyer, 2014), while the Ranz-Marshall model (Eq. (2)) can be applied for high temperature differences ($1 < \mathrm{Re} < 130$) (Ellendt et al., 2018).

There are numerous works on developing models for the Nusselt number associated with droplet evaporation. Evaporation at high temperature differences requires consideration of the variation of thermophysical properties, such as thermal conductivity (λ) and specific heat capacity (c_p). This effect can be accounted for through a correction factor for the Nusselt number (Harpole, 1981), or by introducing a reference temperature (Naraslmhan and Gauvin, 1967; Downingm, 1966; Yuen and Chen, 1978). The reference temperature is then calculated as follows:

$$T_t = tT_\infty + (1-t)T_p, \quad (3)$$

where t is weight factor.

2.2. Effect of Stefan flow on Nusselt number

Different models for the Nusselt number developed for evaporation of single droplets are summarized by Zhifu et al. (2013). They have categorized the available models into theoretical, numerical and experimental models. According to their comparisons, all the models are deviating from experimental results when the evaporation rates are high. Therefore, they have developed a model with a correction factor that is applicable for high evaporation rates as well. In this model, the Nusselt number is given as:

$$\mathrm{Nu}_{Zh} = f_T \mathrm{Nu}, \quad (4)$$

where

$$f_T = (1 + B_{Tp})^{-\frac{2}{3}}, \quad (5)$$

and

$$\mathrm{Nu} = 2 + 0.552\mathrm{Re}^{\frac{1}{2}}\mathrm{Pr}^{\frac{1}{3}}. \tag{6}$$

Here the Spalding heat transfer number (B_{Tp}) is defined as:

$$B_{Tp} = \frac{c_{p,p}(T_\infty - T_b)}{L}, \tag{7}$$

where L is latent heat of evaporation and T_b is the boiling point temperature. The Reynolds number is calculated based on properties at the particle surface, while the Prandtl number is calculated based on far-field condition. The Nusselt number is calculated based on properties at the particle surface condition. It is noticed that the model of Zhifu et al. (2013) has no explicit dependence on the Stefan flow. The effect of Stefan flow is accounted for indirectly through the evaporation rate, characterized by the Spalding heat transfer number.

Niazmand and Renksizbulut (2003) used the model developed for droplet evaporation by Renksizbulut & Yuen (Nu_{RY}) Renksizbulut and Yuen (1983a) for the generalized case of a Stefan flow:

$$\mathrm{Nu}_{RY} = \frac{2 + 0.57\mathrm{Re}^{1/2}\mathrm{Pr}^{1/3}}{(1 + B_{T_f})^{0.7}} \tag{8}$$

where the Reynolds number is calculated based on particle surface conditions, Prandtl number is calculated based on film condition and the Spalding heat transfer number is defined as:

$$B_{T_f} = \frac{\mathrm{PrRe}_{sf}}{\mathrm{Nu}}, \tag{9}$$

where

$$\mathrm{Re}_{sf} = \frac{\rho U_{sf} D}{\mu}, \tag{10}$$

is the Reynolds number based on the Stefan flow velocity (hereafter, called Stefan Reynolds number). The variation of thermophysical properties are neglected for Niazmand and Renksizbulut Niazmand and Renksizbulut (2003) and the selected range of Stefan flows was based on droplet evaporation ($0.01 \geqslant \frac{U_{sf}}{U_\infty} \geqslant 0.04$). Murphy & Shaddix Murphy and Shaddix (2003) have formulated a Nusselt number (Nu_M) correlation, for Stefan flow in a quiescent environment. Assuming constant properties, their expression reads as:

$$\mathrm{Nu}_M = \mathrm{Nu}\frac{(\mathrm{PrRe}_{sf})/\mathrm{Nu}}{e^{(\mathrm{PrRe}_{sf})/\mathrm{Nu}} - 1}, \tag{11}$$

where $\mathrm{Nu} = 2$ is the Nusselt number in a quiescent flow without Stefan flow. Recently, Kestel Kestel (2016) developed a new empirical model applicable for the convective flow environment based on his simulation data that gave better accuracy than the other available models. In this model, which is applicable for $\mathrm{Re} < 200$, $\mathrm{Re}_{sf} < 20$ and $0.744 < \mathrm{Pr} < 1.5$, the Nusselt number ($\mathrm{Nu}_K$) is given as:

$$\mathrm{Nu}_K = \mathrm{Nu}\exp\left(\frac{-0.54\,\mathrm{Pr}\,\mathrm{Re}_{sf}^{1.126}}{\mathrm{Nu}^{1.052}}\right), \tag{12}$$

where

$$\mathrm{Nu} = 2 + 0.39\mathrm{Re}^{0.56}\mathrm{Pr}^{0.45}. \tag{13}$$

In Eq. 12 and 13, all properties are calculated based on the reference temperature as defined in Eq. (3) when the weight factor is $t = 0.9$. This model has a large number of fitting parameters and it does agree better with simulation results. However, it does not necessarily represent the physical phenomena.

In summary, most of the currently available models for Nusselt number for particles with Stefan flow in a convective environment are empirical. One of the very few theoretical models (of Eq. 11) (Murphy and Shaddix, 2003) developed for the Nusselt number of particles with Stefan flow is for a *quiescent* environment and is based on a constant property assumption. Therefore, there are no models for Stefan flow in a convective environment based on physical interpretation while considering variation of properties.

2.3. Drag coefficients at high temperature differences.

The drag coefficient is defined as $C_D = F/(0.5\rho U^2 A)$, where F is the drag force, A is the cross-sectional area of the particle, ρ is the density of the fluid and U is the velocity difference between the particle and the fluid. There are many correlations available to calculate fluid drag on a solid spherical object. However, most of these models have been developed for isothermal or close to isothermal conditions. This makes these models fail at high temperature differences, since variations of properties have to be considered in order to accurately calculate the drag. The Schiller-Naumann model Schiller and Naumann (1935) for the drag coefficient, given as:

$$C_D = \frac{24}{\mathrm{Re}}(1 + 0.15\mathrm{Re}^{0.687}), \tag{14}$$

is a widely used drag model. Recently, Ellendt et al. Ellendt et al. (2018) have suggested a correction factor (ϕ) for the Schiller-Naumann correlation considering non-isothermal effects:

$$\begin{aligned} C_D &= \frac{24}{\mathrm{Re}}(1 + 0.15\mathrm{Re}^{0.687})\phi; \\ \phi &= 0.273(1 - 0.883^{\mathrm{Re}})\left(\frac{\rho_\infty}{\rho_p} - 1\right) + 1, \end{aligned} \tag{15}$$

when $1 < \mathrm{Re} < 130$. Here, the Reynolds number is evaluated at the surface temperature of the sphere, ρ_∞ is the density of the fluid in the far-field and ρ_p is the density of the fluid at the particle surface. The fluid density entering the expression for the drag coefficient ($C_D = F/(0.5\rho U^2 A)$) is at far-field conditions.

2.4. Effects of Stefan flow on drag coefficients.

Similar to the Nusselt number, the models developed for the combustion and evaporation of sprays are available for the drag coefficient under the influence of a Stefan flow (Yuen and Chen, 1976; Eisenkalam et al., 1967; Renksizbulut and Yuen, 1983b). One common approach is the so-called one-third rule proposed by Yuen and Chen Yuen and Chen (1976). The one-third rule uses ordinary drag models, for example the one of Schiller-Naumann Schiller and Naumann (1935) (see Eq. (14)), for an evaporating droplet, but with the Reynolds number calculated as:

$$\mathrm{Re} = \frac{\rho_\infty U D}{\mu_t}, \tag{16}$$

where μ_t is the dynamic viscosity obtained at the reference temperature, as given by Eq. (3), with a weight factor of $t = 1/3$. This model is applicable in the range of $1 < \mathrm{Re} < 2000$ and $0 < B_T < 3$. The same result was confirmed by Renksizbulut and Yuen Renksizbulut and Yuen (1983b) for an evaporating droplet from their simulations. However, the approach described above does not include a dependency on the Stefan velocity and is therefore not expected to be suitable unless the Stefan flow velocity is small compared to the velocity of the mean flow.

Studies of the effect of Stefan flow on the drag coefficient for generalized cases have always assumed isothermal conditions as per the authors knowledge. Most recent works are done by Jayawickrama et al. Jayawickrama et al. (2019), Kestel Kestel (2016) and Miller & Bellan Miller and Bellan (1999). The latter two have developed empirical models for the drag coefficient of a spherical object

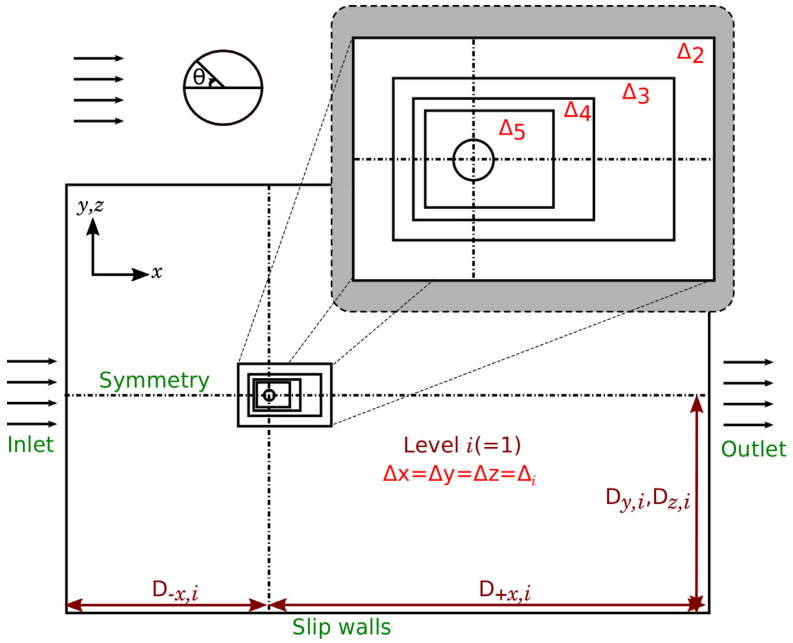

Fig. 1. Computational domain for the simulations. Δ_i, $i = 1$ to 5 representing the coarsest mesh to finest mesh. $D_{-x,i}$ is the distance from the centre of the sphere to negative x-direction and $D_{+x,i}$ is the distance from the centre of the sphere to positive x-direction in level i (See the Table 2).

with a Stefan flow. Kestel's model is applicable for a wider range of Stefan flows ($0 < \mathrm{Re_{sf}} \leqslant 20$ and $\mathrm{Re} \leqslant 200$). Both models have several fitting parameters. Jayawickrama et al. (2019) developed a model based on a physical interpretation of the drag that required only one fitting parameter. This model was validated against numerical simulations in the range of $-1 \leqslant \mathrm{Re_{sf}} \leqslant 3$ (a negative $\mathrm{Re_{sf}}$ means inward Stefan flow) and $\mathrm{Re} < 14$. All three models are applicable for isothermal conditions only. Therefore, it is important to study the effect of a Stefan flow on the drag coefficient including thermal effects as well.

3. Methodology

In the current work, numerical simulations are carried out for a flow around a static, spherical particle with constant size using OpenFOAM. The simulation domain and boundaries are shown in Fig. 1. The incoming gas flow to the simulation domain is uniform and its temperature is kept at 1400 K. A uniform Stefan flow is given as a boundary condition at the particle surface. Different cases are simulated by varying sphere surface temperature, diameter and incoming flow velocity, resulting in a variety of Reynolds numbers. Variation of properties with temperature is considered (See Appendix A for more details.). The Reynolds number is within the limit of steady, axi-symmetric flow ($\mathrm{Re} < 210$) (Johnson and Patel, 2017) and the Mach number of the flow is well below 0.1. Therefore, the flow is essentially in-compressible. The intra-particle heat transfer is not considered and the particle temperature is kept uniform both in space and time. Radiative heat transfer is also neglected. The fluid is governed by the steady, incompressible, laminar flow equations, where mass conservation yields the continuity equation as:

$$\nabla \cdot (\rho \vec{u}) = 0, \tag{17}$$

while momentum conservation gives:

$$(\rho \vec{u} \cdot \nabla)\vec{u} = -\nabla p + \nabla \cdot \mu[\nabla \vec{u} + \nabla \vec{u}^{T} - \frac{2}{3}(\nabla \cdot \vec{u})\vec{I}]. \tag{18}$$

Finally, from energy conservation we get:

$$\nabla \cdot (\rho c_p \vec{u} T) = -\nabla \cdot \lambda \nabla T. \tag{19}$$

Eqs. 17, 18 and 19 were discretized using second-order schemes with the finite volume method.

3.1. Boundary conditions.

The temperature of the inlet boundary is kept at 1400 K. The exit of the domain is considered as an outflow boundary, where the gradients of the velocity and temperature are set to zero. The boundaries at the side of the domain are treated as slip walls. In the slip wall boundary condition, the velocity component normal to the wall is zero. In addition, the gradients of temperature and the other velocity components in the normal direction to the wall are also set to be zero. Along the axis of symmetry, a symmetric boundary condition is applied. In the Symmetric boundary condition, the velocity component normal to the symmetry plane and the gradients of all the other properties normal to the plane are set to zero. Only a quarter of the domain is simulated as the flow is axisymmetric.

A Cartesian mesh is used for the simulation. The immersed boundary method (IBM) was applied for the implementation of the solid boundary. In this work, the discrete forcing approach (Mittal and Iaccarino, 2005), which directly applies the presence of a solid body through boundary conditions (Jasak et al., 2014), is used. The value of any parameter of a cell that crosses the immersed boundary is calculated by interpolating values between the immersed boundary and neighboring cells (Fadlun et al., 2000). The Stefan velocity is considered as a uniform velocity normal

Table 1
Conditions maintained for far-field velocity, particle diameter and particle temperature. Far-field temperature was kept at $T_\infty = 1400$K.

Condition	Inlet velocity (m/s)	Diameter (mm)	T_p(K)	$\mathrm{Re_f}$
1	0.5	1.0	400	4.88
			1200	2.66
			1600	2.10
2	3.0	0.5	400	14.64
			1200	7.98
			1600	6.31
3	3.0	1.0	400	29.29
			1200	15.98
			1600	13.74

to the immersed boundary (Dirichlet boundary condition). For an outwardly directed Stefan flow, the temperature of the outflow is equal to the surface temperature of the particle.

The pressure gradient is set to zero at the solid boundary (Neumann boundary conditions). Treatment of Neumann and Dirichlet boundary conditions in the immersed boundary method is explained in Jayawickrama et al. (2019).

3.2. Simulation conditions and procedure

For all the simulations in this work, the fluid (including the fluid of the Stefan flow) was assumed to be pure nitrogen. The inlet velocity, diameter of the particle and temperature range of the fluid and the sphere were selected based on pulverized combustion and gasification applications at atmospheric pressure. The velocity at the inlet varied between 0.5-3 m s^{-1} and the diameter of the particle is between 0.5-1.0 mm. The range of Stefan flow velocities was selected based on results from Kreitzberg et al. (2016) and Umeki et al. (2012) for devolatilization and char conversion of biomass. The choice of bulk fluid temperature (1400 K) is based on the range of typical bulk fluid temperatures observed in pilot scale experiments of entrained-flow gasification (Sepman et al., 2017). Fuel particles in entrained flow gasifiers are usually colder than the surrounding gas because of predominantly endothermic reactions and the lack of an oxygen rich atmosphere, except for the near burner zone. The particle temperature can, however, exceed the gas temperature by ca. 200 K in pulverized combustion, where oxygen is available for char combustion reactions (Li et al., 2018). Therefore, we selected three different fuel particle temperatures (T_p =400, 1200, and 1600 K), each representing drying, char gasification, and char oxidation stages, respectively. The particle temperatures and far-field conditions studied in this work are shown in Table 1.

We used the OpenFOAM environment *foam-extend*-4.0 (Weller et al., 1998) for the simulations. The immersed boundary solver for incompressible, steady-state conditions was modified to account for non-isothermal, variable density and variable property conditions. The solver uses quadratic interpolation (Jasak et al., 2014) for the reconstruction of the solid phase boundary conditions into the closest fluid cells.

The preliminary domain size and mesh resolution was selected based on previous studies (Jayawickrama et al., 2019; Constant et al., 2017; Richter and Nikrityuk, 2012) for isothermal flow around a sphere. The inlet conditions and Stefan flow velocities are similar to the ones used for the isothermal simulations in our previous work (Jayawickrama et al., 2019). Therefore, the domain size is unchanged for the current non-isothermal simulations ($64D \times 32D \times 32D$). There are, however, two main differences in the non-isothermal cases compared to the isothermal cases.

The first difference is that a reduction (increase) of particle temperature increases (decreases) the Reynolds number (Re), resulting in a thinner (thicker) boundary layer for non-isothermal conditions. Mesh refinement tests therefore had to be carried out. The tests were carried out with the highest Reynolds number conditions (condition 3 of Table 1 with particle temperature 400K) and with the smallest possible boundary layer thickness (inward Stefan flow condition). Two mesh refinement levels were tested, as shown in Table 2 (Mesh I and Mesh III).

Table 2
Distance from the centre of the particle in diameters (D) in the computational domain (See Fig. 1).

(a) Mesh I				
i	$D_{-x,i}$	$D_{+x,i}$	$D_{y,i}, D_{z,i}$	Δ_i/D
1	16	48	16	0.32
2	3	6	3	0.16
3	2	5	2	0.08
4	1.5	3	1.5	0.04
5	1.2	2	1.2	0.02
(b) Mesh II				
i	$D_{-x,i}$	$D_{+x,i}$	$D_{y,i}, D_{z,i}$	$Delta_i/D$
1	16	48	16	0.32
2	6.5	12	6.5	0.16
3	5.5	10	5.5	0.08
4	4.5	6	4.5	0.04
5	3.5	4	3.5	0.02
(c) Mesh III				
i	$D_{-x,i}$	$D_{+x,i}$	$D_{y,i}, D_{z,i}$	Δ_i/D
1	16	48	16	0.16
2	3	6	3	0.08
3	2	5	2	0.04
4	1.5	3	1.5	0.02
5	1.2	2	1.2	0.01

The other difference between the isothermal and non-isothermal cases is due to the difference between the thermal (δ_{th}) and the viscous boundary layer thickness (δ_{vis}). As the Prandtl number (Pr) is less than 1, the thermal boundary layer thickness is larger than the viscous boundary layer thickness ($\delta_{th} > \delta_{vis}$). Therefore, the size of the mesh refinement regions have to be examined. This was carried out for the lowest Reynolds number condition (condition 1 of Table 1 with particle temperature 1600K) with the largest possible boundary layer thickness (highest outward Stefan flow). Two refinement region sizes were tested, which is shown in Table 2 (Mesh I and Mesh II). Difference between Mesh I, II and III were very small in C_D and Nu and the velocity and temperature fields around the boundary layer were also identical when comparing all the meshes. Therefore, Mesh III was used for the simulations.

Table 3 shows the selection of mesh refinement levels and size of refinement regions used for the simulations in this paper. The final mesh for all the conditions was Mesh III with the highest refinement 0.01D.

3.3. Estimation of drag coefficient and Nusselt number

The drag coefficient is a dimensionless quantity used to represent forces acting on the surface of a body immersed in a fluid. For a spherical body with radius R, it can be calculated as:

$$C_{D,f} = \frac{\vec{F}_{P,x} + \vec{F}_{visc,x}}{\frac{1}{2}\rho_f U_\infty^2 (\pi R^2)}, \tag{20}$$

where ρ_f is the fluid density of film condition. The pressure and viscous forces are given as

$$\vec{F}_p = \oint_S p_p \vec{n}\, ds, \tag{21}$$

and

$$\vec{F}_{visc} = -\oint_S \mu_p (\nabla \vec{u} + \nabla \vec{u}^T) \vec{n}\, ds, \tag{22}$$

Table 3
Mesh refinement results and refinement domain size results as explained in section 3.2. The drag (C_D) and Nusselt number (Nu) calculated at far-field conditions and Stefan Reynolds number (Re_{sf}) calculated at particle surface condition.

Re_{sf}	Mesh	C_D	Error (% of mesh III or II)	Nu_∞	Error (% of mesh III or II)
-7.98	mesh I	3.01	10.12	5.40	0.15
	mesh III	3.36	-	5.39	-
2.36	mesh I	10.52	0.25	2.16	2.44
	mesh II	10.55		2.11	-
	mesh III	10.94		2.16	-

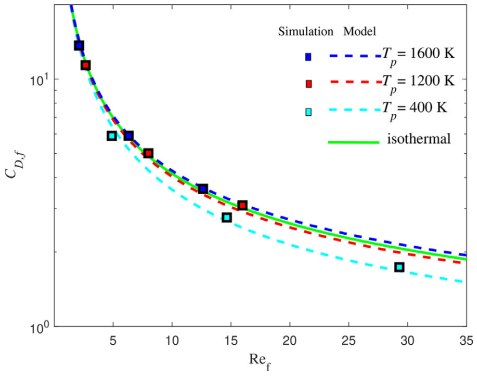

Fig. 2. Drag coefficient (C_D) at film condition for the case where there is no Stefan flow. Lines: Correlations of Ellendt et al. Ellendt et al. (2018) at different particle temperatures (400 K,1200 K,1600 K), symbols: results from our numerical simulations. Green: isothermal. Cyan: T_p = 400 K. Red: T_p = 1200 K. Blue: T_p = 1600 K.

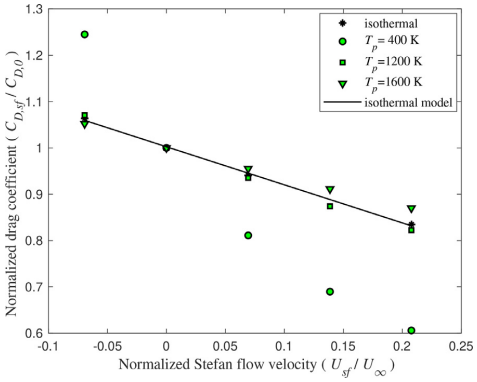

Fig. 3. Normalized drag $C_{D,sf}/C_{D,0}$ at film condition and Normalized Stefan flow velocity U_{sf}/U_∞. $C_{D,0}$ is the drag coefficient without Stefan flow. Simulation conditions: U_∞=3.0 m s^{-1}, T_∞ = 1400 K, and D=1.0 mm.

respectively. Here, the integration is over the surface S of the particle. In the above, p_p is the extrapolated pressure at the particle surface. Only the components $\vec{F}_p$ and $\vec{F}_{visc}$ in the direction of the mean flow are accounted for when calculating the drag coefficient, since the other components are canceled due to symmetry. The Nusselt number is calculated based on the overall difference in enthalpy flux at the boundaries of the simulation domain. Here, the far-field based Nusselt number is calculated as follows:

$$Nu_\infty = \frac{(\rho \vec{u}\, c_p T S)_{in} + \vec{u}_{sf}(\rho c_p T S)_{sph} - (\int(\rho \vec{u}\, c_p T)\vec{n}\, dS)_{out}}{S_{sph}(T_p - T_\infty)} \times \frac{2R}{\lambda_\infty}, \tag{23}$$

where subscripts *in, out* and *sph* refers to the conditions at the inlet boundary, the outlet boundary and the particle surface, respectively, and S is the surface area of the relevant boundary.

3.4. Validation

In order to validate the code, simulations were carried out to examine if the code reproduces known results both for the drag coefficient and the Nusselt number.

For the validation of the code with respect to the drag coefficient, non-isothermal simulations *without* Stefan flow were carried out. The drag coefficients obtained from the simulations based on Eq. 20 were compared with the model suggested by Ellendt et al. Ellendt et al. (2018) (see Eq. 15). As shown in Fig. 2, the numerical results show good agreement with the model of Ellendt et al. Please note that, when determining the model predictions, the Reynolds number is based on film conditions.

We are interested in the Nusselt number at strongly non-isothermal conditions, i.e., where the temperature difference between the particle surface and the far-field is high (> 100 K). In order to validate the code with respect to the Nusselt number, simulations were carried out with a strong temperature difference, but without Stefan flow. The results were compared with the Ranz-Marshall model (Eq. 2), which is applicable for strongly non-isothermal conditions (see section 2.1). Table 4 shows a good agreement between the numerical results and the model data.

4. Results and Discussion

4.1. The effect of Stefan flow on the drag coefficient under non-isothermal conditions

By comparing the simulation results obtained at isothermal and non-isothermal conditions, it is possible to isolate the physical effects of the Stefan flow (*e.g.* due to the change in boundary layer thickness) from thermal effects (*e.g.* variation of thermophysical properties due to the change in temperature). Figure 3 shows the normalized drag coefficient ($C_{D,sf}/C_{D,0}$) against normalized Stefan flow velocity (U_{sf}/U_∞) for both isothermal and non-isothermal conditions (condition 3 of Table 1).

The drag coefficient is normalized by the corresponding drag as obtained *without* a Stefan flow ($C_{D,0}$). Here, $C_{D,0}$ and $C_{D,sf}$ are calculated based on film condition (See Eq. 20). As can be seen from the figure, the temperature difference has a significant effect on the slope of the curve, especially for high temperature differences. The drag reduction by the Stefan flow is more significant when the particle temperature is lower than the surrounding gas ($T_p < T_\infty$) and vice versa. The same behavior can be observed (not shown here) for conditions 1 and 2 (see Table 1) as well. It means that apart from the physical effects of the Stefan flow, the thermal effect has to be considered to describe the change of C_D for non-isothermal conditions.

Table 4
Comparison of Nusselt numbers (Nu) and the drag coefficient (C_D) without Stefan flow from simulations and the Ranz-Marshall model (Eq. 2)), respectively the model of Ellendt et al. (Eq. 15). Far-field temperature (T_∞) is 1400 K for all the cases. Conditions 1-3 are listed in Table 1, while conditions 4-5 are presented in the following: condition 4: $D = 1.0$ mm and $U_\infty = 5.94$ m s^{-1}, Condition 5: $D = 1.0$ mm and $U_\infty = 11.88$ m s^{-1}

Condition	T_p K	$\mathrm{Re_f}$ -	Nu *Sim*	*Model*	Error %	$C_{D,f}$ *Sim*	*Model*	Error %
1	400	4.88	3.16	3.32	4.8	5.90	6.48	8.95
	1200	2.66	2.84	2.89	1.7	11.39	11.53	1.22
	1600	2.10	2.74	2.78	1.4	13.67	14.38	4.98
2	400	14.65	4.04	4.28	5.6	2.76	2.67	1.34
	1200	7.99	3.57	3.55	0.6	5.01	4.76	2.15
	1600	6.31	3.41	3.35	1.8	5.90	5.95	0.30
3	400	29.29	5.16	5.23	1.3	1.74	1.68	0.92
	1200	15.98	4.34	4.20	3.3	3.09	2.92	1.55
	1600	12.63	4.06	3.91	3.8	3.60	3.64	0.24
4	1600	25.0	4.95	4.69	5.5			
5	1600	50.0	6.22	5.80	7.2			

The thermal effects of the Stefan flow can be studied by investigating Fig. 4, which shows the variation of the velocity and temperature fields in the boundary layer. Without the Stefan flow (blue lines), the velocity gradient of the non-isothermal case ($T_p < T_\infty$) is slightly larger than that of the isothermal case. Nevertheless, we can see from Fig. 2 that the drag coefficient for $T_p < T_\infty$ (non-isothermal case) is lower than for the isothermal case. This is because the contribution from the change in thermophysical parameters is more significant than the change in boundary layer thickness (Eq. 20). To be more specific: one would expect the drag coefficient to increase when the boundary layer gets thinner (higher velocity gradients), but this effect is more than compensated by the decrease in viscosity due to the lower temperature. In essence, the local Reynolds number is increased when the particle temperature becomes lower than the far-field temperature, and it is clear from Fig. 2 that the drag coefficient decrease with increasing Re_f.

In contrast, the same non-isothermal case shows a more pronounced expansion of the velocity boundary layer with an outward Stefan flow (red lines) than does the isothermal case. This pronounced change in the velocity is due to the expansion of the gas from the Stefan flow as it is heated. Since it is the *velocity* of the Stefan flow that is kept constant between different cases, the total mass flux due to the Stefan flow is much higher for the non-isothermal case (since the fluid density is more than three times higher at 400 K than at 1400 K). This means that as the initially cold gas emitted from the particle at 400 K is heated up, it accelerates and pushes the boundary layer outwards. In fact, the normalized temperature plot in Fig. 4b shows the decrease in gas temperature near the particle surface with outward Stefan flow. As for the inward Stefan flow, both velocity and thermal boundary layers showed exactly opposite trends from the outward Stefan flow, i.e. steeper velocity gradient and thinner thermal boundary layer. These observations imply the importance to consider the change in thermophysical parameters when modelling the drag coefficient under non-isothermal conditions. Therefore, the model developed in our previous paper (Jayawickrama et al., 2019), which was based on isothermal simulations, needs to be extended to consider the effect of the variation of thermo-physical properties.

Our previous study under isothermal conditions (Jayawickrama et al., 2019) showed that the drag coefficient changes due to a Stefan flow. This change is primarily caused by a modification of the viscous forces due to the change in boundary layer thickness. Following the idea in Jayawickrama et al. (2019), the current study uses a simple model for the effect of a Stefan flow on the drag coefficient. It is related to the change in the volume of the boundary layer due to the Stefan flow, and is

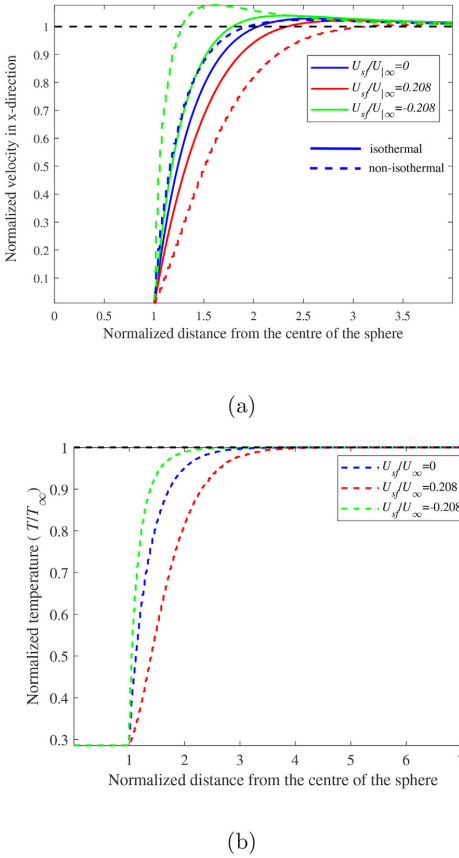

Fig. 4. (a) Normalized velocity in the mean flow direction (U_x/U_∞); (b) Normalized temperature (T/T_∞). Both figures are drawn as functions of the normalized distance from the centre of the sphere (y/R) along the y-axis ($\theta = 90°$). Simulation conditions: U_∞=3.0 m s^{-1}, T_∞ = 1400 K, and D=1.0 mm. Solid lines: isothermal and Dashed lines: non-isothermal results ($T_p = 400$ K).

proposed as:

$$C_{D,sf} = C_{D,0} \times C_{D,r}, \tag{24}$$

when $C_{D,0}$ is the drag coefficient under non-isothermal conditions without a Stefan flow (see e.g. Eq. (15)), and $C_{D,r}$ is a correction term that accounts for the effects of a Stefan flow, in addition to any thermal effects of this Stefan flow. This correction term takes into account two effects: one is due to the temperature difference between the particle surface and the far-field while the other is due to the variation of the temperature field due to the Stefan flow. Both effects can be accounted for by using a modified temperature ($\tilde{T}$) based on the volumetric contribution of the Stefan flow (V_{sf}) and its temperature ($T_{sf} = T_p$), and the volume of the boundary layer without Stefan flow (V_B) and its temperature ($T_f = \frac{T_\infty + T_p}{2}$);

$$\tilde{T} = \frac{V_B T_f + V_{sf} T_p}{V_B + V_{sf}}, \tag{25}$$

where

$$V_{sf} = 4\pi R^2 U_{sf} \tau \tag{26}$$

is the added volume due to the Stefan flow,with the flow time-scale given as:

$$\tau = \frac{2(R+\delta)}{U_\infty}. \tag{27}$$

Furthermore, the volume of the boundary layer is given as:

$$V_B = \frac{4}{3}\pi (R+\delta)^3 - \frac{4}{3}\pi R^3, \tag{28}$$

when

$$\delta = \frac{2AR}{\sqrt{\mathrm{Re}_f}}, \tag{29}$$

is the classical boundary layer thickness, where

$$\mathrm{Re}_f = \frac{\rho_f U_\infty d}{\mu_f} \tag{30}$$

and A is a model constant. By substituting V_{sf} and V_B in Eq. 25 with the corresponding expressions found in Eq. 26 and 28 we obtain:

$$\tilde{T} = \frac{T_f + \frac{U_{sf}}{U_\infty} f(\mathrm{Re}_f) T_{sf}}{1 + \frac{U_{sf}}{U_\infty} f(\mathrm{Re}_f)}, \tag{31}$$

where

$$f(\mathrm{Re}_f) = 3\left(1 + \frac{2A}{\sqrt{\mathrm{Re}_f}}\right) \frac{1}{\left(\frac{3A}{\sqrt{\mathrm{Re}_f}} + 6\left(\frac{A}{\sqrt{\mathrm{Re}_f}}\right)^2 + 4\left(\frac{A}{\sqrt{\mathrm{Re}_f}}\right)^3\right)}. \tag{32}$$

Now, $\tilde{T}$ will be used to calculate the drag coefficient without Stefan flow ($\tilde{C}_{D,0}$) such that the non-isothermal model for $C_{D,sf}$ becomes:

$$C_{D,sf} = \tilde{C}_{D,0} \times C_{D,r}, \tag{33}$$

where $\tilde{C}_D$ is calculated from the modified Schiller-Naumann equation (Eq. 15) for non-isothermal conditions:

$$\tilde{C}_{D,0} = \frac{24}{\tilde{\mathrm{Re}}}\left(1 + 0.15\tilde{\mathrm{Re}}^{0.687}\right)\phi; \qquad \phi = 0.273\left(1 - 0.883^{\tilde{\mathrm{Re}}}\right)\left(\frac{\rho_\infty}{\rho_p} - 1\right) + 1, \tag{34}$$

where $\tilde{\mathrm{Re}}$ is the Reynolds number calculated with properties at $\tilde{T}$. $C_{D,r}$ is calculated based on the model developed from isothermal simulations (Jayawickrama et al., 2019) where:

$$C_{D,r} = \frac{V_B}{V_{sf} + V_B} = \frac{1}{1 + \frac{U_{sf}}{U_\infty} f(\mathrm{Re}_f)}. \tag{35}$$

In the above, the tilde over C_D is used to highlight that it is based on properties calculated at $\tilde{T}$. The constant A is calculated using non-linear least-squares regression to minimize the error between the model and the simulation results (*nlinfit* in MATLAB). The final value of A is 2.93.

Fig. 5, which shows the drag coefficient as a function of the Stefan flow Reynolds number, compares the above model with simulation results. The model is an extension of the previous isothermal model presented in Jayawickrama et al. (2019). This new model captures the effects of non-isothermal, uniform bulk flow and uniform Stefan flow. Model data and simulation results are matching well and it has only one fitting parameter (A). The model has a good qualitative performance for both negative and positive Stefan flow conditions, and it is based on a physical interpretation of thermal effects due to property variations and the Stefan flow, and physical effects due to pressure, viscosity and Stefan flow.

The (relative) root-mean-square error (Eq. 36) with all the data in Fig. 5 was 9.6%. The error was relatively high for $T_p = 400$ K (Fig. 5a), with the maximum value reaching 28%. When only considering the data from the temperature difference of 200 K (Fig. 5b-c), the maximum relative error of the model was 6% and the root-mean-square error was 4.6%. Root-mean-square error ($RMSE_{C_d}$) is calculated as follows:

$$RMSE_{C_d} = 100 \times \sqrt{\frac{\left[\Sigma\left(\frac{C_{d,model} - C_{d,simulations}}{C_{d,simulations}}\right)^2\right]}{n}}, \tag{36}$$

where $C_{d,model}$ is the value predicted by the model Eq. 33-(35) and $C_{d,simulations}$ is the value calculated from the simulations and n is the number of simulations considered.

The models are tested and validated for the particle Reynolds number range of $2 \leqslant \mathrm{Re}_f \leqslant 30$, Stefan Reynolds number range of $-8 \leqslant \mathrm{Re}_{sf,p} \leqslant 25$, and temperature range of $400K \leqslant T_p \leqslant 1600K$ with uniform Stefan flow. The developed model should be applicable for the valid temperature ranges of the modified Schiller-Naumann model (Eq. 34). However, one should be careful when extrapolating the applicability beyond the range of validation conditions. For example, the model might not be valid at higher particle Reynolds number due to flow separation or the change in the relative magnitude between the pressure force and the viscous force.

4.2. Nusselt number with Stefan flow

Murphy & Shaddix Murphy and Shaddix (2003) has developed a theoretical model that accounts for the effect of a Stefan flow when calculating the Nusselt number of a sphere immersed in a quiescent fluid (See Eq. 11). In their model, the Nusselt number is calculated as $\mathrm{Nu}_M = \mathrm{Nu}_0 f_{\mathrm{corr}}$, where $\mathrm{Nu}_0 = 2$ is the Nusselt number of a spherical particle with no Stefan flow in a quiescent fluid and f_{corr} is a correction term that accounts for the effect of the Stefan flow. One way to apply this model directly for the cases with convective flows is to replace the Nusselt number, Nu_0, with the one with a convective flow, as given by e.g. the Ranz-Marshall model. However, the prediction with this approach does not describe the simulation results. The same observation was discussed by Kestel Kestel (2016), who proceeded to develop an empirical model with several fitting parameters Eqs. 12-(13).

As discussed in the previous section, the temperature in the boundary layer changes due to the Stefan flow, especially when the temperature differences are significant. This change should be reflected in the characteristic temperature when calculating the Nusselt number. In this work, we apply a multiplication law to describe the effect of a Stefan flow (by Eq. 11) and the effect of a convective flow (Eq. 2), but considering the change in characteristic temperature. This approach in practice calculates the Nusselt

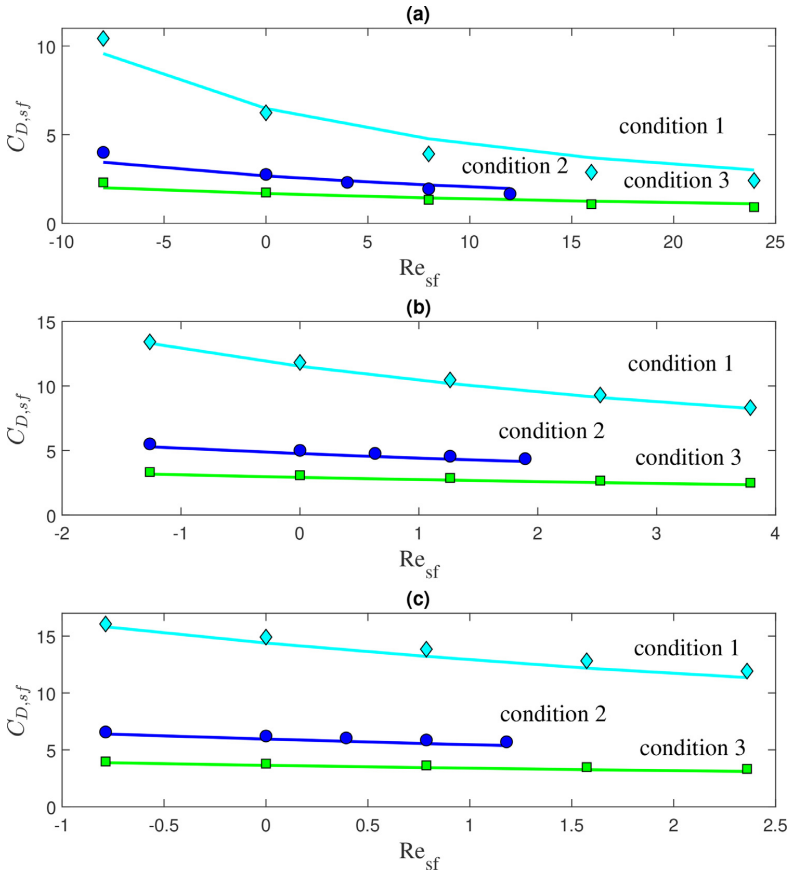

Fig. 5. Comparison of the drag coefficient from the model, i.e. Eqs. 31-35, (lines) and the simulations based on $\tilde{T}$ (symbols). Particle temperature (T_p) is (a) 400 K (b) 1200 K or (c) 1600 K. Condition 1: U_∞=0.5 m s^{-1}and D=1.0 mm. Condition 2: U_∞=3.0 m s^{-1}and D=0.5 mm. Condition 3: U_∞=3.0 m s^{-1}and D=1.0 mm.

number based on the thermophysical properties using the volume averaged temperature derived earlier (Eq. 31). The model for the Nusselt number needs to be applicable for convective flows around a sphere with high temperature differences. Here, we have used a Ranz-Marshall type model by parameter fitting the original Ranz-Marshall model with simulation data without Stefan flow, to obtain:

$$\tilde{\mathrm{Nu}} = 2 + 0.570\tilde{\mathrm{Re}}^{0.537}\tilde{\mathrm{Pr}}^{1/3}, \tag{37}$$

where Re and Pr were calculated based on the volume averaged temperature, $\tilde{T}$, as given in Eq. 31. Now we can replace the Nusselt number without Stefan flow (Nu) in Murphy & Shaddix model (Eq. 11) with the model presented in Eq. 37, such that the final model for Nu, accounting for non-isothermal effects and Stefan flow reads as:

$$\mathrm{Nu}_{sf,f} = \tilde{\mathrm{Nu}}\frac{q}{e^q - 1}, \tag{38}$$

where $q = \frac{\mathrm{Pr}_f \mathrm{Re}_{sf,p}}{\tilde{\mathrm{Nu}}}$ and $\mathrm{Nu}_{sf,f}$ calculated based on film condition for the thermal conductivity (λ_f). The Stefan flow Reynolds number (Re_{sf}) is calculated based on particle surface condition while the Prandtl number (Pr) is calculated based on film condition.

It is clear that the volume averaged temperature must lie between the particle temperature (T_p) and the far-field temperature (T_∞). From the definition of the volume averaged temperature, as given by Eq. 25 (respectively Eq. 31), it can be shown that this is not the case when $V_{sf}/V_B < -0.5$. (This corresponds to a situation where there is a very strong *inward* Stefan flow.) This means that the expression given by Eq. 25 can not be used to define the volume averaged temperature for such a condition. Therefore, the volume averaged temperature is assumed to be equal to the far-field temperature when $V_{sf}/V_B < -0.5$. This means that,

$$\tilde{T} = \begin{cases} \frac{T_f + \frac{u_{sf}}{U_\infty} f(\mathrm{Re}_f) T_{sf}}{1 + \frac{u_{sf}}{U_\infty} f(\mathrm{Re}_f)} \quad \text{(Eq.31)} & \text{for } V_{sf}/V_B \geqslant -0.5, \quad (39) \\ T_\infty & \text{for } V_{sf}/V_B < -0.5, \quad (40) \end{cases}$$

where $f(Re_f)$ is calculated from Eq. 32 and $A = 0.4$.

To validate the model, the Nusselt number was calculated from the simulation with the conditions 1, 2, and 3 (see Table 1) including one negative Stefan flow case with $V_{sf}/V_B < -0.5$. Fig. 6 depicts the comparison between simulation results (symbols) and the predictions obtained with the model presented in Eq. (38) (lines).

The (relative) root-mean-square error (Eq. 36 after replacing the term C_d with Nu) with all the data in Fig. 6 was 12.6%. The error was relatively high for $T_p = 400$ K (Fig. 6a), with the maximum value reaching 73%. When only considering the data from the tem-

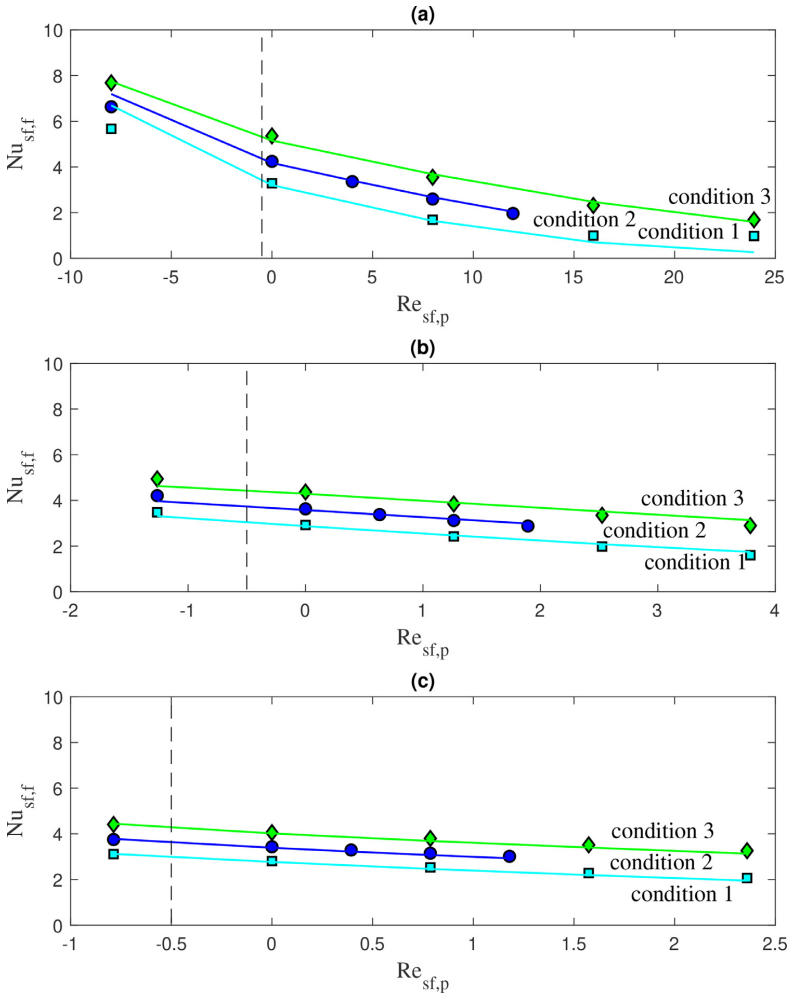

Fig. 6. The Nusselt number comparison between the model (Eq. 38-lines) and simulation (symbols) data with Stefan flow. Particle temperature (T_p) is (a) 400 K (b) 1200 K or (c) 1600 K. Condition 1: U_∞=0.5 m s^{-1}and D=1.0 mm. Condition 2: U_∞=3.0 m s^{-1}and D=0.5 mm. Condition 3: U_∞=3.0 m s^{-1}and D=1.0 mm.

perature difference of 200 K (Fig. 6b-c), the maximum relative error of the model was 9% and the root-mean-square error was 3.8%.

The model is developed for calculating the Nusselt number for a spherical particle with uniform Stefan flow, immersed in a uniform convective flow. It was validated for the Reynolds number (Re_f) $2 \leqslant \mathrm{Re}_f \leqslant 30$, Stefan Reynolds number ($\mathrm{Re}_{sf,p}$) $-8 \leqslant \mathrm{Re}_{sf,p} \leqslant 25$ and temperature range 400 K-1600 K for nitrogen gas atmosphere. The parameters for the Nusselt number without Stefan flow (Eq. 37) were estimated by fitting the simulation data presented in this study. Different sets of parameters might be applicable for different Reynolds number and temperature ranges.

The model for the drag coefficient and the Nusselt number were both developed by assuming that the change in temperature inside the boundary-layer occurs due to variations in Stefan flow velocity, Stefan flow temperature and far-field temperature alone. This would not be the case when there are other phenomena that affect the boundary-layer temperature, such as e.g., homogeneous reactions. The model is based on the assumption that the pressure force and the viscous force are of the same order of magnitude and that only the viscous force is affected by the Stefan flow (see Jayawickrama et al. (2019)). This might not be true for higher Reynolds numbers.

5. Conclusions

The effect of a Stefan flow on the drag coefficient and Nusselt number was studied for a uniform flow around a spherical particle. The effect was investigated at non-isothermal conditions using resolved numerical simulations. Particle diameter, slip velocity, particle temperature, and Stefan flow velocity from/to the particle have been varied during the simulations. The range of Stefan Reynolds number of $-8 \leqslant \mathrm{Re}_{sf,p} \leqslant 25$, Reynolds number of $2 \leqslant \mathrm{Re}_f \leqslant 30$ and particle temperatures (T_p) of 400 K, 1200 K and 1600 K were considered in the simulations. The far-field temperature (T_∞) was kept constant at 1400 K.

The sensitivity of the drag coefficients on the Stefan flow was significantly different between isothermal and non-isothermal conditions. The effect of variation in thermophysical properties, especially at high temperature differences (between particle and far-field), is emphasized. This difference makes isothermal models less accurate for estimation of the drag coefficient.

Our previous model, developed for the drag coefficient with Stefan flow at isothermal conditions, therefore was modified for non-isothermal conditions. The refined model (presented in Eq. 33) introduced the volume averaged film temperature ($\tilde{T}$) to describe the change of thermophysical parameters in the boundary layer by a Stefan flow under non-isothermal conditions. The model is based on the physical interpretations and shows a good agreement with the simulation data. It kept the number of fitting parameter to one, which represents the relationship between the boundary layer thickness and the particle Reynolds number.

Similarly, a new model (see Eq. (38)) that describes the effect of a Stefan flow on the Nusselt number was developed by using the volume averaged temperature ($\tilde{T}$) in combination with models that describe convective flow effects and Stefan flow effects on the Nusselt number. The model agrees well with the simulation data with a single fitting parameter, which represents the relationship between boundary layer thickness and particle Reynolds number.

Declaration of Competing Interest

The authors declare that they have no known competing financial interests or personal relationships that could have appeared to influence the work reported in this paper.

CRediT authorship contribution statement

Thamali R. Jayawickrama: Conceptualization, Methodology, Software, Validation, Formal analysis, Writing - original draft, Visualization. **Nils Erland L. Haugen:** Conceptualization, Writing - review & editing, Supervision, Funding acquisition. **Matthaus U. Babler:** Writing - review & editing, Supervision, Funding acquisition. **M.A. Chishty:** Writing - review & editing, Supervision. **Kentaro Umeki:** Conceptualization, Methodology, Resources, Writing - review & editing, Supervision, Project administration, Funding acquisition.

Acknowledgment

The authors are grateful to the Swedish Research Council (Vetenskapsrådet) for financial support for the study (grant number: 2016-07213). The simulations were performed on resources, *Kebnekaise*, provided by the Swedish National Infrastructure for Computing (SNIC) at High Performance Computing Center North (HPC2N). The authors thank all the staff of HPC2N for the technical assistance and specially to Pedro Ojeda May for the support with OpenFOAM. Furthermore, M.U.B. thanks the Swedish for Gasification Center and its industrial and academic partners for financial suppport. N.E.L.H. acknowledge the Research project Gaspro, financed by the research council of Norway (267916) the European Union's Horizon 2020 research and innovation programme(No 764697). This work also benefitted from computer resources made available through Norwegian NOTUR program, under award NN9405K.

Appendix A. Gas properties

Variation of thermal and physical properties of nitrogen (N_2) with temperature were calculated as follows. Specific heat capacity(c_p) is calculated by NASA polynomials:

$$c_p = R_{c_p}(a_0 + a_1T + a_2T^2 + a_3T^3 + a_4T^4 + a_5/T + a_6/T^2), \quad \text{(A.1)}$$

Table A.5
Coefficients for calculation of heat capacity (c_p) of gas.

Coefficient	$T < 1000$ K	$T > 1000$ K
a_0	3.29868	2.92664
a_1	0.00140824	0.00148798
a_2	-3.96322×10^{-6}	-5.68476×10^{-7}
a_3	5.64152×10^{-9}	1.0097×10^{-10}
a_4	-2.44486×10^{-12}	-6.75335×10^{-15}
a_5	-1020	-922.798
a_6	3.95037	5.98053

where a_0, a_1, a_2, a_3, a_4, a_5, a_6 are one set of constants for $T > 1000$ K and another set of constants for $T < 1000$ K. R_{c_p} (=296.8048) is a constant (Table A.5).

Dynamic viscosity(μ) is calculated from Sutherland formula (Sutherland, 1893):

$$\mu = 1.67212 \times 10^{-6}\sqrt{T}/(1 + 170.672/T), \quad \text{(A.2)}$$

where μ is in Pa.s and T is in K. Density (ρ) is calculated from state equation with constant pressure;

$$\rho = pM/RT, \quad \text{(A.3)}$$

where M is the molecular weight (28.01 g/mol), p atmospheric pressure (101325 Pa) is and R is the gas constant. Thermal conductivity (λ) is calculated from following model:

$$\lambda = 4.8 \times 10^{-4}T^{0.717}, \quad \text{(A.4)}$$

where λ is in W/(K.m) and T is in K.

References

Abramzon, B., Sirignano, W.A., 1989. Droplet vaporization model for spray combustion calculations. International Journal Heat Mass Transfer 32 (9), 1605–1618.
Constant, E., Favier, J., Meldi, M., Meliga, P., Serre, E., et al., 2017. An immersed boundary method in OpenFOAM: Verification and validation. Computers and Fluids doi:10.1016/j.compfluid.2017.08.001.
Downingm, C.G., 1966. The evaporation of drops of pure liquids at elevated temperatures: Rates of evaporation and wet-bulb temperatures. AIChE Journal 12 (4), 760–766. doi:10.1002/aic.690120424. arXiv:1011.1669v3.
Eisenkalam, P., Arunachalam, S.A., Westen, J.A., 1967. Evaporation rates and drag resistance of burning drops. In: Eleventh Symposium (International) on Combustion, Vol. 11, pp. 715–728.
Ellendt, N., Lumanglas, A.M., Moqadam, S.I., Mädler, L., 2018. A model for the drag and heat transfer of spheres in the laminar regime at high temperature differences. International Journal of Thermal Sciences 133, 98–105. doi:10.1016/j.ijthermalsci.2018.07.009.
Fadlun, E.A., Verzicco, R., Orlandi, P., Mohd-Yusof, J., 2000. Combined Immersed-Boundary Finite-Difference Methods for Three-Dimensional Complex Flow Simulations. Journal of Computational Physics 161, 35–60. doi:10.1006/jcph.2000.6484.
Harpole, G.M., 1981. Droplet Evaporation in High Temperature Environments. Jouranl of Heat Transfer 103, 86–91.
Jasak, H., Rigler, D., Tukovic, Z., 2014. Design and implementation of Immersed Boundary method with discrete forcing approach for boundary conditions. In: proceedings of 6th European Congress on Computational Fluid Dynamics - ECFD VI, Barcelona, Spain, pp. 5319–5332.
Jayawickrama, T.R., Haugen, N.E.L., Babler, M.U., Chishty, M.A., Umeki, K., 2019. The effect of Stefan flow on the drag coefficient of spherical particles in a gas flow. International Journal of Multi-phase Flow 117, 130–137. doi:10.1016/j.ijmultiphaseflow.2019.04.022.
Johnson, T.A., Patel, V.C., 2017. Flow past a sphere up to a Reynolds number of 300. J. Fluid Mech 378, 19–70. doi:10.1017/S0022112098003206.
Kestel, M., 2016. Numerical Modeling of Moving Carbonaceous Particle Conversion in Hot Environments. TU Bergakademie Ph.D. thesis.
Kreitzberg, T., Pielsticker, S., Gvert, B.M., Kneer, R., 2016. CO2 and H2O Gasification under Chemically and Diffusion Controlled Conditions. In: 33rd Annual International Pittsburgh Coal Conference, Cape Town.
Li, T., Niu, Y., Wang, L., Shaddix, C., Løvås, T., et al., 2018. High temperature gasification of high heating-rate chars using a flat-flame reactor. Applied Energy 227, 100–107. doi:10.1016/j.apenergy.2017.08.075.
Miller, R.S., Bellan, J., 1999. Direct numerical simulation of a confined three-dimensional gas mixing layer with one evaporating hydrocarbon-droplet-laden stream. J. Fluid Mech 384, 293–338.
Mittal, R., Iaccarino, G., 2005. Immersed Boundary Methods. Annual Review of Fluid Mechanics 37 (1), 239–261. doi:10.1146/annurev.fluid.37.061903.175743.
Murphy, J.J., Shaddix, C.R., 2003. Effects of Stefan Flow on Heat Transfer from reacting Carbon particles. Sandia-Report 2003-8720J 1–24.

Naraslmhan, C., Gauvin, W.H., 1967. Heat and Mass Transfer to Spheres in High Temperature Surroundings. The Canadian journal of Chemical Engineering 45, 181–188.
Niazmand, H., Renksizbulut, M., 2003. Transient three-dimensional heat transfer from rotating spheres with surface blowing. Chemical Engineering Science 58, 3535–3554. doi:10.1016/S0009-2509(03)00191-X.
Nikrityuk, B., Meyer, P.A., 2014. Gasification Processes Modeling and Simulation, 1 Wiley-VCH.
Ranz, W.E., Marshall, W.R., 1952. Evaporation from drops. Chemical Engineering Progress 48 (3), 141–146.
Renksizbulut, M., Yuen, M.C., 1983. Experimental study of droplet evaporation in a high-temperature air stream. Journal of Heat Transfer 105, 384–388.
Renksizbulut, M., Yuen, M.C., 1983. Numerical Study of Droplet Evaporation in a High-Temperature Stream. Journal of Heat Transfer 105 (2), 389–397. doi:10.1115/1.3245591.
Richter, A., Nikrityuk, P.A., 2012. Drag forces and heat transfer coefficients for spherical, cuboidal and ellipsoidal particles in cross flow at sub-critical Reynolds numbers. International Journal of Heat and Mass Transfer 55 (4), 1343–1354. doi:10.1016/j.ijheatmasstransfer.2011.09.005.
Schiller, L., Naumann, A., 1935. A drag coefficient correlation. Zeitschrift des Vereins Deutscher Ingenieure 77, 318–320.
Sepman, A., Ögren, Y., Qu, Z., Wiinikka, H., Schmidt, F.M., et al., 2017. Real-time in situ multi-parameter TDLAS sensing in the reactor core of an entrained-flow biomass gasifier. Proceedings of the Combustion Institute 36 (3), 4541–4548. doi:10.1016/j.proci.2016.07.011.
Sutherland, W., 1893. The viscosity of gases and molecular force. Philosophical Magazine 507–531.
Umeki, K., Kirtania, K., Chen, L., Bhattacharya, S., et al., 2012. Fuel Particle Conversion of Pulverized Biomass during Pyrolysis in an Entrained Flow Reactor. Industrial & Engineering Chemistry Research 51, 13973–13979. doi:10.1021/ie301530j.
Weller, H.G., Tabor, G., Jasak, H., Fureby, C., 1998. A tensorial approach to computational continuum mechanics using object-oriented techniques. Computers in Physics 12, 620–631. doi:10.1063/1.168744.
Whitaker, S., 1972. Forced Convection Heat Transfer Correlations for Flow in Pipes, Past Flat Plates, Single Cylinders, Single Spheres, and for Flow in Packed Beds and Tube Bundles. AIChE Journal 18, 361–371.
Yu, J., Zhou, K., Ou, W., 2013. Effects of Stefan flow and CO oxidation on char particle combustion in O2/CO2 atmosphere. Fuel 106, 576–585.
Yuen, M.C., Chen, L.W., 1976. On drag of evaporating liquid droplets. Combustion Science Technology 14, 147–154.
Yuen, M.C., Chen, L.W., 1978. Heat-transfer measurements of evaporating liquid droplets. International Journal of Heat and Mass Transfer 21 (5), 537–542. doi:10.1016/0017-9310(78)90049-2.
Zhifu, Z., Guoxiang, W., Bin, C., Liejin, G., Yueshe, W., 2013. Evaluation of Evaporation Models for Single Moving Droplet with a High Evaporation Rate. Powder Technology 240, 95–102. doi:10.1016/j.powtec.2012.07.002.

Appendix C

Paper III

The effects of Stefan flow on the flow surrounding two closely spaced particles

Thamali R. Jayawickrama[a,1], M. A. Chishty[a], Nils Erland L. Haugen[a,b], Matthaus U. Babler[c], Kentaro Umeki[a]

[a]*Energy Engineering, Div. Energy Science, Luleå University of Technology, 971 87 Luleå, Sweden*
[b]*Department of Thermal Energy, SINTEF Energy Research, Kolbjørn Hejes vei 1 A, 7491 Trondheim, Norway*
[c]*Department of Chemical Engineering, KTH Royal Institute of Technology, SE-10044 Stockholm, Sweden*

Abstract

The aim of the work was to study the effects of neighboring particles with uniform Stefan flow in particle-fluid flows. Particle-resolved numerical simulations were carried out for particles emitting a uniform Stefan flow into the bulk fluid. The bulk fluid was uniform and isothermal. The Stefan flow volume emitted from the two particles is equal, such that it represents idealized conditions of reacting particles. Particles were located in tandem arrangement and particle distances were varied between 1.1 and 10 particle diameters ($1.1 \leq L/D \leq 10$). Three particle Reynolds numbers were considered during the simulations ($Re = 2.3, 7$ and 14) which is similar to our previous studies. Three Stefan flow velocities were also considered during simulations to represent inward, outward and no Stefan flow. The drag coefficient of the particles without Stefan flow showed that the results fit with the previous studies on neighbor particle effects. When the particle distance is greater than 2.5 diameters($L/D > 2.5$), Stefan flow and neighboring particle effects affect independently, i.e. outward Stefan flow decreases the drag coefficient (C_D) while inward Stefan flow increases it and *upstream* particle has a higher C_D than the *downstream* particle. When $L/D \leq 2.5$, effect of Stefan flow is dominant and, equal and opposite pressure forces acting on the particles which repels each other. Pressure force showed a large increase compared to

[1]Corresponding author. thamalirajika@gmail.com

the viscous force at these distances. The effect of Stefan flow is weakened at higher Reynolds numbers.

Keywords: Drag coefficient, Stefan flow, Neighboring particles, Boundary layer, multiphase reactive flow

1. Introduction

For an isolated particle in a highly dilute flow, accurate expressions for heat, mass and momentum transfer between particle and fluid is well known. This is not, however, the case for particle neighbors, which indirectly influence each other over distance of several particle diameters through their exchange of heat, mass and momentum with the fluid. As a result, the heat, mass and momentum transfer between the fluid and a given particle, may be significantly modified due to the presence of another particle in its vicinity. Understanding the physics behind these effects is therefore important for applications such as droplet evaporation, particle drying and pulverized fuel combustion/gasification.

Droplet evaporation and combustion are complex phenomena involving various interactions such as reaction/phase change, changes to thermophysical properties, droplet break-up and collisions, particle-fluid interactions and many more. A lot of scientific effort based on numerical simulations in droplet evaporation and combustion has exerted more towards creating more realistic conditions, especially chemical reactions in arrays of particles [1, 2, 3, 4, 5]. Work related to droplet evaporation is not discussed here and recent developments can be found in [2, 6]. There are some work also on coal/char combustion simulations with multiple neighboring particles (See for example [7]). Sayadi et al. [7] have investigated the effects of the position of a particle in an array on the char combustion behavior. They have found that particles facing the incoming flow has the highest burning rate, and that the burning rate drops in consecutive particle rows. This effect is stronger when the distance between rows is less than three particle diameters. However, these studies do not provide the fundamental information that is necessary to explain the phenomena causing these effects.

Interactions among particles play a crucial role in non-diluted particle-fluid flows. Particle flows can be categorized into isolated particles, particle arrays, particle streams and particle clouds [8]. In case of very dilute

particle concentrations, a particle can be considered as isolated. Interactions between a bulk fluid and an isolated particle immersed in it are well studied. However, it is clear that individual particles cannot be approximated as isolated in many practical applications, such as e.g. packed and fluidized beds. Furthermore, it is also true that even in significantly more dilute flows, as can be found for example in entrained flow gasifiers or pulverized burners, where particle volume fractions are very low ($10^{-2} - 10^{-4}$) and particle separation distances are high ($L/D \approx 10$) [9, 10], the isolated particle approximation fails. Particle interactions can be categorized in two categories, where particle-particle interactions are direct collisions between particles, while particle-fluid-particle interactions are interactions where the fluid transmit the effect of one particle to another particle (such as the effect of the boundary layer of one particle on a neighboring particle's boundary layer). Particle-fluid-particle interactions are important in arrays, clouds and streams of particles. Lots of work has been done related to particle interactions in structured arrays and particle clouds. However, most of those works are on non-reactive particles (i.e. without Stefan flows).

There are also many instances of reacting particles that create a Stefan flow on the particle surface, where the Stefan flow may be due to either heterogeneous reactions or phase change. The flow characteristics (local pressure and velocity, etc.) and interactions (momentum, heat and mass transfer) in particle-fluid flows can vary when a Stefan flow is present. The effect of a Stefan flow on an isolated particle has been studied by many researchers in the past and is summarized in recent work by Jayawickrama et al. [11, 12] and Chen et al. [13]. According to the literature, a Stefan flow has a strong effect on the drag coefficient and the heat transfer coefficient through its influence on the thickness of the boundary layer.

There are few studies dedicated to the effects of a Stefan flow on the boundary layer at closely spaced particles in a particle-fluid flow [13, 14, 15]. Chen et al. [13] studied the effect of a Stefan flow on the flow past a random array of spheres. They observed that the effect of a Stefan flow is weakened with increased solid volume fraction. This happens due to suppression of the boundary layer thickening created by an outward Stefan flow compared to an isolated particle.Du et al. [14] have studied the effect of Stefan flow on the drag force of a single reactive particle surrounded by inert particles. In addition to the observations of of Chen et al. [13], Du et al. [14] have observed that the reduction of the drag force decreases as Re increases and variation of Re has negligible effects on the reacting particle drag coefficient

(C_D) at the solid volume fraction above 0.5. Here, Re is particle Reynolds number calculated as follows:

$$\mathrm{Re} = \frac{\rho U D}{\mu}, \tag{1}$$

where ρ is fluid density, U is slip velocity between a particle and bulk fluid, D is particle diameter and μ is fluid viscosity. $\mathrm{Re_{Sf}}$ can be calculated by replacing U with Stefan flow velocity, U_{Sf} in Eq. 1. Further, Du et al. [14] have also developed a model to calculate the drag coefficient for a reacting particle surrounded by a sea of inert particles. Wang et al. [15] have studied the effect of a Stefan flow on two particles with the Stefan flow in different particle separation and relative orientation between two particles in supercritical water. They have studied 10 $\leq$Re$\leq$ 200, with the distance between two particles in the range of high particle concentrations ($1 \leq L/D \leq 3$) and 0 $\leq \mathrm{Re_{Sf}} \leq$ 3. They observed that the Stefan flow reduces Nu and C_D. Chen, Du and Wang all have studied quite high solid volume fractions (0.03-0.5), applicable for fluidized-bed conditions. Furthermore, the Reynolds number range studied by Wang et al. [15] was much greater (Re$>$ 10) than the values observed in conditions relevant for combustion and gasification of pulverized solid fuels [16, 17, 18].

All the studies on effects of neighboring particles with Stefan flow (reactive flows) have investigated flows at high particle concentrations that are relevant to fluidized-bed applications ($L/D \leq 3$). Investigations at intermediate and low volume fractions are important for other applications such as pulverized fuel combustion/gasification. Llamas et al. [10] have shown that for pulverized biomass gasification, individual particles are likely to interact with only one or a few particles in vicinity [10]. Therefore, it is important to understand how an isolated pair of reacting particles behave compared to random arrays of reacting particles. As an example, entrained flow biomass gasification (EFBG) has low particle Re ($0 < \mathrm{Re} \leq 14$) and similar magnitudes of $\mathrm{Re_{Sf}}$. The detailed effects in such conditions have not been studied earlier (most studies like Du et al. [14] have studied higher ranges of Reynolds number, i.e. Re > 10 and Re $>>$ $\mathrm{Re_{Sf}}$). Further, none of the studies on effects of Stefan flow with neighboring particles have investigated the details of pressure and viscous forces, and their contribution to the drag coefficient, which is a prerequisite in order to develop a physics based model describing the effects of Stefan flow and neighboring particles.

Different arrangements of two close particles can be considered as building

blocks for arrays with more particles. There are various theoretical, numerical, and experimental studies on the influence of particles located close to each other in different arrangements, like side by side, inline (tandem) and staggered. The main research findings on tandem arrangement can be summarized as follows [19, 20, 21]:

(i) the effect of neighboring particles is weakened at high particle Reynolds number (hereafter, simply referred as Reynolds number),
(ii) the effect of neighboring particles is less on the *upstream* particle compared to the *downstream* particle,
(iii) the sum of drag on both particles is less than twice the drag of an isolated particle,
(iv) the *upstream* particle drag is always higher than the drag on the *downstream* particle .

This work aims at studying the effect of Stefan flow on closely spaced particles in a uniform flow at low Reynolds number that is relevant for applications such as pulverized combustion/gasification. The main idea is to isolate the effect of the Stefan flow and the particle separation and, through this, to develop a deep understanding of the variation of the drag coefficient on each particle. The contribution of each force component on the drag coefficient will be studied to obtain the knowledge required to develop physics based models. This work would then be a starting point for developing such models in the future. To achieve this, two particles inline with each other are considered for different particle Reynolds numbers (Re), Stefan Reynolds numbers (Reynolds number calculated based on Stefan flow velocity ($\mathrm{Re_{Sf}}$)) and particle separation (L/D). Particle separations are varied from very close (L/D=1.1) to intermediate (L/D=10), which will be applicable for both dense and intermediate solid volume fractions.

2. Methodology

Numerical simulations were carried out for a flow around two static, spherical particles with constant size in a tandem arrangement (one behind the other as shown in Fig. 1). The incoming gas flow is uniform and isothermal. A uniform Stefan flow is given as a boundary condition at each particle surface. Different cases were simulated by varying the Reynolds number $\mathrm{Re} = \rho U_\infty D/\mu$, the Stefan Reynolds number $\mathrm{Re}_{Sf} = \rho U_{Sf} D/\mu$ and distance

between the two spherical particles (L/D). In these expressions, ρ is the fluid density, U_∞ is the fluid velocity at the inlet boundary of the domain (hereafter referred to as slip velocity), D is the particle diameter, μ is the dynamic viscosity of the fluid, U_{Sf} is the Stefan flow velocity and L is the center-to-center distance between the particles. The Reynolds number is within the limit of steady, axi-symmetric flow (Re < 210) [22] and the Mach number of the flow is well below 0.1. Therefore, the fluid is governed by the steady, incompressible, laminar flow equations, where mass conservation yields the continuity equation as:

$$\nabla \cdot \overrightarrow{u} = 0, \tag{2}$$

and momentum conservation results in,

$$(\rho \overrightarrow{u} \cdot \nabla) \overrightarrow{u} = -\nabla p + \mu \nabla^2 \overrightarrow{u}, \tag{3}$$

where $\overrightarrow{u}$ is the velocity vector, p is pressure, μ is dynamic viscosity and ρ is fluid density. Equations (2) and (3) are discretized with the finite volume method using second-order schemes. Readers are referred to our previous work for specification of boundary conditions, calculation of Stefan flow velocity and the immersed boundary method [11]. The only difference is that, there are now two solid particles in tandem instead of one.

Table 1: Parameter variation in the simulations.

Slip velocity U_∞ (m/s)	Particle diameter D (mm)	Particle separation L/D	Reynolds number Re
0.5	1.0	1.1, 1.5, 2.5, 5.0, 7.5, 10.0	2.3
3.0	0.5	1.1, 1.5, 2.5, 5.0, 7.5, 10.0	7
3.0	1	1.1, 1.5, 2.5, 5.0, 7.5, 10.0	14

2.1. Simulation conditions

The slip velocity (relative velocity between a particle and the bulk fluid), particle diameter and Stefan flow velocities for the simulations were selected based on pulverized combustion and entrained flow gasification conditions at atmospheric pressure[23, 18]. Details of velocity, diameter and distance between particles are shown in Table 1. The Stefan flow velocity was estimated

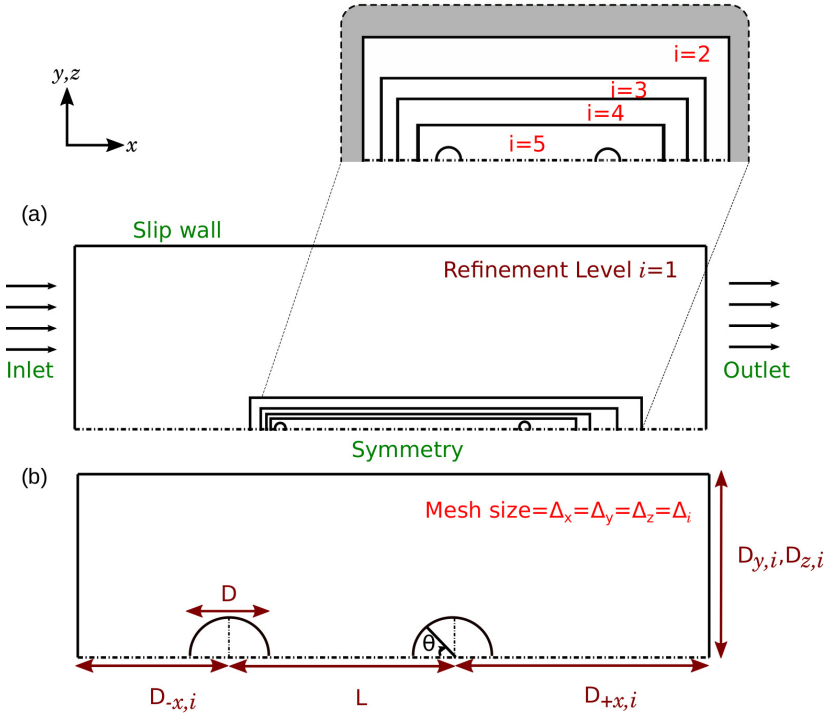

Figure 1: Computational domain for the simulations, with D denoting the particle diameter, and Δ_i, $i = 1$ to 5 representing the coarsest to finest mesh. $D_{-x,i}$ is the distance from the centre of the first sphere to the inlet and $D_{+x,i}$ is the distance from the centre of the second sphere to the outlet (See Table 2). $D_{y,i}$ is the distance from the symmetry line to the boundary in the lateral direction.

Table 2: The sizes and resolutions of the refinement regions in the computational domain (See Fig. 1).

i	$D_{-x,i}$	$D_{+x,i}$	$D_{y,i}, D_{z,i}$	Δ_i/D
1	16	48	32	0.32
2	3	6	3	0.16
3	2	5	2	0.08
4	1.5	3	1.5	0.04
5	1.2	2	1.2	0.02

based on data from devolatilization and char conversion of biomass [24, 23]. Three values of the Stefan flow velocity were considered, namely $U_{Sf} = -0.2$ m/s (inward Stefan flow), 0 m/s (no Stefan flow) and 0.6 m/s (outward Stefan flow). The Reynolds numbers are 2.3, 7 and 14. Since the Reynolds number is less than 20 in this study, the flow is steady and axisymmetric [22]. Therefore, only a quarter of the domain was simulated while symmetric boundary conditions were used at the boundaries with the other three parts.

We used the OpenFoam environment, called *foam-extend*-4.0 [25]. The numerical simulations were carried out using the same solver as in [11]; the incompressible, steady-state, immersed boundary code.

Based on the domain size and mesh refinement tests (see supplementary material), simulations presented in this work used domain 3 as defined in Table A.3, mesh refinement of the smallest mesh close to the particle of $0.02D$ (Level 5 in Fig. 1) and the mesh refinement region sizes as shown in Table 2. Figure 1 shows the details of the domain and mesh refinement regions used for all the simulations. A validation of the code used for the numerical simulations can be found in [11].

2.2. Estimation of the drag coefficient

The drag coefficient is calculated as [11]:

$$C_D = \frac{F_{P,x} + F_{visc,x}}{\frac{1}{2}\rho U_\infty^2 (\pi R^2)}, \tag{4}$$

where the pressure and viscous forces are given as

$$\overrightarrow{F}_P = \oint_S (P_{sur} - P_{ref})\overrightarrow{n}\, ds, \tag{5}$$

and

$$\overrightarrow{F}_{visc} = -\oint_S \mu(\nabla \overrightarrow{u} + \nabla \overrightarrow{u}^t)\overrightarrow{n}\, ds, \tag{6}$$

respectively. Here, the integration is over the surface S of the particle. In the above, P_{sur} and P_{ref} are the interpolated pressure at the particle surface and in the far-field, respectively, and $\overrightarrow{n}$ is the unit vector in the surface-normal direction. Only the components $\overrightarrow{F}_P$ and $\overrightarrow{F}_{visc}$ in the direction of the mean flow were accounted for when calculating the drag coefficient, since the other components are canceled out due to symmetry.

3. Results and Discussion

In this work, we have made a parameter study on the effect of two closely spaced particles on the surrounding fluid flow. The parameters are: 1) Stefan flow velocity (including direction), 2) Reynolds number, and 3) inter-particle distance. First, the effect on the boundary layer is shown through the velocity and pressure fields. Streamlines of the gas velocity are also studied around the two particles. Then, the total pressure and viscous forces on the two particles are investigated to clarify the contribution of each component on the total drag. Pressure and viscous forces are also presented at different positions around the particles to see how the effect of the Stefan flow vary with particle separation at different angular positions.

3.1. Variations on the pressure and velocity fields

3.1.1. Without Stefan flow

Figure 2 shows the relative pressure field around two neighboring particles with different separation for the case without a Stefan flow. The distance between the two particles is represented by the ratio of particle distance to particle diameter (hereafter, L/D ratio). Both *upstream* and*downstream* particles show regions with positive relative pressure in front of the particle and regions with negative relative pressure behind the particle. The effects of the *upstream* particle is visible on the *downstream* particle for all the L/D ratios considered in this work. The positive pressure region of the *downstream* particle shrink as the L/D ratio is lowered, while the negative pressure region display almost no difference. When $L/D < 2.5$, the pressure field around the *downstream* particle has just a very small area with positive pressure. Effects of the *downstream* particle on the *upstream* particle is visible for $L/D < 7.5$. Here, the positive pressure region is hardly affected while the negative pressure region behind the particle is reduced for decreasing particle separation.

Figure 3 shows the velocity contours in the mean flow direction around the particles without Stefan flow. Judging from the outer contour line for $0.8\ U_\infty$, the width of the velocity boundary layer reaches a maximum somewhere after the *downstream* particle. This maximum boundary layer width is slightly smaller for the low L/D ratio. As the L/D ratio decreases, the boundary layers of the two particles start merging. At $L/D \leq 1.5$, the velocity boundary layer from the two particles merge and resemble the boundary

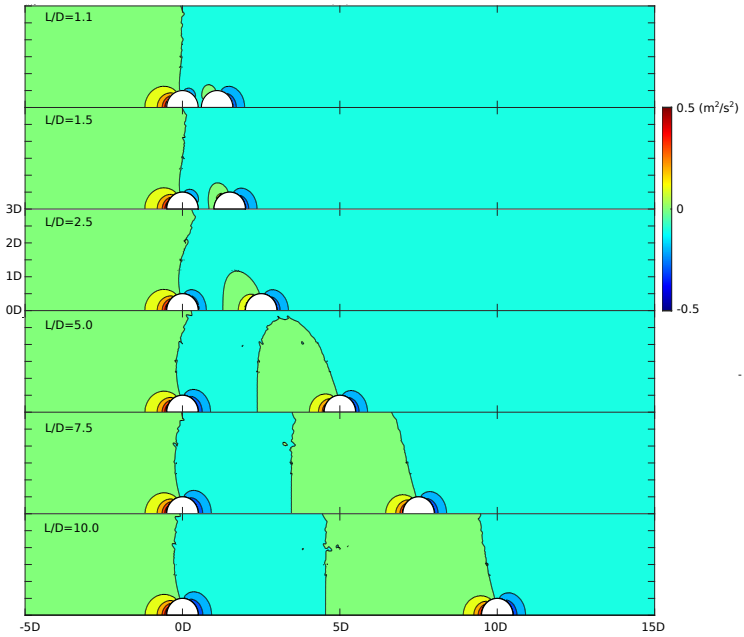

Figure 2: Pressure contours around particles with no Stefan flow and $Re = 2.3$. Pressure is shown as the difference from the reference pressure at the domain outlet. The colormap is adjusted to display positive pressure in green-to-red ranges and negative pressure in green-to-blue ranges.

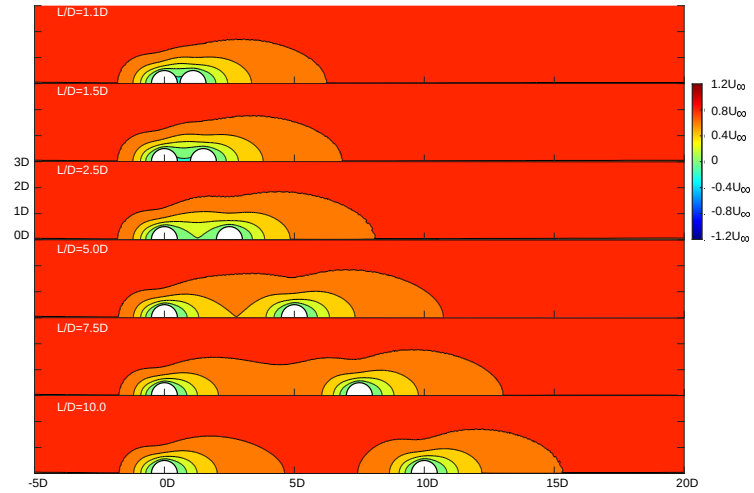

Figure 3: Velocity contours in the mean flow direction around the particles when there is no Stefan flow around the particle at $Re = 2.3$. Here contours start from $0U_\infty$, contour intervals are in $0.2U_\infty$ and far-field velocity is $1U_\infty$.

layer around one particle. There is no flow, or negligible fluid flow, between the particles.

3.1.2. With outward Stefan flow

Figure 4 compares the contour plots of velocity (in the mean flow direction) with and without outward Stefan flow. A clear difference is shown between the cases with and without a Stefan flow. There is a shared boundary layer between the two particles in all cases with an outward Stefan flow considered in this work. An outward Stefan flow makes the size of this boundary layer significantly larger. This could potentially lower the drag force on the particles compared to the drag previously found for an isolated particle [11].

The outward Stefan flow acts as a shield against the bulk flow and makes the velocity profiles around the two particles independent from each other. Streamlines shown in Fig. 5 clearly depict this shielding effect of the Stefan flow around the two particles. It shows the stagnation point between the two particles, which coincide with the point where the velocity magnitude is

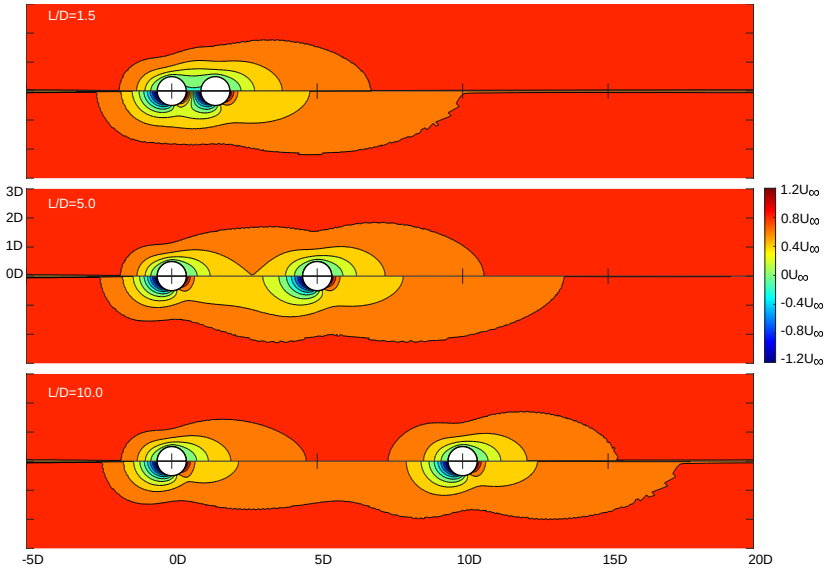

Figure 4: Velocity contours in the mean flow direction around the particles with $Re = 2.3$. The top half of each panel shows the cases without Stefan flow while the bottom half is cases with outward Stefan flow ($U_{Sf} = 0.62$ m/s corresponding to $Re_{Sf} = 2.9$). Here contours start from $0U_\infty$, contour intervals are in $0.2U_\infty$ and far-field velocity is $1U_\infty$.

zero, as also shown in Fig. 4. These observations suggest that the effect of neighbouring particles on the viscous force may become less important with the presence of an outward Stefan flow.

3.1.3. With inward Stefan flow

Figures 6 and 7 compares velocity contours (in the mean flow direction) and streamlines for cases with inward Stefan flow and without Stefan flow. Contrary to the case with outward Stefan flow, an inward Stefan flow makes the size of the boundary layer significantly smaller, both in width and length. This results in a steeper velocity gradient, potentially yielding a larger viscous force and thereby also a larger drag.

No obvious shielding effect between the two particles was observed with an inward Stefan flow. Inward Stefan flows have much smaller effects on the streamlines outside the particles. With inward Stefan flow, the zero velocity zone surrounding the particle surface disappeared. Nevertheless, mergers of the boundary layers of two particles were avoided with inward Stefan flow at low L/D ratios (See Fig. 6, $L/D = 1.5$). These observations imply the presence of an additional effect of Stefan flow with small particle distances (i.e. $L/D < 1.5$).

For inward Stefan flow, there is a separating streamline; flow inside this separating streamline ends up at the particle surface while flow outside will pass the two particles. Due to symmetry, the vertical distance y_∞ of this separating streamline follows as $y_\infty = (2U_{Sf}/U_\infty)^{1/2}D$.

3.2. Drag coefficient

Figure 8 shows the effect of the L/D ratio on the relative drag coefficient, normalized with the value of an isolated particle without Stefan flow. Here, the normalization coefficient corresponding to the drag coefficient of an isolated particle without Stefan flow is found from our previous work [11]. It can also calculated from Haider and Levenspiel model [26]:

$$C_d = \frac{24}{Re}(1 + 0.1806Re^{0.6459}) + 0.4251(1 + \frac{6880.95}{Re})^{-1}. \quad (7)$$

The data is shown for various Reynolds numbers and Stefan Reynolds numbers . The drag coefficient of two neighboring particles with a Stefan flow is clearly different from the drag coefficient of an isolated particle with a Stefan flow alone (mimics a reacting isolated particle) and the drag coefficient of

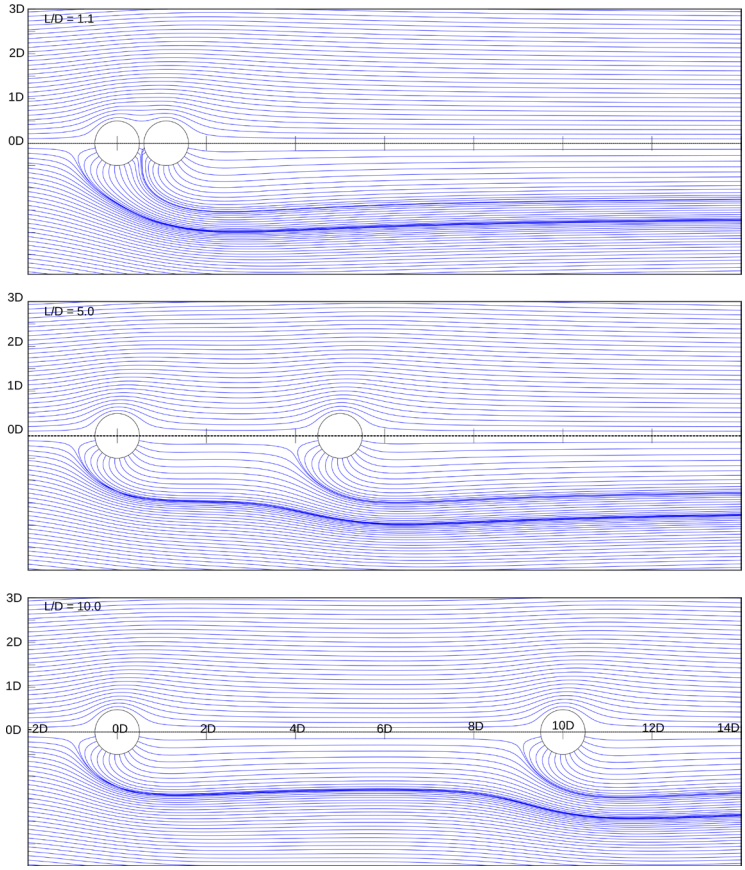

Figure 5: Streamlines surrounding the particles at $Re = 2.3$. The top half of each panel corresponds to the case without Stefan flow while the bottom half represent the case with outward Stefan flow ($U_{Sf} = 0.62$ m/s corresponding to $Re_{Sf} = 2.9$).

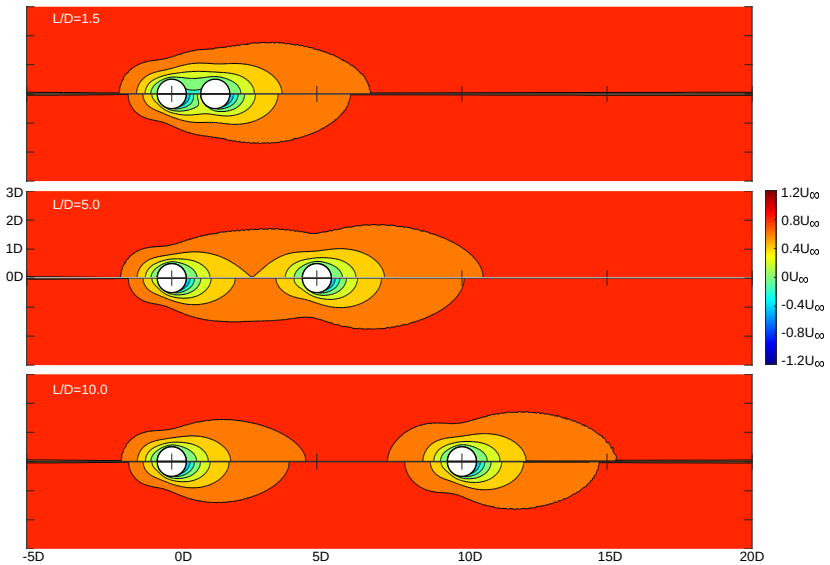

Figure 6: Velocity contours in the mean flow direction around the particles at $Re = 2.3$. Top half of each figure is velocity in the case without Stefan flow and the bottom half is the case with inward Stefan flow ($Re_{Sf} = -0.96$). Here contours start from $0U_\infty$, contour intervals are in $0.2U_\infty$ and far-field velocity is $1U_\infty$.

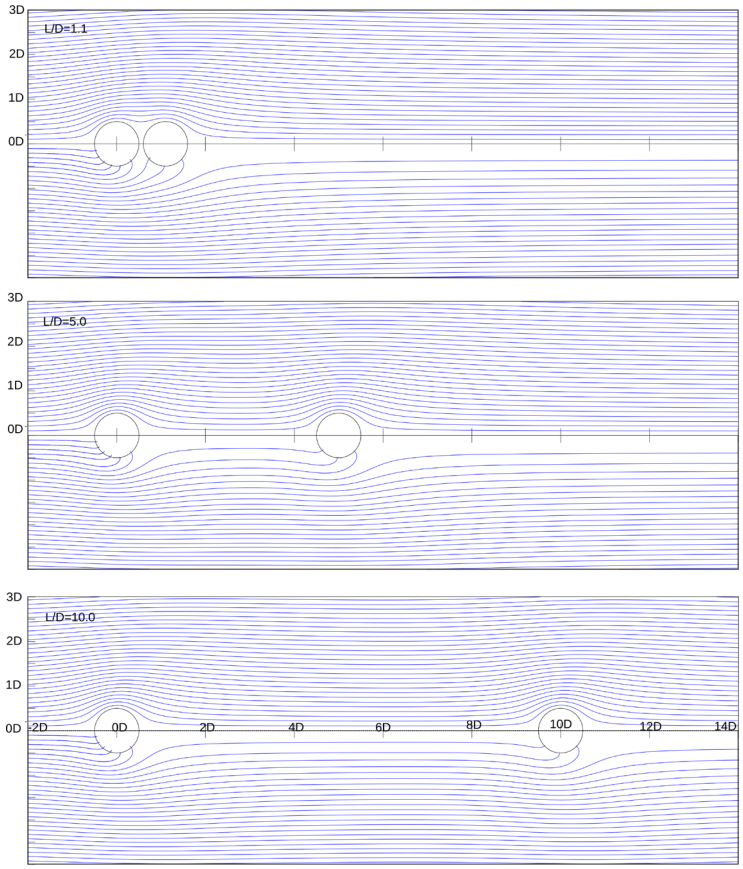

Figure 7: Streamlines surrounding the particles at $Re = 2.3$. Top half of each figure is the case without Stefan flow and the bottom half is the case with inward Stefan flow ($Re_{Sf} = -0.96$). Streamlines are uniform in the incoming flow but due to inward Stefan flow condition where volume flow rate interior to the particle depends on R^2, *downstream* particle reaches less number of streamlines.

two neighboring particles without a Stefan flow (mimics a non-reacting particle surrounded by other particles). Downstream particles have lower drag coefficient than isolated particles even at the largest particle distance investigated in this study (i.e., $L/D = 10$). The drag of *downstream* particles is affected more significantly by *upstream* particles at higher Reynolds number. The drag coefficient of *upstream* particles starts dropping when the particle distance is below $L/D \leq 5$ although this limit depends on the Reynolds number.

These results also agree with other studies [20, 21], i.e., when two particles are in tandem arrangement with another particle, both particles' drag coefficients are less than that of an isolated particle .

The effects of a Stefan flow can be seen by comparing the central figures of Fig. 8 (b,e,h) with the figures to the left (inward Stefan flow) and the right (outward Stefan flow). In general, for $L/D \geq 2.5$, the results agree with the previous studies [11, 2], that is; an outward (inward) Stefan flow decrease (increase) the drag coefficient. Except for the cases with $L/D < 2.5$, the drag coefficients of both *upstream* and *downstream* particles showed similar response to changes in the L/D ratios. As the L/D ratio increases, the drag coefficients of *upstream* particles become asymptotic to those of isolated particles with the same combinations of Re and Re_{Sf}. Although it is slowly approaching the asymptotic values, the drag coefficient of *downstream* particles do not reach that of isolated particles before $L/D = 10$. Stefan flow and neighboring particles seem to affect the drag independently for $L/D > 2.5$.

When the two particles are very close ($L/D < 2.5$), an outward Stefan flow increase the drag of *downstream* particle and reduce the drag of *upstream* particle significantly. This makes the drag of a *downstream* particle exceed that of an *upstream* particle. The point where this change happens depend on the Reynolds number, and potentially on the Stefan flow velocity as well. As shown in Fig. 8 (c,f,i), the effect is more significant at lower Reynolds number. At $Re = 2.3$ and $L/D = 1.1$, the *upstream* particle experienced negative drag, meaning that the net force on the particle is working against the bulk flow direction. At the same time, the drag ratio of the *downstream* particle exceeded one. This can be explained by the results discussed in section 3.1 (Figs. 2 and 3). When $L/D < 1.5$, the two particle behaved like a single particle and no flow from the bulk gas is observed between the particles. Therefore, the Stefan flow effect alone come into play in the volume between the two particles. The outward Stefan flow then results in

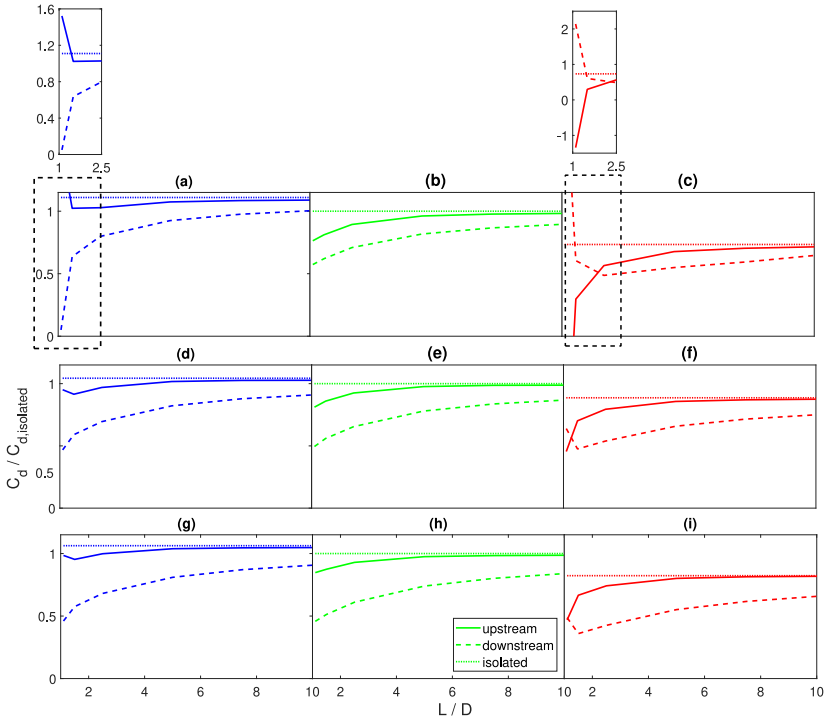

Figure 8: Relative drag coefficient, normalized with the value of an isolated particle without Stefan flow, as a function of the particle separation (L/D). (a-c) $Re = 2.3$; (d-f) $Re = 7$; (g-i) $Re = 14$. (a,d,g) $U_{Sf} = -0.2$ m s^{-1}; (b,e,h) $U_{Sf} = 0$ m s^{-1}; (c,f,i) $U_{Sf} = 0.6$ m s^{-1}. The drag coefficient of an isolated particle without Stefan flow can be calculated using the model of Haider and Levenspiel [26]: $C_d = \frac{24}{Re}(1+0.1806Re^{0.6459})+0.4251(1+\frac{6880.95}{Re})^{-1}$.

high pressure and large velocity gradient between two particles. As a result, the two particles repulses each other. This effect act in the opposite direction on the two particles, but with the same magnitude, as shown in Fig. 8.

The effect of inward Stefan flow show two distinct regimes based on the L/D ratios, similar to what was observed for outward Stefan flow. At high L/D ratios, the effects of Stefan flow and neighbouring particles were independent from each other. At small particle distances ($L/D < 1.5$), an inward Stefan flow increases the drag of the *upstream* particle and reduces that of the *downstream* particle considerably. This transition is similar to the one observed with outward Stefan flow, but the force is in the opposite direction, i.e., the two particles are attracting each other.

In most cases shown in Fig. 8 (except for $L/D < 1.5$), the drag coefficient of the *upstream* particle is always higher than that of the *downstream* particle and both *upstream* and *downstream* particle drag coefficients are positive (drag is in the mean flow direction). Hence, the distance between two particles in tandem will decrease with time if the two particles can move freely. Without a Stefan flow, it is expected that the two particles will eventually collide and either form aggregates or bounce off each other. However, repulsive forces via an outward Stefan flow will become significant at low L/D ratios. Especially at low Reynolds numbers (at least at Re$\leq$ 14), this force may overcome the inertia and particles may not come into physical contact. On the other hand, inward Stefan flows enhance the differences between the drag coefficients of the two particles and accelerate the attraction between them.

The relative importance of inertia over the viscous force increases at higher Reynolds number, resulting in thinner boundary layers. Similarly, the expansion of the boundary layer by an outward Stefan flow becomes less significant at higher particle Reynolds numbers. This difference can be observed by the distance to the stagnation point, as visualized in Fig. 5. As shown in Fig. 9, the stagnation distances significantly decrease as the Reynolds number increases. In addition, downstream particles exhibit longer stagnation distances than upstream particles, and this effect is enhanced as the particles come closer. Since the stagnation distance of the downstream particle cannot exceed the particle separation, high pressure and viscous forces are generated when the particle separation approach the stagnation distances.

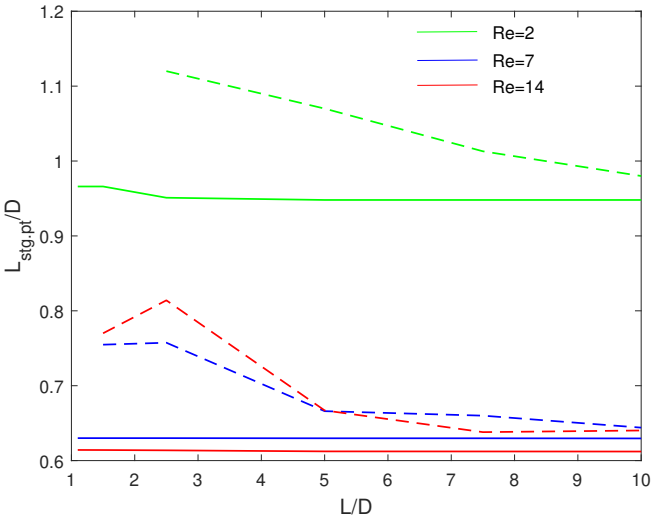

Figure 9: Stagnation point distance from the center of upstream and downstream particle for each Re and L/D with outward Stefan flow ($U_{Sf} = 0.6$ m/s). Solid lines represent upstream particles and dashed lines represent downstream particles.

3.3. Viscous and pressure forces

3.3.1. Overall forces

Figures 10 and 11 show total pressure force and viscous force on the particles for the same conditions as in Fig. 8. Both total viscous and total pressure forces have similar trends as those observed for the drag coefficients. The forces are reduced as the particle distance decrease (except for $L/D < 1.5$). An outward Stefan flow lower the viscous force while an inward Stefan flow increase the force. At $L/D < 1.5$, the effect of a Stefan flow on the forces differs from $L/D > 1.5$. For example, *downstream* particle viscous and pressure forces starts to increase at $L/D < 1.5$ with an outward Stefan flow, instead of following the decreasing trend observed for $L/D > 1.5$ (Fig. 10 and 11 c,f,i). The same effect can be observed on the *upstream* particle with an inward Stefan flow (Fig. 10 and 11 a,d,g).

Meanwhile, the relative changes of pressure and viscous force are quantitatively different from each other. Effects of neighbouring particles can be

observed more profoundly on pressure forces, judging from larger differences in the pressure forces between *upstream* and *downstream* particles. The effect of Stefan flow at low particle distance ($L/D = 1.1$) is also more notable in pressure force. With an outward Stefan flow, the normalized pressure force of the *downstream* particle is as high as 4 and that of the *upstream* particle is negative (≈ -3). The normalized viscous force at the same condition is about 1.5 for the *upstream* particle and about -0.5 for the *downstream* particle. The effect is less significant at higher Reynolds number. Similarly, the effect of an inward Stefan flow at $L/D = 1.1$ is more visible in the pressure force than in the viscous force.

The effects of a Stefan flow for $L/D > 1.5$ is more profound on the viscous force. Compared to the middle panels (Fig. 11 b,e,h), viscous force is shifted upwards for the left panels (Fig. 11 a,d,g) and downward for the right panels (Fig. 11 c,f,i). This means that an outward Stefan flow reduces viscous force while an inward Stefan flow increases viscous force. This behaviour agrees with previous studies [11]. The uniform Stefan flow velocity controls the velocity field around the particle and shifts the boundary layer away from the surface (See Fig.4 all the bottom figures), which reduces the viscous force on the particle. A deviation from this trend occurs when particles are very close. The reason is a total or partial blocking of the fluid flow between the particles. The Stefan flow will create high pressure and steep velocity gradients in that region, which affects the viscous and pressure forces.

3.3.2. Pressure and viscous stress at different angles

At both Reynolds numbers considered in Fig. 12 and Fig. 13, the local pressure force is higher than the local viscous force, i.e. the effect of a neighboring particle is mainly on the pressure force. When $Re = 2.3$ and $L/D = 1.1$, equal and opposite values of the viscous and pressure forces are observed at the back of the *upstream* particle and at the front of the *downstream* particle ((a) and (b) of Fig. 12). These equal and opposite forces are observed only in the pressure force for $Re = 14$ and $L/D = 1.1$ ((a) of Fig. 13). The effect of neighboring particles on the viscous force is not clear for $Re = 2.3$ and $L/D \geq 5$ ((d) and (f) of Fig. 12). However, the effect of neighboring particles on the viscous force is clearly visible at $Re = 14$ and $L/D \geq 5$ ((d) and (f) of Fig. 13). There is a clear net negative viscous force (repulsive) on the *upstream* particle with an outward Stefan flow when $Re = 2.3$ and $L/D = 1.1$. This is due to the high velocity gradients between the particles due to an outward Stefan flow with a velocity magnitude greater

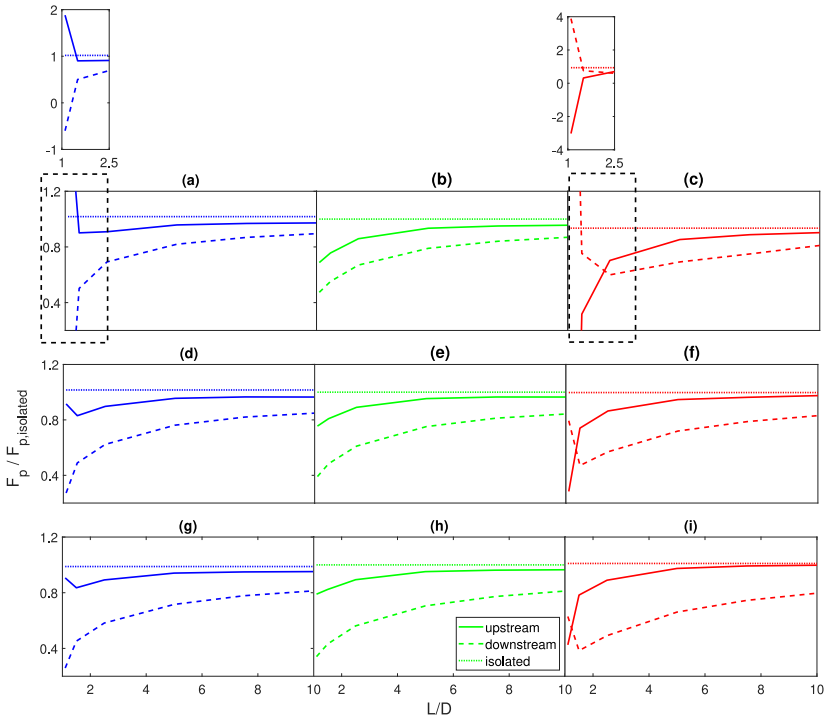

Figure 10: Total pressure force, normalized with the value of an isolated particle without Stefan flow, as a function of the distance between particles (L/D). (a-c) $Re = 2.3$; (d-f) $Re = 7$; (g-i) $Re = 14$. (a,d,g) $U_{Sf} = -0.2$ m s^{-1}; (b,e,h) $U_{Sf} = 0$ m s^{-1}; (c,f,i) $U_{Sf} = 0.6$ m s^{-1}.

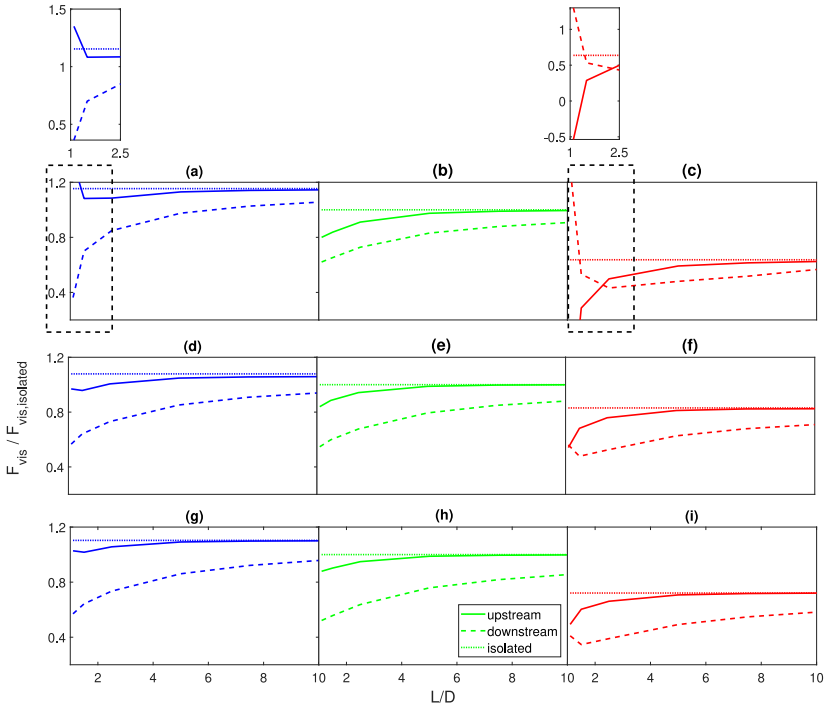

Figure 11: Total viscous force, normalized with the value of an isolated particle without Stefan flow, as a function of the distance between particles (L/D). (a-c) $Re = 2.3$; (d-f) $Re = 7$; (g-i) $Re = 14$. (a,d,g) $U_{Sf} = -0.2$ m s^{-1}; (b,e,h) $U_{Sf} = 0$ m s^{-1}; (c,f,i) $U_{Sf} = 0.6$ m s^{-1}.

than the far-field velocity ($U_{Sf} > U_\infty$).

As we have observed from our previous work, for a single spherical particle, the effect of Stefan flow mainly affects the viscous force, but not the pressure force, at $Re < 14$ [11]. However, Stefan flow effects are visible on the pressure force of the *downstream* particle ((c) and (e) of Figs. 12 and 13) as well. Therefore, existence of particle in *upstream* changes the effect of a Stefan flow on the *downstream* particle or relevance of a Stefan flow depends on the distance to other particles.

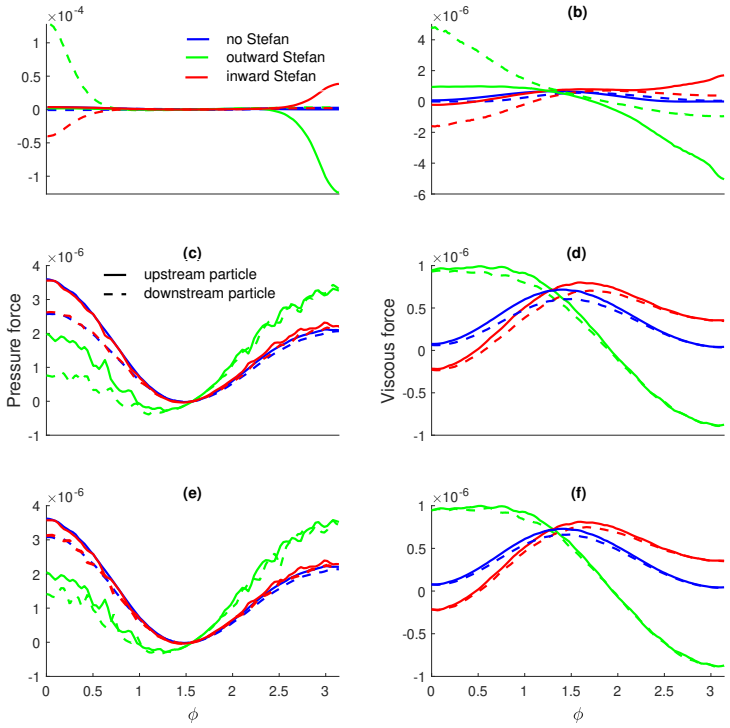

Figure 12: Pressure force components (a,c,e) and viscous force components (b,d,f) of a slice going through the center of the particle in the flow direction ($Re = 2.3$) as a function of angle (ϕ) at the particle surface. Angle 0 corresponds to the front of each particle. (a,b) $L/D = 1.1$; (c,d) $L/D = 5$; (e,f) $L/D = 10$. Solid lines: *upstream* particles; and dashed lines: *downstream* particle. Blue lines: without Stefan flow; green lines: outward Stefan flow; and red lines: inward Stefan flow.

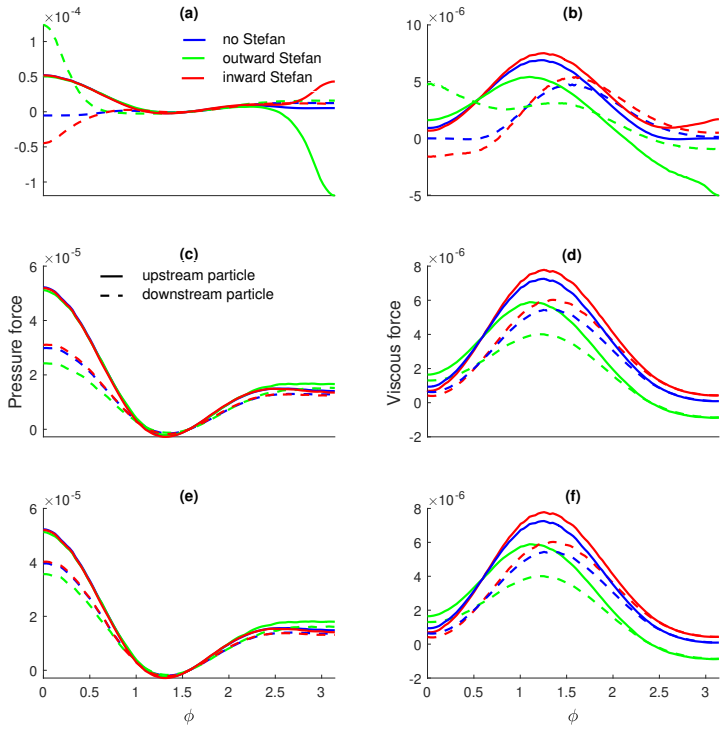

Figure 13: Pressure force components (a,c,e) and viscous force components (b,d,f) of a slice going through the center of the particle in the flow direction ($Re = 14$) as a function of angle (ϕ) at the particle surface. Angle 0 corresponds to the front of each particle. (a,b) $L/D = 1.1$; (c,d) $L/D = 5$; (e,f) $L/D = 10$. Solid lines: *upstream* particles; and dashed lines: *downstream* particle. Blue lines: without Stefan flow; green lines: outward Stefan flow; and red lines: inward Stefan flow.

4. Conclusions

In this study, we have carried out particle-resolved numerical simulations for two reacting particles in tandem arrangement with different distances between the particles. Reaction generated flow (Stefan flow) is considered either outward/inward uniform flow from/to the particle. Particle Reynolds number (Re), Stefan flow (Re_{Sf}) and particle distance has varied during simulations.

Without Stefan flow, the effect of an *upstream* particle on the *downstream* particle is not negligible for any of the particle distances and Reynolds numbers considered in this work ($Re = 2.3 - 14$ and $L/D = 1.1 - 10$). The effect of a *downstream* particle on the *upstream* particle can, however, be neglected when $L/D > 5$. When particles are very close to each other, the fluid flow between the particles is totally ($L/D < 1.5$) or partially ($1.5 < L/D < 2.5$) blocked by the *upstream* particle.

The combined effects of a Stefan flow and neighboring particles on the drag coefficient seem to work independently without any interaction for $L/D > 2.5$. An outward Stefan flow decreases the drag coefficients compared to the cases without a Stefan flow, while an inward Stefan flow increases drag coefficients. Similar to the effects on isolated particles, the effect of an outward Stefan flow on the drag coefficient can be explained by the expansion of the boundary layer and accompanying decrease in viscous force.

A deviation from the previous observations occur when $L/D < 2.5$ since the fluid flow is blocked between the *upstream* and the *downstream* particle. At these distances, the main role of an outward Stefan flow is to create a high pressure and viscous forces between the particles. An outward Stefan flow creates very high pressure in region between closely spaced particles, which results in a repulsive force between the two particles. In contrast, an inward Stefan flow produces an attractive force between the particles.

Acknowledgment

The computations and data handling were enabled by resources provided by the Swedish National Infrastructure for Computing (SNIC), partially funded by the Swedish Research Council through grant agreement no. 2018-05973. This research was conducted using the resources of High Performance Computing Center North (HPC2N). We thank for all the staff for the assistance with the technical and implementation aspects, which was made

possible through application support provided by SNIC. We would like to thank Swedish Research Council (SRC) for the funding to carry out this research. Furthermore, M.U.B. thanks the Swedish for Gasification Center and its industrial and academic partners for financial support. N.E.L.H. acknowledge the Research project Gaspro, financed by the research council of Norway (267916) the European Union's Horizon 2020 research and innovation program(No 764697). This work also benefitted from computer resources made available through the Norwegian NOTUR program, under award NN9405K.

References

[1] J. Wang, X. Huang, X. Qiao, D. Ju, C. Sun, Experimental study on evaporation characteristics of single and multiple fuel droplets, Journal of the Energy Institute 93 (4) (2020) 1473–1480. doi:10.1016/j.joei.2020.01.009.

[2] T. Kékesi, M. Altimira, G. Amberg, L. P. Wittberg, International Journal of Multiphase Flow Interaction between two deforming liquid drops in tandem and various off-axis arrangements subject to uniform flow, International Journal of Multiphase Flow 112 (2019) 193–218. doi:10.1016/j.ijmultiphaseflow.2018.11.009.

[3] H. A. Dwyer, P. Stapf, R. Maly, Unsteady vaporization and ignition of a three-dimensional droplet array, Combustion and Flame 121 (1-2) (2000) 181–194. doi:10.1016/S0010-2180(99)00138-8.

[4] M. S. Raju, W. A. Sirignano, Interaction between two vaporizing droplets in an intermediate Reynolds number flow, Physics of Fluids A 2 (10) (1990) 1780–1796. doi:10.1063/1.857705.

[5] W. A. Sirignano, Fluid Dynamics of Sprays1992 Freeman Scholar Lecture, Tech. rep. (1993).

[6] D. Stefanitsis, G. Strotos, N. Nikolopoulos, M. Gavaises, Numerical investigation of the aerodynamic breakup of a parallel moving droplet cluster, International Journal of Multiphase Flow 121 (2019) 103123. doi:10.1016/j.ijmultiphaseflow.2019.103123.

[7] T. Sayadi, S. Farazi, S. Kang, H. Pitsch, Transient multiple particle simulations of char particle combustion, Fuel 199 (2017) 289–298. doi:10.1016/j.fuel.2017.02.096.

[8] K. Annamalai, W. Ryan, Interactive processes in gasification and combustion. Part I: Liquid drop arrays and clouds, Progress in Energy and Combustion Science 18 (3) (1992) 221–295.

[9] B. Göktepe, K. Umeki, R. Gebart, Does distance among biomass particles affect soot formation in an entrained flow gasification process?, Fuel Processing Technology 141 (2016) 99–105. doi:10.1016/j.fuproc.2015.06.038.

[10] Á. D. García Llamas, N. Guo, T. Li, R. Gebart, T. Løvås, K. Umeki, Morphology and volume fraction of biomass particles in a jet flow during devolatilization, Fuel 278 (2020) 118241. doi:10.1016/j.fuel.2020.118241.

[11] T. R. Jayawickrama, N. E. L. Haugen, M. U. Babler, M. Chishty, K. Umeki, The effect of Stefan flow on the drag coefficient of spherical particles in a gas flow, International Journal of Multiphase Flow 117 (2019) 130–137. doi:10.1016/j.ijmultiphaseflow.2019.04.022.

[12] T. R. Jayawickrama, N. E. L. Haugen, M. U. Babler, M. A. Chishty, K. Umeki, The effect of Stefan flow on Nusselt number and drag coefficient of spherical particles in non-isothermal gas flow, International Journal of Multiphase Flow 140 (2021) 103650. doi:10.1016/j.ijmultiphaseflow.2021.103650.

[13] X. Chen, S. Du, L. Zhao, B. Yang, Q. Zhou, Effect of Stefan flow on the drag force in flow past random arrays of spheres, Chemical Engineering Journal 412. doi:10.1016/j.cej.2021.128691.

[14] S. Du, L. Zhao, X. Chen, B. Yang, Q. Zhou, Effect of Stefan flow on the drag force of single reactive particle surrounded by a sea of inert particles, Chemical Engineering Science (2022) 117546doi:10.1016/J.CES.2022.117546.

[15] Y. Wang, M. Zhang, H. Wang, H. Jin, The influence of Stefan flow on the flow and heat-transfer characteristics of spherical-particle pair in supercritical water, International Journal of Multiphase Flow 151 (2022) 104045. doi:10.1016/j.ijmultiphaseflow.2022.104045.

[16] B. Göktepe, A. H. Saber, R. Gebart, T. S. Lundström, Cold flow experiments in an entrained flow gasification reactor with a swirl-stabilized pulverized biofuel burner, International Journal of Multiphase Flow 85 (2016) 267–277. doi:10.1016/j.ijmultiphaseflow.2016.06.016.

[17] A. H. Saber, B. Göktepe, K. Umeki, T. S. Lundström, R. Gebart, Active fuel particles dispersion by synthetic jet in an entrained flow gasifier of biomass: Cold flow, Powder Technology 302 (2016) 275–282. doi:10.1016/j.powtec.2016.08.071.

[18] Á. D. G. Llamas, N. Guo, T. Li, R. Gebart, K. Umeki, Rapid change of particle velocity due to volatile gas release during

biomass devolatilization, Combustion and Flame 238 (2022) 111898. doi:10.1016/j.combustflame.2021.111898.

[19] C. Zhu, S.-c. Liang, L.-s. Fan, Particle wake effects on the drag force of an interactive particle, Tech. Rep. 1 (1994).

[20] L. Prahl, A. Jadoon, J. Revstedt, Interaction between two spheres placed in tandem arrangement in steady and pulsating flow, International Journal of Multiphase Flow 35 (10) (2009) 963–969. doi:10.1016/j.ijmultiphaseflow.2009.05.001.

[21] G. Wu, W. A. Sirignano, Transient convective burning of interactive fuel droplets in double-layer arrays, Combustion and Flame 158 (12) (2011) 2395–2407. doi:10.1016/j.combustflame.2011.04.011.

[22] T. A. Johnson, V. C. Patel, Flow past a sphere up to a Reynolds number of 300, J. Fluid Mech 378 (1999) 19–70. doi:10.1017/S0022112098003206.

[23] K. Umeki, K. Kirtania, L. Chen, S. Bhattacharya, Fuel Particle Conversion of Pulverized Biomass during Pyrolysis in an Entrained Flow Reactor, Industrial & Engineering Chemistry Research 51 (2012) 13973–13979. doi:10.1021/ie301530j.

[24] T. Kreitzberg, S. Pielsticker, B. M. Gvert, R. Kneer, CO2 and H2O Gasification under chemically and diffusion controlled conditions, in: 33rd Annual International Pittsburgh Coal Conference, Cape Town, 2016.

[25] H. G. Weller, G. Tabor, H. Jasak, C. Fureby, A tensorial approach to computational continuum mechanics using object-oriented techniques, Computers in Physics 12 (6) (1998) 620. doi:10.1063/1.168744.

[26] A. Haider, O. Levenspiel, Drag coefficient and terminal velocity of spherical and nonspherical particles, Powder technology 58 (1989) 63–70. doi:10.1016/0032-5910(89)80008-7.

AppendixA. Domain size and mesh refinement tests

In our previous work [11], we carried out simulations for an isolated spherical particle with a uniform Stefan flow immersed in a uniform, isothermal bulk fluid. The difference between our previous work and this work is the existence of one more particle in the streamwise direction. We used the same mesh refinemnet and the same mesh refinement region sizes of the previous work although the domain size should vary. Therefore, we tested different domain sizes, by varying both streamwise direction and transverse direction lengths. First, we added the length between the two particles (L/D) to the domain used in [11] and kept the same transverse length (domain 1 in Table A.3). Two more domains were also tested as shown in Table A.3. Domain test simulations were carried out for the lowest Reynolds number (Re=2.3) and highest outward Stefan flow case ($U_{Sf} = 0.6$), which generates the largest boundary layer around a particle based on our previous results [11, 12]. Drag coefficients obtained with the different domains were compared with the corresponding results from the largest domain (domain 2). Although domain 1 is smaller and still showed relatively small errors for drag coefficients, based on the velocity profiles around the two particles, domain 3 was selected for the simulations in this work. Drag coefficient results of different domains are shown in Table A.4.

The refinement of the mesh closest to the particle in the single particle simulations was 0.01D, which was too expensive for the bigger domain with two particles. Simulations were also carried out for the smallest possible boundary layer i.e: where the Reynolds number is highest and the Stefan flow is inward. Results of the mesh refinement tests are shown in Table A.5. It is crucial to check whether this refinement (number of mesh between the two particles) is sufficient for $L/D = 1.1$. Therefore, the drag coefficient was compared for $L/D = 1.1$ and Re=2.3, combined with either outward or no Stefan flow conditions, when the highest refinement is $0.01D$ and $0.02D$ (See Table A.6).

Table A.3: Domain test details where $L = 10$, Re=2.3 and $U_{Sf} = 0.624$. All the distances are in units of the particle diameter (D)

Domain	$D_{-x,1}$	$D_{+x,1}$	$D_{y,1}, D_{z,1}$
1	16	48	16
2	35	75	40
3	16	48	32

Table A.4: Domain size test for $Re = 2.3$, $L/D = 10$ and $U_{Sf} = 0.6$ with mesh refinement 0.02D at different domain sizes.

Domain	$C_{D,front}$	$C_{D,back}$	Error(% of domain 2)	
1	9.36	8.25	0.8	1.9
2	9.28	8.41	-	-
3	9.35	8.44	0.75	0.36

Table A.5: Mesh refinement test for $Re = 14$, $L/D = 2.5$ and $U_{Sf} = -0.2$.

refinement	0.04D		0.02D		0.01D		0.005-Richardson extrapolation	
particle	front	back	front	back	front	back	front	back
C_d	3.32	2.95	3.43	2.34	3.47	2.37	3.48	2.38
Error(% of 0.005D)	4.34	24.75	1.18	1.30	0.3	0.3	0	0

Table A.6: Mesh refinement test for $Re = 2.3$, $L/D = 1.1$ and $U_{Sf} = -0.6$ and $U_{Sf} = 0$.

refinement	0.02D		0.01D	
particle	front	back	front	back
$U_{Sf} = 0$				
C_d	9.98	7.49	10.13	7.58
Error(% of 0.01D)	1.48	1.19	0	0
$U_{Sf} = -0.623$				
C_d	-17.58	27.97	-17.67	28.81
Error(% of 0.01D)	0.51	2.92	0	0

Appendix D

Paper IV

Drag during heterogeneous char reactions: particle-resolved approach

Thamali R. Jayawickrama[a,1], Nils Erland L. Haugen[b,c], Matthaus U. Babler[d], M. A. Chishty[a], Kentaro Umeki[a]

[a] *Energy Engineering, Div. Energy Science, Luleå University of Technology, 971 87 Luleå, Sweden*
[b] *Department of Energy and Process Engineering, Norwegian University of Science and Technology, Kolbjørn Hejes vei 1 B, 7491 Trondheim, Norway*
[c] *Department of Thermal Energy, SINTEF Energy Research, Kolbjørn Hejes vei 1 A, 7491 Trondheim, Norway*
[d] *Department of Chemical Engineering, KTH Royal Institute of Technology, SE-10044 Stockholm, Sweden*

Abstract

Drag is one of the most important forces that affects the dynamics of particle-laden flow. Effects of Stefan flows (*i.e.,* flows generated by chemical reactions) on the drag are not well known, especially when intra-particle heat and mass transfer significantly influence the progress of heterogeneous reactions. The main objective of this work is to study how the effects of Stefan flow on drag is altered when heterogeneous reactions progress unevenly inside the particle. Particle resolved numerical simulations were used to solve flow fields, thermophysical parameters, and reaction rates inside and outside a particle undergoing a non-equimolar char gasification reaction ($C+CO_2 \rightarrow 2CO$). The drag coefficient (C_d) of the reacting particles has been calculated and compared with the same conditions without reactions. Two major findings are that: (1) the drag coefficients are higher than or close to the same case without reactions, and (2) the drag coefficients show complex variations at different stages of char conversion. Increase of the drag coefficient by Stefan flow is contradictory to the previous studies that imposed a uniform Stefan flow around a particle. Although the decrease of viscous force shown by previous studies is still valid in this study, significantly high pressure inside the particle and localized reactions at the front of particles increased the pressure

[1] Corresponding author. thamali.rajika.jayawickrama@ltu.se

force even further. At later stage of char conversion, the change in particle size and density (or porosity) also altered the drag coefficient. This effect is highly dependent on the effectiveness factor due to the difference in how uniform the reactions inside the particle progress.

Keywords: Char gasification, Drag coefficient, Stefan flow, reacting particle-laden flows

---

1. Introduction

Particle-laden flows appear in many important natural phenomena and technical applications. One example is coal and biomass combustion and gasification, which is an important conversion technology in energy processes. There are different factors affecting the interactions between fluid and particles in such flows. The interactions can be categorized into momentum, heat and mass exchange. In general, momentum exchange is represented by the drag coefficient (C_d), heat transfer by the Nusselt number (Nu), and mass transfer by the Sherwood number (Sh). These parameters (C_d, Nu, and Sh) are mainly affected by fluid conditions such as Reynolds number, particle concentration, and particle shapes, but heterogeneous and homogeneous reactions also affect them by modifying the fluid conditions in the boundary layer.

Heterogeneous reactions occur in many different particle-laden flows [1, 2, 3, 4, 5]. When a non-equimolar heterogeneous reaction occurs in a particle, either an outward or an inward flow is generated. This flow is called a *Stefan flow*. There are fewer studies on the effects of Stefan flows on reacting particles [1, 6] than on evaporating droplets [2, 5, 7, 8, 9]. In most cases, thermochemical properties of liquid droplets are relatively uniform inside the droplets and Stefan flows are therefore generated uniformly at their surfaces. This is not the case for reacting gas-solid flows because gas can penetrate inside the often anisotropic pore structures and locally non-uniform reactions potentially result in non-uniform Stefan flow. Therefore, the effect of Stefan flow on gas-solid interactions should be investigated by resolving both inside and outside the particles.

This study focuses on the effects of Stefan flow on the momentum exchange (represented by C_d). Some studies already investigated the effects of Stefan flows on isolated particles by numerical analyses [1, 4, 10, 11, 12]. Previous work [10, 12] showed that an outward Stefan flow decreases the

drag coefficient by expanding the velocity boundary layer. This leads to a low viscous component of the drag force, while the change in the pressure component of the drag force is negligible. The conditions investigated in these studies were $0.2 \leq \mathrm{Re} \leq 14$ and $0.2 \leq \mathrm{Re}_{Sf} \leq 14$, where Re is the Reynolds number of the particle based on the relative velocity between the particle and the surrounding fluid and $\mathrm{Re}_{\mathrm{Sf}}$ is the corresponding Reynolds number based on the velocity of the Stefan flow. Kestel [1] has studied the effect of Stefan flow on the drag coefficient under pressurized conditions and developed models for C_d and Nu for $\mathrm{Re} < 200$ and $\mathrm{Re}_{\mathrm{Sf}} < 20$. All the above studies used the assumption of uniform and isothermal Stefan flow and bulk fluid flow around the particle. Kurose et al. [11] further showed that the Stefan flow also affects the lift coefficient in a shear flow. Later, Jayawickrama et al. [4] developed models for drag and heat transfer (C_d and Nu) accounting for Stefan flows and non-isothermal conditions. Here, the Stefan flow was still considered to be uniform over the particle surface.

Apart from the uniform Stefan flow assumptions, the above studies neglect the multi-species nature of the bulk fluid. Farazi et al. [13] have studied the effect of Stefan flow on char particle combustion in an oxygen-enriched oxy-fuel environment. They found that the Stefan flow from the particle surface yields a lower drag force on the reacting particle compared with a non-reactive particle. Zhang et al. [14] have carried out particle resolved simulations for a burning char particle, considering both heterogeneous and homogeneous reactions. They observed that the drag coefficient increased with increasing heterogeneous and homogeneous reactions, which contradicts with previous work where explicit accounts for chemical reactions were not made. It calls for further investigations on the effects of Stefan flow with more detailed consideration to develop reliable subgrid models. Here, one should note that Zhang et al. [14] consider char combustion, which is an equimolar reaction with respect to gas species ($\mathrm{C} + \mathrm{O}_2 \rightarrow \mathrm{CO}_2$). Therefore, it represents the effects of species and temperature distributions without a Stefan flow. In addition, both Zhang et al. [14] and Farazi et al. [13] still do not resolve the temperature and gas flow inside the particle, which is a oversimplified assumption for the zone II conditions of char conversion. In most practical conditions, neither gas species nor reaction rates distribute uniformly throughout the particles [15, 16]. Therefore, it is necessary to resolve the particle interior in order to study the effects of potentially non-uniform reactions and Stefan flow.

Based on known shortcomings of existing studies identified above, this

work aims to investigate the effect of a Stefan flow on momentum transfer between a particle and bulk fluid for conditions relevant for entrained flow biomass gasification. Particle-resolved direct numerical simulations were carried out for porous particles undergoing heterogeneous reactions. To highlight the effects of Stefan flow, a non-equimolar heterogeneous reaction ($C + CO_2 \rightarrow 2CO$) was considered without gas-phase reactions.

2. Methodology

To investigate the effect of Stefan flow in particle-fluid flows during heterogeneous reactions, entrained flow biomass gasification (EFBG) is considered as a case study here. We have chosen to study char gasification process of EFBG in this work. More details about char gasification modeling can be found in these references [16, 17, 18, 19]. In this work, only the Boudouard reaction ($C + CO_2 \rightarrow 2CO$), which is a non-equimolar reaction, is considered as the gasification reaction between particle and gas to study the effects of the Stefan flow. In EFBG, pulverized particles are suspended in the bulk gas at particle concentrations below 0.001. Therefore, an isolated particle immersed in a uniform, non-isothermal bulk gas is considered here. Particle diameters and slip velocities in EFBG vary within the range of <1 mm and $0.1 - 3$ ms^{-1}, respectively [20]. Therefore, the same ranges are used for this work. The char particle is modeled as a porous media (See Fig. 1). Since there is no oxygen in the simulation domain, gas-phase reactions are neglected. This makes it easier to isolate effects due to the Stefan flow.

Particle Reynolds numbers considered here are equal or less than 3. Therefore, the flow around the cylindrical particles is axisymmetric and two-dimensional without flow separation, which is a valid assumption when the Reynolds number is less than 3.2 [21].

The following assumptions and simplifications were used for the simulations;

1. the particle is an infinitely long cylinder and consists only of ash-free carbon (no impurities)
2. the bulk fluid flow entering the simulation domain consists of only nitrogen (N_2) and carbon monoxide (CO_2).
3. the solid particle is stationary, and only the local porosity is increasing with the progress of the reaction,
4. the fluid is incompressible (variable density condition was used),

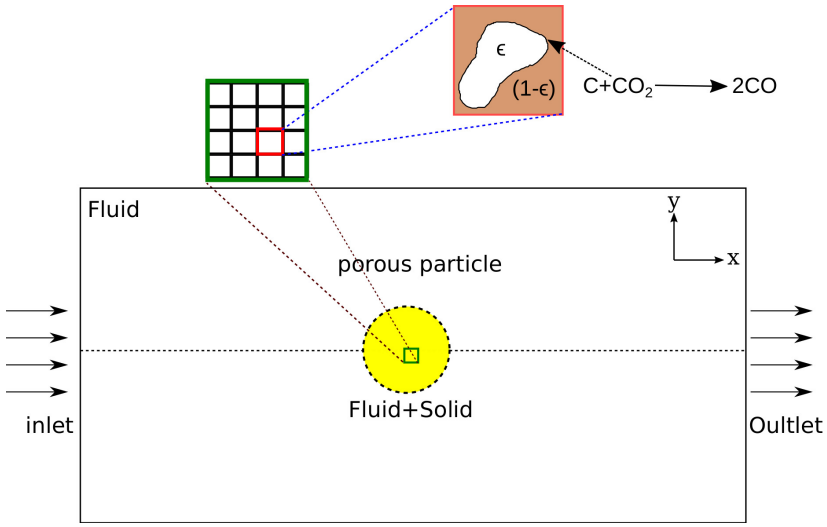

Figure 1: Overview of the case domain.

5. the gas and solid phases inside the particle are in local thermal equilibrium ($T_g = T_s$),
6. radiative absorption in the gas phase is neglected (i.e., particles exchange radiation directly with the reactor wall).

Inside the particle, the fluid flow follows Navier-Stokes equation with a resistance due to the existence of the solid phase. The resistance is calculated using Darcy-Forchheimer law [22, 23]. Further details of the equations can be found in the following section.

2.1. Governing equations outside the particle

The continuity equation is given by

$$\frac{\partial \rho_g}{dt} + \nabla \cdot (\rho_g \overrightarrow{u}) = 0, \tag{1}$$

where ρ_g is gas phase density and $\overrightarrow{u}$ is the velocity of the gas phase. Momentum conservation gives:

$$\frac{\partial (\rho_g \overrightarrow{u})}{dt} + (\rho_g \overrightarrow{u} \cdot \nabla)\overrightarrow{u} = -\nabla p + \nabla \cdot \mu[\nabla \overrightarrow{u} + \nabla \overrightarrow{u}^T - \frac{2}{3}(\nabla \cdot \overrightarrow{u})\overrightarrow{I}], \tag{2}$$

where p is pressure, μ is dynamic viscosity, and $\overrightarrow{I}$ is the identity matrix. The energy conservation equation reads as

$$\frac{\partial(\rho_g c_{p,g} T)}{dt} + \nabla \cdot (\rho_g c_p \overrightarrow{u} T) = -\nabla \cdot \lambda_g \nabla T, \tag{3}$$

where c_p is specific heat capacity, T is temperature, and λ_g is thermal conductivity. Models used for estimation of all the thermophysical and transport properties are shown in Appendix A.

2.2. Governing equations inside the particle

Since the solid phase inside the particle is stationary, the conservation of momentum is solved only for the gas phase, while the account is made for the local porosity. Hence, the continuity equation reads as:

$$\frac{\partial(\epsilon \rho_g)}{dt} + \nabla.(\rho_g \overrightarrow{u}) = R_C, \tag{4}$$

where ϵ $(= V_g/V_{cell})$ is the porosity of a cell in the computational domain where V_g is volume of the gas and V_{cell} is total voulme of the cell. R_C is char gasification rate due to the Boudouard reaction (in kg m^{-3} s^{-1}). The momentum equation for the gas phase inside a porous medium is given by

$$\frac{\partial(\epsilon \rho_g \overrightarrow{u})}{\partial t} + (\rho_g \overrightarrow{u} \cdot \nabla) \overrightarrow{u} = -\nabla p + \nabla \cdot \mu [\nabla \overrightarrow{u} + \nabla \overrightarrow{u}^T - \frac{2}{3} (\nabla \cdot \overrightarrow{u}) \overrightarrow{I}] - F_d, \tag{5}$$

where

$$F_d = \frac{\mu}{K} \overrightarrow{u}, \tag{6}$$

is the momentum transfer calculated based on Darcy-Forchcheimer law [22, 23] and

$$K = \frac{d_{pore}^2 \epsilon^3}{150(1-\epsilon)^2}, \tag{7}$$

is the permeability as given by the Carman-Kozney equation with an average pore diameter d_{pore} [24, 25].

A single energy equation can be used for the gas and solid phases due to the assumption of local thermal equilibrium of the two phases (see assumption 5):

$$\frac{\partial[\epsilon \rho_g c_{p,g} + (1-\epsilon)\rho_s c_{p,s}]T}{\partial t} + \nabla.(\epsilon \rho_g c_{p,g} \overrightarrow{u} T) = \nabla(\nabla.\lambda_{eff} T) + \dot{Q}_{rad,p} + \dot{Q}_s, \tag{8}$$

where $c_{p,g}$ is specific heat capacity of the gas, $c_{p,s}$ is specific heat capacity of char, ρ_s is the true density of char and λ_{eff} is the effective thermal conductivity calculated as:

$$\lambda_{eff} = \epsilon\lambda_g + (1-\epsilon)\lambda_s. \tag{9}$$

The radiative exchange between the reactor wall and the external particle surface is given by

$$\dot{Q}_{rad,p} = \sigma\alpha(T_w^4 - T_p^4), \tag{10}$$

where σ is Stefan-Boltzmann constant, α is the emissivity of char, T_w is wall temperature and T_p is particle surface temperature. This term is zero for the internal cells. Furthermore, the enthalpy change due to the solid phase reaction reads as

$$\dot{Q}_s = \Delta H R_C, \tag{11}$$

where ΔH is the reaction enthalpy and R_C is the char reaction rate due to Boudouard reaction. The latter is expressed through the char conversion rate as

$$R_C = (1-\epsilon_0)\rho_s \frac{\partial X_C}{\partial t}, \tag{12}$$

where the char conversion rate reads as

$$\frac{\partial X_C}{\partial t} = A \exp\left(-\frac{E_A}{RT}\right) p_{CO2}^n . f(X_C). \tag{13}$$

where A is the kinetic prefactor, E_A is the activation energy, p_{CO2} is the partial pressure of CO_2 and $f(X_C)$ is the conversion function. Following the random pore model, the latter read as

$$f(X_C) = \frac{S_g}{S_{g,0}} = (1-X_C)\sqrt{1-\psi\ln(1-X_C)} \tag{14}$$

where $S_g, S_{g,0}$ are the instantaneous and initial local specific surface areas of the char particle, respectively, and ψ is the structure parameter of the random pore model. The char conversion rate X_C is related to the local porosity, ϵ, via

$$\epsilon = \epsilon_0 + X_C(1-\epsilon_0), \tag{15}$$

where ϵ_0 is the initial porosity of the char.

The gas species equation reads as

$$\frac{\partial(\epsilon\rho_g Y_i)}{\partial t} + \nabla.(\rho_g \overrightarrow{u} Y_i) = -\nabla.(Y_i \rho_g \overrightarrow{v_i^c}) + \nu_i R_C, \tag{16}$$

where Y_i is mass fraction of gas species i, ν_i is stoichiometric coefficient in the Boudouard reaction related to species i, and v_i^c is diffusion velocity of gas species i. The calculation of v_i^c can be found in Appendix B.

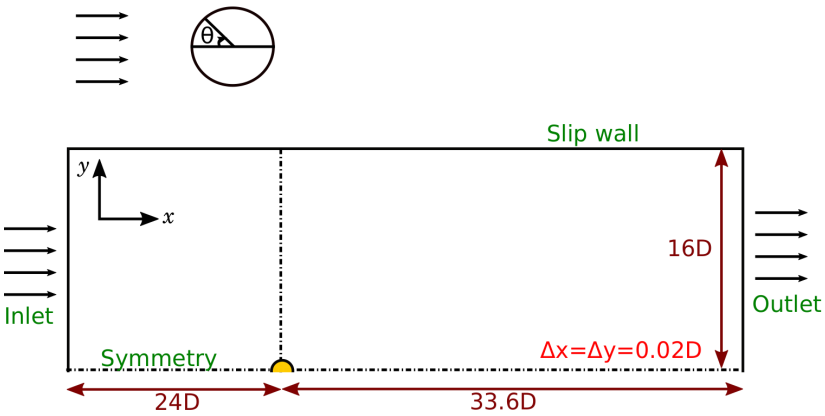

Figure 2: The schematic image of the computational domain with the boundary condition, domain size, and mesh size. Here D is diameter of the cylindrical particle, and Δj is the size of the mesh in direction j.

2.3. Boundary conditions and initial conditions.

The overall approach of the simulation is summarized in Fig. 1, while the simulation domain is shown in Fig. 2. The domain has the following boundaries: *inlet*, *outlet*, *slip wall*, and *symmetry*. At the *inlet* boundary, all the physical, chemical, and transport properties were uniform across the boundary except for pressure, where the Neumann boundary condition was used. The temperature was increased from room temperature (300 K) to reactor temperature within 10 ms, while the density was decreased accordingly. Neumann boundary condition was applied at the *outlet* boundary except for pressure where a specific value is defined. *Slip wall* boundary condition was

used on the upper wall of the domain where the surface normal velocity is zero. The velocity normal to the boundary was zero, and all the other properties have Neumann boundary conditions for the *symmetry* plane.

The cases for the simulations were designed to keep all parameters within EFBG range. Here, the main focus was to investigate the effects of varying particle Reynolds number (Re), Stefan Reynolds number ($\mathrm{Re_{Sf}}$), and effectiveness factor (η).

The Reynolds number is defined as

$$\mathrm{Re} = \frac{\rho_g U d_p}{\mu}, \tag{17}$$

where U is the relative velocity between the particle and the bulk flow, ρ_g is fluid density, μ is fluid viscosity and d_p is particle diameter. The effectiveness factor (η) is given by

$$\eta = \frac{Actual\ overall\ particle\ consumption\ rate}{Particle\ consumption\ rate\ at\ particle\ surface}. \tag{18}$$

Finally, the Stefan Reynolds number is calculated by replacing the slip velocity in Eq. 17 with the Stefan flow velocity. The values of 0.5 or 3 are chosen for the Reynolds number, while the effectiveness factor (η) is either considered as low; 0.2-0.3 (cases 1-3) or high; 0.6-0.7 (cases 4-6). Note that the exact effectiveness factor was not possible to estimate in advance due to uncertainties in the existing analytical models. Six cases were used for the analysis as shown in Table 1.

The initial velocity and pressure fields were obtained based on isothermal simulation results at room temperature (300 K). Initial conditions, boundary conditions and dimensionless numbers for the cases are shown in the Table 1. Other constant parameters that are common for all the cases are tabulated in Table 2. Hereafter, the cases with higher η means cases 4-6 in Table 1 and cases with lower η means cases 1-3 in Table 1.

2.4. Numerical code validation and solution procedure

Simulations were carried out with the finite volume computational fluid dynamics (CFD) code OpenFOAM v6 [28] with our own numerical solver based on the governing equations described above. The pressure-Implicit with Splitting of Operators (PISO) algorithm was used for the pressure-velocity coupling. All the finite volume schemes used were second-order accurate.

Table 1: List of parameters that were varied for different simulation cases. Effectiveness factor (η), particle Reynolds number (Re), and Stefan Reynolds number (Re_{Sf}) are the values estimated from the results of the resolved particle simulation.

Case	T_∞ (K)	p_∞ (atm)	d_p (μm)	U_∞ (m/s)	$Y_{CO_2,\infty}$ (-)	η	Re	Re_{Sf}
1	1999	1.807	189.3	0.45	0.512	0.23	0.5	0.09
2	1999	1.807	189.3	2.70	0.512	0.44	3.0	0.03
3	1851	4.201	442.6	0.44	0.512	0.21	3.0	0.04
4	1891	4.506	97.21	0.32	0.512	0.74	0.5	0.08
5	1891	4.506	97.21	1.93	0.512	0.69	3.0	0.02
6	1735	7.672	228.1	0.32	0.99	0.58	3.0	0.03

Table 2: Constant parameters used for the simulations.

Type	**parameter**	**value**	**unit**
Char	ρ_s	1200	$\mathrm{kgm^{-3}}$
	λ_s	0.13	$\mathrm{Wm^{-2}s^{-1}}$
	$c_{p,s}$	1500	$\mathrm{Jkg^{-1}s^{-1}}$
	ϵ_0	0.7917	-
	τ_0	1.2632	-
	d_{pore}	250×10^{-9}	m
	ψ	1	-
	$S_{p,0}$ [26]	1.267×10^7	$\mathrm{m^2/m}$
Reaction kinetics[27]	E_A	2.62×10^5	$\mathrm{Jmol^{-1}}$
	A	1.19×10^9	$\mathrm{s^{-1}MPa^{-n}}$
	n	0.46	-
	ΔH_f°	17.78×10^6	$\mathrm{Jkg^{-1}}$
Radiation	ε	0.8	-

The initial domain size was selected from previous studies of flow around a circular cylinder [29, 30, 31, 32] to be $57.6D \times 16D$. Domain size tests and refinement tests were carried out by comparing C_d and Nu values obtained with different domains (lateral direction domain sizes of $12D, 16D$ and $24D$)

and different refinements ($0.04D, 0.02D$ and $0.01D$). Drag coefficient is;

$$C_d = \frac{F_p + F_{vis}}{0.5\rho_g A U_\infty^2}, \tag{19}$$

where F_p, F_{vis} are pressure force and viscous force acting on the particle's outer surface, A is the cross-sectional area of the cylinder, which is D. Similarly, C_p and C_{vis} can also calculated by replacing $F_p + F_{vis}$ by F_p and F_{vis}. Mesh refinement tests were carried out for the case with the highest Reynolds and Stefan Reynolds numbers, while the domain size tests were carried out for the case where the same numbers were the lowest.

Figures 3 and 4 show domain test results and mesh refinement results for both C_d and Nu. The maximum difference between the domain $16D$ and $24D$ for C_d is around 1.2% (see Fig. 3). The Nusselt number shows a negligible difference for domains $12D$ and $16D$ compared to the largest lateral domain size of $24D$. The maximum error in mesh refinement of $0.02D$ is about 5.8% compared to the mesh $0.01D$ for C_d, while it is about 4.4% for Nu. The error in C_d of $0.01D$ mesh when compared with the value obtained from Richardson extrapolation for a mesh of $0.005D$ is about 3.84% [33]. Since errors of domain 16D and mesh refinement 0.02D are small errors compared to the largest domain and most refined mesh, we used lateral domain size of 16D and mesh refinement of 0.02D for the rest of the simulations.

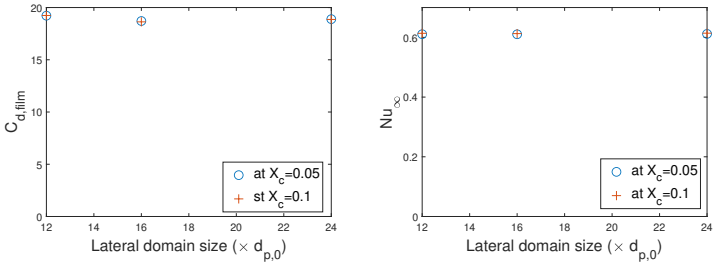

(a) (b)

Figure 3: Domain tests for the lateral width of the domain (y-direction of Fig. 1. (a) Comparison of drag coefficient (C_d). (b) Comparison of Nusselt number (Nu).

The initial time step for all the simulations were selected based on the Courant number (Co=0.5) used in the work by Tufano et al. [22]. Some cases

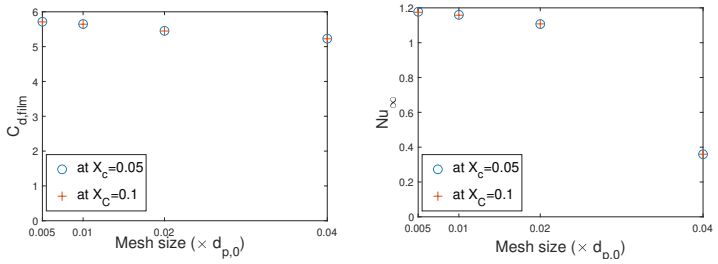

(a) (b)

Figure 4: Comparison of C_d and Nu at different mesh refinements. The mesh size is uniform all over the domain. C_d and Nu at $0.005D$ mesh are based on Richardson Extrapolation. (a) Comparison of drag coefficient (C_d). (b) Comparison of Nusselt number (Nu).

created wiggles with time on the C_d with the Courant number 0.5 although the Nu was stable. Therefore, Courant number was reduced until C_d values were stabilized for those cases.

The numerical code was further compared with experimental data for coal particle conversion time in a pressurized entrained flow gasifier (EFG) [27]. Some of the essential information was missing in the source [27] and assumed from literature (The values used for the simulations are shown in Table C.3). Simulation data were compared with the full conversion time of the particle from [27]. For this comparison, the coal char entitled "*coal char SM*" in [27] was selected. Figure 5 shows the char conversion with time. It shows that the total conversion time agreed well, while a deviation was observed during the conversion.

3. Results and Discussion

The variation of the drag coefficient (C_d) of a cylindrical particle during reactions has been compared to a non-reacting case. The main objective is to see how a Stefan flow created by the reactions affects these parameters. As shown in Table 1 and Table 2, six cases have been run and analyzed for various ranges of Reynolds numbers, effectiveness factors, and Stefan Reynolds numbers. Calculation procedures for C_d are described in Appendices D. C_d is normalized by the corresponding values obtained from the steady state values of simulations without reactions.

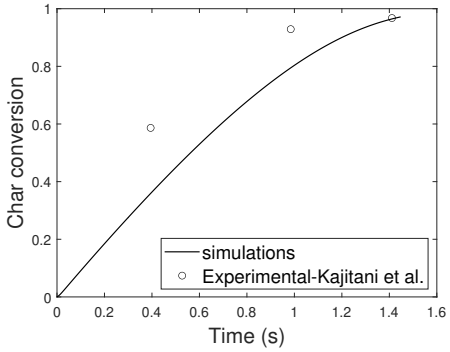

Figure 5: Char conversion with time of 'Extreme I' case. Full char conversion takes 1.52s. Details of parameters used for the simulation of the case 'Extreme I' can be found in Appendix C.

3.1. Effect of Stefan flow on the drag coefficient

Figures 6 and 7 show how the normalized C_d, normalized particle diameter (d_p), normalized particle density (ρ), and effectiveness factor (η) vary from start to full conversion of the particle by gasification due to the Boudouard reaction alone.

The drag coefficients for reactive cases in this study exceeded or equaled those for the non-reactive cases (Fig. 7a). This is in stark contrast to our previous work under the assumption of uniform Stefan flows [4, 10], which showed the reduction of drag coefficient with outgoing Stefan flows. In all cases, the normalized C_d initially increases to around 1 before the particle starts to react ($X_p = 0$). This period represents the transient period, where the flow inside the boundary layer of the particles approaches that is seen for non-reactive conditions. Thereafter, all the low η cases showed very complicated transitions, while there are only two distinctive phases for high η cases.

To explain the different phases of changes in C_d of lower η cases clearly, Fig. 8 shows the variation of C_d for case 1. C_d initially increases as described above (up to point 'A'). Then, there is an almost constant period of C_d (A-B) and a peak (B-C), followed by a gradual decrease. Finally, the declining trends of C_d halt with significant noises being induced in the calculated values in C_d. This instant coincides with the onset of particle shrinkage (Fig. 6b).

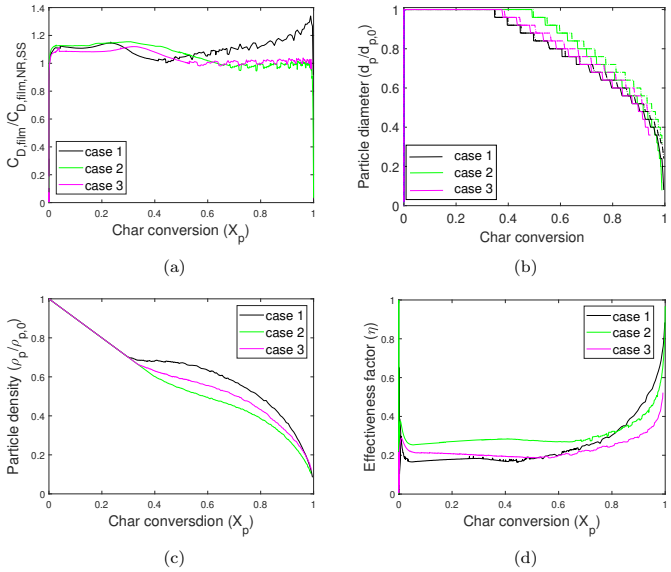

Figure 6: (a) Comparison of normalized average drag coefficient (C_d) of the particles in cases 1-3 in Table 1 (low η cases). C_d is normalized by the steady-state values of the same case without reactions $C_{d,film,NR,SS}$. (b) Normalized particle diameter variation. (c) Normalized particle density variation. (d) Effectiveness factor variation of all cases.

The decrease in particle size results in a lower Reynolds number (Eq. 17) and therefore higher C_d [34, 35]. The source of noise is mainly due to the discontinuity in particle size due to the limited mesh resolutions. Note that C_d continuously increases from point 'D' onwards for case 1, but the other two cases with low η end up at constant values of C_d close to one (Fig. 6a).

For high η cases (Fig. 7a), C_d gradually decreases as the char conversion progress. At the end of conversion, when particle diameter starts to decrease, the declining trend of C_d is interrupted, and the C_d stays almost constant. The effect of shrinking particle size was similar to that observed in low η cases. The gradual decrease of C_d below 90% of char conversion can be explained either by the decrease of reaction rate (see Fig. 9) or by the gradual increase of porosity throughout particles, which is known to reduce the drag [31, 36].

The differences in the effectiveness factors among cases seem to have dom-

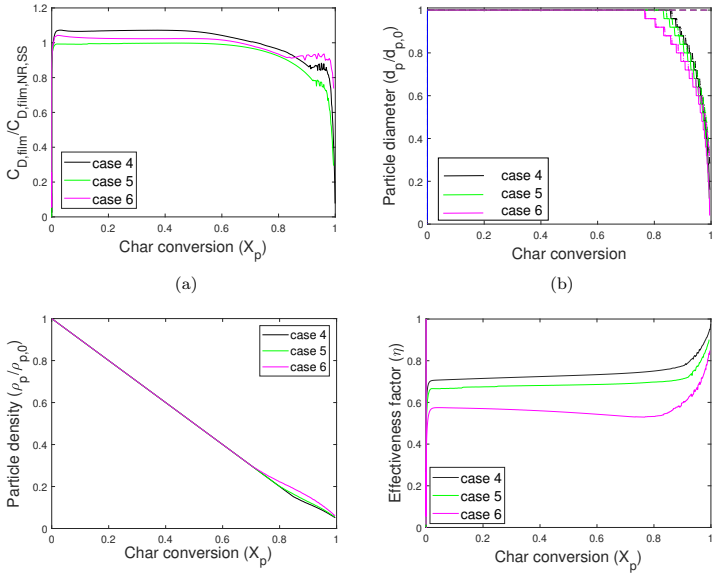

Figure 7: (a) Comparison of normalized average drag coefficient (C_d) of the particle for cases 4-6 in Table 1 (high η cases). C_d is normalized by the steady-state values of the same case without reactions $C_{d,film,NR,SS}$. (b) Normalized particle diameter variation. (c) Normalized particle density variation. (d) Effectiveness factor variation of all cases.

inant effects on how the drag coefficients behave during the char conversion. Although all the cases are affected by intra-particle transport phenomena to some degree (zone II), cases 1-3 had relatively low, η in the range of 0.1-0.3 (Fig. 6d), which is closer to zone III conditions. Meanwhile, cases 4-6 are closer to zone I conditions as their effectiveness factors are close to unity (Fig. 7d). The differences are clearly seen in Figs. 6b and 7b where diameter starts to change much later ($X_p > 0.75$) in the high η cases than in low η cases ($0.35 < X < 0.5$). A more detailed investigation of momentum exchange can be found in the following subsections separately for low and high η cases.

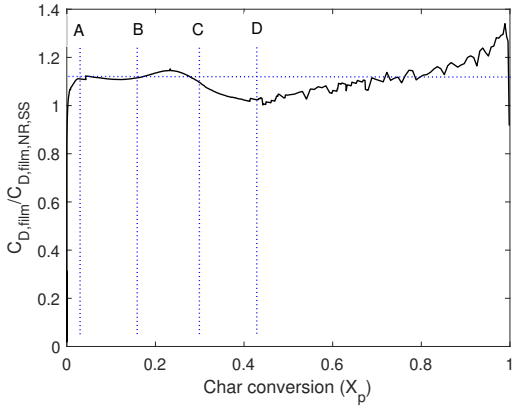

Figure 8: Normalized drag coefficient (C_d) of the case 1 at different conversion stages.

3.2. Momentum exchange of low η cases

To study the variation of C_d at low η cases, Figure 10a shows the contribution of the pressure and viscous components to C_d separately for each case. In all cases, two components are in the same magnitude, but the viscous component is smaller than the pressure component except for case 1 at very low char conversions ($X_p < 0.2$). Furthermore, Figure 10c (comparison with non-reactive cases) shows that the normalized viscous force is also lower than unity except $X_p < 0.2$ for case 1 while the normalized pressure force is above unity. Note that the values here are forces, and the effects of particle shrinkage seen in the drag coefficient have been eliminated (see Appendix D). Our previous studies with uniform Stefan flow [4, 10] have also shown a decrease in the viscous force with increasing Stefan flow, which dominated the effects of Stefan flow on the overall drag coefficients. Therefore, the higher C_d of lower η cases can be attributed to the pressure force, mostly due to the effects of a non-uniform Stefan flow. The pressure force increases slightly after the particle starts to react and before the diameter of the particle starts to decrease.

Particle porosity is known to affect the drag coefficients, especially for values above 0.8 [31, 36]. It also gives indications about the regions of the reactions inside the particle because the porosity increases due to the hetero-

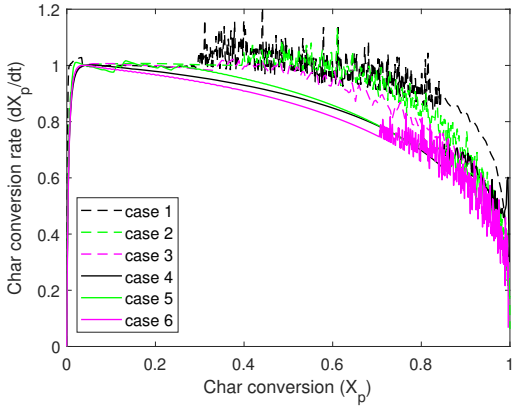

Figure 9: Char conversion rate as a function of char conversion. The conversion rates were normalized by the maximum rate at the initial stage of conversion.

geneous reactions (Eq. 15). In Fig. 11, contour plots of porosity for cases 1 (low η) and 4 (high η) are compared for char conversions ranging from 0.1 to 0.8. The figure also depicts the particle size and shape variation at different conversions. The figures show that the porosity inside the particles, except for the areas close to the external surface, hardly increases from the initial value of $\epsilon_0 = 0.7917$ for low η cases. It means that, for the low η cases, the increase in the particle porosity can be ruled out from affecting the drag coefficient. The figures also show that the particle starts shrinking at the conversion between 0.3 and 0.4, and from there, it constantly decreases in size. This result can partially explain the gradual decrease of the viscous force at the later stage of the conversion ($X_p > 0.4$). As shown in Fig. 9, the reaction rate stayed almost constant for conversion less than 0.75 ($X_p < 0.75$). The decrease in particle size at the later stage of conversion means that the Stefan velocity increases as the external surface area decreases while the total volume of Stefan flow stays constant, as observed in Fig. 12. The viscous force has likely been reduced due to the expansion of the boundary layer as observed in the previous work [4, 10]. However, the potential effect of a non-uniform distribution of the Stefan flow should be investigated. In fact, Fig. 11a shows that the upstream side (left in the figure) seems to react faster than the downstream side, which is illustrated by the center of the particle

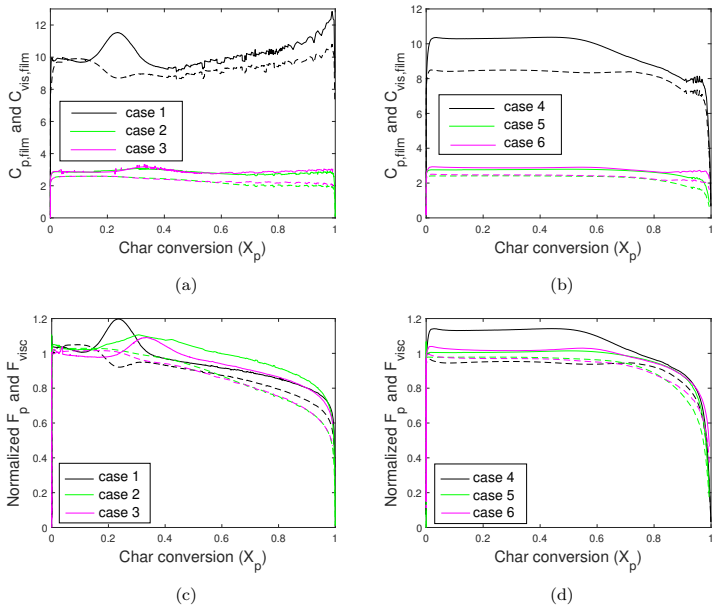

Figure 10: Comparison of the pressure component of the drag coefficient (solid lines) and the viscous component of the drag coefficient (dashed lines) for (a) low η cases and (b) high η cases. Comparison of normalized pressure force and viscous force (c) low η cases and (d) high η cases. Forces are normalized with the pressure force and viscous force of the same case without reaction at a steady state.

moving rightward as the conversion progresses.

From Fig. 13a, we see the temporal bump in pressure force; the pressure force of case 1 starts to increase around $X_p = 0.12$, reaches the highest value at around $X_p = 0.24$, and the bump settles around $X_p = 0.36$. Therefore, the porosity and temperature field around the particle were examined at X=0.12, 0.24, and 0.36. Figure 14 shows the boundary of the particle and pressure, temperature, and mass fraction profiles during the five conversions. There is a clear connection between the high-pressure force region and localized particle conversion, which can be seen from the temperature contours at the front side of the particle. Localized particle conversion can be further identified through the Stefan flow velocity around the particle surface. Stefan

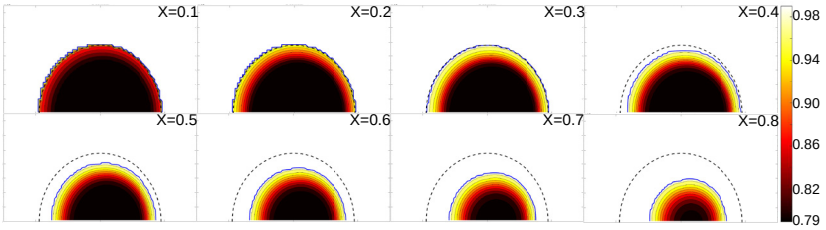

(a)

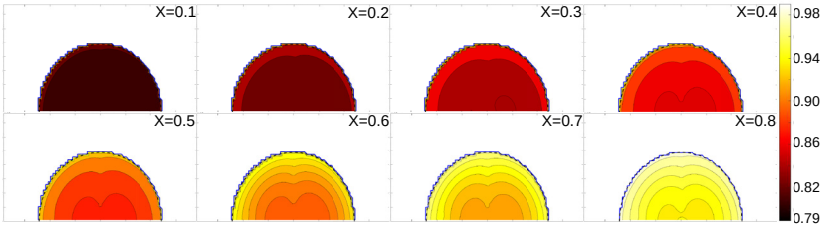

(b)

Figure 11: The changes of internal porosity at different conversion stages: case 1 as an example for low η conditions (a), and case 4 as an example for high η conditions (b) . Dashed circle indicates the original location of the particle surface.

flow velocity at the particle surface vs. angle from the front to the back of the particle is shown in Fig. 13b at three conversions: a, b and c. We can see from the figures that there is a high velocity at the front of the particle compared to the back of the particle at a and b and almost balanced surface velocities at the front and back at c. This will lead to a higher pressure force compared to what would be found due to a uniform Stefan flow around the particle. According to previous studies [4, 10], it was observed that a uniform Stefan flow around a particle does not affect the pressure force. Apart from that, the particle boundary also shows that the pressure force is reduced when the particle starts to react all around the particle (compare Fig. 14c points a-b with c). Therefore, we could say that the high-pressure region in Fig. 14b is due to the localized non-equimolar reaction producing more product gas than reactant gas.

To find out the reason for the low viscous force at the same region of high-pressure force, viscous force at the surface of the particle is plotted against

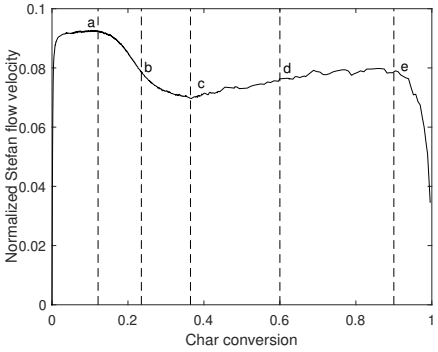

Figure 12: Variation of normalized Stefan flow velocity as a function of char conversion for case 1.

the angle from front to the back of the particle in Fig. 13c. The figure shows that the lowest average viscous force of the particle at b is due to the positive and negative force at the particle surface's front and back, which cancels each other in average viscous force. From a-b average viscous force is decreasing, and from b-c, it is increasing, which can be decided based on the area under each curve for a-c in Fig. 13c. Since the average viscous force is settling around the char conversion of c, where the particle starts to produce symmetric Stefan flow velocities, we could say that the reason for the low viscous force range is the localized reaction at the front of the particle.

3.3. Momentum exchange of high η cases

Even with higher η, the normalized C_d is higher than, or equal to, unity for $X_p < 0.6$ for all cases (see Fig. 7). Figures 10b and 10d confirms that this is due to the pressure force. According to Fig. 15a, the increase of pressure force is closely related to the magnitudes of normalized Stefan Reynolds number ($\mathrm{Re}_{Sf}/\mathrm{Re}$). Together with the low η cases, it highlights the importance of pressure components for the Stefan flow effects on the drag coefficient. Moreover, high η cases do not exhibit strong variations in conversion at the front and back of the particle. It implies that the increase of pressure components in drag may not be due to non-uniform Stefan flows due to the localized reactions. Instead, this is probably due to the increase in the pressure inside particles, which was not considered in previous work, *e.g.,*

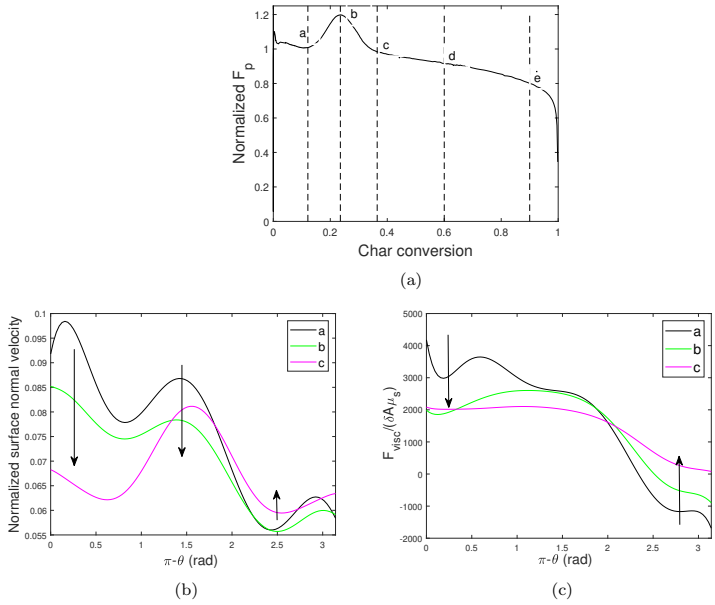

Figure 13: Normalized pressure force acting on the particle during conversion for case 1 (a). Char conversion at point a is 0.12, point b is 0.24, point c is 0.36, point d is 0.6 and point e is 0.9. Normalized velocity ($U_{r,s}/U_\infty$) (b) and viscous force (c) at the particle surface with the angle from the front of the particle to the back of the particle. Velocities and viscous forces are at three char conversions: a, b, and c.

[4, 10], because they do not resolve the particle interiors in the simulation.

The viscous force slightly decreases when the particle starts to react and continue at almost a constant value until the particle shape starts to change (see Figure 10d). As mentioned earlier, the viscous force is reduced by the boundary layer expansion due to an outwards Stefan flow [4, 10]. The constant viscous force for high η cases cannot be explained by the variation of Stefan flow alone since Re_{Sf} and U_{Sf} are not constant with conversion (see Fig. 15). Between the char conversion of 0.1 to 0.7, Stefan flow velocity decreases monotonically, which should increases the viscous force. However, the porosity of the char particles simultaneously decreases throughout the particle as shown in Fig. 11b. Therefore, the constant viscous force can be

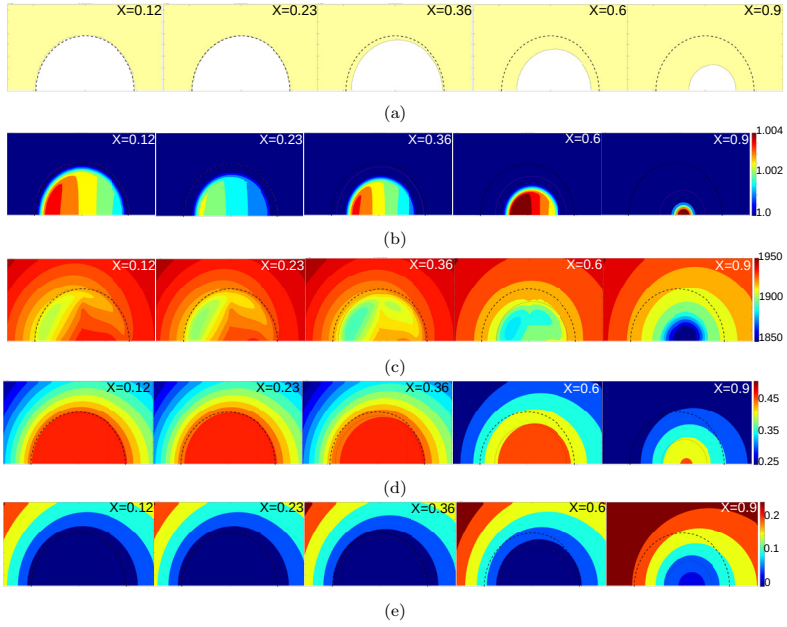

Figure 14: Variation of particle boundary (a), pressure contours (b), temperature contours (c), carbon monoxide contours (d) and carbon dioxide contours (e) at different char conversion stages.

explained as a combined effect of Stefan flow velocity and porosity increase at the surface of the particle [31, 36].

4. Conclusions

A numerical platform was developed for a reacting particle with a heterogeneous reaction immersed in a uniform, incompressible bulk flow. The particle is considered to be a porous, infinitely long cylinder that has resistance to the flow inside it. The values of drag coefficients (C_d) from the simulations were compared with the values of the same case without reactions at the steady state. Results showed complex variations throughout the conversion of the particle. In general, C_d is higher than or close to the case without reactions for all the cases. The reason for the higher drag coefficient

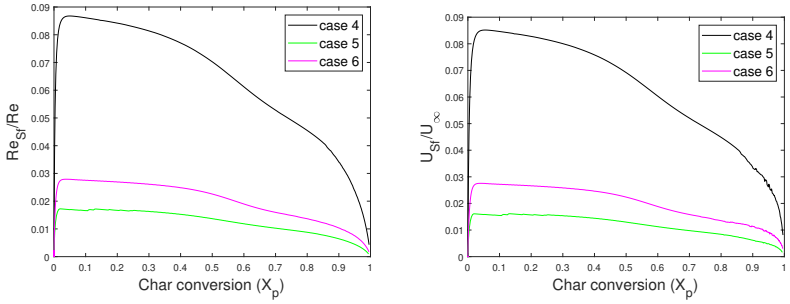

(a) (b)

Figure 15: Comparison of normalized Stefan Reynolds number, Re_{Sf}/Re, (a) and normalized Stefan velocity, U_{Sf}/U_{∞}, (b) for cases 4-6 (high η cases) as a function of char conversion.

is the pressure force, while the viscous force was less than the case without reactions almost throughout the conversion. The increase in pressure force was observed both at low and high effectiveness factor cases. The most likely reason for the active role of pressure force observed in this study is the fact that the particle interior has several orders of magnitude higher increase of pressure than the variation outside the particle. Apart from that, there is a region of a bump in pressure force and a pothole in viscous force for low effectiveness factor cases due to localized conversions. The lower viscous force of the particle during conversion agrees with our previous findings of low viscous force under the uniform Stefan flow around a particle. However, the reduction of viscous forces cannot be attributed to the Stefan flow alone in high effectiveness factor cases where an increase of porosity also contributes to lowering viscous force. For high effectiveness factor cases, the porosity changes throughout the particle as the reactions progress, which has effects to lower the drag. These effects are usually not considered when modeling gas-solid reacting flows, which calls for the development of more general models of the Drag coefficient.

Acknowledgment

The authors are grateful to the Swedish Research Council (Vetenskapsrådet) for financial support for the study (grant number: 2015-05588). The simu-

lations were performed on resources, *Kebnekaise*, provided by the Swedish National Infrastructure for Computing (SNIC) at High Performance Computing Center North (HPC2N). The authors thank all the staff of HPC2N for the technical assistance and specially to Pedro Ojeda May for the support with OpenFOAM. Furthermore, M.U.B. thanks the Swedish for Gasification Center and its industrial and academic partners for financial suppport. N.E.L.H. acknowledge the Research project Gaspro, financed by the research council of Norway (267916) and the research projects CHEERS, financed by the European Union's Horizon 2020 research and innovation program (grant agreement No. 764697) This work also benefitted from computer resources made available through Norwegian NOTUR program, under award NN9405K.

References

[1] M. Kestel, Numerical Modeling of Moving Carbonaceous Particle Conversion in Hot Environments, Ph.D. thesis, TU Bergakademie (2016).

[2] R. Miller, J. Bellan, Direct numerical simulation of a confined three-dimensional gas mixing layer with one evaporating hydrocarbon-droplet-laden stream, J. Fluid Mech 384 (1999) 293–338.

[3] X. Chen, S. Du, L. Zhao, B. Yang, Q. Zhou, Effect of Stefan flow on the drag force in flow past random arrays of spheres, Chemical Engineering Journal 412 (may 2021). doi:10.1016/j.cej.2021.128691.

[4] T. R. Jayawickrama, N. E. L. Haugen, M. U. Babler, M. A. Chishty, K. Umeki, The effect of Stefan flow on Nusselt number and drag coefficient of spherical particles in non-isothermal gas flow, International Journal of Multiphase Flow 140 (2021) 103650. doi:10.1016/j.ijmultiphaseflow.2021.103650.

[5] M. Renksizbulut, M. C. Yuen, Numerical Study of Droplet Evaporation in a High-Temperature Stream, Journal of Heat Transfer 105 (2) (1983) 389–397. doi:10.1115/1.3245591.

[6] H. Niazmand, M. Renksizbulut, Transient three-dimensional heat transfer from rotating spheres with surface blowing, Chemical Engineering Science 58 (2003) 3535–3554. doi:10.1016/S0009-2509(03)00191-X.

[7] B. Abramzon, W. A. Sirignano, Droplet vaporization model for spray combustion calculations, International Journal of Heat and Mass Transfer 32 (9) (1989) 1605–1618. doi:10.1016/0017-9310(89)90043-4.

[8] M. Renksizbulut, M. C. Yuen, Experimental Study of Droplet Evaporation in a High-Temperature Air Stream, Journal of Heat Transfer 105 (1983) 384–388.

[9] M. C. Yuen, L. W. Chen, On Drag of Evaporating Liquid Droplets, Combustion Science Technology (2008). doi:10.1080/00102207608547524.

[10] T. R. Jayawickrama; N. E. L. Haugen; M. U. Babler; M.A. Chishty; K. Umeki, The effect of Stefan flow on the drag coefficient of spherical particles in a gas flow, InternationalJournalofMultiphaseFlow 117 (2019) 130–137. doi:10.1016/j.ijmultiphaseflow.2019.04.022.

[11] R. Kurose, H. Makino, S. Komori, M. Nakamura, F. Akamatsu, M. Katsuki, Effects of outflow from the surface of a sphere on drag, shear lift, and scalar diffusion, Citation: Physics of Fluids 15 (2003). doi:10.1063/1.1591770.

[12] A. Cliffe, Isothermal flow past a blowing sphere, International Journal for numerical methods in fluids 5 (March) (1985) 709–725.

[13] S. Farazi, T. Sayadi, H. Pitsch, Numerical Analysis of the Drag Force Acting on the Reactive Single Char Particle under Oxy-Fuel Condition, in: Proc. of the China National Symposium on Combustion 2016, Ma'anshan, 2016, pp. 1–9.

[14] H. Zhang, K. Luo, N. E. L. Haugen, C. Mao, J. Fan, Drag force for a burning particle, Combustion and Flame 217 (2020) 188–199. doi:10.1016/j.combustflame.2020.02.016.

[15] M. B. Tilghman, N. E. L. Haugen, R. E. Mitchell, Comprehensive Char Particle Gasification Model Adequate for Entrained-Flow and Fluidized-Bed Gasifiers, Energy & Fules (2016). doi:10.1021/acs.energyfuels.6b02148.

[16] T. Kreitzberg, A. Phounglamcheik, C. Bormann, R. Kneer, K. Umeki, The change in size of char particles during combustion and gasification in regime II, in: MCS11, Tenerife, 2019.

[17] T. Kreitzberg, S. Pielsticker, B. M. Gvert, R. Kneer, CO2 and H2O Gasification under chemically and diffusion controlled conditions, in: 33rd Annual International Pittsburgh Coal Conference, Cape Town, 2016.

[18] N. E. L. Haugen, B. K. Y. Loong, R. E. Mitchell, Numerical approaches for thermochemical conversion of char, Progress in Energy and Combustion Science 91 (jul 2022). doi:10.1016/J.PECS.2022.100993.

[19] N. E. L. Haugen, M. B. Tilghman, R. E. M. Mitchell, The conversion mode of a porous carbon particle during oxidation and gasification, Combustion and Flame 161 (2014) 612–619. doi:10.1016/j.combustflame.2013.09.012.

[20] Á. D. G. Llamas, N. Guo, T. Li, R. Gebart, K. Umeki, Rapid change of particle velocity due to volatile gas release during

biomass devolatilization, Combustion and Flame 238 (2022) 111898. doi:10.1016/j.combustflame.2021.111898.

[21] D. J. Tritton, Experiments on the flow past a circular cylinder at low Reynolds numbers, Journal of Fluid Mechanics 6 (1959) 547–567. doi:10.1017/S0022112059000829.

[22] G. L. Tufano, O. T. Stein, A. Kronenburg, G. Gentile, A. Stagni, A. Frassoldati, T. Faravelli, A. M. Kempf, M. Vascellari, C. Hasse, Fully-resolved simulations of coal particle combustion using a detailed multi-step approach for heterogeneous kinetics, Fuel (2019). doi:10.1016/j.fuel.2018.11.139.

[23] E. Ranzi, T. Faravelli, F. Manenti, Pyrolysis, Gasification, and Combustion of Solid Fuels, Advances in Chemical Engineering 49 (2016) 1–94. doi:10.1016/bs.ache.2016.09.001.

[24] J. Szekely, J. Evans, H. Sohn, Gas-solid reactions, Academic Press, 1976.

[25] P. A. Nikrityuk, B. Meyer, Gasification Processes Modeling and Simulation, 1st Edition, Wiley-VCH, 2014.

[26] J. Szekely, J. Evans, H. Sohn, Gas-Solid Reactions, Academic Press Inc, 1976.

[27] S. Kajitani, N. Suzuki, M. Ashizawa, S. Hara, CO 2 gasification rate analysis of coal char in entrained flow coal gasifier, Fuel 85 (2005) 163–169. doi:10.1016/j.fuel.2005.07.024.

[28] H. G. Weller, G. Tabor, H. Jasak, C. Fureby, A tensorial approach to computational continuum mechanics using object-oriented techniques, Computers in Physics 12 (1998) 620–631. doi:10.1063/1.168744.

[29] E. Constant, J. Favier, M. Meldi, P. Meliga, E. Serre, An immersed boundary method in OpenFOAM: Verification and validation, Computers and Fluids (2017). doi:10.1016/j.compfluid.2017.08.001.

[30] S. Bhattacharyya, S. Dhinakaran, A. Khalili, Fluid motion around and through a porous cylinder, Chemical Engineering Science 61 (13) (2006) 4451–4461. doi:10.1016/j.ces.2006.02.012.

[31] K. Wittig, P. Nikrityuk, A. Richter, Drag coefficient and Nusselt number for porous particles under laminar flow conditions, International Journal of Heat and Mass Transfer 112 (2017) 1005–1016. doi:10.1016/j.ijheatmasstransfer.2017.05.035.

[32] P. Yu, Y. Zeng, T. S. Lee, X. B. Chen, H. T. Low, Steady flow around and through a permeable circular cylinder, Computers and Fluids 42 (1) (2011) 1–12. doi:10.1016/j.compfluid.2010.09.040.

[33] A. Meana-Fernández, J. M. Fernández Oro, K. M. Argüelles Díaz, M. Galdo-Vega, S. Velarde-Suárez, Application of Richardson extrapolation method to the CFD simulation of vertical-axis wind turbines and analysis of the flow field, Engineering Applications of Computational Fluid Mechanics 13 (1) (2019) 359–376. doi:10.1080/19942060.2019.1596160.

[34] B. Huner, Cylinder Drag at Low Reynolds Number., Ph.D. thesis (1977).

[35] W. A. Khan, J. R. Culham, M. M. Yovanovich, Fluid flow around and heat transfer from an infinite circular cylinder, Journal of Heat Transfer 127 (7) (2005) 785–790. doi:10.1115/1.1924629.

[36] S. Tao, Q. He, X. Yang, J. Luo, X. Zhao, Numerical study on the drag and flow characteristics of porous particles at intermediate Reynolds numbers, Mathematics and Computers in Simulation 202 (2022) 273–294. doi:10.1016/j.matcom.2022.06.001.

[37] NIST Standard Reference Database 13, 1998. doi:10.18434/T42S31. URL `https://janaf.nist.gov/`

[38] N. Babkovskaia, N. E. L. Haugen, A. Brandenburg, A high-order public domain code for direct numerical simulations of turbulent combustion, Journal of Computational Physics 230 (1) (2011) 1–12. doi:10.1016/j.jcp.2010.08.028.

[39] Don W. Green, James O. Maloney, Robert H. Perry (Eds.), Perry's chemical engineering handbook, 7th Edition, McGraw-Hill.

[40] C. Di Blasi, Combustion and gasification rates of lignocellulosic chars (apr 2009). doi:10.1016/j.pecs.2008.08.001.

[41] R. G. Kim, C. W. Hwang, C. H. Jeon, Kinetics of coal char gasification with CO2: Impact of internal/external diffusion at high temperature and elevated pressure, Applied Energy 129 (2014) 299–307. doi:10.1016/j.apenergy.2014.05.011.

[42] B. Feng, S. K. Bhatia, Variation of the pore structure of coal chars during gasification, Carbon 41 (3) (2003) 507–523. doi:10.1016/S0008-6223(02)00357-3.

[43] B. Göktepe, A. H. Saber, R. Gebart, T. S. Lundström, Cold flow experiments in an entrained flow gasification reactor with a swirl-stabilized pulverized biofuel burner, International Journal of Multiphase Flow 85 (2016) 267–277. doi:10.1016/j.ijmultiphaseflow.2016.06.016.

[44] T. Maffei, R. Khatami, S. Pierucci, T. Faravelli, E. Ranzi, Y. A. Levendis, Experimental and modeling study of single coal particle combustion in O2/N2 and Oxy-fuel (O2/CO2) atmospheres, Combustion and Flame 160 (11) (2013) 2559–2572. doi:10.1016/j.combustflame.2013.06.002.

Appendix A. Thermophysical property calculation

Appendix A.1. Dynamic viscosity

Dynamic viscosity of a gas component i (μ_i), is calculated using Sutherland formula:

$$\mu_i = \frac{A_{s,i}\sqrt{T}}{1 + \frac{T_{s,i}}{T}}, \tag{A.1}$$

where A_s and T_s are constants. Viscosity of the gas mixture is calculated as follows;

$$\mu = \sum_{i=1}^{N_s} \frac{X_i \mu_i}{\Sigma_{j=1}^{N_s} X_j \phi_{ij}}, \tag{A.2}$$

where X_i is molar fraction of gas component i, N_s is number of gas components and ϕ_{ij} is calculated as follows;

$$\phi_{ij} = \frac{1}{\sqrt{8}} \left(1 + \frac{Mi}{M_j}\right)^{-1/2} \left\{1 + \left(\frac{\mu_i}{\mu_j}\right)^{1/2} \left(\frac{M_j}{M_i}\right)^{1/4}\right\}^2, \tag{A.3}$$

where M_i is molar mass of gas component i.

Appendix A.2. Density of the fluid

Density is calculated using state equation for the gas mixture:

$$\rho = \frac{pM}{RT}, \tag{A.4}$$

where p is the pressure at the *outlet* boundary of the simulation domain and $M = \Sigma_{i=1}^{N_s} m_i X_i$.

Appendix A.3. Thermal conductivity

Thermal conductivity of a gas component i (λ_i) is calculated using:

$$\lambda_i = R_{c_p}(a_{0,i} + a_{1,i}T + a_{2,i}T^2 + a_{3,i}T^3 + a_{4,i}T^4), \tag{A.5}$$

and mixture gas density (λ_g) is calculated based on molar averaging :

$$\lambda = \frac{1}{2}\left(\sum_{i=1}^{N_s} X_i \lambda_i + \frac{1}{\Sigma_{i=1}^{N_s} X_i/\lambda_i}\right). \tag{A.6}$$

Appendix A.4. Specific heat capacity

Specific heat capacity of gas component i ($c_{p,i}$), is calculated using *JANAF* tables [37]:

$$c_{p,i} = b_{0,i} + b_{1,i}T + b_{2,i}T^2 + b_{3,i}T^3 + b_{4,i}T^4 \tag{A.7}$$

where $b_{0,i}$, $b_{1,i}$, $b_{2,i}$, $b_{3,i}$, $b_{4,i}$ are constants for each gas. Specific heat capacity of gas mixture ($c_{p,g}$) is calculated based on mass averaging :

$$c_{p,g} = \Sigma(Y_i c_{p,i}). \tag{A.8}$$

Appendix B. Velocity correction factor calculation

$$\overrightarrow{v_i^c} = \overrightarrow{v_i} + \overrightarrow{v^c}, \tag{B.1}$$

$$\overrightarrow{v_i} = -\frac{D_{eff,i}}{Y_i}\nabla Y_i, \tag{B.2}$$

$$\overrightarrow{v^c} = -\Sigma\overrightarrow{v_i}, \tag{B.3}$$

where $D_{eff,i}$ is effective diffusion coefficient of gas component i, calculated by molecular diffusion and Knudsen diffusion as follows:

$$D_{eff,i} = [\frac{1}{D_i^m} + \frac{1}{D_i^{Kn}}]^{-1}.\frac{\epsilon}{\tau}, \tag{B.4}$$

where τ is tortuosity and D_i^{Kn} is Knudsen diffusion coefficient for gas component i, due to pore diffusion inside the porous particle:

$$D_i^{Kn} = \frac{d_{pore}}{3}\sqrt{\frac{8RT}{\pi M_i}} \tag{B.5}$$

where d_{pore} is average diameter of the pores, M_i is molecular mass of gas component i. Diffusion coefficient of i (D_i^m) is [38] :

$$D_i^m = \frac{1 - Y_i}{\Sigma_{j(j\neq i)} X_j/D_{ij}} \tag{B.6}$$

where Y_i is mass fraction of gas component i and X_j is the molar fraction of gas component j. Binary diffusion coefficient (D_{ij} in m^2/s) is calculated based on Fuller-Schettler-Giddings equation [39]:

$$D_{ij} = \frac{0.1031T^{1.75}\sqrt{\frac{1}{M_i} + \frac{1}{M_j}}}{p_{tot}((\Sigma\nu)_i^{\frac{1}{3}} + (\Sigma\nu)_j^{\frac{1}{3}})^2} \tag{B.7}$$

where $\Sigma\nu_i$ is diffusion volume of i-th gas in $10^{-6}\mathrm{m}^3/\mathrm{mol}$, M_i and M_j in g/mol, p_{tot} is total pressure in pascal.

Tortuosity τ is considered to be varying linearly with solid phase conversion:

$$\tau = \tau_0 + X_C(1 - \tau_0), \tag{B.8}$$

where τ_0 is initial tortuosity.

Appendix C. Comparison study-Property values

Data is not available for porosity (ϵ), initial pore diameter range ($d_{pore,0}$), density of char (ρ_s), relative velocity of air entering (U), initial tortuosity (τ_0), thermal conductivity of char (λ_s) and heat capacity of char ($c_{p,s}$). The range of values for each property obtained from literature were used for the simulations, which are shown in Table C.3. Information available in [27] is also shown in Table C.3. Two cases with highest and lowest possible conversion time based on porosity (ϵ) and average pore diameter (d_{pore}) selected for the validation is shown in the Table C.4.

Table C.3: Values used for properties in simulations: from [27] and for the data not available in [27] other values from literature is used. Here pore diameter is in nm, pressure is in atm, temperature is in K, Activation energy is in $\mathrm{kgm^2s^{-2}/mol}$ and pre-exponential factor is in $\mathrm{kg^{-0.46}m^{0.46}s^{-0.08}}$.

Property	**Values from literature**	**Values from [27]**	**This work**
Porosity (ϵ)	0.02-0.4 [40, 41]		0.4
Pore diameter range (d_{pore} (nm))	1-250 [42]		1
Density of char (ρ_s (kgm^{-3}))	1800-2200 [42]		1800
Relative velocity of air (U ($\mathrm{ms^{-1}}$))	0.1-1.0 [43]		0.1
Initial tortuosity (τ_0)	1.414 [44]		1.414
Thermal conductivity of char (λ_s)	0.13		0.13
Heat capacity of char ($c_{p,s}$)	1500		1500
Diameter of the particle (D (μm))		44	44
Pressure (p (atm))		5	5
Temperature of inlet (T_{in} (K))		1673	1673
Structure parameter (ψ)		1	1
Activation energy (E_A)		2.62×10^5	2.62×10^5
Pre-exponential factor (A_0)		1.19×10^9	1.19×10^9

Table C.4: Parameter variation in 2 cases simulated for the comparison with [27].

Parameter	**Value**	**Unit**	**Extreme I**	**Extreme II**
ρ_s	1800-2200	kg/m^3	1800	2200
$d_{pore,0}$	1-250 [42]	nm	250	1
U	1.0-0.1	m/s	0.1	0.1
ϵ	0.1-0.4	1.0	0.4	0.1

Appendix D. calculation of drag coefficient

The drag coefficient can be calculated as

$$C_d = \frac{\overrightarrow{F}_{p,x} + \overrightarrow{F}_{\text{vis},x}}{\frac{1}{2}\rho U_\infty^2(d_p)}, \tag{D.1}$$

when the pressure and viscous forces are given as

$$\overrightarrow{F}_p = \oint_S (p_{sur} - p_{ref})\overrightarrow{n}\, ds, \tag{D.2}$$

and

$$\overrightarrow{F}_{\text{vis}} = -\oint_S \mu(\nabla\overrightarrow{u} + \nabla\overrightarrow{u}^t)\overrightarrow{n}\, ds, \tag{D.3}$$

respectively. Here, the integration is over the surface S of the particle. In the above, p_{sur} and p_{ref} are the interpolated pressure at the particle surface and in the far field, respectively, and $\overrightarrow{n}$ is the unit vector in the surface-normal direction. Only the components $\overrightarrow{F}_p$ and $\overrightarrow{F}_{\text{vis}}$ in the direction of the mean flow were accounted for when calculating the drag coefficient since the other components are canceled out due to symmetry.

Appendix E. calculation of Nusselt number

$$q_{tot} = \Sigma(dA \times \lambda_p \nabla T_p) - \nabla.(\rho \overrightarrow{u} c_{p,g} T)_p, \tag{E.1}$$

$$\nabla.(\rho \overrightarrow{u} c_{p,g} T)_p = \oint \rho \overrightarrow{u} c_{p,g} T_p.ndA = \Sigma(\rho_p \overrightarrow{u}_{r,p} c_{p,g_p} T_p dA) \tag{E.2}$$

$$h_{therm} = \frac{q_{tot}}{A_p(T_\infty - T_{surfave})} \tag{E.3}$$

$$Nu = \frac{h_{therm} d_p}{\lambda} \tag{E.4}$$

Appendix E

Paper V

On the inaccuracies of point-particle approach for char conversion modeling

Thamali R. Jayawickrama[a,1], Nils Erland L. Haugen[a,b], Kentaro Umeki[a]

[a] *Energy Engineering, Div. Energy Science, Luleå University of Technology, 971 87 Luleå, Sweden*
[b] *Department of Thermal Energy, SINTEF Energy Research, Kolbjørn Hejes vei 1 A, 7491 Trondheim, Norway*

Abstract

Char conversion is a complex phenomenon that involves not only heterogeneous reactions, but also external and internal heat and mass transfer. Reactor-scale simulation often uses a point-particle approach (PPS) as submodels for char conversion because of its low computational cost. Despite a number of simplifications involved in the PPS, there are very few studies that systematically investigate the inaccuracies of the PPS. This study aims to compare and identify when and why the PPS deviates from resolved-particle simulations (RPS). Both PPS and RPS have been carried out for a char particle undergoing CO_2 gasification under zone II conditions (*i.e.,* pore diffusion control). Results showed significant deviations between RPS and PPS for the effectiveness factor, gas compositions, particle temperature, and particle diameter. The most significant sources of inaccuracies in the PPS are negligence of the non-uniform temperature inside the particle and inability to accurately model external heat transfer. At low effectiveness factor, the errors of intra-particle processes were dominant while the errors of external process became dominant at the effectiveness factor close to unity. Because it ignore non-uniform temperature, the PPS always predicted higher effectiveness factor than the RPS despite its accurate estimation of intra-particle mass diffusion effects. As a cosequence, the PPS failed to predict the particle size changes accurately. Meanwhile, no conventional term for external heat transfer could explain the inaccuracy, indicating other sources of errors such as 2D/3D asymmetry or penetration of external flows inside the particles.

[1] Corresponding author. thamali.rajika.jayawickrama@ltu.se

Manuscript *November 21, 2022*

Keywords: char gasification, point-particle method, particle-resolved simulation, Stefan flow

1. Introduction

Biomass is a source of renewable energy that is carbon neutral, since it absorbs CO_2 from the atmosphere during photosynthesis. Therefore, it is an attractive option for replacing fossil fuels to mitigate climate change effects. However, biomass is cumbersome to use directly as a source of energy. Gasification is a convenient way of utilizing biomass and other solid fuels and gas produced from the process has a wide range of applications. Entrained flow gasification has the highest share of large-scale gasifiers of coal in the world [1], and the process can produce high-quality syngas, which is favorable for the synthesis of biofuel [1, 2, 3]. However, entrained flow biomass gasification is still not at the industrial level due to some barriers [2, 4].

One way to study gasification is by using numerical simulations. A major challenge of numerical simulations is the large variation of time and length scales existing in the gasification process. As an example, particle sizes are very small ($\mathcal{O}(10^{-6} - 10^{-3})$ m) compared to the reactor size ($\mathcal{O}(10^{0} - 10^{1})$ m) of an entrained-flow gasifier. Due to the wide gap, not only in length scales but also in time scales, fully resolved simulations of entire gasifiers are not practical with contemporary computational resources and methods. In entrained flow biomass gasification, particles are suspended in the fluid, and the particles can therefore interact with the fluid or neighboring particles through momentum, heat, and mass transfer. The current state-of-the-art is to use sub-grid models to mimic small-scale phenomena (such as particle-fluid interactions) such that larger mesh sizes and time steps can be used. Therefore, the fidelity of simulations is highly dependent on the accuracy of the sub-grid models. One such method is the so-called point-particle (PP) method, where every particle is considered as a point in space occupying a zero volume. The momentum, heat, and mass transfer between a particle and the fluid are calculated through drag coefficient (C_D), Nusselt number (Nu), and Sherwood number (Sh) models, respectively. Furthermore, it is essential to have models to calculate the variation of particle diameter, density, and evolution of internal particle surface area with the progress of the heterogeneous reactions. As particles are considered as points in space (in the PP approach), properties such as temperature and gas compositions throughout

the particles are considered uniform. The change of reaction rates due to internal mass diffusion is often accounted for through the Thiele modulus and the associated effectiveness factor.

The most widely used constitutive models for C_D, Nu and Sh of a particle immersed in a bulk fluid were developed under simplified conditions, such as non-porous particle, isothermal conditions, neglecting neighbor particle effects, and neglecting effects of Stefan flow [5, 6, 7]. Recently, a lot of improvements in the models for C_D [8, 9, 10], Nu [8, 10, 11] and Sh [12] in terms of different shapes, the effect of porosity, the effect of Stefan flow, and effect of neighboring particles have been made. However, most recent works such as [13, 14, 15, 16] consider the constitutive models with an improvement for Stefan flow effects based on a model developed for Stefan flow in a quiescent environment. More surprisingly, no previous study has considered additional transport mechanisms in the boundary layer, such as Stefan flow-driven advection and Dufour effects. Therefore, it is vital to know how these models perform for the simulation of reactive particles in convective flows using PP methods[17]. Especially it is important for model improvements to elucidate what models predict better and the reasons for deviations. Such studies are possible only through the comparison of PP method results with results produced from fully particle-resolved simulations (both particle interiors and the boundary layer), which are rare in the literature.

Char gasification is the rate-limiting step during gasification. Apart from that, char gasification usually occurs in zone II, where the gasification reaction is controlled by both pore diffusion inside the char particle and chemical kinetics [18, 19, 20]. This makes the process harder to model in comparison with zone I and zone III processes. Zone I is where the reaction rate is controlled by chemical kinetics (diffusion is fast). Therefore, the reaction rate can be modeled by the kinetics rate. The particle density is varying and the diameter of the particle is constant. Zone III is where the reaction rate is controlled by diffusion. Here, the kinetics are fast, and diffusion rates are low, such that reactions occur only at the surface of the particle. Therefore, the density is constant, and the diameter varies in zone III. The reaction rate can be modeled by the mass transfer coefficient at the external surface of the particle. In zone II, both particle diameter and density decrease with the progress of the reactions. The apparent reaction rate of a char particle in zone II depends on many parameters, such as particle size, porosity, pore size distribution, diffusion rates of the gases into the pores, and intrinsic reaction rate [21]. Therefore, detailed studies of char conversion in zone II would

provide deeper insights into important parameters and modeling approaches.

The objective of this study is to identify and quantify the origins of inaccuracies in the point-particle approach for char gasification modeling. We carried out particle-resolved simulations of char particle gasification under different conditions. Both the exterior and interior of the particle are resolved. A non-equimolar gasification reaction is considered to create a Stefan flow. The results of simulations are compared with the point-particle approach. Then, we try to identify the differences between the two approaches and the reasons behind the differences. Suggestions for improvements of the point-particle approaches are made.

2. Methodology

2.1. Simulation case setup

Figure 1 shows the overall arrangement of the simulation cases. Particle-resolved simulations were carried out for a particle undergoing on single heterogeneous reaction ($C + CO_2 \rightarrow 2CO$). The particle is considered an infinitely long cylinder immersed in a uniform flow of bulk fluid consisting of N_2 and CO_2. Homogeneous reactions in the fluid are neglected. The particle is stationary and the bulk fluid enters the domain at slip velocity between the particle and the bulk fluid. Simulations were carried out for 6 cases representing the combinations of high and low values of the; Reynolds number, Stefan Reynolds number, and effectiveness factor. The upper and lower limits for these parameters were selected based on the realistic ranges in entrained-flow biomass gasification (EFBG). Table 1 shows details of the six cases. Table 2 shows the common parameters for all the simulation cases. The same parameters were later used also in the point particle simulations. The details of particle-resolved simulations are described in our previous work [22]. Therefore, only the point-particle calculation methodology is discussed in this paper.

2.2. Point particle model

2.2.1. Conservation of enthalpy and mass of the particle

Enthalpy of the particle varies due to diffusion of heat in the boundary layer (convective heat transfer), radiative heat transfer with the walls of the reactor, enthalpy changes due to the Boudouard reaction, advective heat transfer due to the Stefan flow and enthalpy transfer due to diffusion of gas

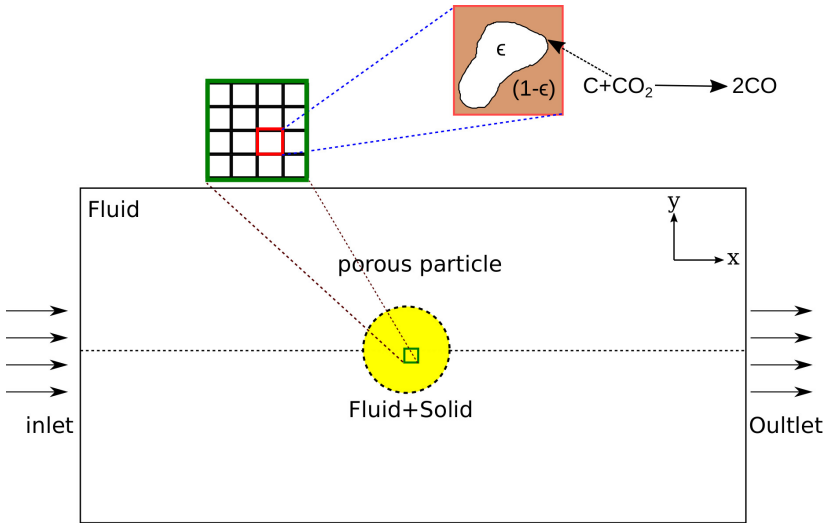

Figure 1: Overview of the simulation domain.

Table 1: List of parameters that were varied for different simulation cases. Effectiveness factor (η), particle Reynolds number (Re), and Stefan Reynolds number (Re_{Sf}) are the values estimated from the results of the resolved particle simulation.

Case	T_∞ (K)	p_∞ (atm)	d_p (μm)	U_∞ (m/s)	$Y_{CO_2,\infty}$ (-)	η	Re	Re_{Sf}
1	1999	1.807	189.3	0.45	0.512	0.23	0.5	0.09
2	1999	1.807	189.3	2.70	0.512	0.44	3.0	0.03
3	1851	4.201	442.6	0.44	0.512	0.21	3.0	0.04
4	1891	4.506	97.21	0.32	0.512	0.74	0.5	0.08
5	1891	4.506	97.21	1.93	0.512	0.69	3.0	0.02
6	1735	7.672	228.1	0.32	0.99	0.58	3.0	0.03

species (Dufour effect), such that the particle temperature evolution is given by:

Table 2: Common parameters used for all the simulation cases.

Type	**Parameter**	**Value**	**Unit**
Char	ρ_c	1200	kg m^{-3}
	λ_c	0.13	W m^{-2} s^{-1}
	$c_{p,c}$	1500	J kg^{-1} s^{-1}
	ϵ_0	0.7917	-
	τ_0	1.2632	-
	d_{pore}	250×10^{-9}	m
	ψ	1	-
Reaction kinetics [23]	E_A	2.62×10^5	J mol^{-1}
	A	1.19×10^9	s^{-1} MPa^{-n}
	n	0.46	-
	ΔH_0	17.78×10^5	J kg^{-1}
Radiation	α	0.8	-

$$[\epsilon\rho_g c_{p,g} + (1-\epsilon)\rho_c c_{p,c}]V_p\frac{dT_p}{dt} = hA_p(T_\infty - T_p) + \sigma\alpha A_p(T_w^4 - T_p^4) \\ -R_C\Delta H - Q_{Sf} - Q_{Dufour}, \tag{1}$$

where ρ_g is the gas density inside the particle, $c_{p,i}$ are specific heat of gas ($i = g$) and char ($i = c$) inside the particle, h is heat transfer coefficient, A_p is the external surface area of the particle, T_∞ and T_w are far-field gas and wall temperature, σ is Stefan-Boltzman coefficient, and α is the emissivity. Heat of reaction is temperature dependent, and expressed as:

$$\Delta H = \Delta H_0 + \sum_i (\nu_{i,\text{Boud}}\frac{W_i}{W_C}\int_{T_0}^{T_p} c_{p,i}\, dT), \tag{2}$$

where ΔH_0 is the heat of reaction at the standard temperature, ν_i is the stoichiometric coefficient of species i, W_i is the molar mass of species i and W_i is the molar mass of char. The advective transport of heat by the Stefan flow is expressed as:

$$Q_{Sf} = R_C\frac{W_{g,T_p}}{W_C}\int_{T_0}^{T_p} c_{p,g}dT_p. \tag{3}$$

The dofour term is the enthalpy transfer due to gas species diffusion to/out of the particle;

$$\begin{aligned} Q_{Dufour} = &\sum_i max\left\{0, h_{m,i}(C_{i,p} - C_{i,\infty})A_p \int_{T_0}^{T_p} cpdT\right\} \\ &- \sum_i max\left\{0, h_{m,i}(C_{i,\infty} - C_{i,p})A_p \int_{T_0}^{T_\infty} cpdT\right\} \end{aligned} \tag{4}$$

where $h_{m,i}$ (see Eq.14 for details) is the mass transfer coefficient of gas species i, and $C_{i,p}$ and $C_{i,\infty}$ are gas concentration of species i at particle surface and far-field, respectively.

The mass fraction of gas species inside the particle was calculated from the species balance considering convective mass transfer, consumption or generation by reactions, and advective transport by Stefan flow as:

$$\epsilon\rho_g V_p \frac{dY_{i,p}}{dt} = h_{m,i}W_i A_p(C_{i,\infty} - C_{i,p}) + \nu_{i,\text{Boud}}\frac{W_i}{W_C}R_C - M_{i,Sf}, \tag{5}$$

where $Y_{i,p}$ is the mass fraction of species i inside the particle, $h_{m,i}$ is the mass transfer coefficient of species i on a molar basis, C_i is the concentration of species i, and the advective transport of species by the Stefan flow is given by:

$$M_{i,Sf} = \left(\sum_i \nu_{i,\text{Boud}}\right) R_C \frac{W_{g,p}}{W_C} Y_{i,p}. \tag{6}$$

2.2.2. Heat and mass transfer coefficients

Heat transfer coefficient without the effect of Stefan flow was calculated by:

$$h_0 = \text{Nu}\lambda_{g,\infty}/d_p, \tag{7}$$

where the Nusselt number was calculated based on Whitaker [6] as:

$$\text{Nu} = (0.4\text{Re}_\infty^{\frac{1}{2}} + 0.06\text{Re}_\infty^{\frac{2}{3}})\text{Pr}_\infty{}^{0.4}(\frac{\mu_\infty}{\mu_p})^{\frac{1}{4}}. \tag{8}$$

Reynolds and Prandtl numbers were calculated from:

$$\text{Re}_\infty = \frac{\rho_\infty U_\infty d_p}{\mu_\infty}, \tag{9}$$

and

$$\mathrm{Pr}_\infty = \frac{c_{p,\infty}\mu_\infty}{\lambda_\infty}, \tag{10}$$

where subscript ∞ represents the gas properties based on far-field conditions and p based on particle conditions.

Mass transfer coefficient without the effect of Stefan flow was calculated by:

$$h_{m0,i} = \frac{D_{iN_2}\mathrm{Sh}_i}{d_p}, \tag{11}$$

in m s^{-1}, and D_{iN2} is the binary diffusion coefficient between N_2 and species i. The Sherwood number is also calculated based on the Whitaker model:

$$\mathrm{Sh}_i = (0.4\mathrm{Re}_\infty^{\frac{1}{2}} + 0.06\mathrm{Re}_\infty^{\frac{2}{3}})Sc_{i,\infty}^{0.4}(\frac{\mu_\infty}{\mu_p})^{\frac{1}{4}}, \tag{12}$$

where Schmidt number was calculated from:

$$\mathrm{Sc}_{i,\infty} = \frac{\mu_\infty}{\rho_\infty D_{iN_2,\infty}}. \tag{13}$$

Parameters with sub-script ∞ are calculated based on temperature (T_∞), CO_2 mass fraction ($Y_{CO_2,\infty}$), and CO mass fraction ($Y_{CO,\infty}$), all at far-field conditions.

The effects of Stefan flow were considered for both heat and mass transfer coefficients as [24]:

$$h_i = h_{0i} \cdot \frac{\phi_{Stf,i}}{e^{\phi_{Stf,i}} - 1}, \tag{14}$$

where the correction term for the heat transfer coefficient was calculated as:

$$\phi_{Stf,th} = \frac{1}{h_0}\frac{R_C c_{p,g}}{\pi d_p}, \tag{15}$$

and that for mass transfer coefficient was calculated as:

$$\phi_{Stf,mass,i} = \frac{\dot{n}_{total}}{h_{0,mass,i}}, \tag{16}$$

where

$$\dot{n}_{total} = \frac{R_C}{W_C A_p}\left(\sum_i \nu_{i,\mathrm{Boud}}\right). \tag{17}$$

2.2.3. Reaction rate

The rate of carbon consumption by the Boudouard reaction, R_C in kg s^{-1}, is calculated from the particle conversion, X_p, the initial void fraction of the particle, ϵ_0, the true density of char, ρ_c, and the volume of the particle, V_p, as:

$$R_C = \frac{dm_c}{dt} = (1-\epsilon_0)\rho_c V_p \cdot \frac{dX_p}{dt}. \tag{18}$$

The conversion rate considers the effects of intra-particle diffusion via the effectiveness factor as [23, 25]:

$$\frac{dX_p}{dt} = \eta \cdot k_c \cdot f(X_p), \tag{19}$$

where η is the effectiveness factor. An Arrhenius type expression with n-th order model was applied for the rate constant, k_c, as:

$$k_c = A \exp\left(-\frac{E_A}{RT_p}\right) p_{CO_2,p}^n, \tag{20}$$

where A is the pre-exponential factor, E_A is the activation energy, R is the ideal gas constant, T_p is particle temperature, and $p_{CO_2,p}$ is the partial pressure of CO_2 at the particle surface. The structure-function, representing the change of the specific surface area from the initial value is given by:

$$f(X_p) = \frac{\rho_p}{\rho_{p,0}} \sqrt{1 - \psi \log\left(\frac{\rho_p}{\rho_{p,0}}\right)}, \tag{21}$$

where ψ is the structure parameter determined form the initial pore structure. The effectiveness factor for the cylinder particles can be calculated as:

$$\eta = f_c \frac{1}{\phi} \cdot \frac{I_1(2\phi)}{I_0(2\phi)}, \tag{22}$$

where f_c is the correction factor as suggested in [26] and $I_i(a)$ is the modified Bessel function of i-th kind [27]. The Thiele modulus, ϕ, is calculated as [27]:

$$\phi = \frac{d_p}{4} \sqrt{\frac{(n+1)}{2D_{e,CO_2}} \frac{k_c f(X_p) \rho_{char}(1-\epsilon_0)}{W_C} \frac{RT}{p_{CO_2}}}, \tag{23}$$

where D_e is the effective diffusion coefficient of the porous particle. Calculation of D_e is shown in Appendix B.

2.2.4. Variation of particle diameter and density

The particle diameter is constant until the conversion at the surface of the particle is converted to a critical value of 99%. The surface conversion was calculated in parallel through the integration of local conversion rate at the particle surface as:

$$\frac{dX_s}{dt} = k_c \cdot f(X_s). \tag{24}$$

Once X_s reached critical conversion (95% in this study), the particle size is calculated based on [19]:

$$\frac{dr_p}{dt} = \frac{dm_p}{dt}\frac{1-\eta}{2\pi r_p \rho_p}, \tag{25}$$

where the particle density is calculated as:

$$\frac{d\rho_p}{dt} = \frac{dm_p}{dt}\frac{\eta}{\pi r_p^2}. \tag{26}$$

2.2.5. Calculation procedures

After deciding the time step for the point-particle calculations, temperature and gas species mass fractions were calculated using Eq.1 and 5. Then all the time-varying parameters were calculated using the Euler-explicit method at each time step. The more detailed sequence of point-particle calculations can be found in Appendix D. The point-particle results were compared with volume-averaged parameters from particle-resolved simulations for the 6 cases in Table 1.

3. Results and Discussion

3.1. The comparisons of the point-particle and resolved-particle approaches

Simulation results from the point-particle approach (PPS) and resolved-particle approach (RPS) were compared with respect to particle diameter (d_p), particle temperature (T_p), gas composition ($Y_{i,p}$), char conversion (X_p), char conversion rate ($\frac{dX_p}{dt}$) and the effectiveness factor (η). The data from RPS were averaged over the entire particle volume (volume-averaged) and over the external curved surface of the particle (surface-averaged). Changes in particle diameter from RPS were evaluated as the average distances between the initial center of the particle and the surface at the front, side, and back of the particle. It should be noted that cases $1-3$ have lower η values

$(0.2-0.4)$ than cases 4-6 $(0.6-0.7)$. Here, we call the cases $1-3$ as "low η cases" and the cases $4-6$ as "high η cases" .

Figure 2 shows char conversion plotted against time and char conversion rate plotted against char conversion for all the cases as a comparison between the RPS and the PPS. All the cases show a significant difference between two approaches. The predictions by the PPS and the RPS are closer to each other in high η cases (Fig. 2c) than in low η cases (Fig. 2a). Moreover, the PPS underestimate conversion rates for high η cases while they overestimate the conversion rates for low η cases. It indicates the existence of at least two sources of errors in the PPS.

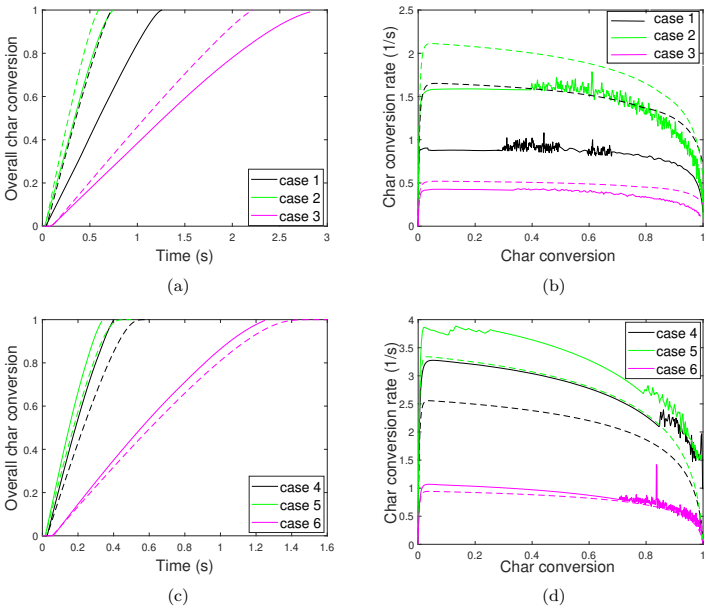

Figure 2: Time vs. char conversion (a and c) and char conversion vs. conversion rate (b and d). Solid lines - RPS; Dashed lines - PPS.

Another interesting observation is that the deviation of the PPS from the RPS is most profound for cases 1 and 4. The common properties of the case 1 and the case 4, apart from the particle Reynolds number, are high

ratios of Stefan Reynolds number to particle Reynolds number ($\mathrm{Re}_{Sf}/\mathrm{Re} \approx 0.16 - 0.18$). The ratios for other cases were $\mathrm{Re}_{Sf}/\mathrm{Re} \approx 0.007 - 0.013$, which are one order of magnitude lower than cases 1 and 4.

Figure 3 shows the effectiveness factor plotted against char conversion. The effectiveness factor of RPS here was calculated as the ratio between the sum of the local reaction rates from the simulations and the reaction rate based on the surface averaged temperature, mass fractions of the gas species, and average particle conversion (see Appendix E for more details). It clearly depicts that the PPS overestimate the effectiveness factors. The relative differences become more pronounced at lower η cases. It explains the overestimation of the conversion rate by the PPS at low η cases as it directly affects the conversion rates as shown in Eq. 19. Several potential reasons exist for overestimating the effectiveness factors in the PPS. Firstly, the PPS do not consider the change of temperature inside the particles even though it considers mass diffusion resistance. Reactions in this study are endothermic, and they can lower the internal particle temperatures. Therefore, in reality, the effectiveness factor can result in a much lower value than the model in the PPS with uniform temperature assumption. Secondly, the effectiveness factor in the PPS was developed based on the mass diffusion through quiescent gas inside the pores. In reality, the non-equimolar reactions create the net outgoing flows, which can increase the diffusion resistance.

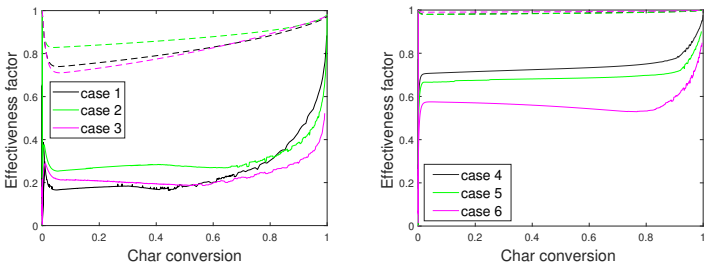

(a) (b)

Figure 3: Effectiveness factor variation as a function of char conversion for low η cases (a) and high η cases (b). Solid lines - RPS; Dashed lines - PPS.

As previously discussed in our studies [19, 18], the errors in the estimations of the effectiveness factor may result in the error in particle size prediction. Figure 4 shows the change of particle diameter at different char

conversions as the comparison of the PPS and RPS. The onset of particle shrinkage in the PPS was much later in char conversion than the RPS. This is reasonable because the PPS overestimated the effectiveness factors (Fig. 3), which delays the start of shrinkage with respect to char conversion [19, 18].

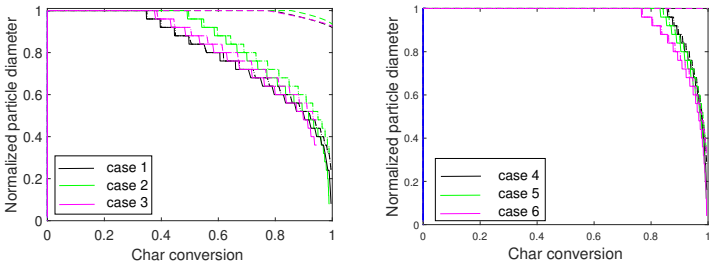

(a) (b)

Figure 4: Normalized particle diameter variation with char conversion for low η cases(a) and high η cases (b). Solid lines - RPS; Dashed lines - PPS. The diameter is normalized with the initial diameter of each case. Each case has three plots based on the diameter variation of the front, side, and back of the particle. In the future, diameter is referred to as the average of the three diameters.

Figure 5 shows the normalized particle temperature, $\theta = T_p/T_\infty$, as a function of char conversion. The temperature was normalized because each case has a different far-field temperature. The volume-averaged temperature was calculated based on the temperature field over the particle of the RPS. All the data show a similar general trend; the particle temperature quickly rose to around 90% of the far-field temperature and slowly increased toward the far-field temperature toward the end of the conversion. In all the cases, the particle temperatures from the PPS are lower than those from RPS. The difference was more significant for the cases with low η, which tends to have higher temperature difference inside the particle. The results clearly show that the heat of the reaction was large enough to affect the particle temperature. The difference in the particle temperature is quite important for the estimation of conversion rate as it is very sensitive to the temperature (Eq. 20). In fact, conversion rates of the high η cases from the PPS are lower than the RPS (Fig. 2d) despite overestimating the effectiveness factors by two-fold (Fig. 3b).

The PPS calculates the effectiveness factor to account for the effects of

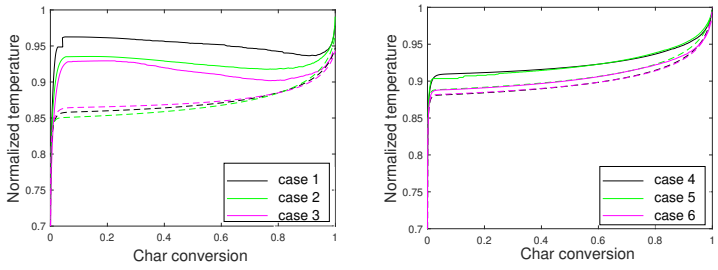

(a) (b)

Figure 5: Volume averaged temperature variation with char conversion. Solid lines - RPS; Dashed lines - PPS. Temperature is normalized with a far-field temperature of each case.

mass diffusion resistance under the assumption that the particle temperature is uniform. To have a better understanding of the gasification conditions inside the particle, contour plots of temperature from RPS are studied. Figure 6 shows the temperature contours for cases 1 and 4 at different char conversions. These cases have high $\mathrm{Re}_{Sf}/\mathrm{Re}$ ratios while case 1 has low η and case 4 has high η. It is apparent that there are non-negligible temperature gradients within the particle at all the conversion stages ($X_p = 0.1 - 0.8$) for both cases. In addition, case 1 (low η) shows asymmetric temperature distribution with the front side of the particle having lower temperature, indicating more intense reaction zones there. It is also an indication that the consumption of reactant gas (CO_2) at the front of the particle may affect the reactions at the back of the particle. Such phenomena have not been considered even with three-dimensional particle models in recent studies [28] because the direction of bulk gas flows are not considered in such studies. Case 1 (Fig. 6a) has about 50 K, and case 4 (Fig. 6b) has about 70 K of temperature difference within the particle, which results in the variation of local rate constant by $60 - 80\%$. All the cases in Table 1 have shown temperature differences close to or more than 50 K within the particle at the char conversions of $0.1 - 0.8$. Temperature contours of the other 4 cases are presented in Appendix C.

Figure 7 shows the contours of CO_2 mass fraction (Y_{CO_2}) for the cases 1 (low η) and 4 (high η). It is very clear that CO_2 mass fraction inside the particle is almost zero for case 1. We could say that there is strong diffusion resistance, and all the CO_2 that reaches the particle surface is consumed by reactions near the particle surface, which is similar to the zone III conditions.

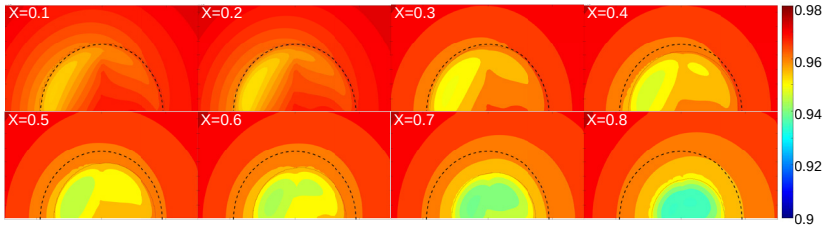

(a)

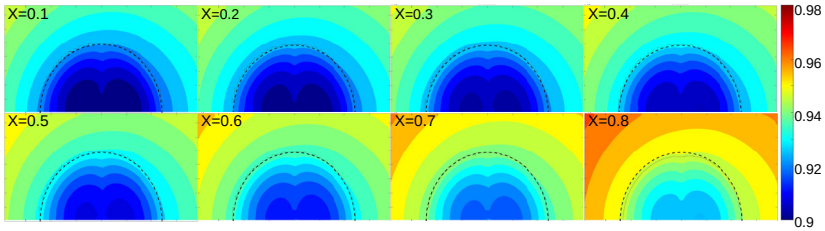

(b)

Figure 6: Temperature contours of case 1 (a) and case 4 (b) of the normalized temperature (T/T_∞, where T is the temperature at each point of the particle surface). Both cases have similar Reynolds numbers. Case 1 has low values of effectiveness factor, and case 4 has high values.

In fact, there is a low-temperature region near the particle surface (see Fig. 6) because of the heat of the reaction. To get a clearer idea about what is happening inside the particle with the reaction, Fig. 8 shows CO mass fraction (Y_{CO}) contours for the cases 1 and 4. CO (reaction products) is most likely generated near the external surface of the particle for case 1. The uniform CO distribution in case 1 shows that it has not only produced outward Stefan flow but also diffused inward and accumulated inside the particle.

Case 4 (high η) has non-zero but lower Y_{CO_2} inside the particle than at the particle surface. CO (reaction products) is most likely generated throughout the particle. The CO generated at the outer region of the particles may diffuse or advect outward from the particle and create a non-uniform Y_{CO} profile inside the particle.

The PPS assumes uniform temperatures within the particle, which did not happen in the RPS for the cases simulated in this work. In addition,

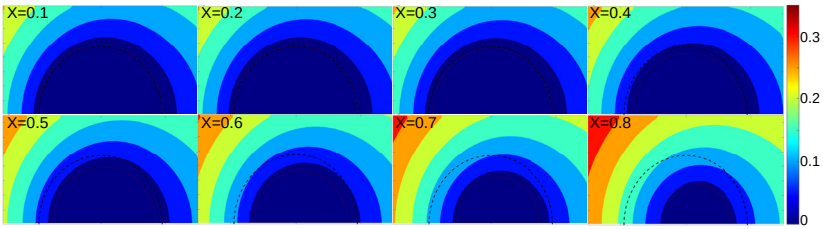

(a)

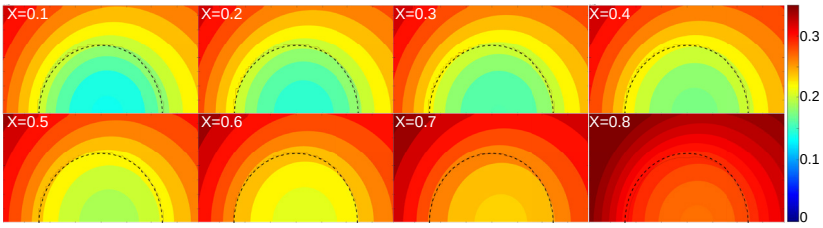

(b)

Figure 7: CO_2 mass fractions contours of case 1 (a) and case 4 (b). Both cases have similar Reynolds numbers. Case 1 has low values of effectiveness factor, and case 4 has high values.

effectiveness factor (η) correlations do not consider the convective effects due to reactions (Stefan flow) inside the particle. Finally, the 3D effects (asymmetrical thermophysical parameters inside the particles) are not considered in the PPS. These assumptions can be identified as potential sources of deviations between the results of the RPS and PPS. In addition, the deviation of particle temperature between the RPS and PPS (see Fig. 5) throws doubt upon the accuracy of external heat transfer models. The next section is dedicated to studying possible deviations between the two approaches in detail.

3.2. Origins of deviations between RPS and PPS

The simulation with a point-particle approach (PPS) applies various submodels and assumptions. Simulation with resolved particle approach (RPS) eliminates the use of some of the models and solves directly by numerical simulations, which are much closer to reality than the PPS. Therefore, the RPS results can be used to identify the sources of inaccuracies of the PPS.

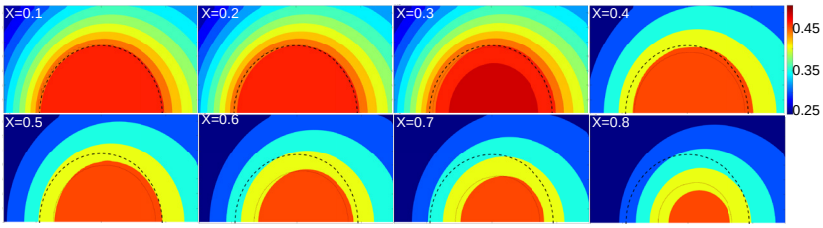

(a)

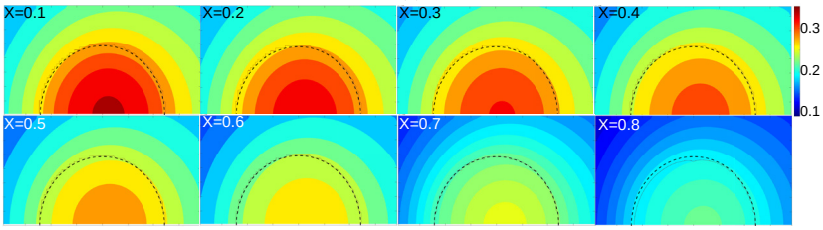

(b)

Figure 8: CO mass fractions contours of case 1 (a) and case 4 (b). Both cases have similar Reynolds numbers. Case 1 has low values of effectiveness factor, and case 4 has high values.

When used to model a reacting particle with a Stefan flow, the possible error sources can be listed as follows based on findings of the previous section and by studying the PPM equations:

1. 3D/2D asymmetry within the particle due to the effects of external flows
2. non-uniform temperature within the particle
3. neglecting the effects of convective flow inside the particle
4. external heat and mass transfer from/to the particle

In order to gain insights into these potential errors, we have carried out the following procedures to test the significance of some of the uncertainties:

1. RPS with significantly high thermal conductivity of char to examine the effects of non-uniform temperature within the particle,
2. PPS using particle surface-averaged temperature from the RPS results instead of solving Eq. 1 to examine the effects of the uncertainty in external heat transfer models,

3. PPS using particle surface-averaged Y_{CO_2} from the RPS instead of solving Eq. 5 to examine the effects of deviations due to external mass transfer models of CO_2,
4. PPS using both particle surface-averaged temperature and Y_{CO_2} to examine the uncertainty in internal particle phenomena independent of external processes except for the 3D asymmetry

Remaining uncertainties, such as the effects of intraparticle convective flow due to Stefan flow and 3-D/2-D asymmetry due to the interaction between internal and external phenomena, were set to be outside the scope of this work, and they will be addressed in future work by comparing the results with, for example, 1D particle models. The above 5 tests were carried out for case 4 (high η case with highest $\mathrm{Re}_{Sf}/\mathrm{Re}$ ratio). Char conversion was plotted against time while other parameters such as conversion rate, effectiveness factor, normalized particle diameter, particle temperature, and CO and CO_2 mass fraction were plotted against char conversion.

3.2.1. Non-uniform temperature inside the particle

Figures 9 and 10 show the comparisons between an ordinary RPS, a RPS with 100 times higher thermal conductivity of char, and PPS for case 4. The high conductivity RPS made an almost uniform temperature within the particle, which is in line with the underlying assumption of the PPS. However, the conversion rates of the high conductivity RPS (green-dashed-dot line in each figure) deviated more against the PPS than the ordinary RPS (black-solid line in each figure). The surface temperature of the ordinary RPS is higher than the average particle temperature, and reduces the external heat transfer due to conduction through the boundary layer. Therefore, the high conductivity RPS gives higher particle temperature (see Fig. 10a). Meanwhile, the effectiveness factor of the ordinary RPS, when considering only the distribution of Y_{CO_2}, is slightly higher but comparable to that of the high conductivity RPS. When the effects of the temperature is considered, the effectiveness factor of the ordinary RPS becomes significantly lower than the high conductivity RPS. Hence, the high conductivity RPS results in a faster char conversion rate (see Fig. 9a and 9b).

When looking closely at the particle temperature and mass fractions of CO_2 and CO (Fig. 10), the PPS underestimates the particle temperature and Y_{CO} while it overestimates Y_{CO_2}. The application of high conductivity RPS makes the deviation between the RPS and PPS even larger. It means

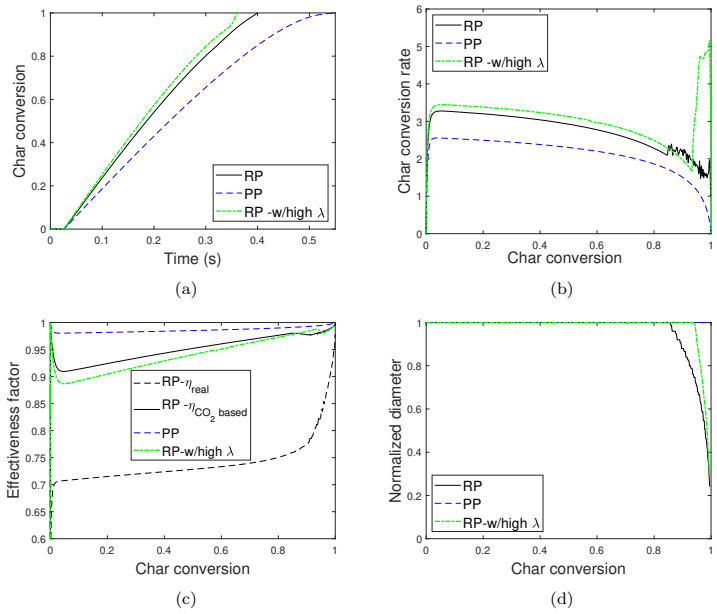

Figure 9: Comparison of resolved-particle approaches (RPS) with ordinary conductivity for char, RPS with high conductivity for char, and point-particle approach (PPS). (a) Time vs. char conversion. (b) Char conversion vs. char conversion rate. (c) Char conversion vs. effectiveness factor. Black-dashed lines is η_{real} and black-solid line is $\eta_{CO_{2,based}}$ for RPS (Appendix E for more details). (d) Char conversion vs. normalized particle diameter.

that the external heat transfer models used in the PPS underpredict the heat transfer rates while the external mass transfer models for the PPS overpredict the mass transfer rates.

In summary, uniform particle temperature assumption alone cannot explain the reason why the PPM cannot reproduce the conversion rates predicted from the RPS. It is highly likely that the two sources of errors, that is, the underestimation of external heat transfer rates and the uniform particle temperature assumptions, cancel their effects on conversion rates. Therefore, the current test does not give an individual insight of non-uniform temperature effects. Therefore, we will look further on the performance of PPS when removing the inaccuracies of external heat and mass transfer models.

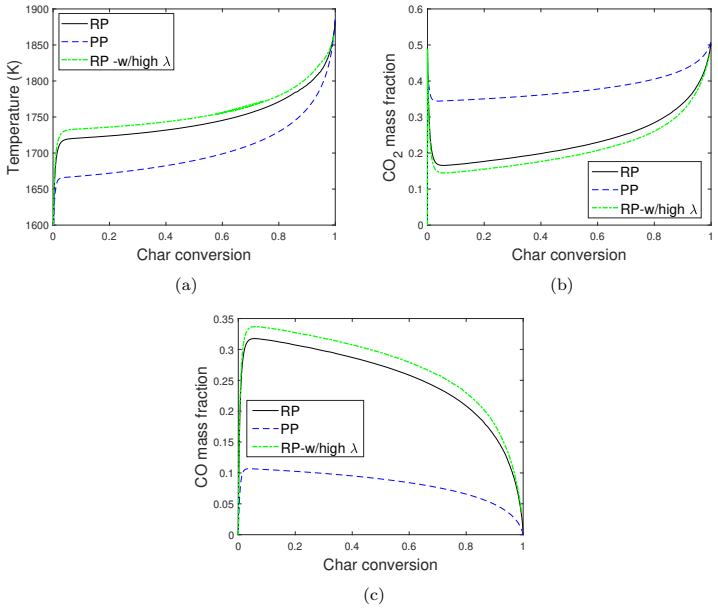

Figure 10: Comparison of resolved-particle approaches (RPS) with ordinary conductivity for char, RPS with high conductivity for char, and point-particle approach (PPS). (a) Char conversion vs. volume-averaged particle temperature. (b) Char conversion vs. CO_2 mass fraction. (c) Char conversion vs. CO mass fraction.

3.2.2. External heat transfer

When we use the average surface temperature from the RPS results in the PPS instead of solving the energy equation (Eq. 1), we can remove the inaccuracies created from the errors in the model terms for external heat transfer. The terms in question are heat transfer coefficient (h), the advective term due to Stefan flow (Q_{Sf}), and Dufour terms (Q_{Dufour}). Figures 11 and 12 examine how the PPS results improve by using the surface averaged temperature from the RPS results.

The largest improvement is in gas mass fractions (see Fig. 12b and 12c) although it can simply be the coincidence, considering the large deviation in the prediction of char conversion (Fig. 11a). High consumption (over-prediction) of the CO_2 and CO production in the particles is most likely

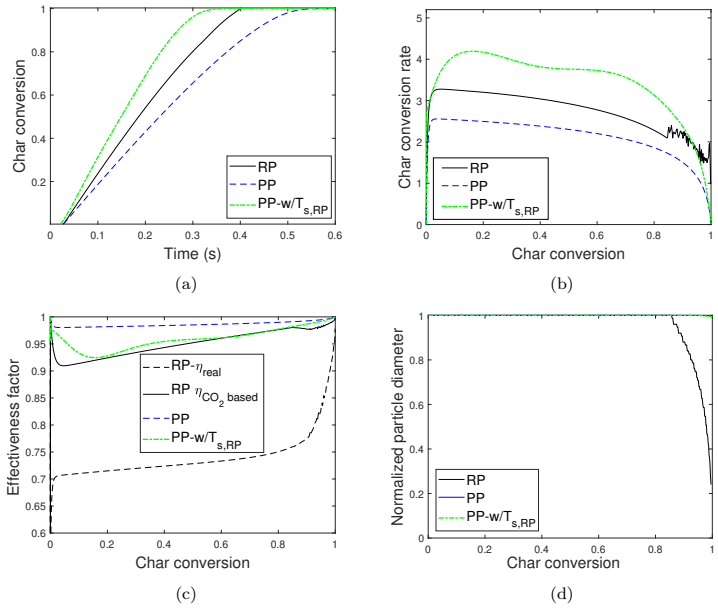

Figure 11: Comparison of the resolved-particle approach (RPS), the point-particle approach (PPS), and the PPS using average surface temperature from the RPS instead of Eq. 1. (a) Time vs. char conversion. (b) Char conversion vs. char conversion rate. (c) Char conversion vs. effectiveness factor. Black-dashed lines is η_{real} and black-solid line is $\eta_{CO_{2,based}}$ for RPS (Appendix E for more details). (d) Char conversion vs. normalized particle diameter.

compensated with the previously discussed overprediction of external mass transfer rates. When looking at particle temperature (Fig. 12a), the particle average temperature of the RPS is slightly lower than that of the surface-averaged temperature used in the PPS. The PPS with the given surface temperature shows a comparable effectiveness factor (Fig. 11c) to the RPS with the consideration of Y_{CO_2} variation only. It is still higher than the effectiveness factor of the RPS with the consideration of both temperature and mass fraction variations inside the particle. From these results, we can interpret that the deviation of the conversion rate originated from the failure of the PPM in considering the drop in the temperature inside the particle.

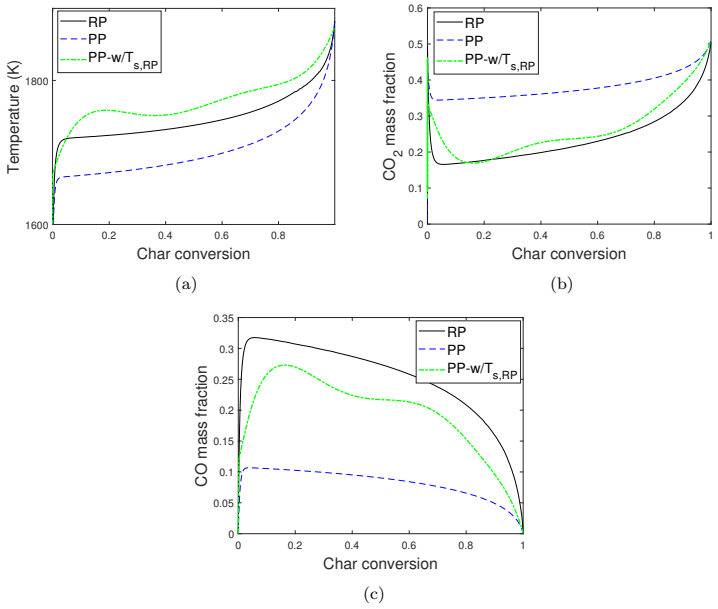

Figure 12: Comparison of the resolved-particle approach (RPS), the point-particle approach (PPS), and the PPS using average surface temperature from the RPS instead of Eq. 1. (a) Char conversion vs. volume-averaged particle temperature. (b) Char conversion vs. CO_2 mass fraction. (c) Char conversion vs. CO mass fraction.

Then, questions about the external heat transfer rates arise. The inaccuracies must be originated from the errors in h, Q_{Sf}, or Q_{Dufour}. We can examine the contribution of terms Q_{Sf}, Q_{Dufour}, $M_{i,Sf}$ by removing them from Equations 1 and 5. The effect of the Nusselt number (Nu) can be examined by replacing model-based Nu with Nu calculated from RPS. Figure 13 shows the volume-average temperature when the terms are removed (Q_{Sf}, Q_{Dufour}, $M_{i,Sf}$) or replaced by values from RPS (Nu). It shows that the effects of terms Q_{Sf}, Q_{Dufour}, $M_{i,Sf}$ are negligible compared to the effect of the Nusselt number. This can be seen from the improvement in the particle-averaged temperature by using Nu from RPS. We could say the rest of the deviation of the temperature could be due to hot gas entering the particle or something missing in the calculations.

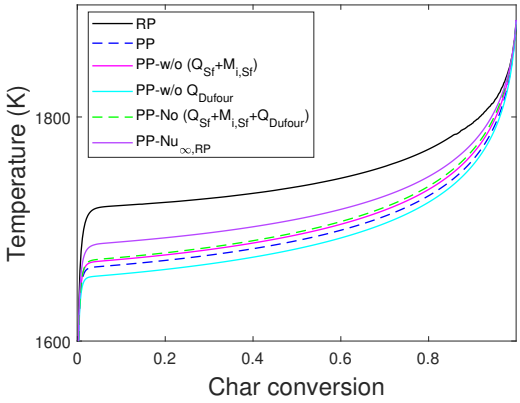

Figure 13: Comparison of the particle temperature from resolved-particle approaches (RPS) with point-particle approach (PPS) using different approaches. The exclusions of heat and mass transfer by advection due to Stefan flow, PP-w/o (Q_{Sf}+$M_{i,Sf}$), the exclusion of Dufour term, PP-w/o Q_{Dufour}, and the use of Nusselt number extracted from the RPS, PP-$Nu_{\infty,RP}$, in Eq. 1 and Eq. 5 were considered.

3.2.3. External mass transfer

As discussed in the previous section, the PPS seems to tend to overpredict mass transfer rates of CO_2. By eliminating the inaccuracy of external mass transfer rates, we can evaluate how errors of PPM in external heat transfer and uniform temperature assumption inside the particle compensate each other. Hence, we compared the PPS and RPS results with PPS results using the surface-averaged mass fraction of CO_2 from the RPS instead of solving Eq. 5 for CO_2 in this section. Figures 14 and 15 shows the comparison of results from the RPS and PPS with the PPS using given CO_2 mass fraction.

Instant observation is that the PPS results with the given mass fraction of CO_2 show a very close char conversion rate and particle temperature to those from RPM results. However, a large deviation from the RPS remains for the effectiveness factor, CO gas composition, and particle size changes. The deviation of CO is relatively expected because overprediction of the mass transfer rates of CO is not adjusted in the model. The PPS with the given mass fraction of CO_2 showed a higher effectiveness factor than the RPS, while their conversion rates showed similar values. This can be due to

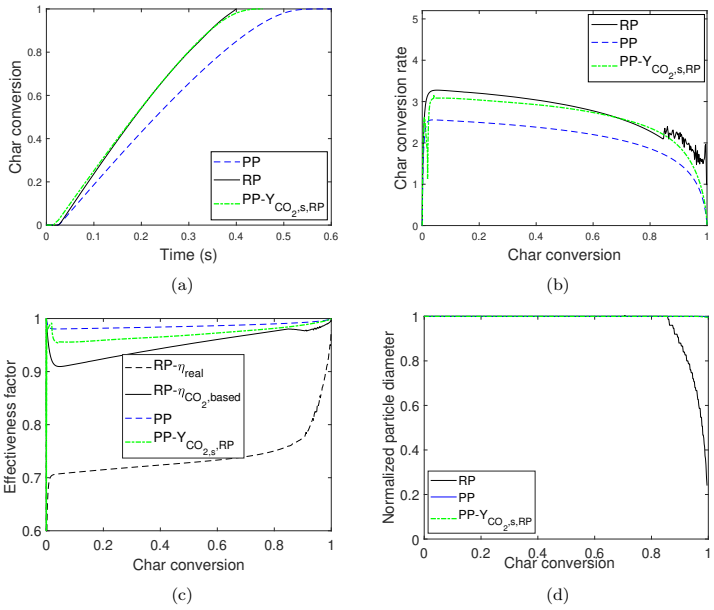

Figure 14: Comparison of resolved-particle approaches (RPS), point-particle approach (PPS), and PPS using the average surface mass fraction of CO_2 from RPS instead of solving Eq. 5. (a) Time vs. char conversion. (b) Char conversion vs. char conversion rate. (c) Char conversion vs. effectiveness factor. Black-dashed lines is η_{real} and black-solid line is $\eta_{CO_{2,based}}$ for RPS (Appendix E for more details). (d) Char conversion vs. normalized particle diameter.

the compensation of the high effectiveness factor in PPS with non-uniform temperature in RPS. In conclusion, it is a coincidence that the reaction rates of the two simulation results show a negligible difference in this case. The difference in conversion rates may become apparent under different reaction conditions, especially at different effectiveness factors.

3.2.4. Intra-particle heat and mass transfer

When the PPS is carried out by using both surface-averaged particle temperature and CO_2 mass fraction from the RPS, we can eliminate the inaccuracy of external heat and mass transfers. The comparison of PPS results

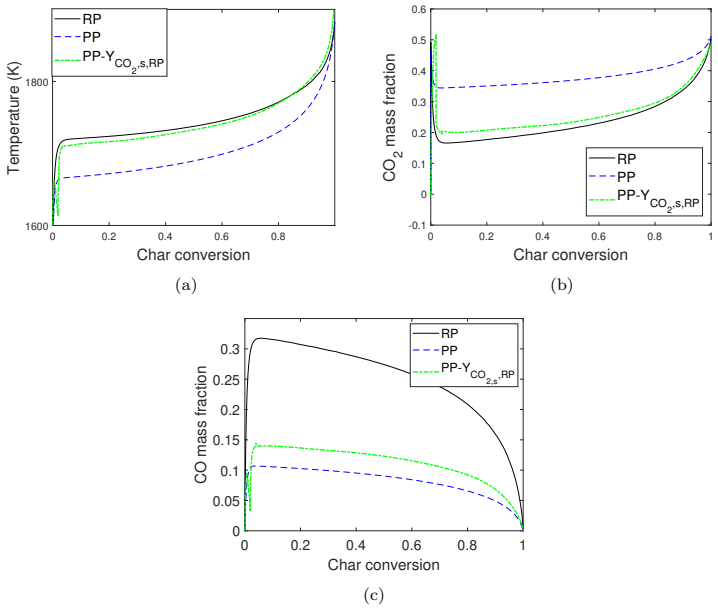

Figure 15: Comparison of resolved-particle approaches (RPS), point-particle approach (PPS), and PPS using the average surface mass fraction of CO_2 from RPS instead of solving Eq. 5. (a) Char conversion vs. volume-averaged particle temperature. (b) Char conversion vs. CO_2 mass fraction. (c) Char conversion vs. CO mass fraction.

with such treatment with the RPS results can highlight the inaccuracies in the intra-particle transport phenomena. Figures 16 and 17 show the results of such simulation cases, *i.e.,* the PPS using the pre-determined particle temperature and CO_2 mass fraction as surface averaged values in RPS results.

The effectiveness factor from the PPS using the given temperature and Y_{CO_2} shows a relatively similar value as the effectiveness factor of the RPS considering only the variation of Y_{CO_2} inside the particle (*i.e.,* no consideration of the effects of the temperature or local conversion variation). Nevertheless, the effectiveness factor of the PPS is slightly higher than that of RPS without temperature consideration. One potential reason for this deviation is the outward convective flow inside the particle. The effectiveness factor used in the PPS was developed based only on mass diffusion and without convec-

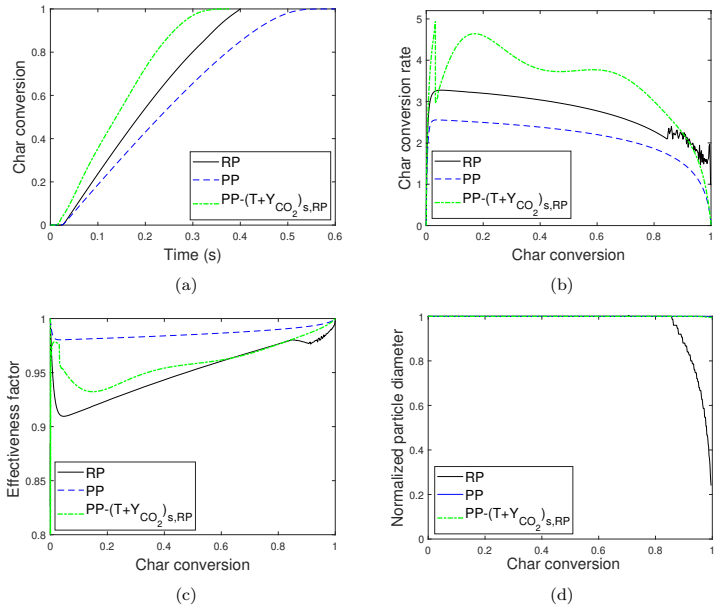

Figure 16: Comparison of resolved-particle approaches (RPS), point-particle approach (PPS), and PPS using the average surface mass fraction of CO_2 and average surface temperature from RPS instead of solving Eq. 5 and Eq. 1. (a) Time vs. char conversion. (b) Char conversion vs. char conversion rate. (c) Char conversion vs. effectiveness factor. Black-dashed lines is η_{real} and black-solid line is $\eta_{CO_{2,based}}$ for RPS (Appendix E for more details). (d) Char conversion vs. normalized particle diameter.

tive flows due to non-equimolar equations. When the real effectiveness factor of the RPS is used as a reference, the difference becomes more significant, which indicates that the effect of non-uniform temperature is larger than the effects of internal convective flows.

The PPS results do not indicate any onset of the decrease in particle size for this condition as well. The point particle approach does not include the effect of the non-uniform temperature inside the particle. This intrinsic inaccuracy makes the effectiveness factor of PPS always deviate from that of reality (or RPS) as long as the heat of the reaction is not zero. Therefore, it is reasonable that the PPS overestimates the critical conversion for the onset

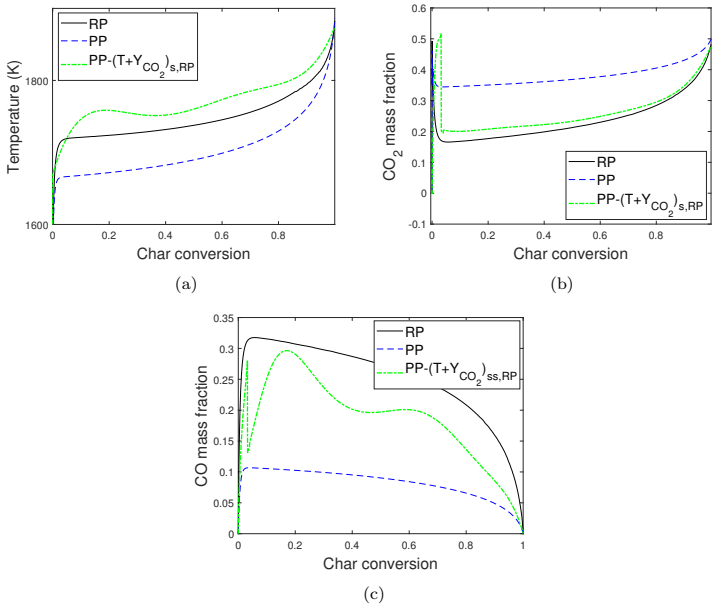

Figure 17: Comparison of resolved-particle approaches (RPS), point-particle approach (PPS), and PPS using the average surface mass fraction of CO_2 and average surface temperature from RPS instead of solving Eq. 5 and Eq. 1. (a) Char conversion vs. volume-averaged particle temperature. (b) Char conversion vs. CO_2 mass fraction. (c) Char conversion vs. CO mass fraction.

of particle shrinkage.

None of the tests discussed in sections 3.2.2-3.2.4 did not improve the prediction of variation in particle diameter. One reason is the inability of PPS to consider the effects of non-uniform porosity inside the particles caused by earlier stages of reactions for zone II conditions. When the effectiveness factor is significantly lower than unity, the porosity near the particle surface becomes higher than the particle core. Therefore, the inherent assumption of the effectiveness factor, that is, the uniform porosity inside the particles, increases the effectiveness factor at the later stage of conversion than the reality. This deviation can result in a delay in the onset of particle shrinkage by PPS.

4. Conclusions

A series of simulations using the resolved particle and point particle approaches highlighted a few important sources of inaccuracies when applying the point particle approach. None of the tests made the results of resolved particle approach (RPS) and point particle approach (PPS) match perfectly.

Analyses of external heat and mass transfer showed that existing models of external heat transfer underestimate and those of external mass transfer overestimate their rates. The overall effects of external heat and mass transfer are dominated by the low particle temperature prediction, mainly due to the strong temperature dependence of reaction rates.

Dominant source of inaccuracies for the intra-particle heat and mass transfer is the effects of non-uniform temperature distribution, *i.e.,* lower particle temperature due to endothermic reactions. Since the effectiveness factors commonly applied in char conversion models do not consider the effects of non-uniform temperature, the PPS always overestimates the effectiveness factor. The inaccuracy in predicting the effectiveness factor also results in the inability to predict the particle size changes.

When the inaccuracies of both external and internal heat and mass transfer are considered, the eventual outcome is dependent on the effectiveness factor because of the shift in their relative importance. When the effectiveness factors are relatively large (close to zone I conditions), the errors in external heat transfer dominate the overall conversion rates. When the effectiveness factors are smaller (near zone III conditions), the inaccuracy of using uniform particle temperature becomes more important, and the PPS tends to overestimate the conversion rates. Interestingly, this study sheds light on many occasions when one or more parameters from the PPS results agreed very well with the RPS, solely by the coincidence of two or more errors canceling each other. It strongly suggests that the accuracy of the point particle approach shall be examined thoroughly by comparing several parameters, preferably at a wide range of reaction conditions.

Other potential sources of errors, such as the 2D/3D asymmetry and intra-particle convective flows, were also identified. Future studies should include comprehensive comparisons of several different modeling approaches, such as the point particle approach, one-dimensional particle model, and multi-dimensional resolved-particle model with and without the direct solution of external flows.

Acknowledgment

The authors are grateful to the Swedish Research Council (Vetenskapsrådet) for financial support for the study (grant number: 2015-05588). The simulations were enabled by resources provided by the Swedish National Infrastructure for Computing (SNIC) at High-Performance Computing Center North (HPC2N), partially funded by the Swedish Research Council through grant agreement no. 2018-05973. We thank all the staff of HPC2N for their technical assistance. This work also benefited from computer resources made available through the Norwegian NOTUR program under the award NN9405K. N.E.L.H. acknowledge the Research project Gaspro, financed by the research council of Norway (267916) and the European Union's Horizon 2020 research and innovation program (No 764697).

References

[1] C. Higman, M. Burgt, Gasification, Gulf Professional Publishing, 2008.

[2] F. Weiland, Pressurized entrained flow gasification of pulverized biomass: Experimental characterization of process performance, Ph.D. thesis, LuleåUniversity of Technology (2015).

[3] P. A. Nikrityuk, B. Meyer (Eds.), Gasification Processes Modeling and Simulation, 1st Edition, Wiley-VCH, 2014.

[4] B. Goktope, Entrained Flow Gasification of Biomass Soot Formation and Flame Stability, Ph.D. thesis, Luleå University of Technology (2015).

[5] L. Schiller, A. Naumann, A drag coefficient correlation, Zeitschrift des Vereins Deutscher Ingenieure 77 (1935) 318–320.

[6] S. Whitaker, Forced Convection Heat Transfer Correlations for Flow in Pipes, Past Flat Plates, Single Cylinders, Single Spheres, and for Flow in Packed Beds and Tube Bundles, AIChE Journal 18 (1972) 361–371.

[7] W. Ranz, W. Marshall, Evaporation from drops, Chemical Engineering Progress 48 (3) (1952) 141–146.

[8] Y. Chen, P. Jiang, T. Xiong, W. Wei, Z. Fang, B. Wang, Drag and heat transfer coefficients for axisymmetric nonspherical particles: A LBM study, Chemical Engineering Journal 424 (nov 2021). doi:10.1016/J.CEJ.2021.130391.

[9] S. K. Sanjeevi, J. A. Kuipers, J. T. Padding, Drag, lift and torque correlations for non-spherical particles from Stokes limit to high Reynolds numbers, International Journal of Multiphase Flow 106 (2018) 325–337. doi:10.1016/j.ijmultiphaseflow.2018.05.011.

[10] A. Richter, P. A. Nikrityuk, Drag forces and heat transfer coefficients for spherical, cuboidal and ellipsoidal particles in cross flow at sub-critical Reynolds numbers, International Journal of Heat and Mass Transfer 55 (4) (2012) 1343–1354. doi:10.1016/j.ijheatmasstransfer.2011.09.005.

[11] H. Ma, Y. Zhao, Convective heat transfer coefficient for a rod-like particle in a uniform flow, International Journal of Heat and Mass Transfer 147 (2020) 118742. doi:10.1016/j.ijheatmasstransfer.2019.118742.

[12] M. G. Nugraha, R. Andersson, B. Andersson, On the Sherwood number correction due to Stefan flow, Chemical Engineering Science 249 (2022) 117292. doi:10.1016/j.ces.2021.117292.

[13] M. Muto, K. Yuasa, R. Kurose, Numerical simulation of ignition in pulverized coal combustion with detailed chemical reaction mechanism, Fuel 190 (2017) 136–144. doi:10.1016/j.fuel.2016.11.029.

[14] Y. Bai, K. Luo, K. Qiu, J. Fan, Numerical investigation of two-phase flame structures in a simplified coal jet flame, Fuel 182 (2016) 944–957. doi:10.1016/J.FUEL.2016.05.086.

[15] M. Rieth, A. M. Kempf, A. Kronenburg, O. T. Stein, Carrier-phase DNS of pulverized coal particle ignition and volatile burning in a turbulent mixing layer, Fuel 212 (2018) 364–374. doi:10.1016/J.FUEL.2017.09.096.

[16] K. Luo, H. Wang, J. Fan, F. Yi, Direct Numerical Simulation of Pulverized Coal Combustion in a Hot Vitiated Co-flow, Energy and Fuels (2012). doi:10.1021/ef301253y.

[17] R. Cai, K. Luo, H. Watanabe, R. Kurose, J. Fan, Recent advances in high-fidelity simulations of pulverized coal combustion, Advanced Powder Technology 31 (7) (2020) 3062–3079. doi:10.1016/J.APT.2020.05.001.

[18] T. Kreitzberg, A. Phounglamcheik, N. E. L. Haugen, R. Kneer, K. Umeki, A shortcut method to predict particle size changes during char combustion and gasification under regime ii conditions, Combustion Science and Technology 194 (2) (2022) 272–291. doi:10.1080/00102202.2019.1678919.

[19] N. H. L. Erland, M. B. Tilghman, R. E. M. Mitchell, The conversion mode of a porous carbon particle during oxidation and gasification, Combustion and Flame 161 (2014) 612–619. doi:10.1016/j.combustflame.2013.09.012.

[20] M. B. Tilghman, N. Erland, L. Haugen, R. E. Mitchell, Comprehensive Char Particle Gasification Model Adequate for Entrained-Flow and Fluidized-Bed Gasifiers, Energy and Fuels (2016). doi:10.1021/acs.energyfuels.6b02148.

[21] N. E. L. Haugen, B. K. Y. Loong, R. E. Mitchell, Numerical approaches for thermochemical conversion of char, Progress in Energy and Combustion Science 91 (jul 2022). doi:10.1016/J.PECS.2022.100993.

[22] Thamali R. Jayawickrama; Nils Erland L. Haugen; Matthaus U. Babler; M.A. Chishty; Kentaro Umeki, Drag and Nusselt number during heterogeneous char reactions: particle-resolved approach, Manuscript, submitted (2022).

[23] S. Kajitani, N. Suzuki, M. Ashizawa, S. Hara, CO2 gasification rate analysis of coal char in entrained flow coal gasifier, Fuel 85 (2005) 163–169. doi:10.1016/j.fuel.2005.07.024.

[24] J. J. Murphy, C. R. Shaddix, Combustion kinetics of coal chars in oxygen-enriched environments, Combustion and Flame 144 (2006) 710–729. doi:10.1016/j.combustflame.2005.08.039.

[25] S. Kajitani, Y. Zhang, S. Umemoto, M. Ashizawa, S. Hara, Co-gasification reactivity of coal and woody biomass in high-temperature gasification, Energy and Fuels 24 (1) (2010) 145–151. doi:10.1021/ef900526h.

[26] J. Hong, W. C. Hecker, T. H. Fletcher, Improving the Accuracy of Predicting Effectiveness Factors for mth Order and Langmuir Rate Equations in Spherical Coordinates, Energy and Fuels 14 (3) (2000) 663–670. doi:10.1021/EF9902193.

[27] O. Levenspiel, Chemical Reaction Engineering, 3rd Edition, John Wiley & Sons, 1999.

[28] T. Martí-Rosselló, J. Li, L. Lue, O. Karlström, A. Brink, Comprehensive Assessment of Particle-Scale Modeling for Biomass Pyrolysis: One-Dimensional versus Three-Dimensional Models, Energy and Fuels 35 (12) (2021) 9937–9949. doi:10.1021/ACS.ENERGYFUELS.1C00283.

[29] Shen, V.K., Siderius, D.W., Krekelberg, W.P., and Hatch, H.W., Eds. (Ed.), No TNIST Standard Reference Simulation Websiteitle, NIST Standard Reference Database Number 173, National Institute of Standards and Technology, Gaithersburg MD, 20899,, 2022. doi:10.18434/T4M88Q.

[30] N. Babkovskaia, N. Haugen, A. Brandenburg, A high-order public domain code for direct numerical simulations of turbulent combustion, Journal of Computational Physics 230 (1) (2011) 1–12. doi:10.1016/j.jcp.2010.08.028.

[31] Don W. Green, James O. Maloney, Robert H. Perry (Eds.), Perry's chemical engineering handbook, 7th Edition, McGraw-Hill, 1997.

Appendix A. Thermophysical property calculation

Appendix A.1. Dynamic viscosity

Dynamic viscosity of a gas component i (μ_i), is calculated using Sutherland formula:

$$\mu_i = \frac{A_{s,i}\sqrt{T}}{1 + \frac{T_{s,i}}{T}}, \tag{A.1}$$

where A_s and T_s are constants. The viscosity of the gas mixture is calculated as follows;

$$\mu = \sum_{i=1}^{N_s} \frac{X_i \mu_i}{\Sigma_{j=1}^{N_s} X_j \phi_{ij}}, \tag{A.2}$$

where X_i is molar fraction of gas component i, N_s is number of gas components and ϕ_{ij} is calculated as follows;

$$\phi_{ij} = \frac{1}{\sqrt{8}} \left(1 + \frac{Mi}{M_j}\right)^{-1/2} \left\{1 + \left(\frac{\mu_i}{\mu_j}\right)^{1/2} \left(\frac{M_j}{M_i}\right)^{1/4}\right\}^2, \tag{A.3}$$

where M_i is molar mass of gas component i.

Appendix A.2. Density of the fluid

Density is calculated using state equation for the gas mixture:

$$\rho = \frac{pM}{RT}, \tag{A.4}$$

where p is the pressure at the *outlet* boundary of the simulation domain and $M = \Sigma_{i=1}^{N_s} m_i X_i$.

Appendix A.3. Thermal conductivity

Thermal conductivity of a gas component i (λ_i) is calculated using:

$$\lambda_i = R_{c_p}(a_{0,i} + a_{1,i}T + a_{2,i}T^2 + a_{3,i}T^3 + a_{4,i}T^4), \tag{A.5}$$

and mixture gas density (λ_g) is calculated based on molar averaging :

$$\lambda = \frac{1}{2}\left(\sum_{i=1}^{N_s} X_i \lambda_i + \frac{1}{\Sigma_{i=1}^{N_s} X_i/\lambda_i}\right). \tag{A.6}$$

Appendix A.4. Specific heat capacity

Specific heat capacity of gas component i ($c_{p,i}$), is calculated using *JANAF* tables [29]:

$$c_{p,i} = b_{0,i} + b_{1,i}T + b_{2,i}T^2 + b_{3,i}T^3 + b_{4,i}T^4 \tag{A.7}$$

where $b_{0,i}$, $b_{1,i}$, $b_{2,i}$, $b_{3,i}$, $b_{4,i}$ are constants for each gas. Specific heat capacity of gas mixture ($c_{p,g}$) is calculated based on mass averaging :

$$c_{p,g} = \Sigma(Y_i c_{p,i}). \tag{A.8}$$

Appendix B. Effective diffusion coefficient

$$D_{eff,i} = [\frac{1}{D_i^m} + \frac{1}{D_i^{Kn}}]^{-1} . \frac{\epsilon}{\tau}, \tag{B.1}$$

where τ is tortuosity and D_i^{Kn} is Knudsen diffusion coefficient for gas component i, due to pore diffusion inside the porous particle:

$$D_i^{Kn} = \frac{d_{pore}}{3}\sqrt{\frac{8RT}{\pi M_i}} \tag{B.2}$$

where d_{pore} is average diameter of the pores, M_i is molecular mass of gas component i. Diffusion coefficient of i (D_i^m) is [30] :

$$D_i^m = \frac{1 - Y_i}{\Sigma_{j(j\neq i)} X_j / D_{ij}} \tag{B.3}$$

where Y_i is mass fraction of gas component i and X_j is the molar fraction of gas component j. Binary diffusion coefficient (D_{ij} in m^2/s) is calculated based on Fuller-Schettler-Giddings equation [31]:

$$D_{ij} = \frac{0.1031 T^{1.75} \sqrt{\frac{1}{M_i} + \frac{1}{M_j}}}{p_{tot}((\Sigma\nu)_i^{\frac{1}{3}} + (\Sigma\nu)_j^{\frac{1}{3}})^2} \tag{B.4}$$

where $\Sigma\nu_i$ is diffusion volume of i-th gas in $10^{-6} m^3/mol$, M_i and M_j in g/mol, p_{tot} is total pressure in pascal.

Tortuosity τ is considered to be varying linearly with solid phase conversion:

$$\tau = \tau_0 + X_C(1 - \tau_0), \tag{B.5}$$

where τ_0 is initial tortuosity.

Appendix C. Temperature contours inside the particle

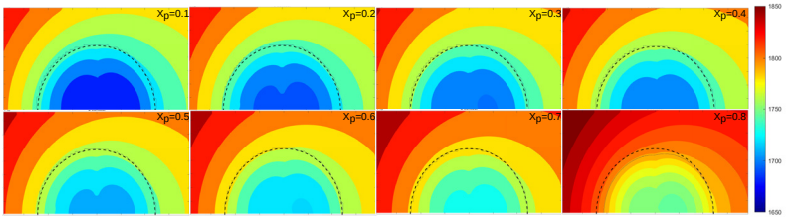

(a)

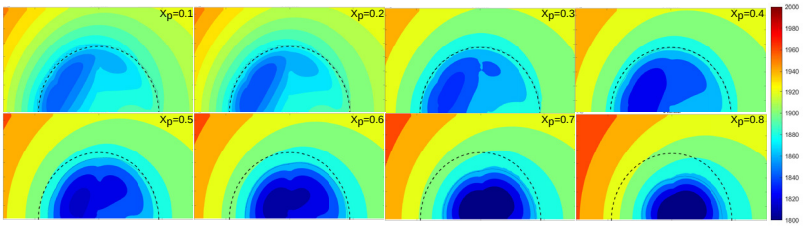

(b)

Figure C.18: Temperature contours of case 5 (a) and case 2 (b). Both cases have similar Re. η is in high range for case 5 and low range for the case 2.

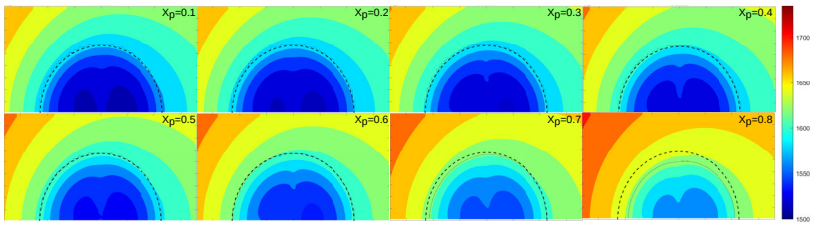

(a)

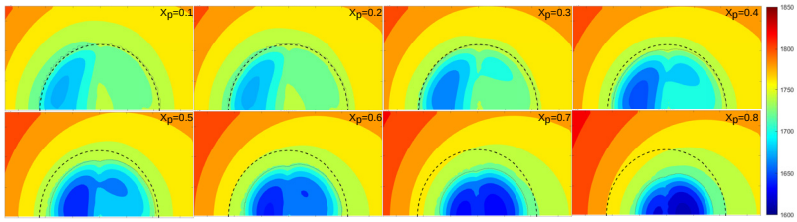

(b)

Figure C.19: Temperature contours of case 6 (a) and case 3 (b). Both cases have similar Re. η is in high range for case 6 and low range for the case 3.

Appendix D. Calculation procedure of the point-particle method

The below sequence is carried out for the point-particle calculations. Different time steps (Δt) were tested for convergence of results.

1. Define time step (Δt), initial conditions ($e.g., d_p, \rho_p$) and values ($e.g., \eta, f(X)$), far-field conditions ($e.g., U_\infty, T_\infty$) and all constants necessary for calculations,
2. calculate all the thermo-physical properties using the models
3. calculate heat transfer coefficients and using enthalpy conservation of the particle, calculate the new T_p at $\Delta t \times i$,
4. calculate mass transfer coefficients and using mass conservation of the particle (each specie), calculate the new Y_{CO}, Y_{CO_2} at $\Delta t \times i$,,
5. calculate new effectiveness factor (η) based on analytical methods of Thiele modulus, (Th) at $\Delta t \times i$,
6. calculate the mass conversion (X_c) at $\Delta t \times i$,
7. calculate the new diameter (d_p) at $\Delta t \times i$,

8. calculate the new density (ρ_p) at $\Delta t \times i$,
9. go to step 2 and repeat until step 8 for time, $\Delta t \times (i + 1)$.

Appendix E. Calculation of effectiveness factor

Effectiveness factor (η) is:

$$\eta = \frac{Actual\ overall\ particle\ consumption\ rate}{Particle\ consumption\ rate\ at\ particle\ surface}. \tag{E.1}$$

η can be calculated as follows based on RPS:

$$\eta_{real} = \frac{\Sigma f(X_{cell}) k_{c,cell} p^n_{CO_2,cell}}{n_{cells} f(X_{avg}) k_{c,surf-avg} p^n_{CO_2,surf-avg}}, \tag{E.2}$$

where $surf - avg$ is values based on averaging over the outer surface of the particle. When it is important to know only the effect of gas composition, we can calculate η as follows:

$$\eta_{CO_{2,based}} = \frac{\Sigma (X_{avg}) k_{c,surf-avg} p^n_{CO_2,cell}}{n_{cells} f(X_{avg}) k_{c,surf-avg} p^n_{CO_2,surf-avg}}. \tag{E.3}$$

Department of Engineering Sciences and Mathematics
Division of Energy Science

ISSN 1402-1544
ISBN 978-91-8048-202-8
ISBN 978-91-8048-203-5

Luleå University of Technology 2022

Print: Lenanders Grafiska, 455133

LULEÅ
UNIVERSITY
OF TECHNOLOGY